The Dual Development of an Optical Tomographic Scanner and Three Dimensional Gel Dosimeter for Complex Radiotherapy Verification

Alan D. Heathcote

Department of Physics
University of Hull

Thesis submitted for the degree of Doctor of Philosophy (PhD)
at the University of Hull

Jan 2008

Abstract

The state-of-the-art radiotherapy delivery treatments available today require that the intended dose distributions delivered are verified by volumetric gel dosimetry. The development of tissue equivalent gel dosimeters that provide an integrated assessment of the dynamic treatments, are primarily imaged with Magnetic Resonance Imaging (MRI).

This thesis describes the dual development and assessment of an optical tomographic scanner and normoxic gel dosimeter. MRI centers are currently limited in both time and resources in providing the routine imaging necessary for treatment verification. An alternative bench top imaging modality has been designed, built and developed to provide both complementary and comparable observations to MRI. It is hoped that this cost effective optical imaging system could alleviate this technological reliance. The optical tomography scanner is evaluated from a series of investigations into the capabilities and limitations of optical tomographic imaging used in conjunction with gel dosimetry.

Previously, the manufacture of gel dosimeters required anoxic environments in which the presence of oxygen in the dosimeter is limited. This requirement limited the production of gel dosimeters to chemistry laboratories that possessed the required technical expertise. MRI and optical imaging have been used to investigate the properties, dose response and the batch-to-batch reproducibility of a normoxic MAGIC gel dosimeter.

The results obtained are encouraging having shown successfully reconstructed optical images obtained from various dose distributions delivered to the MAGIC gel dosimeter.

Acknowledgments

I would like to firstly to acknowledge and thank the late Dr Alan Jenner and my external NHS supervisor Professor Andrew Beavis, for their support and encouragement during this period of research. I must also express my gratitude to Dr Gary Liney for all his help and enthusiasm concerning the MRI scanning, imaging and analysis of the gels, of which played a large part in my research.

I would also like to thank the late Alan Boyer, the late Paul Monk and Gordon Sowersby for all their expertise and tireless hard work they gave me during the scanner development.

The submission of this thesis would not have been possible without the contribution and encouragement given to me by Professor Peter Dyer who at a very late stage agreed to help me by giving me his suggestions and opinions and vitally by proof reading the thesis. I would also particularly like to thank Dr Simon Macleod for generously giving up his time to help proof read the thesis, also Dr Andrew Critchley for his help and understanding during this writing up period.

And finally, to my family and friends for all their loving support they have given me over these many years.

TABLE OF CONTENTS

List of Figures

Figure [2-1] Schematic, showing the development of the CT scanner from a) the 1st generation architecture using a rotate and translate method to detect the X-ray pencil beam used for scanning. The 2nd generation is shown in b). Here the imaging time is reduced due to the diverging fan beam and multiple detectors used. The 3rd and the 4th generation scanning geometries, c) and d) respectively, incorporate both moving source and detectors to further reduce scanning times. As described previously, the 5th generation scanner has a fixed detector bank that covers the full 360 degree arc.

Figure [2-2] Image illustrating a conventional chest X-ray radiograph of a patient. Reproduced from http://science.cancerresearchuk.org/.

Figure [2-3] Illustration of the principle of accumulative radiation therapy where radiation beams are combined to deliver dose to the tumour at the beam cross over region of interest. The radiation beam in both cases originates from the top of the images at 0 cm depth. The scale on both images shows higher absorbed doses within the red regions conversely the blue regions indicate low levels of absorbed dose.

Figure [2-4] a) Transaxial 2D CT image of the patient's abdomen, b) Transaxial 2D computerised interpretation of the 2D CT image, c) 3D computer simulation of the tumour volume (TV) and organs at risk (OAR) and d) showing a 3D rendering of the patients abdomen. Reproduced from http://science.cancerresearchuk.org/.

Figure [2-5] Illustration of the dynamic treatments of IMRT. Through a) to d) the multi-leaf collimators (MLC's) are continuously changing during the irradiation process and treatment plan. This is shown by the changing pink regions and details the shaped x-ray beam passing through the 10 cm by 10 cm collimator. This dynamically changes the radiation flux, field and dose incident upon the patient during the treatment plan.

Figure [2-6] A series of images showing a) the prostate and region of interest (ROI), b) the seminal vesicles, c) the bladder and d) the rectum. Reproduced from http://www.geocities.jp/nekoone2000v/BBS/physical/comp_methodEnglish.html.

Figure [2-7] Prostate treatment plans from a) two opposing beams, b) four beams, c) a treatment plan from 3D–CRT and d) an IMRT treatment plan. Reproduced from http://www.geocities.jp/nekoone2000v/BBS/physical/comp_methodEnglish.html.

Figure [2-8] Diagram showing the simplified steps discussed in this thesis.

Figure [3-1] A simplified illustration of the projections required for tomographic image reconstruction where $\mu(x, y)$ are the Cartesian sampling points within the object medium. Here two projections, P1 and P1+n, illustrate the pathlengths and the cross over data points (sampling) the laser light source defines through the object medium. For a comprehensive reconstructed image 100 to 180 projections would be required.

Figure [3-2] Initial image of a magic box problem with a 6 by 6 matrix showing in (a) the unknown elements within the box and in (b) the corresponding projections taken to provide the resulting gross attenuation values.

Figure [3-3] Illustration of the first back-projection taken shown in a) and the corresponding back-projected image this generates in b).

Figure [3-4] Illustration of the second back-projection taken shown in a) and the corresponding generated back-projected image in b).

Figure [3-5] Illustration of the accumulative back-projected values a) and image b) from the previous two axis examples shown in Figures [3-4] and [3-5].

Figure [3-6] Showing the comparison between $\mu(x, y)$ and the resulting attenuation values (navy blue squares shown in b) derived from two simple back projections.

Figure [3-7] Showing, a-c), the associated attenuation distributions from two projections of the metal cylinder (see Figure [5-2]), taken at 0 and 90 degrees and, d), the corresponding Fourier domain sampling. The degree of sampling is proportional to the number of projection elements (10 shown here) and can be inferred from the number of points on both the x and y axis shown in the 2D Fourier domain.

Figure [3-8] Showing in a), a more thorough sampling of the spatial domain. The black dots represent the elements within the projections from which data is collected and relates the degree of sampling undertaken during data collection and therefore the available image resolution upon reconstruction. The degree of the sampling shown in b) would be obtained from an infinite number of projections i.e. taking the limits of projection increments tending to zero. The presentation of data in Radon space in 2-D image form is often called a sinogram and is shown in c). The sinogram represent the accumulation of projection data through 0-360 degrees showing the attenuated blue regions and the unattenuated red regions during the tomographic scanning. The resulting back-projected image shown in d) illustrates the high-intensity areas of the image corresponding to the crossover points. The original real space image is shown in Figure [3-7a].

Figure [4-1] The optical tomography scanner and gel flask and waterbath arrangement with peripheral components, clockwise L-R, laser power source, stepper motor control unit, lock-in-amplifier and AD/DAC breakout box.

Figure [4-2] Schematic diagram of the scanner arrangement showing the main components of the scanner. The laser driver stepper motor controls the laser motion and produces a fan beam arc (red lines) that scans the central gel flask. The lock-in-amplifier transfers the transmitted laser beam collected by the stationary integrating sphere to the computer *via* the ADC/DAC signal box. The base plate stepper motor and the vertical motor control the degree of rotation the base plate turns through during scanning and the vertical scanning height respectively.

Figure [4-3] Photograph of the internal components of the optical scanner. The gel flask is probed by a laser diode *via* a stepper motor driven fan beam projection, moving left to right. The irradiated gel flasks are white, although here the gel appears pink, a consequence of the volumetric scattering of the 655 nm (red) wavelength. The transmitted laser beam is collected by the 1 inch diameter port of the integrating sphere and detected by a fixed BPX-65 photodiode detector.

Figure [4-4] Waterbath arrangement showing the different diameter vessels the scanner can incorporate.

Figure [4-5] Photograph of the modulatable laser diode and the driving stepper motor positioned on the scanning arm above the rotating base plate.

Figure [4-6] Schematic plan view showing the possible ray paths from a focused laser beam incident upon the waterbath arrangement and for a 1mm diameter collimated laser beam. The line integral data collected by the photodiode detector will provide the attenuation values for a larger volume of gel than intended by the diverging laser beam and therefore devalue the data.

Figure [4-7] Schematic of the conversion box used to convert electrical signals between the computer and the optical scanner. The stepper motor turning rate is controlled by the CL input, the direction by the DIR input, all of which are grounded (G) to pin 17 on the D type connector used. BNC type connections are provided for both A/D and DAC data conversion inputs. The 50-way D-connector provides the capability to add further connections if required from the available pins.

Figure [4-15] A screen capture from Beam2 showing the optical setup workspace. Here the optical surfaces which the rays pass through are specified including the refractive index, distance on the z-axis (units in cm), curvature of the interface and the diameter (units in cm).

Figure [4-16] Screen capture of the ray workspace in which the number, orientation and position within the XZ coordinate system during translation from X_0 to X_{final} are presented. U0 refers to the sine of the angle ϕ the ray makes with the optical axis. The distance (units in cm) of the individual surfaces along the optical axis (Z_{n+1}, Z_{n+2} etc) and away from the optical axis (X_n) is given. The final status of all the input rays is shown in the notes column.

Figure [4-17] A schematic showing the simulation output from the data shown in Figures [4-15] and [4-16]. Initially the simulation shows that 15 rays leave the origin point at the left hand side. Under the interactions detailed in the optics spreadsheet, (Figure [4-16]), proceed along the optical axis to the right and final surface. The inset shows the magnified positions of the X and Z interfaces with respect to the optical axis. The units in X and Z are in cm.

Figure [4-18] Photograph showing, a) the diode laser and the photodiode detector connected on the same scanning arm and, b) a schematic diagram for clarity.

Figure [4-19] Beam2 simulation of the effect of refraction at the optical interface. The laser beam is inverted after passing through the calibration bottle and is analogous to an object image after passing light through a lens. All units are in cm.

Figure [4-20] Beam2 ray trace for the optical system where a waterbath of 13 cm diameter has a 5 cm diameter calibration (gel) bottle located centrally. All units are in cm.

Figure [4-21] Screen capture for 12 surfaces from the Beam2 simulation showing the results from an un-radiated calibration bottle. The input parameters for the optical surfaces between the laser diode source and the post transmission beam focus point are given. The parameters include the refractive indices of the input surfaces, position along the optical Z axis (Zvalue of vertex) and the curvature and diameter of the waterbath and calibration bottle.

Figure [4-22] A screen capture of the computed ray path data from the simulation.

Figure [4-23] a) The resulting ray path simulation for an un-irradiated Wheaton calibration bottle with a 5 cm diameter, positioned centrally in the waterbath. The output ray paths were focused by a 2 inch diameter bi-convex lens with a 5 cm focal length. b) The focus point showing that the focal spot diameter is approximately 0.15 cm and occurs 26.7 cm from the beam origin. All units are in cm.

Figure [4-24] Screen capture from the Beam2 simulation showing the results for an irradiated calibration bottle. The dose absorbed by the gel and the subsequent increase in refractive index (*n* =1.4) was estimated and incorporated into this simulation. The input parameters of the optical surfaces between the laser diode source and the post transmission beam focus point are given. The parameters include the refractive indices of the input surfaces, position along the optical axis and the curvature and diameter of the waterbath and calibration bottle.

Figure [4-25] Screen capture from Beam2 showing the calculated ray path data from the simulation. For this simulation 11 rays were required to adequately sample the calibration bottle and detail the focal point of the emanating ray paths. All but 2 rays converged in the common focal point at 24 cm from the beam origin.

Figure [4-26] The resulting ray path simulation for an irradiated calibration flask positioned centrally in the waterbath. The output of the approximately parallel ray paths were focused by a 2 inch diameter bi-convex lens with a 5 cm focal length. b) The focus point showing that the focal spot diameter is approximately 0.2 cm and occurs 23.5 cm from the beam origin. All units are in cm.

Figure [4-27] The simulated Beam2 transition of the laser beam transition through the scanning geometry showing the parallel ray paths in the central gel flask. The addition of a larger diameter waterbath produced parallel rays through the central region as required for the *Iradon* reconstruction algorithm. The removal of the lens increased the focal distance from the waterbath from approximately 25 cm to 46 cm. All the units are in cm.

Figure [4-28] The corresponding Beam2 screen capture showing the ray path simulation data illustrated in Figure [4-27]. The highlighted ‘U6’ column shows that the central ray paths are approximately parallel to one and another. Parallel lines would be simulated by 0.000 values.

Figure [4-29] Screen capture detailing the required ray path input data that would provide collimated rays to fully sample the larger gel flask. Particular attention should be drawn to the U4 column showing how parallel the ray paths are prior to crossing the gel flask. For the example shown on Figure [4-31], the data suggests for the input optical parameters used (see Figure [4-30]) the rays are approximately parallel.

Figure [4-30] Showing the optical system parameters used in the larger flask simulation. Units are in cm.

Figure [4-31] Beam2 ray trace of the complete laser to detector path showing the parallel transmission of the collimated rays through the flask and the successful convergence of the laser fan beam to a fixed focal point along the optical axis. The calculated ray paths and input parameters are detailed in Figures [4-29] and [4-30] respectively. All units are in cm.

Figure [4-32] Schematic diagram of the inherent 3D scattering from a tissue equivalent volume.

Figure [4-33] Photograph of the scanning system enclosed by a blacked-out protective cabinet (the front face has been removed). The enclosure is required to eliminate the possibility of ocular exposure to the scattered or reflected laser beams.

Figure [4-34] Illustration of a) the free induction decay (FID), a consequence of the de-phasing spin-spin magnetism and b) the R_2 signal intensities (S) at the associated echo times (TE). Here TE_{1a}, TE_{2a}, TE_{1b} and Te_{2b} were collected at 24, 60, 109 and 145 ms respectively.

Figure [4-35] Plot of the natural logarithms of the signal intensity versus time (ms). The data shows that the signal intensity is reduced for both increasing time and increasing dose values.

Figure [4-36] Plot of R2 (s^{-1}) versus dose (Gy) showing how the unknown dose value is obtained from the calculated R2 value.

Figure [4-37] Schematic plan view of the initial gel radiation dosing setup.

Figure [4-38] Lateral view of the X-ray field bathing the calibration bottles at the 1 m iso-centre (not to scale).

Figure [4-39] Illustration of the dosing Steps 1 to 4 as outlines in the text.

Figure [4-40] Steps required for a uniform dose delivery.

Figure [4-41] Bottle positioning for doses of 20 to 28 Gy.

Figure [4-42] The ‘Boost’ dose and final dose delivery steps.

Figure [4-43] Illustration of the final steps to complete the dosing method.

Figure [4-44] Diagram showing the 22 by 9 cm radiation field used to deliver a uniform 5 Gy dosing to the 7 cm diameter gel flasks from opposite sides.

Figure [4-45] Diagram showing the additional exposure required to boost gel flask 2 to a uniform 15 Gy dosing.

Figure [4-46] Illustration of the uniform single strip distribution in gel flasks.

Figure [4-47] Illustration of the 3D ‘Cross’ dose distribution from the MAGIC gel Batch number 6.

Figure [4-48] Outline for the procedure for delivering a quadrant distribution to a 90 mm gel flask.

Figure [5-1] Scanning geometry showing the optical ray paths from the laser source to the detector when the laser is rotated through a range of angles. The rays make a parallel translation through the waterbath and sample vessel and converge to a focus on emerging. All units are in cm.

Figure [5-2] A photograph showing the waterbath, gel flask and cylinder used to evaluate the reconstruction methodology. A metallic cylinder was imaged to provide a binary data set and therefore a black and white reconstructed image.

Figure [5-3] Photograph of the experimental setup showing the waterbath and metal cylinder *in situ* prior to image acquisition.

Figure [5-4] A typical display screen image showing a scanning projection of a gel flask containing water only. The fan beam scanning is shown moving left to right on the screen display. The unattenuated (upper plateau) voltage values are approximately 50 mV compared to the attenuated values of approximately 0 mV. The readings did however fluctuate around the zero value with 0.6 mV shown here corresponding to the far right reading.

Figure [5-5] Attenuated data projection with the steel cylinder as the object in the gel flask. The trace illustrates that the passage of the laser beam is blocked by the cylinder so the detector does not record a corresponding signal voltage. The detected voltage values for the upper unattenuated region shown here is approximately 50 mV compared to 0 mV (0.8 mV shown above) at the baseline.

Figure [5-6] A 3D mesh figure showing the full sinogram projection data obtained from optically scanning the metal cylinder shown in Figure [5-2]. The laser scan was set to acquire 250 elements per projection (x-axis) whilst scanning through one revolution i.e. between 0 and 360 degrees (y-axis). The base plate was rotated at 10-degree intervals shown on the right hand side. The differences in transmitted intensity are shown on the z-axis on the left indicating both attenuated and unattenuated values ranging from 0 to 40 mV respectively.

Figure [5-7] Alternative sinogram obtained from a cylinder projection data set showing the corresponding elements within the projection and the period of rotation during scanning. Here the image has been inverted showing the unattenuated voltage signal in white and the attenuated signal in black.

Figure [5-8] The 2D cross section of the 15 mm diameter cylinder reconstructed from the scanner data using the Iradon function within Matlab.

Figures [5-9] A 3D representation constructed from a series of 2D planar attenuation maps acquired from the 15 mm diameter steel cylinder over a 55 mm vertical region of interest. The 3D image was formed by interpolating the 2D data sets with the IRIS image rendering software.

Figure [5-10] The three-dimensional sinogram produced from the attenuated laser light from the centred Allen key.

Figure [5-11] A cropped 2D reconstruction of a 2 mm Allen key clearly revealing its hexagonal cross-section.

Figure [5-12] An unprocessed reconstructed tomographic 2D image of a 9 volt rectangular battery.

Figure [5-13] A sketch of both the cylinder and battery cross-sections with their corresponding projections at 0 and 90 degrees are shown in a), the resulting raw data sinogram from the 0 to 180 degree image scan is shown in b), the reconstructed images produced by method A and method B are shown in c) and d) respectively.

Figure [5-14] Illustration of a) the projection sinogram of the pencil with inherent artefacts and b-d) a representation of the possible attenuation profiles produced by beam wander during the scanning process.

Figure [5-15] Reconstructed cross section of a 7 mm diameter pencil illustrating the possible image artefacts originating from optical tomography.

Figure [5-16] Reconstructed cross-sectional image of a pencil obtained by replacing the 10 mm^2 detector (S-2387-1010R, Hamamatsu) with the integrating sphere and BPX-65 detector combination. Here the effect of beam wander and loss of transmission signal is reduced. This therefore allows a representative image to be reconstructed.

Figure [5-17] Optical tomography reconstruction of the 'cross' distribution produced from dosing Batch 13 as shown in a). The basic reconstruction obtained from the basic method is shown in b) and is accompanied by a legend indicating the relative dose absorbed within the gel flask. Both c) and d) show the reconstructions obtained from using the method that required further data manipulation. Here the details of the 'cross' distribution are discernable when compared to b), but are sill somewhat un-defined. The degree of image intensity can be varied by choosing a different multiplication factor in the Matlab syntax used. Here different values have been chosen to further enhance the central 15 Gy region.

Figure [5-18] a) showing the reconstructed image obtained from using the less exhaustive method A (see section 4.5.3.2); the central 15 Gy square region can be seen with no indication that a cross distribution was delivered to the flask. b) and c) show the reconstructed images obtain using method B (see section 4.5.3.2) whereby the 5 and 10 Gy areas of the distribution can be distinguished from one another. The full 'cross' distribution can be clearly seen. Additional image contrast can be produced by changing the scaling factors used in the Matlab syntax. Here the lower dose regions of the cross can be clearly seen above the un-irradiated background. d) shows the corresponding MRI image with the legend showing the calibrated dose absorbed from 0 to 15 Gy.

Figure [5-19] The 3D representation of the dose varying 'cross' distribution formed in Batch 11 gel from a 90 mm diameter optical friendly gel flask. 2D optical tomography images were collected from over 90 mm within the flask, stacked and interpolated with imaging software IRIS to render the 3D image.

Figure [5-20] Reconstructed images of the 'cross' showing how the rate of data capture influences the quality of the image. a) The fast data capture rate collected data every 3 ms and shows the cross details. b) shows the blurred reconstructed image produced from the data collected from the slower data capture rate of 100 ms.

Figure [5-21] Reconstructed optical tomographic images of uniformly irradiated large gel flasks with a) = 4 Gy, b) = 8 Gy, c) = 12 Gy and d) = 16 Gy. The 90 mm diameter flasks attenuate the laser beam to such a degree that when reconstructed, doses above 8 Gy cannot be distinguished from one another. Here, optically, there are no perceivable differences between c) the 12 Gy and d) the 16 Gy gel flasks.

Figure [5-22] The optical density (OD) response of gel Batch 13 versus dose. The plot compares well to the optically reconstructed images illustrated in Figure [5-21]. There is an initial strong response to OD for the dose regions between 0 and 8 Gy. Beyond the 8 Gy region the dose response is negligible and the OD curve forms a plateau.

Figure [5-23] Comparative study of Gel batch repeatability using 9 % MAA per batch volume.

Figure [5-24] Graph showing batch-to-batch repeatability in terms of the R2-dose line gradient, R2 intercept at zero dose and the figure of merit for the individual batches. The graph shows that all the batches with the highest sensitivity values (B6, B10 and B11) have intercept values ≤ 2 s^{-1} and that the intercept value is the limiting factor to sensitivity. The units of the y axis are s^{-1} Gy^{-1} for gradient, s^{-1} for intercept and Gy^{-1} for FOM.

Figure [5-25] Graph showing the dose response (R2 (s^{-1}) versus dose for both the 0 - 16 Gy and 16 - 28 Gy regions. The linear regression fits for both the blue line (0-16 Gy range) and the red line (16 - 28 Gy range) are shown. The corresponding fit data is inserted adjacent to both lines and indicates that the initial gradient and therefore response to the radiation absorbed is approximately double that of the higher dosed region.

Figure [5-26] Graph of R2 (s^{-1}) versus dose from Batch 13 (12 % MAA) showing the differing MRI signal readouts from using different echo times (T_E) during the gel interrogation. A higher response to dose was observed from the longer 180 ms echo time than the 90 ms echo. Linear regression lines (hashed) and corresponding values have again been inserted that show the line details in terms of gradient, intercept and the R^2 value indicating to what degree the lines are linear.

Figure [5-27] Graph of R2 (s^{-1}) versus dose from Batch 16 (12 % MAA) obtained from MRI readout using 180 ms echo times (T_E). A linear regression has been fitted; the resulting line data has been inserted adjacent to the line and from which the low gradient indicates the batch responded poorly to the dose absorbed.

Figure [5-28] R2 (s^{-1}) versus dose plot for Batch 17 containing 15 % MAA by volume. The 90 mm diameter gel flasks were irradiated at 6 Gy intervals from 0 – 24 Gy. A linear regression was fitted and the corresponding data inserted adjacent to the line.

Figure [5-37] a) The IMRT beam configuration showing the transversal view of a proposed treatment. The central white region is the target and a series of beam deliveries are considered that would minimise the dose delivered to the surrounding regions. The coloured lines (dose envelopes) indicate what dose would be delivered to the areas surrounding the central white region. b) MRI image taken inside a head coil of the gel phantom *in situ* showing the resulting dose delivered to the phantom. The lower black circles are fiducial markers and are used to indicate the orientation of the gel flask from intended treatment plan with respect to the IMRT plan in a).

Figure [6-1] Illustrates a) a familiar 2D MRI image of a ‘cross’ distribution within a radiotherapy gel flask, b) MRI image of a complex dose distribution using multiple beams to irradiate a central region.

Figure [6-2] Schematic showing a) both early and late arriving photons passing through the highly scattering gel medium and b) the corresponding gated time acquisition required to collect the early arriving photons and neglect the pulse width broadened late arriving photons.

List of Tables

LIST OF ACRONYMS

1D	One dimensional
2D	Two dimensional
3D	Three dimensional
3D–CRT	Three dimensional conformal radiotherapy treatments
AD	Analogue to Digital
ART	Algebraic reconstruction technique
BANANA	Bis, acrylamide, nitrous oxide and agarose dosimeter
BANG	Bis, acrylamide, nitrogen and aqueous gelatin dosimeter
bis	N,N'-methylene-bis-acrylamide
CAT	Computer Assisted (or Axial) X-ray tomography
CT	Computerised Tomography
DAC	Digital to Analogue Conversion
DOS	Disc operating system
DMLC	Dynamic multi-leaf collimators
FBX	Ferrous sulphate benzoic xylenol orange dosimeter
FSE	fast spin echo
FOV	Field of view
Gy	Gray
HCl	Hydrochloric acid
ICRP	International Commission on Radiological Protection
IMRT	Intensity-modulated radiation therapy
MAA	Methacrylic acid
MAGAS	Methacrylic acid, ascorbic acid, gelatin
MAGAT	Methacrylic acid, gelatintetrakis (hydoxymethyl) phosphonium chloride
MAGIC	Methacrylic and ascorbic acid in gelatin initiated by copper
MRI	Magnetic Resonance Imaging
MU	Monitor unit
MV	Mega-voltage
NMAG	Methacrylic acid, gelatin Bis[tetrakis (hydoxymethyl) phosphonium] sulphate

NPAG	-	Acrylamide, N,N-methylene-bis-acrylamide, Bis[tetrakis (hydoxymethyl) phosphonium] sulphate, gelatin
PAGAS	-	Acrylamide, N,N-methylene-bis-acrylamide, gelatin Ascorbic acid
PAGAT	-	Acrylamide, N,N-methylene-bis-acrylamide, tetrakis (hydoxymethyl) phosphonium chloride, hydroquinone, gelatin
NMR	-	Nuclear Magnetic Resonance
OAR	-	Organ at Risk
OCT	-	Optical Computerised Tomography
OD	-	Optical density
OF	-	Optically friendly
PAG	-	Polymer acrylamide gel
PC	-	Personnel computer
PET	-	Positron Emission Tomography
PTV	-	Planning treatment volume
QA	-	Quality and Assurance
ROI	-	Region of Interest
RPC	-	Radium Protection Committee
SPECT	-	Single Photon Emission Computed Tomography
TLD	-	Thermoluminescent dosimeter
TV	-	Tumour volume
US	-	Ultra-Sound
RF	-	Radio-frequency
THP	-	Tetrakis (hydroxymethyl) phosphonium chloride

Chapter 1 Introduction

The introduction of three dimensional conformal radiotherapy treatments (3D–CRT) to the field of oncology over the last decade has highlighted the limitations of existing conventional dosimetry methods. These new conformal approaches to radiation therapy provide improved local tumor control via detailed beam shaping from high dose gradients and both static and dynamic intricate beam delivery methods. This additional delivery accuracy allows an increased radiation dose to be delivered to a patient whilst continually ensuring minimum radiation damage to surrounding tissue and neighbouring radiosensitive organs.

The dynamic deliveries provided by 3D-CRT require a time integrated tissue equivalent volumetric dosimeter that can provide the level of resolution and accuracy required for accurate treatment verification. The associated quality assurance (QA) of such treatments, have been constrained to existing conventional verification methods using 1D and 2D approaches. The degree of resolution that 1D dosimeters i.e. ion chambers, can provide is limited by the physical dimension of the detection area. This will result in the loss of accurate dose detail from regions of high dose gradients using the 1D method. Volumetric representation of the dose can be collected by carefully stacking sheets of 2D film to eventually form a detector volume. This process is laborious and ultimately inadequate for the modern requirements of QA.

The physical dimensions of delivered radiation dose can be preserved by gel dosimeters. The addition of a gelling agent e.g. agarose or gelatin to liquid dosimeters, allow the subsequent radiation induced changes to be ‘fixed’ and therefore imaged at a later time. The first gel dosimeter investigated (Gore *et al.*, 1984) used Nuclear Magnetic Resonance (NMR) to investigate the proportional change in the paramagnetic moments of Fe^{2+} to Fe^{3+}, resulting from irradiation. However, imaging limitations and time constraints set by the inherent ionic diffusion in the Fricke dosimeter prompted the further development of alternative dosimeters that were not limited in this way.

Polymer acrylamide gel (PAG) dosimeters were developed in an attempt to combat the imaging constraint. The degree of polymerisation within PAG gels was proportional to the amount of dose absorbed. This response to dose absorbed could be investigated with the existing MRI modality and more recently, optical methods. However, although PAG dosimeters overcame the ionic diffusion limitations experienced using Fricke dosimeters, the carcinogenic and neurotoxic ingredients used for PAG manufacture added alternative concerns to their general application within the clinical community. In addition to the harmful components used, the manufacturing process required that the gels be prepared in hypoxic environments. The removal of oxygen was crucial to the dosimeter performance. This limited where gels could be manufactured to chemistry laboratories. A typical method for oxygen removal was to perfuse a fume cupboard with nitrogen or argon. It would therefore be advantageous to develop a gel dosimeter that could be produced in less specialised environments like hospital and university research laboratories.

This prompted further investigation into gels that could be manufactured within aerated laboratory environments and without the need for carcinogenic constituents. The development of normoxic gel (Fong *et al*., 2001) dosimetry overcame this serious drawback. Fong produced a MAGIC gel dosimeter that when irradiated underwent polymerisation reactions proportional to the amount of dose delivered. This reaction utilised an organo-metallic reaction that removed oxygen from the dosimeter. This removed the requirement to use fume cupboards for oxygen removal and therefore greatly reduced the manufacturing complexity.

Radiation sensitive gels have been investigated using MRI for over two decades since the pioneering undertaken by Gore (Gore *et al*., 1984). Unfortunately, MRI centres and resources are currently limited. It would therefore be advantageous if an alternative imaging modality could be developed that would alleviate this reliance on MRI technology within the field of radiotherapy. The development of an optical tomography system as an alternative imaging modality could be used to provide both independent and comparative verification techniques to dose distributions produced by MRI.

Optical tomographic techniques were being continuously developed and evaluated in the early 1990's. This imaging modality can be used to reconstruct tomographic images from the proportional changes in optical attenuation that results from radiation dose delivered to the gel dosimeters. The radiation induced polymerisation reactions attenuate laser light during tomographic scanning from both absorption and scattering mechanisms. The degree of polymerisation was found to be proportional to the dose absorbed, which allowed representative 2D attenuation dose maps to be reconstructed. Optical tomography is analogous to 1st generation X-ray computer tomography (CT) scanners that acquired data using the translate-and-rotate method.

The dual development of both normoxic gel dosimetry and optical tomography should facilitate the reconstruction of 3D gel distributions from a relatively inexpensive optical method with relative ease and used to verify the MRI result. It is important to develop a portable optical scanner that can be used to image gel dosimeters in various locations i.e. universities and hospitals.

The structure of this thesis is as follows. Chapter 2 provides an overview of the historical development of radiotherapy, including the discovery of ionising radiation, the subsequent development of radiotherapy treatments and the limitations to verifying treatment plans with conventional 1D and 2D dosimetry techniques required for modern day radiotherapy.

Chapter 3 describes the development of 3D gel dosimetry, specifically the evolution from the original liquid dosimeters (used for absolute dose measurements), to the volumetric gels used today for treatment verification. The physics and chemistry of radiation sensitive gels are also summarised, indicating the radiation induced reactions from which the degree of polymerisation is produced from the dose delivered. An introduction to optical tomography and concepts used to reconstruct the tomographic images is also given.

Chapter 4 reports the dual research and development of an optical tomography scanner and gel dosimeter at the University of Hull. The chapter will outline the various experimental considerations necessary to develop the hybrid 1st generation CT scanner including opto-mechanical, software control, data acquisition and image construction. In addition, the methods used to irradiate the calibration bottles and gel flasks with various dose distributions are given.

Chapter 5 describes the results obtained from both the optical scanner and MRI. Initially, the image reconstruction method, using Matlab, was validated using solid objects. The ability of the scanner to accurately reconstruct objects was assessed in terms of image resolution, scanning time and the subsequent effect on image quality and a combination of multiple objects with differing 2D cross sections.

Investigations into the reproducibility of the MAGIC gel batch properties are also reported. The optical scanner was used, when possible, to reconstruct various dose distributions for comparison with MRI results. During the development of the optical scanner, the dose response studies were conducted using with MRI specifically because the technique was well established and reported within the literature. The gels were investigated in terms of dose response in relation to the concentration of methacrylic acid (MAA), linearity and dynamic range. The homogeneity of the manufactured gels was also investigated. The method of gel production and in particular the rate of gelation was varied to try and reduce the formation of polymer strands. The existence of polymer strands effectively restricts the areas from which MRI signals can be obtained.

Chapter 6 summarises the developmental process of the optical tomography scanner, the ability of the scanner to reconstruct images and in particular what modifications are required to address current scanning limitations. The gel investigations, results and possible modifications are also discussed. Finally, it is suggested that in future work, the scanning system and quality of reconstructed images would be enhanced by the incorporation of time gated tomography.

Chapter 2 Overview of Radiotherapy

2.1 Historical Review

Wilhelm Roentgen’s discovery of X-rays in 1895 provided the initial step towards medical imaging with ionising radiation. The first application of Roentgen’s discovery within clinical practice took place 2 months later on the 13th January 1896.

Although fundamental methods and a basic awareness of X-ray protection were well known by 1905, ten years after the discovery, implementation of radiation protection measures were in some regards non-existent. The potential of harm caused by working with ionising radiation wasn’t fully appreciated until acute and chronic biological effects soon became evident to both researchers and medical practitioners. During the 1920’s it was not uncommon to find medical X-ray units with virtually no safety precautions in place. Early radiotherapy practices routinely delivered X-ray doses to staff and patients in all directions from gas X-ray tubes maintained behind primitive lead shields. X-rays were initially dismissed as the cause despite of these acute and chronic effects, an awareness to the effects of direct exposure to high levels of ionising X-ray radiation could lead to dermatological effects similar to sunburn at one extreme, to an early radiation induced death at the other see for example (Webb, 1988).

Steps were subsequently taken that would limit and effectively reduce radiation exposures and facilitate the development of radiation protection protocols. The 1920's also saw the advancement in radiation protection through the introduction of film badges for routine personnel monitoring, in recognition of the genetic effects of X-rays (for which Hermann Muller was awarded the Nobel Prize in 1946).

The continued recognition of radiation hazards and the need for control led to the formation of the International X-ray and Radium Protection Committee (RPC), forerunner of the current International Commission on Radiological Protection (ICRP).

The ICRP was set up in 1928 to evaluate the risks to mankind of all exposures to ionising radiation and to set limits on maximum permissible levels of exposure.

Working with X-rays, early radiotherapists collected a growing body of empirical results from clinics and laboratories. There was great difficulty, however, in comparing or duplicating beneficial results from particular treatment methods. With no reliable way to measure dosage and no standardised equipment, it was impossible to replicate previously recorded findings.

Early academic centres enhanced radio-diagnosis, X-ray therapy, and radium therapy with basic research in biology, pathology, and physics. In almost all academic and clinical settings, radiation treatment was still linked to diagnostic radiology, although special sections on X-ray therapy could be found. The American Board of Radiology, founded in 1934, included radiotherapy as part of the standard examination. Basic and applied research in radiation physics in the 1930s and 1940s provided results that would change radiation therapy into modern radiation oncology.

In the early part of the 20th century the only clinical method of imaging was *via* planar X-ray imaging. This limitation denied radiographers knowledge of the tumour volume and therefore understanding of the planning treatment volume (PTV). Prior to the 1960’s, non-invasive medical diagnoses were performed by the specialised X-ray diagnostic and therapeutic methods that had been developed. Today the various specialised modifications of simple projection X-ray radiotherapy are by far the most frequently used diagnostic techniques within medicine.

Research into radiological tomography has been ongoing since the 1940’s. However the first radical change in the medical application of X-rays since Roentgen’s discovery began in 1972 with Hounsfield’s announcement at the annual British Institute of Radiology Conference detailing a practical computer assisted X-ray tomographic (CAT) scanner or CT. X-ray CT is one of the most important developments in the field of radiotherapy along-side the discovery of X-rays. It has subsequently revolutionised both diagnosis and radiotherapy treatment planning with equal efficacy see for example (Webb, 1988).

Initial tomographic scans proved to be very time consuming to record, leaving the patient motionless in the scanner for up to one hour whilst the 1st generation scanners obtained the required cross sectional patient data. It was therefore essential to develop faster tomographic scanning methods firstly to reduce the stress of prolonged immobility incurred by the patient and also to improve the tomographic data acquired.

The scanning development process can be summarised as follows and illustrated in Figure [2-1].

a) In 1st generation scanners, a pencil beam of X-rays and a single detector were used. For each projection, the source and detector scanned along a line before being rotated for the next projection.

b) For 2nd generation scanners, the pencil beam was replaced with a fan beam with multiple linear detectors allowing larger translation steps and simultaneous collection of multiple measurements.

c) In 3rd generation scanners, the detectors were arranged in an arc. Both the X-ray tube and the detectors are then rotated about the patient.

d) With 4th generation scanners, a fixed circle of detectors is used and only the X-ray tube rotates.

The latest 5th generation scanners, as with the 4th generation's scanners, have a ring of detectors, but here no motion is required, the X-ray source is moved electronically.

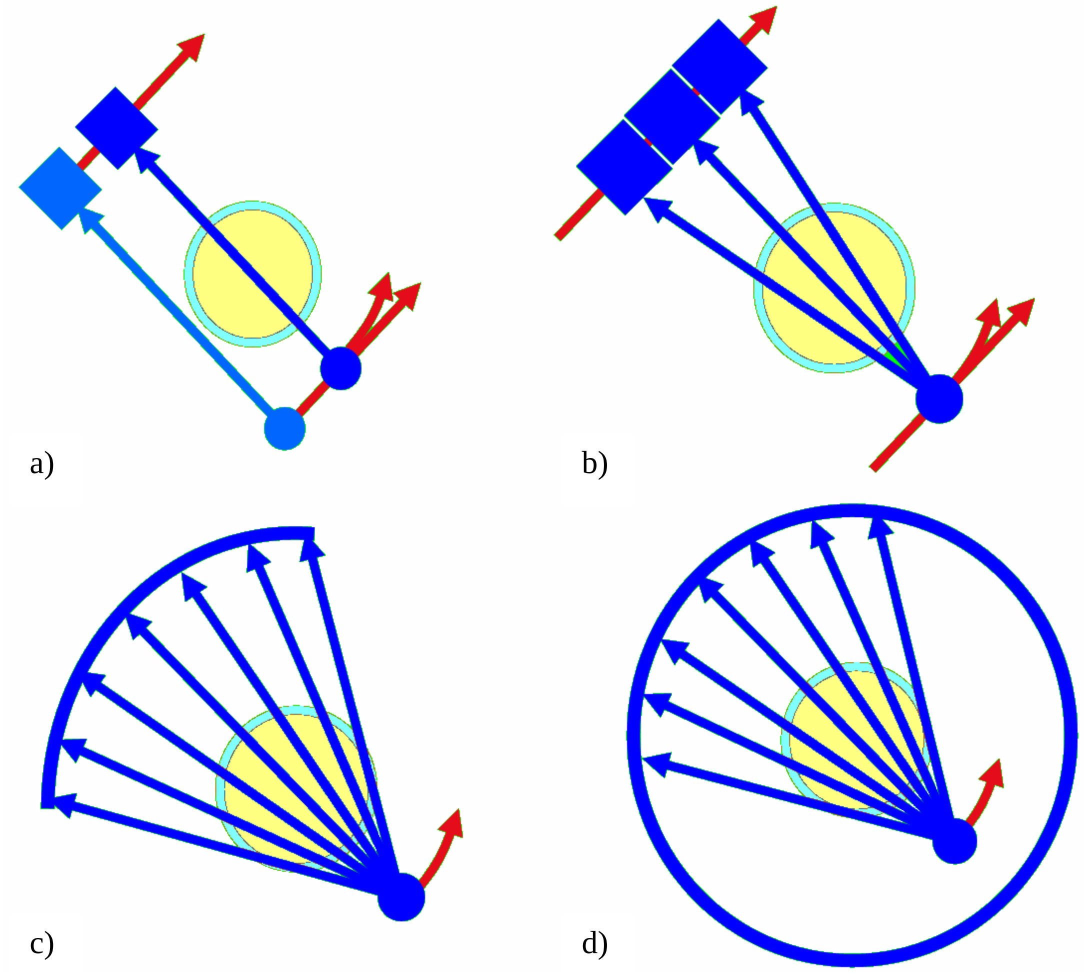

Figure [2-1] Schematic, showing the development of the CT scanner from a) the 1st generation architecture using a rotate and translate method to detect the X-ray pencil beam used for scanning. The 2nd generation is shown in b). Here the imaging time is reduced due to the diverging fan beam and multiple detectors used. The 3rd and the 4th generation scanning geometries, c) and d) respectively, incorporate both moving source and detectors to further reduce scanning times. As described previously, the 5th generation scanner has a fixed detector bank that covers the full 360 degree arc.

A century after Roentgen's discovery, the suite of radiotherapy techniques available for cancer treatments with oncology is vast. The revolution in diagnosis occasioned by the advent of the so-called 'new modalities' (Computed Tomography (CT), Ultrasound (US), Magnetic Resonance Imaging (MRI), Single Photon Emission Computed Tomography (SPECT) and Positron Emission Tomography (PET)) has improved both the identification of tumours and the precision of treatment planning.

Today, the advancement in digital computing and diagnostic radiology enables radiographers and treatment planners to plan therapeutic procedures more accurately than ever before. For example, computer guided therapy based on beam eye views and multidimensional planning with dynamic adaptive field shaping, bring pinpoint accuracy to patient care (Webb, 1988).

2.2 Conventional Treatment Planning

A conventional treatment plan would generally consist of the following:

A conventional radiograph (e.g. chest X-ray image) is taken of the patient to ensure the correct area of the body is treated. This static image allows the radiographer to plan the treatment initially by drawing the basic radiation fields intended for the treatment on the radiograph. In addition the X-ray will provide basic anatomical information including the ribs, shoulder blades and internal organs. Figure [2-2] shows a typical chest radiograph.

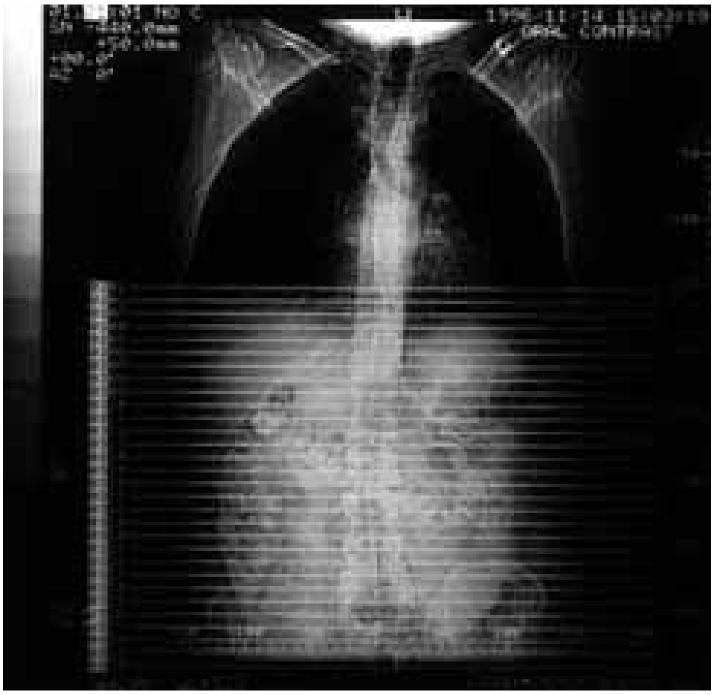

Figure [2-2] Image illustrating a conventional chest X-ray radiograph of a patient. Reproduced from http://science.cancerresearchuk.org/.

A CT scan is then performed on the patient to identify the three dimensional shapes of organs of interest. A simulator, used for this purpose, is a machine that allows the treatment diagnostics to be ‘simulated’. The simulator mimics the delivery capabilities of the radiation delivering linear accelerator and is used to assess the possible beam directions and radiation field sizes for the treatment. Treatments are then planned using the simulated results. Eventually the optimum treatment plan using radiography is selected and administered to the patient.

Whilst every patient is different and every cancer is possibly unique, calculations can be performed based on contours from the patients shape to ensure the correct radiation dose is delivered in the treatment volume. The contour maps are measured from the plaster-of-paris bandages from the patient. The maps are then traced onto paper and transferred onto the computer system. The patient is immobilised in an individual plaster cast so that the location of the treatment region remains the same for the rest of treatment process.

Radiation therapy is delivered by medical linear accelerators, which use microwave energy to accelerate electrons to nearly the speed of light in a short distance. As they reach maximum speed, the electrons collide with a tungsten target, which in turn releases X-rays focused to the area of interest. As the radiation enters human tissue, it produces highly energized ions that are lethal to both normal and cancerous cells. Healthy cells can adapt over time, but cancer cells do not. Further, since tumour cells divide and reproduce more rapidly than normal cells, they become more sensitive. As a result, radiation therapy is given in multiple treatments rather than a single overall dose.

After conducting a physical exam and a medical history review, the radiation oncologist determines an individualized course of treatment for each patient. The radiation oncologist works closely with other doctors and heads a team that generally includes nurses and technical staff such as radiation physicists and dosimetrists. The latter group is integral in designing how the beam arrangement and radiation dose is to be delivered. A radiation physicist uses a trial-and-error approach to determine how many beams of radiation are needed, which beam angles are optimal, and what weight should be assigned to each beam. When the oncologist and principal medical physicist are satisfied with the treatment plan the patients' treatment can be administered. Radiation therapy usually is given in short sessions, five days a week for six or seven weeks. The small doses and weekend breaks allow normal cells in the treatment area to recover. The total dose of radiation given and the number of sessions a patient needs depend on the size and location of the tumour, the type of tumour, the patient's general health and other factors.

Although simple tumour volumes e.g. a well defined sphere, can be treated relatively easily with conventional treatment approaches, limiting radiation dose in surrounding healthy tissues is highly desirable. Figure [2-3] shows two simulated treatments the first one delivering the dose from a single beam, the other from four beams. The figure illustrates that within the single beam unacceptably high doses would be delivered to regions surrounding the central area of interest. Here for example the red/orange regions indicate that high dose levels would be delivered to the patient from 0 to 5 cm depths compared to much less at the tumour site (enclosed white region) during the single beam treatment. In comparison the four beam approach reduces the dose to these areas and provides the required level of dose at the iso-centre, enveloping the tumour volume (central red region) *via* accumulative doses delivered.

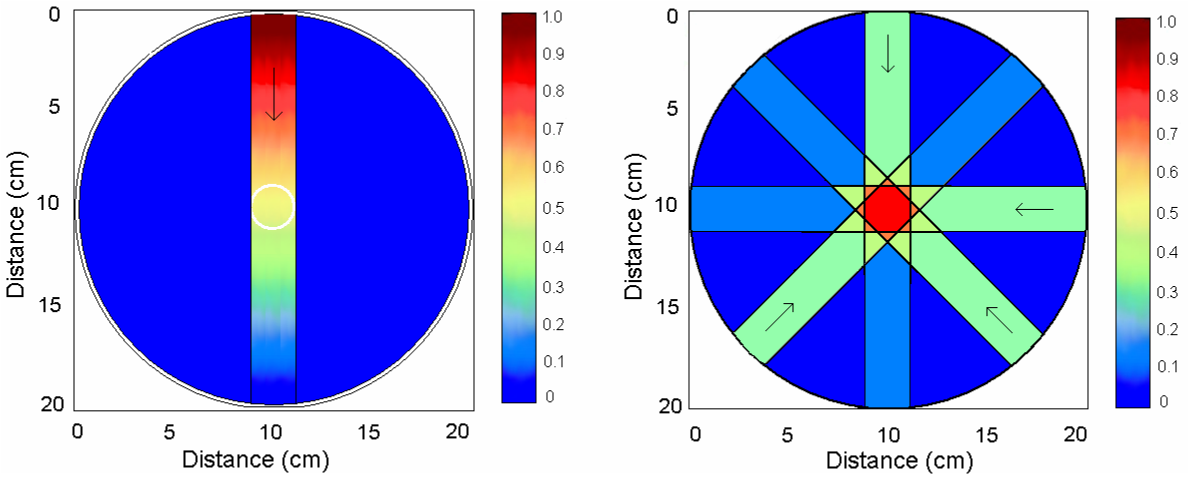

Figure [2-3] Illustration of the principle of accumulative radiation therapy where radiation beams are combined to deliver dose to the tumour at the beam cross over region of interest. The radiation beam in both cases originates from the top of the images at 0 cm depth. The scale on both images shows higher absorbed doses within the red regions conversely the blue regions indicate low levels of absorbed dose.

However, all tumour volumes are different and some form very complex shapes, for example around the spinal chord, throat and within the prostate region. The ability to continuously improve treatment outcomes is related to the consistently evolving treatment verification techniques.

2.3 Complex Radiotherapy Treatment Methods

In recent years new complex radiotherapy treatments have been emerging within the field of oncology. These new approaches to radiation therapy will provide improved local tumor control thus allowing increased dose deliveries whilst minimising damage to surrounding tissue and neighbouring radiosensitive organs. Running parallel with these improvements is the unavoidable necessity to improve the verification techniques used for conventional treatments; one cannot exist without the other. The following sections will briefly introduce these treatment techniques and the quality and assurance, (QA), which are vital for confidence in the treatment outcome.

2.3.1 Three-Dimensional Conformal Radiotherapy

Three-dimensional conformal radiotherapy (3D-CRT) is a complex process that begins with the creation of individualised, 3D digital data sets of patient tumours and normal adjacent anatomy. These data sets are then used to generate 3D computer images and to develop complex plans to deliver highly “conformed” (focused) radiation while sparing normal adjacent tissue (see Figure 2-3]). Due to the complex nature of 3D-CRT, high doses of radiation can be delivered to cancer cells whilst significantly reducing the amount of radiation received by surrounding healthy tissues. The technique thereby increases the rate of tumour control while decreasing side effects.

3D-CRT is used to treat tumours that in the past may have been considered to close to vital organs and structures for radiation therapy. For example, 3D-CRT allows radiation to be delivered to head and neck tumours in a way that minimizes exposure of the spinal cord, optic nerve, salivary glands and other important structures.

3D-CRT begins with a “virtual simulation” in which computed tomography (CT) scans of the region of interest are obtained. The image scans of the tumours are in two dimensions (2D) – width and height. With computer technology it is now possible to see the tumour in three dimensions (3D) – width, height and depth, again using CT scans or MRI scans. This is shown in Figure [2-4].

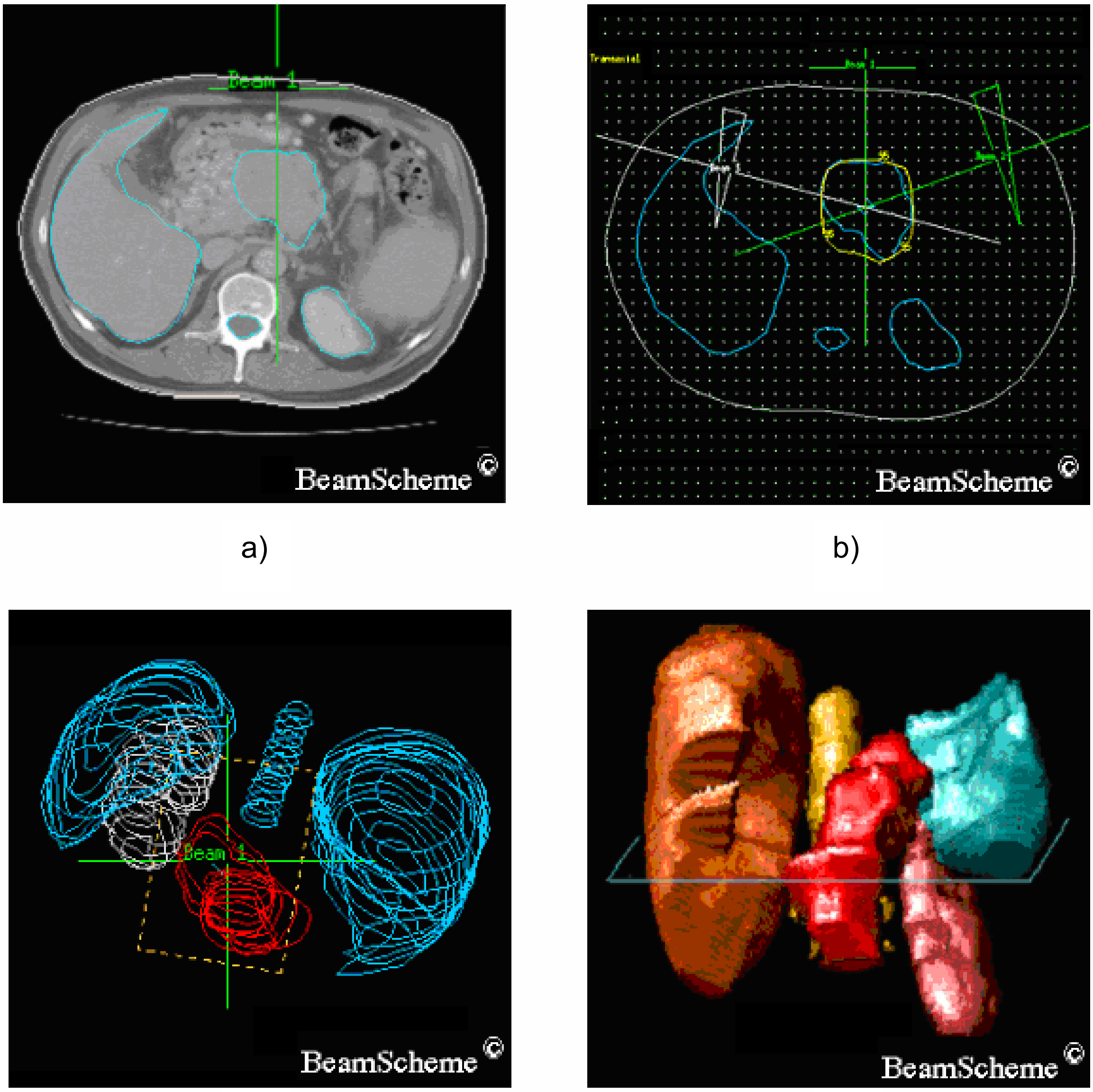

a) b)

c) d)

Figure [2-4] a) Transaxial 2D CT image of the patient’s abdomen, b) Transaxial 2D computerised interpretation of the 2D CT image, c) 3D computer simulation of the tumour volume (TV) and organs at risk (OAR) and d) showing a 3D rendering of the patients abdomen. Reproduced from http://science.cancerresearchuk.org/.

The virtual simulation creates a permanent digital file that can be accessed by the treatment planning group to develop multiple, specific courses of radiation therapy. Scanned images are then linked into treatment planning software that allows physicians to visualise the treatment area in three dimensions. With this capability, radiation beam direction and intensity can be selected to more precisely target the tumour while sparing surrounding tissue. Clinicians input these selections into computer systems that control treatment delivery.

Forward planning is generally associated with 3D-CRT and in essence is when the chosen dose distribution does not treat the tumour volume to the degree of accuracy that the oncologist requires. Therefore different treatment plans will be considered until one fits the necessary criteria. The opposite of this process involves complex tumour volumes that cannot be treated with shaping beams alone, and modified beams are used to treat areas such as the rectum and spinal cord. The oncologist will determine the dose distribution required and a computer begins literally thousands of treatment simulations until the conditions set are met. This is called inverse planning.

2.3.2 Intensity Modulated Radiotherapy

Intensity-modulated radiation therapy (IMRT) is an advanced form 3D-CRT. It uses sophisticated software and hardware to dynamically vary both the shape and intensity of radiation delivered to different parts of the treatment area. It is one of the most precise forms of external beam radiation therapy available.

Like conventional 3D-CRT, IMRT links CT scans to treatment planning software that allows the cancerous area to be visualised in 3D. However, regular 3D-CRT and IMRT scans differ in how the pattern and volume of radiation delivered to the tumour is determined. In conventional 3D-CRT, clinicians input delivery patterns into the computer. In IMRT, the physician designates specific doses of radiation (constraints) that the tumour and normal surrounding tissues should receive. The physics team then uses a sophisticated computer program to develop an individualized plan to meet the constraints. This process is termed “inverse treatment planning”. IMRT uses the same medical linear accelerators that deliver X-ray beams in conventional 3D-CRT. As a unique feature, it also involves dynamic multi-leaf collimators (DMLC's), computer-controlled devices that can use in advance of 100 movable "leaves" to conform the radiation beam to the shape of the tumour from any angle, while protecting normal adjacent tissue as much as possible. Four instances during a dynamic treatment are shown in Figure [2-5]. For this example a 10 cm by 10 cm collimator is considered. The moveable leaves are coloured green and dynamically change position during the treatment (see green arrows). This has the effect of varying the radiation field (pink region) and thus shapes the radiation field and therefore dose delivered to the tumour volume.

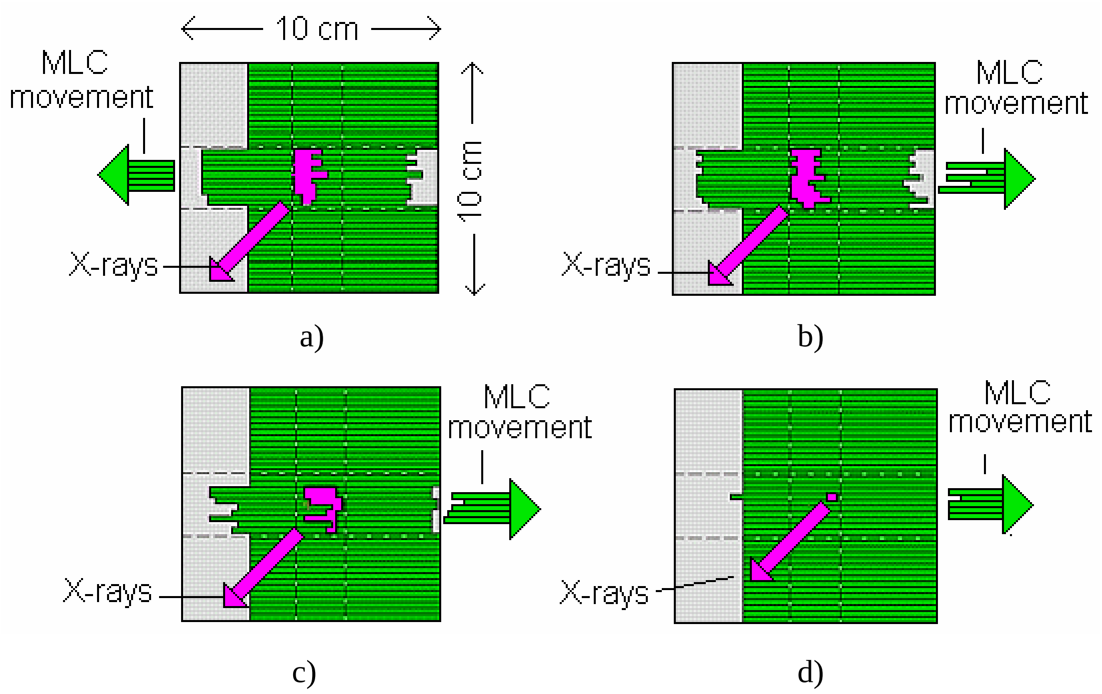

Figure [2-5] Illustration of the dynamic treatments of IMRT. Through a) to d) the multi-leaf collimators (MLC's) are continuously changing during the irradiation process and treatment plan. This is shown by the changing pink regions and details the shaped x-ray beam passing through the 10 cm by 10 cm collimator. This dynamically changes the radiation flux, field and dose incident upon the patient during the treatment plan.

DMLC's allow the radiation dose delivered to vary within a single beam i.e. the capability to deliver higher radiation in some areas and lower radiation in others. Earlier technology could also shape radiation beams but could deliver them only at a single, constant dose. The ability to vary the radiation dose with DMLC's is accomplished by “sliding windows” of radiation beams across the target cancerous area.

To emphasise the requirement for accurate delivery of radiation a prostate treatment will be considered using conventional, 3D CRT and IMRT treatments. The target for irradiation is the prostate gland and is surrounded by seminal vesicles, bladder and the rectum and is shown in Figure [2-6].

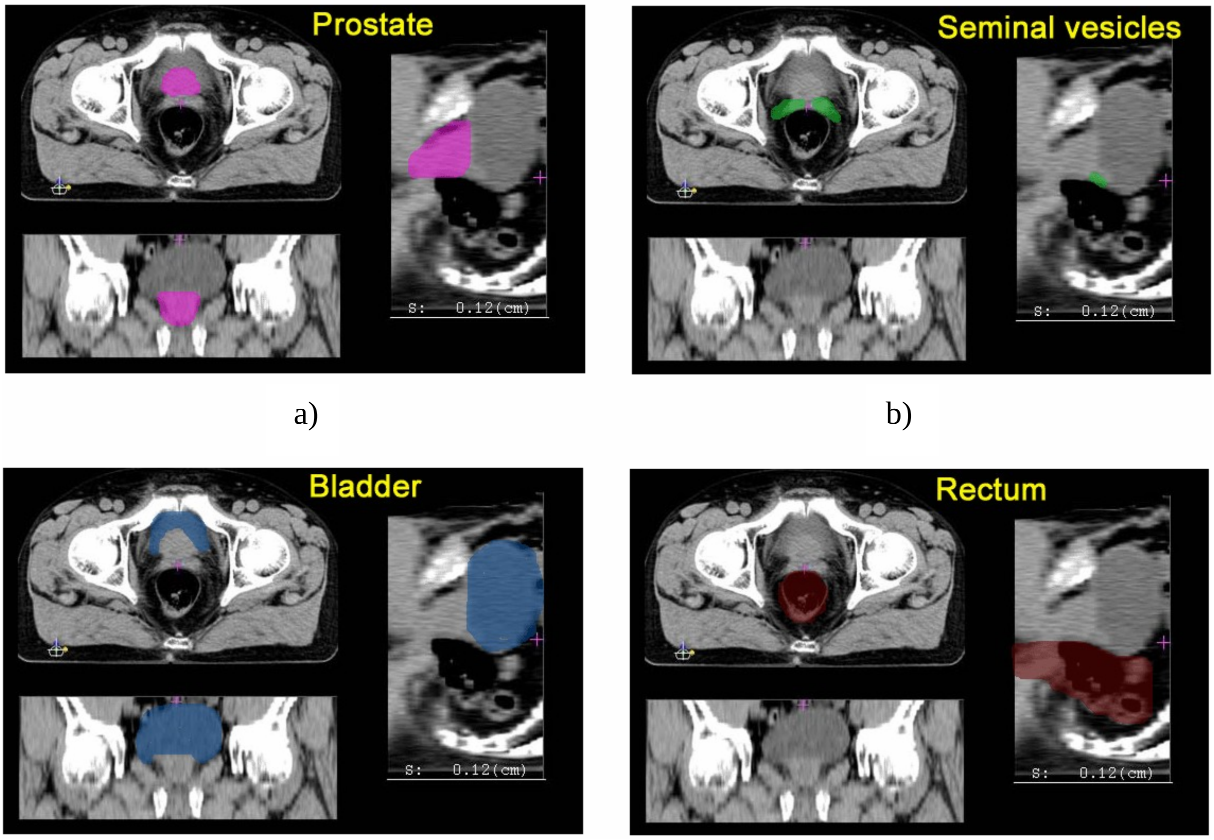

a) b)

c) d)

Figure [2-6] A series of images showing a) the prostate and region of interest (ROI), b) the seminal vesicles, c) the bladder and d) the rectum.

Reproduced from http://www.geocities.jp/nekoone2000v/BBS/physical/comp_methodEnglish.html.

The close proximity of the rectum, seminal vesicles and the bladder limits the amount of radiation that can be delivered from conventional treatment plans. Multiply beam deliveries that employ dynamically changing radiation fields can be used to optimise the treatment and are shown in Figure [2-7].

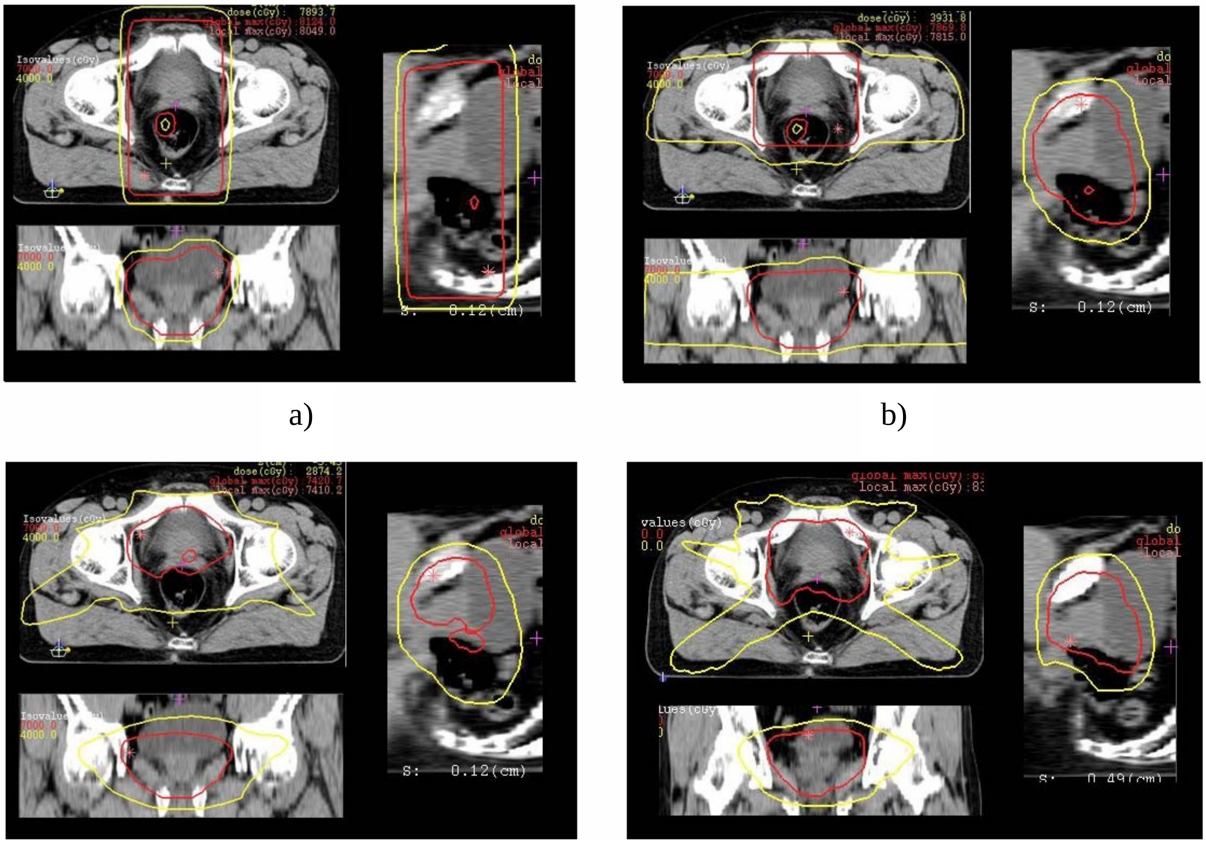

a) b)

c) d)

Figure [2-7] Prostate treatment plans from a) two opposing beams, b) four beams, c) a treatment plan from 3D–CRT and d) an IMRT treatment plan. The yellow and red areas enclosed indicate the increasing amount of dose (Gy) that could be delivered to the prostate whilst avoiding the surrounding regions. The conformal treatments in c) and IMRT plan in d) illustrate that lower dose would be delivered to the surrounding area and in particular the rectum when compared to the two and four beam plans a) and b) respectively.
Reproduced from http://www.geocities.jp/nekoone2000v/BBS/physical/comp_methodEnglish.html.

Both the two and four beam treatment plans show that areas surrounding the prostate, (rectum, bladder and seminal vesicles) will be irradiated during the process. Both 3D-CRT and IMRT treatments, c) and d), allow precise targeting of the cancer with multiple X-ray beams, but IMRT allows physicians to modulate the radiation dose intensity with far smaller radiation beams. Thus, doses of radiation to the bladder and rectum can be limited. Reducing radiation exposure to healthy normal tissue and other vital organs helps prevent once common side effects such as urinary frequency and diarrhoea.

Quality assurance in IMRT is mainly founded on quantitative comparisons between computed and/or measured dose distributions. Differences between measurement and calculation are principally caused by an error in planning, positioning, delivery or measurement technique. A detector is required that has good spatial resolution and is energy independent of the spectrum to provide knowledge about the peripheral and shielded doses. An example is the contribution of low energy photons *via* transmission leakages from scatter and through the collimator system.

2.4 Requirement for 3D Dose Verification and Assurance

In earlier times when radiotherapy treatments were less complex, verification was only possible and achieved using conventional dosimetry techniques like one dimensional (1D) ionisation chambers and thermoluminescent dosimeters (TLD's).

The measurements of absolute dose to a high precision at single points were consistently labour intensive and ultimately repetitive and generally involved large water phantoms. The fundamental limitation to resolving areas of high dose gradients is the finite size of the detectors. The large active areas and limited intricacy has made recording dose measurements extremely difficult.

This limitation can be emphasised with the example of treating a wrap tumour which is in close proximity to the spinal chord. The treatment would unavoidably require steep dose gradients to be positioned around the spine to accurately treat the cancer volume effectively. With the limited resolving ability of the existing 1D detectors, valuable information would be lost prior to the treatment. This would result in a data set with reduced accuracy and therefore introduce uncertainties to the proposed spinal wrap treatment and ultimately reduce the confidence of that particular treatment.

Absolute and relative doses can also be measured using appropriately calibrated radiographic films where high resolution in 1D and 2D is achievable. Although conventional two-dimensional film dosimetry can provide excellent precision, resolution and benchmarking, it is generally limited due to its poor reproducibility, energy dependency, non-tissue equivalency and the general difficulty of working with it quantitatively. To achieve a 3D dose representation using 2D film dosimeters requires a laboured effort to carefully position and stack the films in multiple planes.

Conventional techniques therefore do not meet the requirements of fast and accurate time-integrated volumetric dose distribution measurements acquired throughout the entire volume of interest.

The solution, a primary goal of radiation dosimetry at present, is the development of an efficient, accurate and precise system that allows measurement of the full 3D dosimeter volume with time-integrated high spatial resolution. The search for a dosimetry technique that allows 3D imaging of complex radiation dose distributions has led to the research and development of radiation sensitive gels.

2.4.1 Volumetric Gel Dosimetry

A promising development in volumetric radiation dosimetry is gel dosimetry, a technique based on radiosensitive aqueous gels that physically retain information of the three dimensional delivered treatment plans. The radiation-induced chemical changes within the gel can then be quantified by various physical methods and imaging modalities.

The research and development of 3D radiation sensitive gels has in recent years generated much interest with many research groups as it facilitates the measurements of complex radiation dose distributions. Dose calculation algorithms have improved, to a point, where they may be more accurate than physical dose measurements themselves. Therefore, the focus of dosimetry has been to change from dose determination to dose verification. Gel dosimetry, with its inherently three dimensional approach, has significant advantages over other dosimetric verification tools which make it a highly promising method to address the emerging needs of radiotherapy dosimetry. Modern radiotherapy gels have properties that can be summarised as follows (Oldham *et al*., 1998; 2003):

1) They exhibit a linear dose response over the relevant clinical range (0 - 20 Gy) and provide high sensitivity, accuracy and precision allowing small volumes e.g. 1 mm^3, to be successfully interrogated with MRI.

2) They operate as volumetric dose integrators and are independent of radiation direction, energy dependence and dose rate.

3) They can be prepared as soft-tissue equivalent phantoms and can be manufactured to represent human anatomy i.e. head phantoms.

4) They can be evaluated with Magnetic Resonance Imaging (MRI) or alternatively Optical Computerised Tomography (OCT) the latter providing a compact optical scanning method for ‘real time’ dose distribution analysis.

During early development of 3D dosimetry the data sets available were limited to two as opposed to three dimensions. This was due to limitations in the data acquisition methods and the available hardware in part because of the long time required acquiring 3D data-sets with both MRI and OCT.

Continuing development and innovation of this gel dosimetry technique has now led to a significant reduction in the duration of data acquisition scanning. Examples include the extension to existing two dimensional fan beam geometries to fully three dimensional cone beam OCT methods and very fast MR sequences that are going a long way to address the earlier shortcoming.

In 1984, it was proposed that a gelling matrix could be added to the existing Fricke dosimeter to help preserve a three dimensional radiation dose distribution (Gore *et al*., 1984). Fricke dosimeters had previously been used and developed for absolute dose measurements in the form of liquid dosimeters (see Chapter 3). He proposed using existing Nuclear Magnetic Resonance (NMR) technology to probe the Fricke gel dose distributions and gain dose information to a higher accuracy than previously attainable from the dose distributions. This method, now referred to as Magnetic Resonance Imaging (MRI), is still the most common modality choice to obtain three dimensional dose information required for verification and assurance of proposed radiotherapy treatments. This is mainly due to the significant development of MRI techniques over the years within specialised areas of research required for specific diagnostic imaging of human physiology.

In present times MRI centres are over worked and therefore have limited resources for research related development. The limited access, availability and the associated high scanning costs reduce the potential for developing routine three-dimensional gel dosimetry verification experimentation. A consequence of this current MRI limitation has been the encouragement of novel imaging techniques that can stand by themselves as a fully independent and cost effective imaging modality that would be advantageous to the radiotherapy community. In this way dependence on MRI could be reduced or eliminated.

One such alternative imaging method that has been under development in one form or another since the late 1980’s is optical tomography. This in its simplest terms is analogous to X-ray CT (realised in 1972). However, here X-rays are replaced with laser light and the scattering/absorption properties of the exposed radiotherapy gels provide the attenuation variation that allows the planar reconstruction.

Ideally a modern day dosimetric verification tool would routinely provide:

1) High spatial resolution scans.

2) High accuracy and excellent precision per pixel.

3) Shorter imaging times, moving towards real-time verification methods.

4) Be mobile and sufficiently low in manufacturing costs to be effective within all clinical departments.

A prototype fan beam optical tomography scanner has been designed and developed at the University of Hull to aid and assist current MRI technology in providing detailed verification details from gel dosimetry.

The simplified treatment verification method is shown in Figure [2-8]. Once the tumour volume has been diagnosed from either CT or MRI the intended treatment plan is assessed by irradiating a tissue equivalent gel flask. The time-integrated three dimension treatment is fixed within the flask and ready for interrogation by both MRI and OCT. Once the volumetric absorbed dose has been imaged, the treatment plan can be assessed over the tight treatment constraints. If the treatment is not validated another treatment plan is attempted. This process is repeated until a suitable treatment plans is finalised that will treat the tumour volume and not the surrounding healthy tissue.

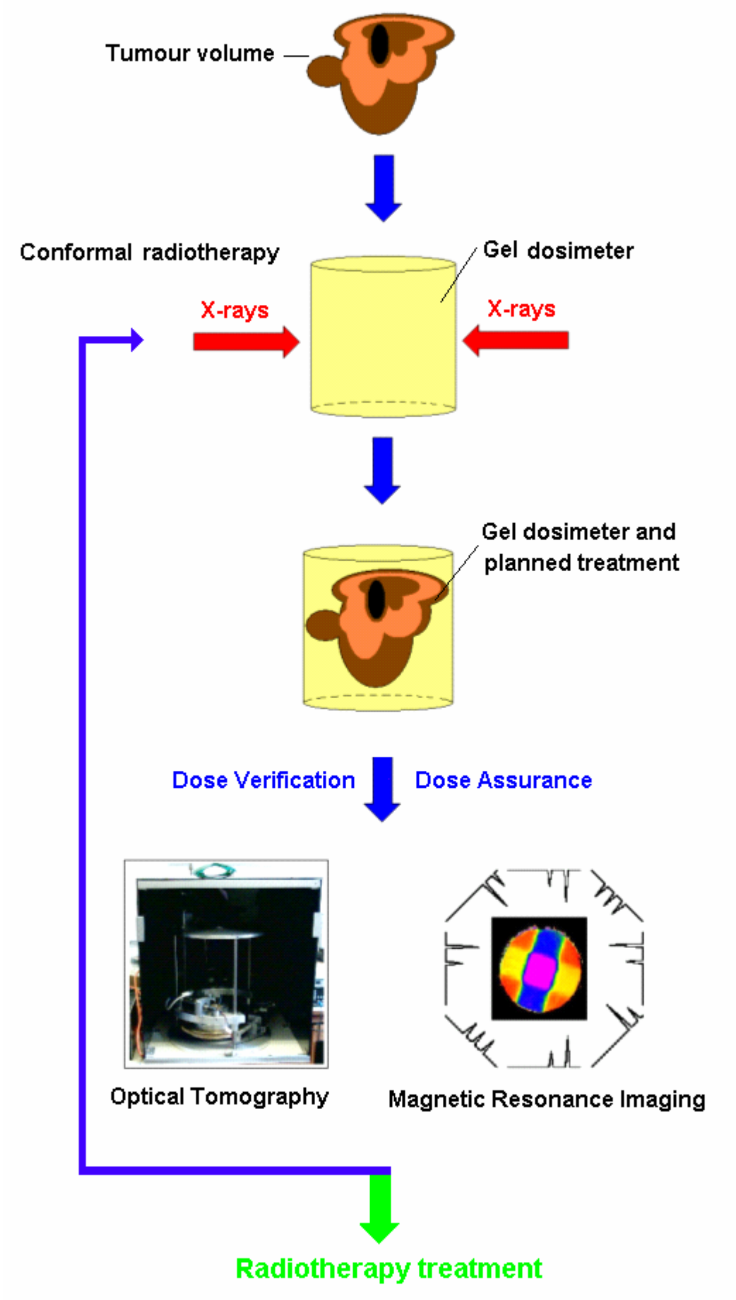

Figure [2-8] Diagram showing the simplified steps discussed in this thesis.

Chapter 3 Radiosensitive Gels

3.1 Radiosensitive Gels

Radiation sensitive gels have been used for many decades for the derivation of absolute dose and, more recently with use of a matrix dose fixing gel structure, for relative absorption measurements.

In chemical dosimeters the gross diffusion of radiation products is reduced by a gel matrix while still permitting the microscopic diffusion necessary for interaction between the radicals and the radiation sensitive chemical.

3.1.1 Absolute Dose Liquids

Radiation sensitive gels were first developed in the 1950s when Day and Stein investigated a colour change upon irradiation of a gel containing Folin's phenol (Day *et al*., 1950). Spectro-photometry based studies were performed by Fricke and Harte which utilized Fricke solutions and gels to measure absolute dose (Fricke *et al*., 1927).

The first gel dosimeter dates back to 1957 (Andrews *et al*., 1957) when measurements were made of photon and electron depth doses using agar gels. In these early first gel dosimeters, chloral hydrate was used as a radiation sensitive chemical. In these gels, Hydrochloric acid (HCl) is produced upon irradiation, which can be measured using electrical conductivity, pH or Cl^- analyses. The best spatial resolution was obtained using electrical resistance as a measure for absorbed radiation. For this, a fine probing electrode was moved around in the irradiated gel. It was found that the dosimeter gel was susceptible to diffusion of the radiochemical products, leading to a deterioration of the dose distribution. In 1958, Hoecker and Watkins studied an alternative method (Hoecker *et al*., 1958) based on radiation-induced polymerisation in monomer and polymers.

3.2 Fricke Gel Dosimetry

In 1984 it was proposed that the radiation induced changes in the well-established aqueous ferrous sulphate Fricke dosimeter (Fricke *et al*., 1927; Andrews *et al*., 1957) could be probed with Nuclear Magnetic Resonance (NMR) relaxation measurements rather than the conventional spectro-photometry (Gore *et al*., 1984). An important aspect of this development was the stabilization of the spatial dose information by incorporating the aqueous Fricke solution into a gel matrix. With the increasing availability of Magnetic Resonance Imaging (MRI) scanners, the medical imaging modality based on NMR, the field of gel dosimetry for radiation therapy was established.

The radiation-induced changes in the paramagnetic moment (Fe^{2+} to Fe^{3+}) within the Fricke solution may be quantified by NMR relaxation measurements (Gore *et al*., 1984) or optical techniques (Appleby *et al*., 1991). It was shown that the NMR spin-lattice relaxation rate, $R_1 = 1/T_1$, and spin-spin relaxation rate, $R_2 = 1/T_2$, of the gel dosimeter were closely correlated to the amount of the Fe^{3+} ions produced by the irradiation of Fe^{2+} in the Fricke solution (Gore *et al*., 1984). As the ferrous ions are oxidized to ferric ions, a change in the net paramagnetic moment is produced. This alters the spin-lattice relaxation of the water molecules near the coordination shells of the ions (De Deene *et al*., 2000). Ferric ions produce paramagnetic enhancement of the water-proton relaxation rates, which can then be measured with MRI (Maryanski.*et al*., 1994).

3.2.1 Fricke Gel Composition

The required constituents for a typical Fricke gel are: distilled or well de-ionised water, ferrous ion (usually from ferrous ammonium sulphate), sulphuric acid, air or oxygen, and a gel. The ferrous ion provides the chemical probe for the dosimeter while the gel provides some spatial localisation of the radiation-induced changes. Air or oxygen is bubbled through the solution during the entire process to ensure that the dosimeter is well oxygenated, since oxygen is required for the radiation chemistry to proceed.

After preparation, the solution is usually kept cool and in the dark to limit spontaneous oxidation (i.e., the spontaneous conversion of Fe^{2+} to Fe^{3+} which inevitably occurs). It can be noted here that the procedures and facilities for preparing reproducible Fricke gel dosimeters are considerably simpler than required for most polymer based dosimeters (which contain toxic constituents and usually require anoxic conditions during preparation). With all gel dosimeters there is a selection of gelling agents that can be used. The most common are Agarose (Appleby *et al*., 1987; 1988; Olsson *et al*., 1989; 1990; 1991) and gelatin systems (Audet *et al*., 1997; Olsson *et al*., 1989).

3.2.2 Fricke Dosimeter Reaction Process

The dosimetric basis of the Fricke solution is provided by the dose dependent transformation of ferrous (Fe^{2+}) ions into ferric (Fe^{3+}) ions (Fricke *et al*., 1927).
A Fricke solution consists of 1 x 10^{-3} M ferrous ammonium sulphate and 1 x 10^{-3} M sodium chloride dissolved in 0.4 M sulphuric acid solution. Consequently, the solution is 96 % water and it is the radiation chemistry of water that determines the yield of the Fricke solution. The chemical stage of water radiolysis occurs from 10 to 100 ps after the passage of the primary ionising particles and consists of the diffusion of radiation-produced ions and radicals through the bulk water (Shortt, 2001).

The yield ($G(Fe^{3+})$) for the Fricke solution is given in equation (3-1)

$$G(Fe^{3+}) = 2G(H_2O_2) + 3G(H) + G(OH) \tag{3-1}$$

Due to the presence of the sulphuric acid, solvated electrons combine with H^+ and so the initial yield $G(e_{aq}^-)$ is combined with $G(H)$ in equation (3-1). Because the Fricke solution is aerated, the H radical reacts with dissolved O_2 to produce a hydroperoxyl radical, HO_2 which oxidizes one ferrous ion according to

$$Fe^{2+} + HO_2 \rightarrow Fe^{3+} + HO_2^- \qquad (3\text{-}2)$$

and thus forms hydrogen peroxide according to

$$HO_2^- + H^+ \rightarrow H_2O_2 \qquad (3\text{-}3)$$

The hydrogen peroxide oxidizes one ferrous ion according to

$$Fe^{2+} + H_2O_2 \rightarrow Fe^{3+} + OH + OH \qquad (3\text{-}4)$$

and a second one according to

$$Fe^{2+} + OH \rightarrow Fe^{3+} + OH- \qquad (3\text{-}5)$$

Thus a ferrous ion is oxidized per hydroxyl radical, two per hydrogen peroxide molecule and three per hydrogen atom (or solvated electron) (Shortt, 2001).

3.2.3 Practical Fricke Dosimetry

Much research effort has gone into the development and utilisation of the Fricke gel dosimeter although it has not gained widespread acceptance in clinical practice, primarily due to the unpreventable ionic diffusion present within the gel dosimeter.
Ferric ions (Fe^{3+}) are small in dimension and are observed to diffuse through the gel matrices leading to the degradation of the recorded dose distribution with time. In order to obtain a spatially useful image of the dose distribution, the imaging had to be completed generally within 1 hour. With this time constraint, it was found to be extremely difficult to image the dose distributions using spectro-photometry and MRI in sufficient time to maintain high resolution and an accurate depiction of the dose distribution.

Due to the conformal techniques of modern day radiotherapy treatments high dose gradients exist. In these circumstances the inherent ionic ferric diffusion means the 3D dose distributions are inevitably destroyed (Schulz *et al*., 1993; Baldock *et al*., 1994; 2001; Olsson., *et al* 1992; Kron *et al*., 1997 and Chu *et al*., 2001). Solutions to this post irradiation ionic diffusion have been to either reduce the diffusion mechanism by using Polyvinyl Alcohol (PVA) based formulations (Chu *et al*., 2000) or acquiring much faster MRI measurements using calibrations based on relative signal changes rather than absolute T_1 measurements (Chu *et al*., 1998).

The diffusion of ferric and ferrous ions has led to the implementation of fast T_1 imaging methods (Kron, 1997), and the proposal to use T_1-weighted images instead of real T_1 maps and other T_1 fitting algorithms based on Bayesian statistics (de Pasquale *et al*., 2000). The diffusion time of ferrous and ferric ions can be reduced significantly by using polyvinyl alcohol instead of gelatin or agarose as the gel (Chu *et al*., 2000).

3.2.4 Fricke Gel Variants

Gupta's work with radiosensitive gels, (Gupta *et al*., 1973; 1974; 1978; and 1983) led him to in effect bring together the gel work of Day and Stein (Day *et al*., 1950) and Fricke and Hart (Fricke *et al*., 1927). Gupta and fellow workers introduced a radio-chronic metal indicator dye to the established Fricke solution. The chosen indicator was xylenol orange, which used in conjunction with benzoic acid, yielded the ferrous sulphate benzoic xylenol orange dosimeter, (FBX).

This new radiation sensitive gel, in addition to radiation induced ferrous oxidation, allowed improved optical observation of the dose distribution within the solution.
The combination of the oxidised Fe^{3+} ions and the xylenol orange dye increased the absorption wavelength used by the spectro-photometry technique. This increase in wavelength effectively limited unwanted scattering effects from the ferrous molecules originating from Rayleigh scattering (which is proportional to λ^{-4}).

It was shown that the addition of a metal ion indicator such as xylenol orange induced colour changes (Appleby *et al*., 1991) in the gel upon irradiation enabling the gel to be scanned optically (Gore *et al*., 1996, Kelly *et al*., 1998). This again is advantageous in countering the limited access to MRI centres. The optical CT scanning approach was applied by Kelly (Kelly *et al*., 1998) to imaging a Fricke-benzoic-xylenol gel using the optical scanning technique to map radiation induced changes in the local optical absorption coefficients. This followed work undertaken (Gore *et al*., 1996) imaging polyacrylamide gel dosimeters.

More recently, work has been reported with FBX dosimeters in which the absorption properties of the dosimeter were utilised (Kelly *et al*., 1998). A 543 nm probe was used to image the dosimeter rather than the previously used spectro-photometric wavelengths of 224 nm and 304 nm (Fricke *et al*., 1927). The incorporation of the xylenol orange indicator reduced the Rayleigh scattering within the dosimeter and increased the absorption wavelength of the gel on the whole. The colour of an un-irradiated gel is light purple and then changes to a dark orange/purple colouration with increased absorbed dose.

3.3 Polymer Gel Dosimetry

The differences in paramagnetism of ferrous ions from their ferric form obtained after irradiation i.e. Fricke dosimetry (see previous section), was used to obtain a dose dependent contrast in magnetic resonance images. However due to the inherent ionic diffusion, the use of Fricke gel dosimeters was limited by the image degradation over time. This was the main motivation for the development, and increased clinical use, of poly-acrylamide gel dosimeters (PAG), (Maryanski *et al*., 1993; 1994).

Polymerisation reactions were first reported by Alexander detailing the effects of ionising radiation on polymethylmethacrylate (Alexander *et al*., 1954), and radiation induced polymerisation reactions by Hoecker and Watkins (Hoecker *et al*., 1958). It was known in the 1970's that the irradiation of polymers or macromolecules could alter their molecular dynamics and structures. Irradiation can induce the polymerisation, cross-linking or degradation of many synthetic polymers and bipolymers. In its simplest terms, a gel dosimeter is a hydrogel in which monomers are dissolved.

The fundamental principle of polymer gel dosimeters involves the radiation-induced polymerisation of monomer (and often co-monomer) species suspended in a gelatin matrix. Upon irradiation, water molecules are dissociated into several highly-reactive radicals and ions (Spinks *et al*., 1964; Magee *et al*., 1996), a process termed "radiolysis". Thus radiation induced polymerisation occurs from the monomer reservoir and long-chained polymers are created that are spatially retained in the gelatin matrix. The spin-spin relaxation rate, $R_2 = 1/T_2$, of neighbouring water protons increases in proportion to the absorbed dose (Haraldsson *et al*., 2000). Thus, MRI can be used to visualize the absorbed dose distribution.

After irradiation, a gel will contain regions that are polymerised and cross-linked. This is the origin of the gels spatial dose-response characteristics, as a degree of polymerisation depends on the initial quantity of free radicals generated by the incident radiation and, therefore on the absorbed dose. The free radical chains produced upon polymerisation lead to the formation of polymer micro-particles which remain attached to or entangled with the gelling substance. The magnitude and strength of the micro-particles formed directly indicates the level of absorbed dose from subsequent free radical generation. The high molecular weight of the compounds produced by the absorbed dose cause no diffusion in the matrix being observed over a long period of time, so that the spatial information on the absorbed dose is greatly improved. The formation of cross-linked polymers in the irradiated region of the gel increases the proton transverse relaxation rate ($R_2 = 1/T_2$) in proportion to the dose.

3.3.1 Polymer Gel Reaction Process

The water content of gel dosimeters is generally of the order of 90 %. To understand the physical mechanisms that take place in a gel dosimeter upon irradiation, we can rely to a large extent on the physical processes that occur in water. Basic experimental observation is that, for numerous solutions of different compounds in water, the solute not being affected directly by the radiation but indirectly by some entity or entities produced from water (Swallow, 1973). The passage of high energy ionizing radiation through water and solutions of water initially produces electrons, positively charge water ions and excited water molecules (Allen, 1961) and (Brandrup *et al.*, 1999). The primary reactions resulting from the radiolysis of water are shown in equation (3-6) (Whittaker, 2001).

$$H_2O \rightarrow e^-, H_2O\cdot^+, H_2O* \tag{3-6}$$

The electrons lose further energy by collisions until they reach thermal energies and become solvated

$$e^- + nH_2O \rightarrow e_{aq}^- \tag{3-7}$$

The positive ions are energetically very unstable, and decompose rapidly to give H^+ ions and $\cdot OH$ radicals

$$H_2O\cdot^+ + H_2O \rightarrow H_3O^+ + \cdot OH \tag{3-8}$$

The processes drawn in (3-7) and (3-8) occur rapidly (<10^{-11} seconds). The excited state molecules are believed to decompose to form radical species

$$H_2O* \rightarrow H\cdot + \cdot OH \tag{3-9}$$

However it is believed that none of the species present within the polymer gel dosimeters are susceptible to the primary radiolysis reactions detailed above. Secondary reactions may occur amongst these primary species trapped within the radiation spurs, to form water molecules, molecular hydrogen or hydrogen peroxide. Thus approximately 10^{-8} seconds after irradiation species present include: e_{aq}^-, $H\cdot$,

$\cdot OH$, H_2 , H_2O_2 , H_3O^+ , H_2O* and $H_3O\cdot$ and are able to contribute to the polymerisation of the monomers present within the gel dosimeters.

3.3.2 BANG ® Gel Dosimetry

In 1992 a new gel dosimetry formulation was proposed, which was based on the polymerisation of acrylamide and N,N'-methylene-bis-acrylamide (bis) monomers infused in an aqueous agarose matrix (Maryanski *et al*., 1992). This system was given the acronym BANANA due to the use of the chemical components (bis, acrylamide, nitrous oxide and agarose) (Maryanski *et al*., 1993). This type of gel dosimeter did not have the associated diffusion problem of Fricke gels and was shown to have a relatively stable post-irradiation dose distribution. The polymerisation reaction occurred by cross-linking of the monomers induced by the free radical products of water radiolysis. In 1994 the BANANA formulation was refined (Maryanski *et al*., 1994) by replacing agarose with gelatin and given the acronym BANG (bis, acrylamide, nitrogen and aqueous gelatin), the first of a series of new polymer gel formulations.

BANG® gels were produced to provide a gel solution with a greater sensitivity to radiation dose than its BANANA predecessor. Agarose was replaced with gelatin to provide the gelling agent which led to the current generations of BANG I, 2 and 3 (bis acrylamide nitrogen and gelatin) polymer gels (Maryanski *et al*., 1994). Nitrous oxide and nitrogen are added to the gel mixture to displace oxygen from the gel during manufacture (Maryanski *et al*., 1994; McJury *et al*., 2000) BANG-1® and BANG-2® gels were the first models of BANG® gels developed. The former was made using acrylamide in powder form, while the latter replaces acrylamide with acrylic acid and NaOH to buffer the pH. Gel response is improved with acrylic acid compared to acrylamide, allowing larger relaxation-rate changes per unit dose.

BANG-3® gels have recently been developed. This type of gel has strong optical and MR responses (Maryanski *et al*., 1994; McJury *et al*., 2000). With the BANG-3® gel, acrylic acid is replaced with methacrylic acid.

Table [3-1] summarizes the gel types and compositions. Of the BANG® polymer gels, BANG-3® polymer gel reportedly has the highest MR sensitivity upon photon irradiation (Maryanski *et al*., 1996).

Gel Acronym	Gel Constituents				
BANANA	BIS	Acrylamide	Nitrous oxide		Agarose
BANG-1™	BIS	Acrylamide	Nitrogen		Gelatin
BANG-2™	BIS	Acrylic acid	Nitrogen	Sodium hydroxide	Gelatin
BANG-3™	BIS	Methacrylic acid	Nitrogen	Sodium hydroxide	Gelatin

Table [3-1] Summary of the various compositions during polymer gel development.

In 1994 this formulation was patented (Maryanski *et al*., 1994) and became commercially available through MGS Research Inc. as BANG®. Subsequently, due to the naming of the commercial product, PAG (Baldock *et al*., 1998) became the polymer gel dosimeter acronym of choice for most authors (Baldock *et al*., 2006).

3.4 Normoxic Gel Dosimetry

Although PAG gels have to some extent reduced the dose migration and subsequent loss of spatial dose information post irradiation, there still exists limitations to using them.

1) The presence of oxygen inhibits the polymerisation process and results in reduced gel performance. Therefore PAG gels require hypoxic environments for gel manufacture and ideal storage. This constrained manufacture requirement is generally accomplished by using a glove box with a continuous inert gaseous purge to limit the presence of molecular oxygen.

2) Commonly used ingredients such as bis and acrylamide within the PAG gels are both neurotoxins and carcinogens and thus require careful handling and secure storage due to their potential hazardous nature.

Therefore the ease and application of PAG gels within universities and small hospital departments are limited by these essential requirements. Due to these limitations, new gel mixtures have been investigated that can be manufactured in an anoxic environment and that can respond to radiation in the presence of oxygen. Further, the manufacturing process has been simplified such that fume cupboards are not extensively required to limit oxygenation of the gel solution. This investigation was guided by earlier studies of oxygen catalyzed polymerisation of the acrylic monomer methyl methacrylate in solution (Reddy *et al*., 1982; Taqui Khan *et al*., 1967).

3.4.1 MAGIC Gel Dosimetry

In the system proposed, (Fong *et al*., 2001), a chemical is added to the polymer gel that scavenges the oxygen present. It was observed that in one reaction a bivalent metal may complex and join with ascorbic acid and molecular oxygen and subsequently allow an electron to transfer the complex to an external species, thus generating free radicals which may initiate polymerisation. This system had not previously been used with ionizing radiation and required the presence of oxygen to be effective. The full reaction process is described by De Deene (De Deene *et al*., 2002). This new type of polymer gel dosimeter was known as MAGIC (methacrylic and ascorbic acid in gelatin initiated by copper). The principle behind the gel was to bind atmospheric oxygen in a metallo-organic complex thus removing the problem of oxygen inhibition via scavenging and enabling polymer gels to be manufactured on the bench-top in the laboratory. This created what was to be known as a normoxic gel dosimeter, compared with the previous PAG formulation, which subsequently became known as a hypoxic gel dosimeter.

Since the introduction of normoxic MAGIC gels (Fong *et al*., 2001), they have shown considerable promise as radiation dosimeters. The gels overcome the manufacturing sensitivity issues with oxygen that previous polymer gels have and they are more convenient to store, use and dispose of. From their constituent parts MAGIC gels can be made into tissue equivalent anthropomorphic irradiation vessels of arbitrary shape for *in situ* experimentation. The average atomic weight of the human body (fat, muscle, bone etc) can be characterised by a Z_{eff} value that simply details the average weight of all the elements present i.e. carbon, oxygen and nitrogen etc for the specimen. The Z_{eff} value for a MAGIC gel is 7.07, which compares to 6.92 for muscle and 7.22 for water. The dose response can also be varied by altering the precise composition of the gels, for example, increasing the amount of methacrylic acid acting as the single monomer. The method used to manufacture the MAGIC gel described here was reproduced from Fong (Fong *et al*., 2001).

The gels are produced with using the following ingredients: gelatin (300 bloom), 80 grams per litre (~ 8 % by weight); hydroquinone, 1.8×10^{-2} M; ascorbic acid, 2.0×10^{-3} M; copper (II) sulphate-pentahydrate 99.9 %, 8.0×10^{-5} M; methacrylic acid 99 %. The manufacture of 1 litre of the gel (9 %) of methacrylic acid (MAA) can be summarised as follows.

1. 700 ml of water is heated to 50 ^{o}C and the gelatin added.

2. Two grams of hydroquinone in 48 ml of distilled water is then added at this stage and then the mixture is allowed to cool.

3. At 37 ^{o}C, 0.352 g of ascorbic acid dissolved in 50 ml of water and 0.02 g of copper sulphate in 30 ml of water is added.

4. Finally 90 g of methacrylic acid is added to the mixture before being carefully transferred to a suitable container for gelation and storage.

5. The containers are then sealed and allowed to cool to room temperature.

3.4.2 Normoxic Variants

It was subsequently shown (De Deene *et al*., 2002) that other antioxidants could be used in the manufacture of normoxic gels including tetrakis (hydroxymethyl) phosphonium chloride (THP). Numerous authors subsequently published the results of work investigating different compositions and formulations of normoxic polymer gel dosimeters and these were recently summarised (Senden *et al*., 2006). Table [3-2] shows various formulations reproduced from (Baldock *et al*., 2006).

Normoxic Dosimeters	Reference	Polymer gel dosimeter formulation
MAGIC	Fong *et al.,* 2001 De Deene *et a.,* 2000 De Deene *et al.,* 2002	Methacrylic acid, ascorbic acid, hydroquinone, $CuSO_4 \cdot 5H_2O$, gelatin.
MAGAS	De Deene *et al.,* 2002 Venning *et al.,* 2005	Methacrylic acid, ascorbic acid, gelatin.
MAGAT	De Deene *et al.,* 2002 Brindha *et al.,* 2004 Hurley *et al.,* 2005	Methacrylic acid, gelatin tetrakis (hydoxymethyl) phosphonium chloride.
nMAG	De Deene *et al.,* 2006	Methacrylic acid, gelatin Bis[tetrakis (hydoxymethyl) phosphonium] sulphate.
PAGAS	De Deene *et al.,* 2002	Acrylamide, N,N-methylene-bis-acrylamide, gelatin Ascorbic acid.
PAGAT	Brindha *et al.,* 2004 Venning *et al.,* 2005a Jirasek *et al.,* 2006	Acrylamide, N,N-methylene-bis-acrylamide, tetrakis (hydoxymethyl) phosphonium chloride, hydroquinone, gelatin.
nPAG	De Deene *et al.,* 2006	Acrylamide, N,N-methylene-bis-acrylamide, Bis[tetrakis (hydoxymethyl) phosphonium] sulphate, gelatin.

Table [3-2] Summary of normoxic gel formulations investigated by various workers.

3.5 Retrieving Information from Gels

The possibility of using nuclear magnetic resonance (NMR) as a method of retrieving radiotherapy dose information from radiosensitive gels was first suggested by Gore. In a seminal paper, a proposal of using a gelling matrix i.e. agarose and gelatine to capture and 'fix' the radiation dose in the gel was made (Gore *et al*., 1984). The continuing research and developments within NMR methods and better understanding of the techniques allowed various specialisations to be developed. For example, magnetic resonance imaging (MRI) could be applied to this new gel dosimetry.

3.5.1 Optical Computerised Tomography

Methods used to detect radiation induced changes had been established well in advance of the onset of the MRI imaging modality. While X-ray CT may be the most familiar application of tomography, the same concept can be applied in medicine using other imaging modalities, including MRI, Ultrasound, Nuclear-medicine and the relatively new technique of Optical Computerised Tomography (OCT). The development of OCT for gel dosimetry was delayed due to the fact that MRI was developed primarily for medical applications and then applied as a mature imaging modality to 3D-CRT and state-of-the-art IMRT. It has only been since the late 1990's that the technology needed for such measurements has been developed to deliver the required performance at the appropriate cost. The advancement of digital computers, including their miniaturisation, enhanced memory performance and available software applications, to the available laser diodes and imaging software, (see Chapter 4) has allowed such novel imaging possibilities to be realised and applied to interrogate radiation sensitive gels.

3.5.1.1 Image Reconstruction Theory

Computerised tomography (CT) proceeds by a series of slicing steps that reduce a 3D volume, first to a collection of 2D sections or slices. Then each slice is cross-hatched with lines to produce a collection of 1D strips or projections. This process reduces the amount of information at each step so that eventually the detectors can transfer the data to a computer-based reconstruction algorithm that can reconstruct the slice with the required resolution. To faithfully reconstruct the intended 2D slices requires vast amounts of information that strongly revolve around the manipulation of simultaneous equations and Fourier integrals. The principal method employed for deriving 2D dose distributions from changes in the optical density in an ideal radiosensitive gel is similar to that used in X-ray CT and simply involves replacing the x-rays with monochromatic laser light at the desired wavelength.

Within X-ray computed tomography a planar image of an object is reconstructed from a series of line integrals obtained from parallel projections taken from different angles and directions through a region of interest as a function of $\mu(x, y)$, see Figure [3-1]

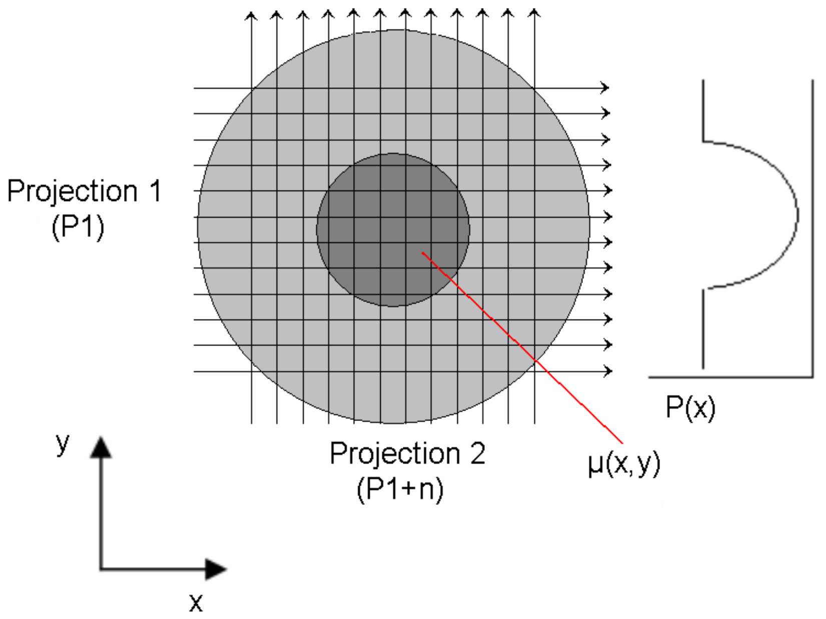

Figure [3-1] A simplified illustration of the projections required for tomographic image reconstruction where $\mu(x, y)$ are the Cartesian sampling points within the object medium. Here two projections, P1 and P1+n, illustrate the pathlengths and the cross over data points (sampling) the laser light source defines through the object medium. For a comprehensive reconstructed image 100 to 180 projections would be required.

The intensity of a monochromatic light beam passing through a medium is attenuated exponentially under narrow beam conditions. If $\mu(x, y)$ denotes the optical attenuation coefficient per unit length in a section of the object and I_0 is the incident intensity, then the intensity exiting the sample at position x is $I(x)$ and given by

$$I(x) = I_0 \exp(-\mu x), \tag{3-10}$$

Optical tomography has been shown to satisfy the ideal requirements for dosimetric verification, providing high spatial resolution and accuracy in short imaging times and producing a high precision per pixel within reconstructed 2D images (McJury *et al.*, 2000).

3.5.1.2 Simple Back-Projection

The basic mathematical method (analogous to the filtered back-projection used in CT) uses the addition and division operators and is only realistically applicable for relatively small matrices i.e. 6 by 6. To reconstruct an image from this matrix would require 36 simultaneous equations, and for modest images, for example, a 128 by 128 matrix, would require in excess of 16 thousand equations. A simple example of the back-projection method demonstrated in Figures [3-2] to [3-6] with the intention of illustrating the basic concepts before a more applicable method is described in section [3.6.1.2]. This simple example shows how the unknown values can be obtained from simple back projection. Firstly, in Figure [3.2] a 6 by 6 square a) can be seen with 36 unknown values and with gross attenuation values on the two axes. The corresponding experimental situation is illustrated in b) and shows the projections used to obtain the gross attenuation values shown in a).

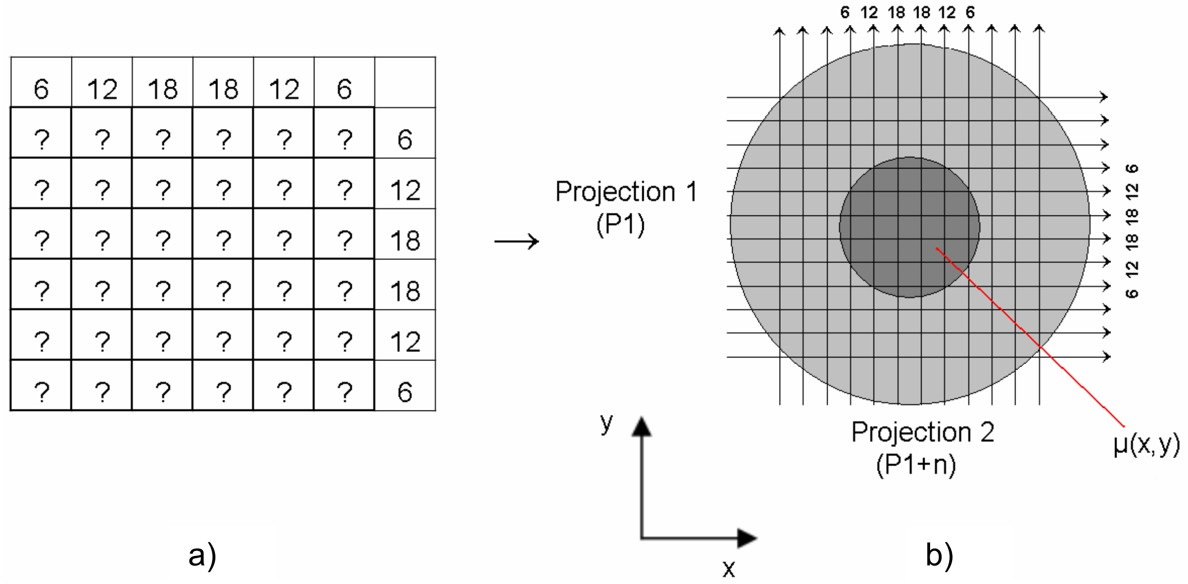

6	12	18	18	12	6	
?	?	?	?	?	?	6
?	?	?	?	?	?	12
?	?	?	?	?	?	18
?	?	?	?	?	?	18
?	?	?	?	?	?	12
?	?	?	?	?	?	6

Figure [3-2] Initial image of a magic box problem with a 6 by 6 matrix showing in a), the unknown elements within the box and in b), the corresponding projections taken to provide the resulting gross attenuation values.

Firstly the P1 (horizontal) values are ‘back-projected’ along the elements associated with the P1 gross attenuation value (6). The concept is to divide this horizontal attenuation value by the number of elements along the line integral, hence equally distributing the value throughout the line. This process in continued until all the P1 projection values have been distributed evenly within the projection elements.

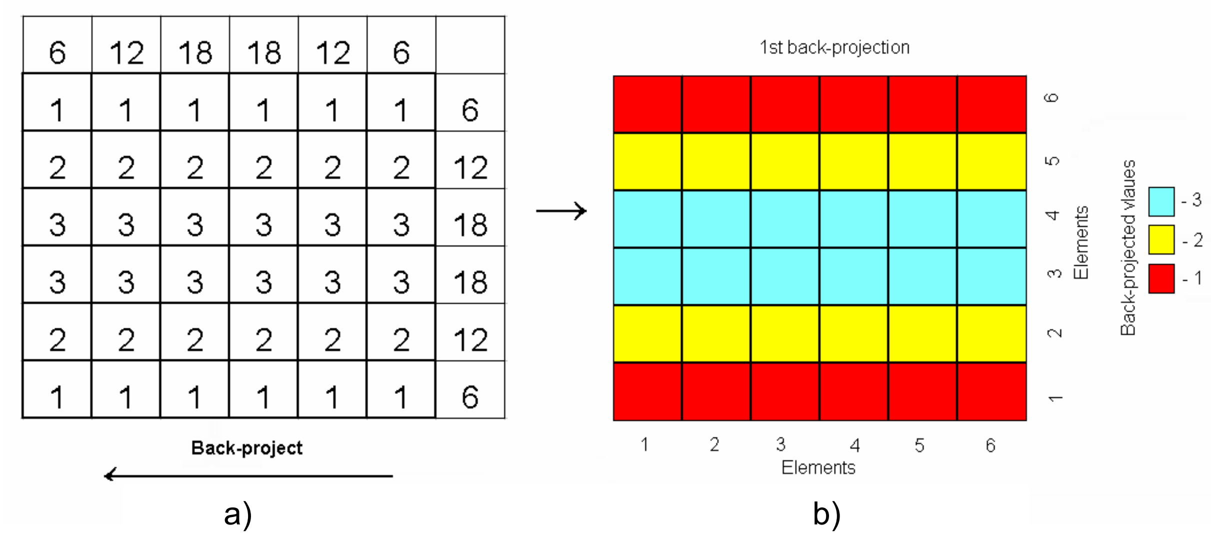

6	12	18	18	12	6	
1	1	1	1	1	1	6
2	2	2	2	2	2	12
3	3	3	3	3	3	18
3	3	3	3	3	3	18
2	2	2	2	2	2	12
1	1	1	1	1	1	6

Figure [3-3] Illustration of the first back-projection taken shown in a) and the corresponding back-projected image this generates in b).

This ‘back-projecting’ is repeated for all projections (P1+n) each time adding the average values to the preceding projection averages and hence accumulating elemental averages within the 2-D slice, see Figure [3-4].

The method can be described elsewhere when considering that a single projection is formed from many discrete line integrals acquired from finitely sized detectors. Each line integral will have a specific gross attenuation value formed from many local elements along the line integral.

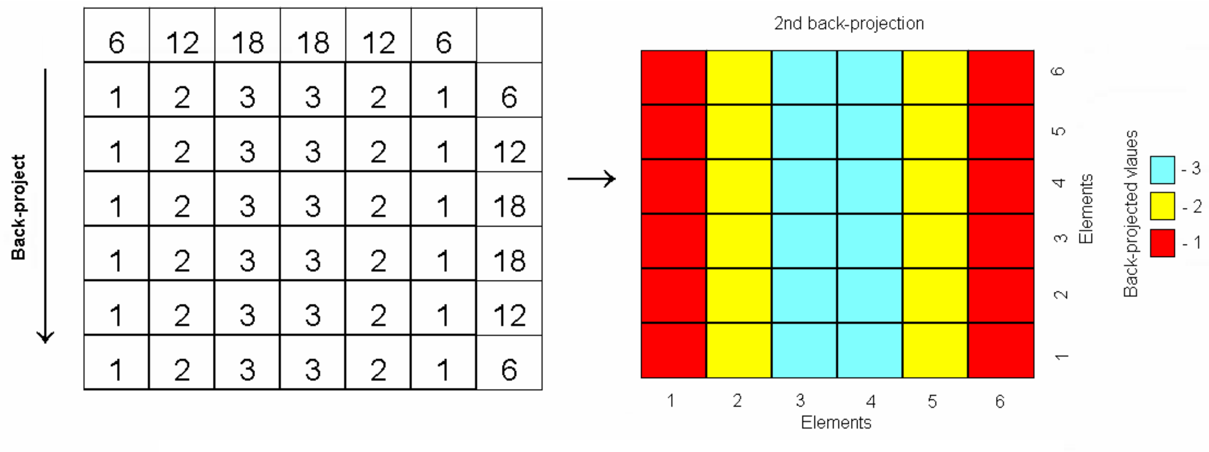

6	12	18	18	12	6	
1	2	3	3	2	1	6
1	2	3	3	2	1	12
1	2	3	3	2	1	18
1	2	3	3	2	1	18
1	2	3	3	2	1	12
1	2	3	3	2	1	6

a) b)

Figure [3-4] Illustration of the second back-projection taken shown in a) and the corresponding generated back-projected image in b).

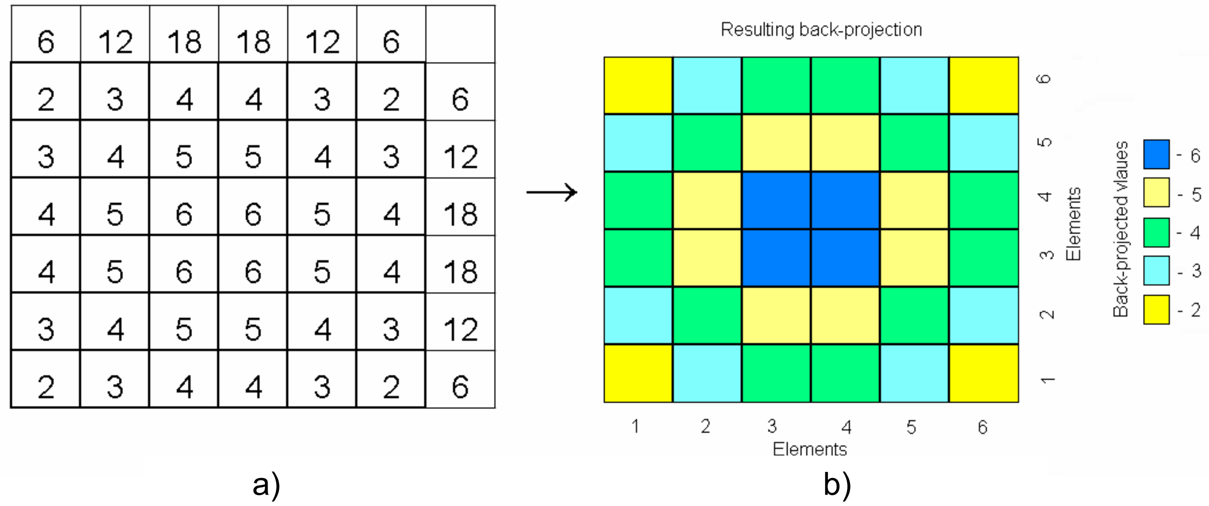

6	12	18	18	12	6	
2	3	4	4	3	2	6
3	4	5	5	4	3	12
4	5	6	6	5	4	18
4	5	6	6	5	4	18
3	4	5	5	4	3	12
2	3	4	4	3	2	6

a) b)

Figure [3-5] Illustration of the accumulative back-projected values a) and image b) from the previous two axis examples shown in Figures [3-4] and [3-5].

This basic method and resulting image shown in Figure [3-5] can be compared to the original object in Figure [3-1] and indeed does suggest that a basic correlation exists between the object and reconstructed image. This is illustrated in Figure [3-6].

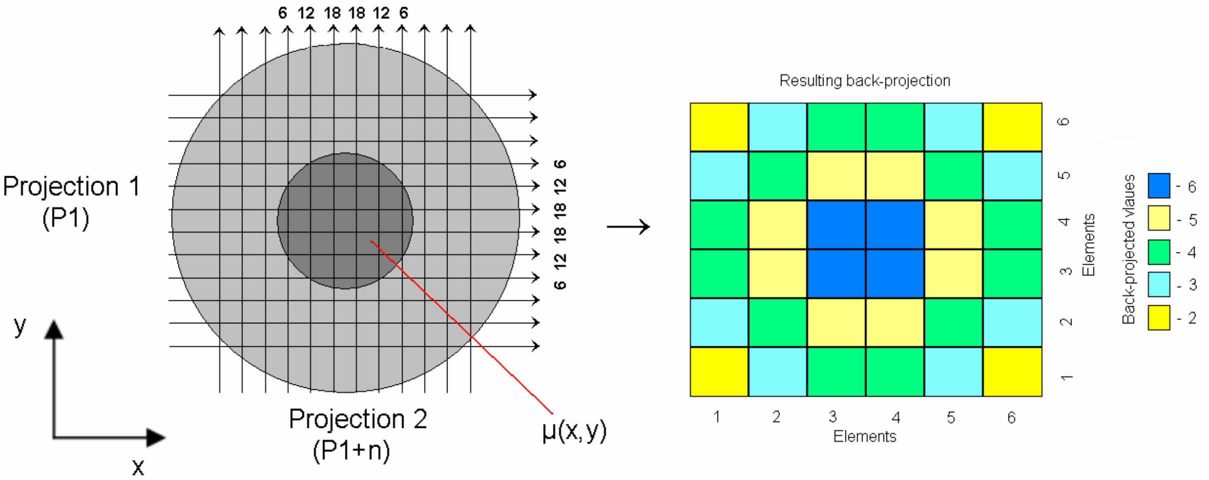

a) b)

Figure [3-6] Showing the comparison between $\mu(x,y)$ and the resulting attenuation values (navy blue squares shown in b) derived from two simple back projections.

The mathematical process of reconstruction in the very simplest of terms could be achieved, although quite laboriously, with a hand held calculator, using the operations of addition and division. The development and the use of dedicated digital computers allowed images to be reconstructed too much higher degrees of both accuracy and resolution. Unfortunately simple back-projection has severe limitations as far as real imaging is concerned. This averaging method will assign positive attenuation values to areas within the slice that do not contribute to the gross attenuation. On a much larger scale and level of matrix complexity, this leads to an inherent fogging within the reconstructed image that would be unacceptable.

There are, however more robust and sophisticated mathematical techniques that can be applied to image reconstruction at the detailed level required. An example is the algebraic reconstruction technique (ART). Mathematical techniques like ART can provide increased flexibility and allow one to correct for various deficiencies in the raw projection data, though they are time consuming to perform.

To overcome this, the Radon transform method or the filtered back-projection is generally used as it produces much more reliable results than the simple back-projection method of reconstruction described above.

3.5.1.3 Filtered Back Projection

Any of several algorithms available can then be used to reconstruct its 2D cross-sectional image from its projections. The property that is actually computed is the linear attenuation coefficient of that object, at various points in the object's cross-section. If this process is repeated at various heights along the object, we obtain several 2D cross-sectional images, which can then be stacked one on the top of another to get internal 3D volume visualization of the object.

The Filtered Back Projection algorithm uses Fourier theory to arrive at a solution to the problem of finding the linear attenuation coefficient at various points in the cross-section of an object. A fundamental result linking Fourier transforms to cross-sectional images of an object is the Fourier Slice Theorem. A detailed account of the Fourier slice theorem and other CT based algorithms can be obtained from Kak and Slaney (Kak and Slaney, 1988).

The aim of OCT is to obtain the optical attenuation of the sample (which is related to the absorbed dose) as a function of spatial position by acquisition of a set of projections. Figure [3-7] and Figure [3-8] offers a more simplified illustration of the back-projection method of converting Radon space back into the spatial domain. This is shown by taking two projections at ϕ = 0 and ϕ = 90 degrees of a simple cylinder geometry and demonstrates how Radon space or the Fourier domain is ‘filled up’ or sample prior to reconstruction. The presentation of data in Radon space, in 2-D image form, is often called a sinogram. The sinogram, in the Fourier domain, is then back-projected or ‘smeared’ out into the spatial domain and reproduces the 2D image.

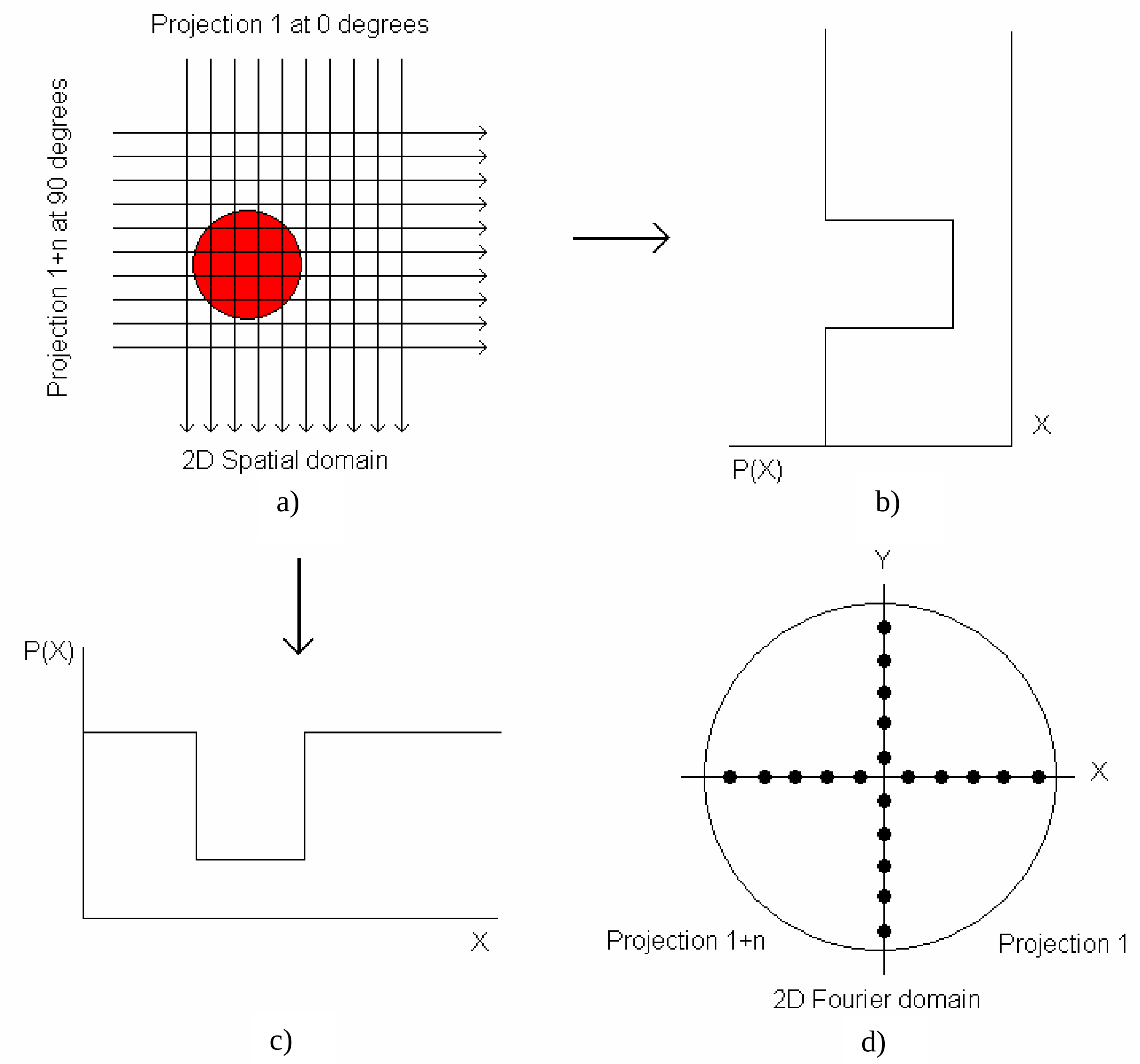

Figure [3-7] Showing, a-c), the associated attenuation distributions from two projections of the metal cylinder (see Figure 5-2]), taken at ϕ = 0 and ϕ = 90 degrees and, d), the corresponding Fourier domain sampling. The degree of sampling is proportional to the number of projection elements (10 shown here) and can be inferred from the number of points on both the x and y axis shown in the 2D Fourier domain.

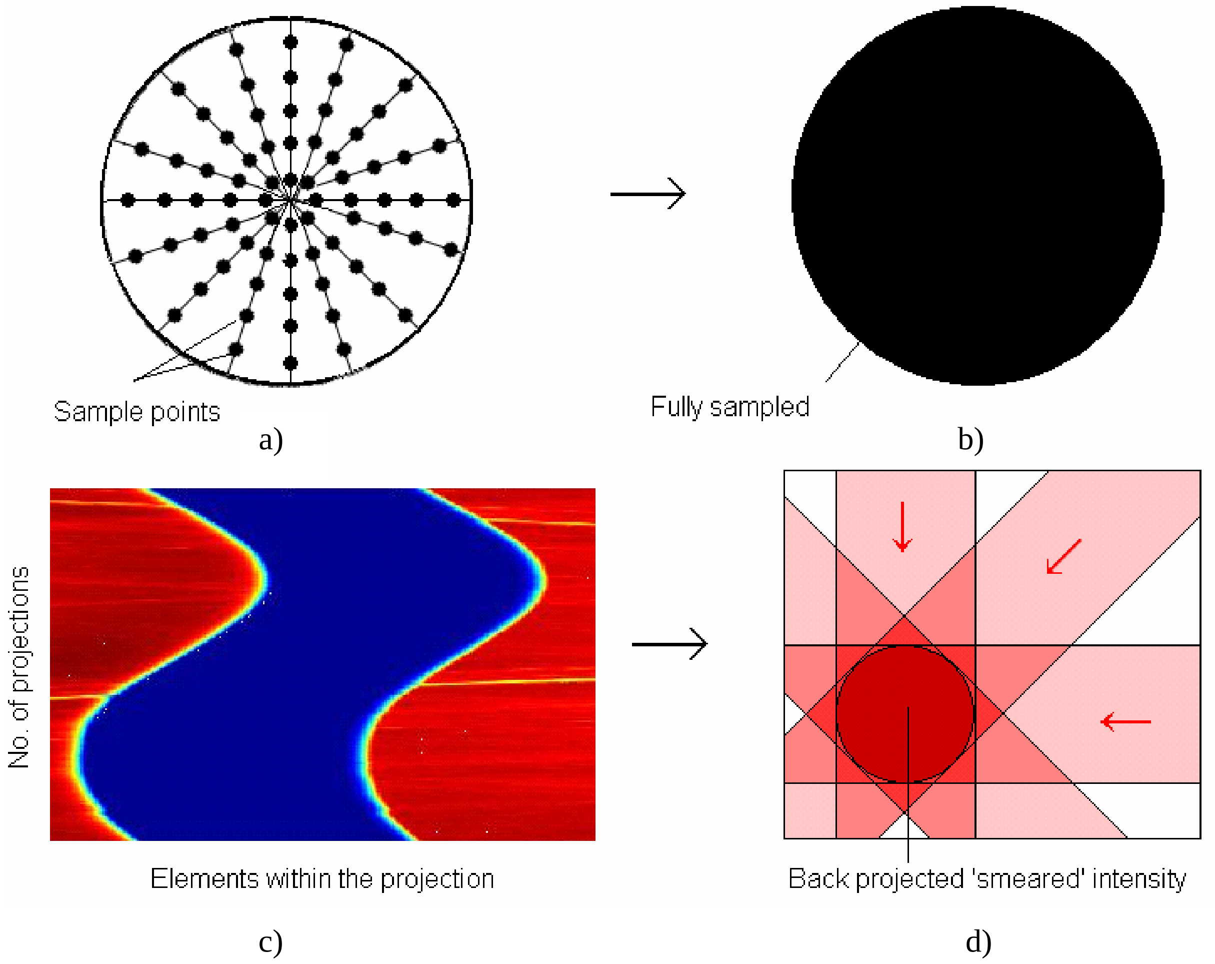

Figure [3-8] Showing in a), a more thorough sampling of the spatial domain. The black dots represent the elements within the projections from which data is collected and relates the degree of sampling undertaken during data collection and therefore the available image resolution upon reconstruction. The degree of the sampling shown in b) would be obtained from an infinite number of projections i.e. taking the limits of projection increments tending to zero. The presentation of data in Radon space in 2-D image form is often called a sinogram and is shown in c). The sinogram represent the accumulation of projection data through 0-360 degrees showing the attenuated blue regions and the unattenuated red regions during the tomographic scanning. The resulting back-projected image shown in d) illustrates the high-intensity areas of the image corresponding to the crossover points. The original real space image is shown in Figure [3-7a].

Back-projection can be summarised by the following points:

1) Consider one row of the sinogram, corresponding to angle ϕ.
2) Place the sinogram row at an angle ϕ in real space. Then 'smear it out' evenly all the way along the perpendicular direction. This is called back-projecting the data.
3) Repeat steps 1 and 2 for all the lines in the sinogram. Where the back-projections overlap, the signals add constructively to give high intensity image regions.

3.5.2 Magnetic Resonance Imaging

MRI is a tomographic imaging technique that produces images of internal physical and chemical characteristics of an object from externally measured nuclear magnetic resonance signals. Like many other tomographic imaging devices, an MRI scanner outputs a multidimensional data array (or image) representing the spatial distribution of some measured physical quantity. But unlike many of them, MRI can generate two-dimensional sectional images at any orientation, three-dimensional volumetric images, or even four-dimensional images representing spatial-spectral distributions (Webb, 1988). In addition, no mechanical adjustments to the imaging machinery are involved in generating these images. MRI operates in the radio-frequency (RF) range and therefore the imaging process does not involve the use of ionizing radiation and does not have the associated potential harmful effects. However, because of the unique imaging scheme used, the resulting spatial resolution of MRI is not limited by the "probing" (or working) frequency range as in other remote-sensing technologies.

A brief introduction to MRI, summarising the basic aspects of the technique that are touched upon in the thesis are described in Appendix A. A more in-depth description of MRI can be found in many standard texts such as that by Webb (Webb, 1988).

Chapter 4 Experimental Method

4.1 Optical Scanner and System Development

An alternative method for deriving dose delivered information from 3D polymer gel dosimeters was initially realised by Gore (Gore *et al*., 1996). He proposed that an optical tomographic based scanning approach could primarily provide useful dose information to aid and assist basic treatment plans and secondly recognised that optical tomography could prove to be a useful alternative to MRI, previously used to acquire gel dosimetry dose information.

It is currently understood from research based on the original scanner described by Gore (Gore *et al*., 1996) that the majority of existing optical tomography systems are configured to hold all scanning machinery within a cubical water tank. This system configuration could limit the ease of installation and implementation in radiotherapy centres and/or university research laboratories due to the complexity of housing all the components within the water and the difficulties that could arise. In view of this, a cylindrical scanner geometry was used here. This design, with an internal waterbath' avoided the need to mount the principal components in the water tank, therefore reducing the experimental complexity that radiotherapy workers could experience.

In the present work, a prototype optical computed tomography (OCT) scanner has been constructed that allows optical attenuation profiles of irradiated 3D gel distributions to be determined. With further developments, the scanner could be used in practical situations to provide information resulting in full volumetric data sets that could be used to examine the absorbed dose details of particular treatments.

4.1.1 Optical Tomographic Scanner

In designing the scanner a principal objective was that it should be relatively compact so that it could be positioned and installed on any suitable bench top in an oncology department or university laboratory. The scanning dimensions and available cavity space should also accommodate any reasonably sized radiotherapy phantom. The scanner was also designed with the foresight that should there be a requirement to modify it or the scanning method at a later time there was the available space to do so. Figure [4-1] shows the scanner and its peripheral components.

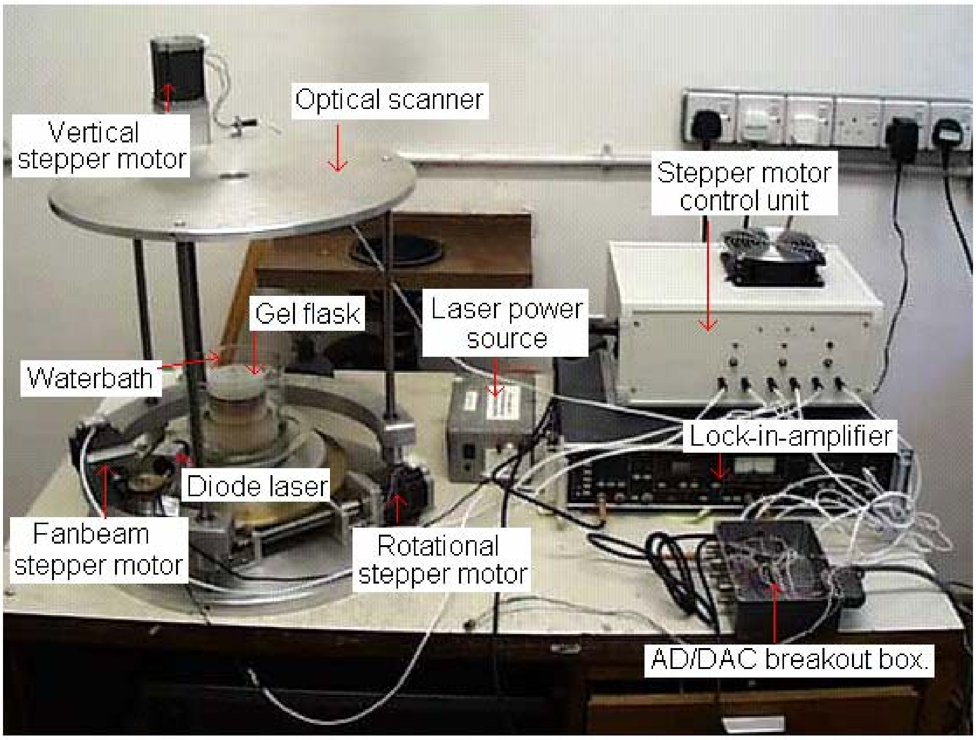

Figure [4-1] The optical tomography scanner and gel flask and waterbath arrangement with peripheral components, clockwise L-R, laser power source, stepper motor control unit, lock-in-amplifier and AD/DAC breakout box.

The scanner is cylindrical in dimension and designed to hold a waterbath and gel flask phantom up to 200 mm in diameter and 400 mm high. All optical components are therefore centred on a rotational base plate arrangement that can accept a variety of phantom dimensions.

An advantage of 3D dosimetry is that anthropomorphic phantoms can be manufactured that physically resemble body parts, for example a head and neck phantom. The scanner could therefore incorporate such a phantom within the available scanner cavity.

4.1.2 Peripheral Scanning Instruments

The optical tomography system comprises various peripherals that contribute to the data acquisition, data processing and optical reconstruction of the acquired 2D projection data sets. The main system components are illustrated in Figures [4-1] to [4-3]. These include a laser unit with a dedicated power supply and three independent computer controlled stepper motors to drive the dosimeter flask rotation, fan beam movement and the height manoeuvrability. The main acquisition peripherals are an integrating sphere, lock-in amplifier, signal conversion box and a dedicated computer system.

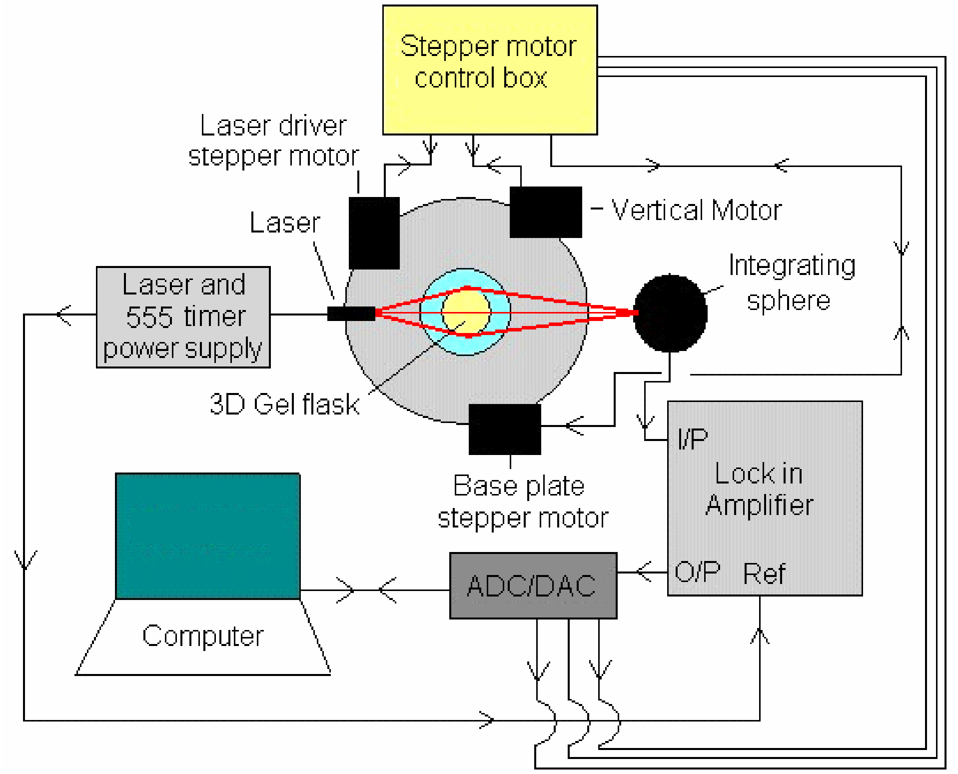

Figure [4-2] Schematic diagram of the scanner arrangement showing the main components of the scanner. The laser driver stepper motor controls the laser motion and produces a fan beam arc (red lines) that scans the central gel flask. The lock-in-amplifier transfers the transmitted laser beam collected by the stationary integrating sphere to the computer *via* the ADC/DAC signal box. The base plate stepper motor and the vertical motor control the degree of rotation the base plate turns through during scanning and the vertical scanning height respectively.

The essential scanning movements required for data acquisition are provided by stepper motors (Model 103H7823-0440, Sanyo Denki). The stepper motors are two-phase 60 mm square, offering high torque, low noise and are relatively easy to connect. Three motors are used to independently drive the fan beam scanning arc, base plate rotation and scanning height and are powered by three 24 series stepper drives (Model PVP2435, Alzanti Ltd, UK) and assembled in a dedicated control unit. The analogue to digital (A/D) to digital to analogue conversion (DAC) signal box allows both data acquisition and stepper motor control.

The internal setup of the scanner can be seen in Figure [4-3]. A waterbath was used to produce the required laser beam transition though the gel from which accurate image reconstruction could be achieved (see section 4.3.3).

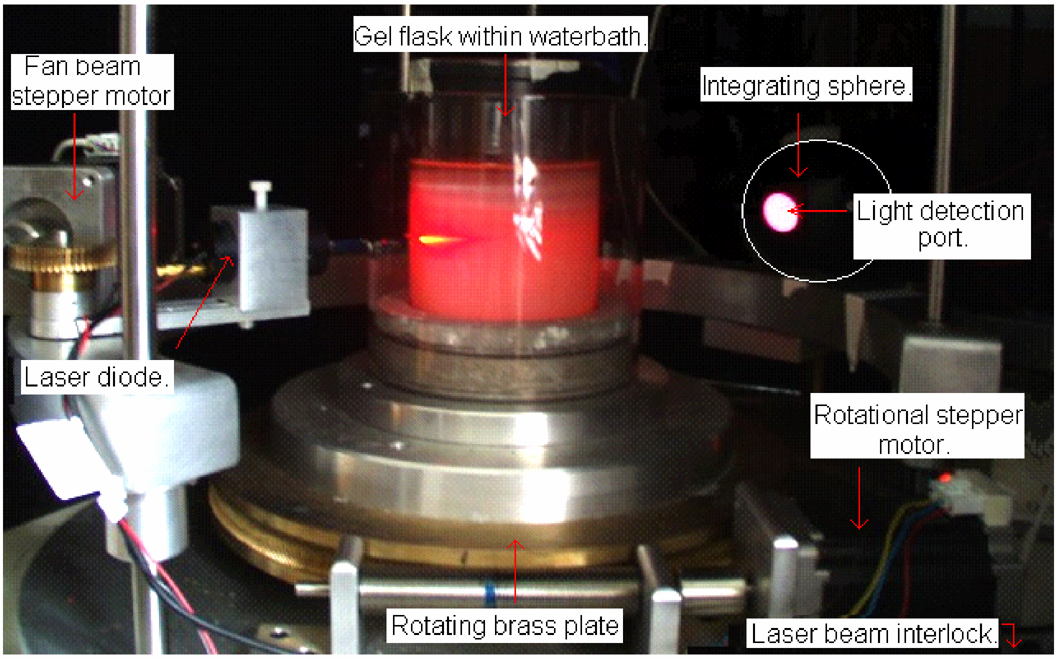

Figure [4-3] Photograph of the internal components of the optical scanner. The gel flask is probed by a laser diode *via* a stepper motor driven fan beam projection, moving left to right. The irradiated gel flasks are white, although here the gel appears pink, a consequence of the volumetric scattering of the 655 nm (red) wavelength. The transmitted laser beam is collected by the 1 inch diameter port of the integrating sphere and detected by a fixed BPX-65 photodiode detector.

The brass plate has been inversely tapped with a fine thread. This in conjunction with the rotational stepper motor drive thread allows the gel flask to be rotated small increments. This provides the capability to collect high resolution projection data from tomographic scans. The waterbath holder illustrated in Figure [4-3], is positioned centrally on the rotating brass platform and consists of a number of layered discs that can accept a variety of phantoms with differing diameters. The discs have been manufactured in such a way that all gels with varying diameters are centred on the rotating base plate. The layered discs are illustrated in Figure [4-4].

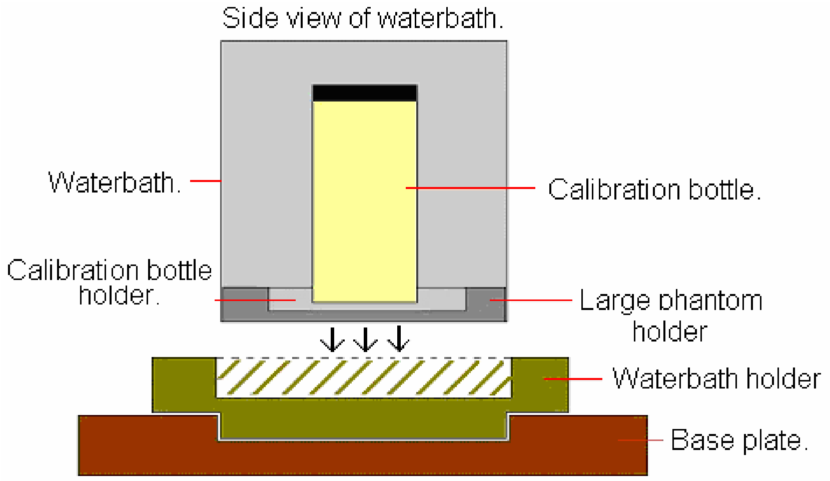

Figure [4-4] Waterbath arrangement showing the different diameter vessels the scanner can incorporate.

4.1.3 Optical Radiation Source

A solid state laser (model: LD1392, Laser 2000) emitting 7 mW at 655 nm was chosen as the radiation source for the scanner, as these are available in a compact form and with a range of output powers and wavelengths. The elliptical beam emanating from the diode laser was corrected to a circular beam by compound lenses in the laser head. This had the effect of reducing the output power by approximately 50 % to 4 mW. An additional advantage of this type of laser was that its output could be modulated *via* an external frequency generator by varying the drive current. This allowed enhanced signal to noise detection possibilities by using a phase sensitive detector (lock-in-amplifier). Although the laser used was rated class 3R, the scanning system remained class 1 laser system when enclosed in a blacked out protective cabinet (see Figure [4-33]).

The diode laser was of a suitable size that it could be mounted on the horizontal scanner arm (shown in Figure [4-5]) allowing direct illumination of the phantom gel arrangement without the need to significantly alter the optical beam path with mirrors.

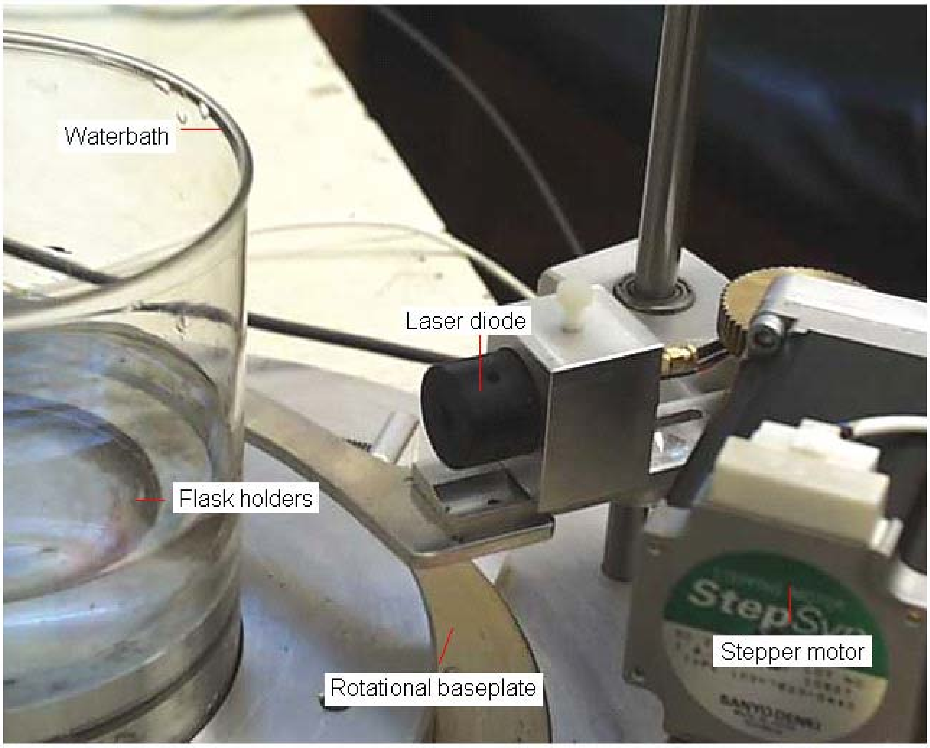

Figure [4-5] Photograph of the modulatable laser diode and the driving stepper motor positioned on the scanning arm above the rotating base plate.

The laser beam is initially attenuated by reflections at the interfaces between the source and detector, specifically the waterbath arrangement. The gel flask then further attenuates the beam *via* polymer aggregates that are formed by the polymerisation of monomers in direct proportion to absorbed x-ray dose. The transmitted beam finally passes into an integrating sphere with a 1 inch diameter port.

The laser beam diameter should be as small a possible when interrogating the gel medium. This is to ensure that the laser beam will probe the smallest volume possible and therefore provide good spatial resolution within the gel. A direct and meaningful relationship can then be obtained between the transmitted beam intensity and corresponding line integral.

An optical ray tracing simulation package called Beam2, (Optical Ray Tracer software package from Stellar Software, California, USA Stella, 1999), was used to investigate how the scattering light would propagate within the gel for both a focused and collimated laser beam. The 4 mW laser diode shown in Figure [4-5] has a variable focal length that can be changed to meet the experimental arrangement.

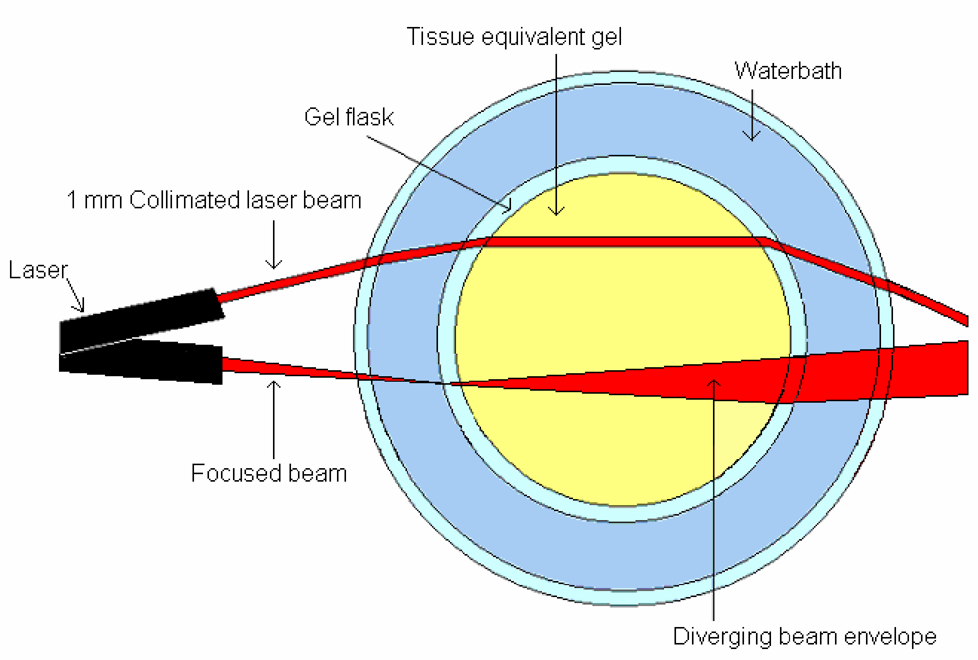

Figure [4-6] Schematic plan view showing the possible ray paths from a focused laser beam incident upon the waterbath arrangement and for a 1mm diameter collimated laser beam. The line integral data collected by the photodiode detector will provide the attenuation values for a larger volume of gel than intended by the diverging laser beam and therefore devalue the data.

The investigations suggested that the de-focusing laser beam would interact more with the surrounding gel during its passage through the phantom onto the detection port of the integrating sphere when compared to a collimated beam. Therefore, the detected light from the focused beam example would contain scattered light from other regions (more so than for the collimated light example) of the gel than that particular line integral pathlength. To minimise the extent of the volumetric forward scattering of the laser beam in the gel phantom and to maximise the accuracy of the data collected, the output laser beam was collimated over a distance of 500 mm. In addition, the laser had an adjustable focus that allowed the focal position with respect to the phantom to be varied so as to maintain the smallest spot size at the desired point.

4.1.4 Acquisition of Projection Data

The level of gel opacity (clouding) and the resulting light attenuation along the optical axis is directly proportional to the X-ray radiation absorbed within the gel and therefore a limiting factor for the optical system. It is therefore extremely important to maximise the throughput of the laser beam intensity for detection. This can be attained to some degree by increasing the laser output power above 4 mW whilst maintaining a class 1 system. To maximise the optical signal-to-noise ratio, use was made of a lock-in-amplifier technique. The laser output was current modulated at 900 Hz. This adjustable modulation was achieved by using a standard NE555 timer circuit built into the laser power supply (see Figure [4-1]) and set to operate in the astable mode. The modulated current frequency was also connected to a lock-in-amplifier (Model 5210, EG&G, Princeton, USA) *via* a reference input channel. The most convenient method for detecting the transmitted laser beam during optical scanning was to use a large area photodiode detector. The large area was required to accommodate the two dimensional scattering and consequent spot wandering occurring during the laser beam translation. Initially a large area 10 mm^2 square silicon photodiode detector (S-2387-1010R, Hamamatsu) was used to detect the transmitted laser beam. The S-2387 detector offered high sensitivity, high linearity and a low dark current, ideal for the optical measurements. The degree of total scatter during optical scanning and subsequent beam wandering was sufficient to make the beam miss the detector at the scanning extremes i.e. where the glassware curvature is at a maximum. A signal was then not detectable even with the current large area detector. It was imperative to ensure that the beam wandering and subsequent loss of signal was minimised in order to limit unrepresentative data from being collected.

The degree of scattering was determined by a number of factors:

1) The total pathlength between the source and the detector.

2) The absorbed dose and the related proportional change in refractive index of the gel and as a consequence, beam trajectory within the gel flasks and surrounding waterbath.

3) The quality and finish of the glassware interfaces between the source and detector can influence the degree of scatter.

A solution to the varying loss of transmitted signal due to beam wander was to use a high speed BPX-65 photodiode detector and an 8 inch diameter optical sphere (Pro-light Ltd). The positioning of the integrating sphere can be seen in Figure [4-3], and shows all the internal instruments required for tomographic data acquisition and image reconstruction. The BPX-65 photodiode detector was positioned within an available 1 inch optical port that had been reduced in size to accommodate the circular 1 mm^2 detector. The detector was positioned behind a light baffle (used to restrict direct light incidence on the detector). Another available 1 inch detector port was used to collect the transmitted laser beam. This method had the desired effect of transforming a small active area detector into a 1 inch diameter active area detector that successfully accepted the entire transmitted laser beam during image scanning onto the BPX-65 *via* diffuse scattering within the sphere. Although it is acknowledged that this method was inherently flawed with respect to directly imaging the transmitted laser beam onto a detector, the initial results obtained were encouraging. It was believed that through further development the beam wandering problem could be reduced allowing detection by a high speed photodiode detectors similar to the 10 mm^2 device detailed previously.

By connecting the BPX-65 detector to a lock-in-amplifier (Model 5210, EG&G, Princeton, USA), unwanted external interference from ambient noise from surrounding electromagnetic sources (from internal light sources (50 Hz)) could be reduced. Prior to digitisation, the signal was amplified between 0 and 10 volts within the lock in amplifier and conveyed to the data conversion box. A high performance 12 bit data acquisition board (PC-30/D, Amplicon Liveline Ltd) was used for data conversion and data acquisition in the computer system. The AD/DAC data conversion box is shown in Figure [4-1] and is another integral part of the scanner that controls the data flow between the controlling PC and the scanner. The schematic for the conversion box is shown in Figure [4-7].

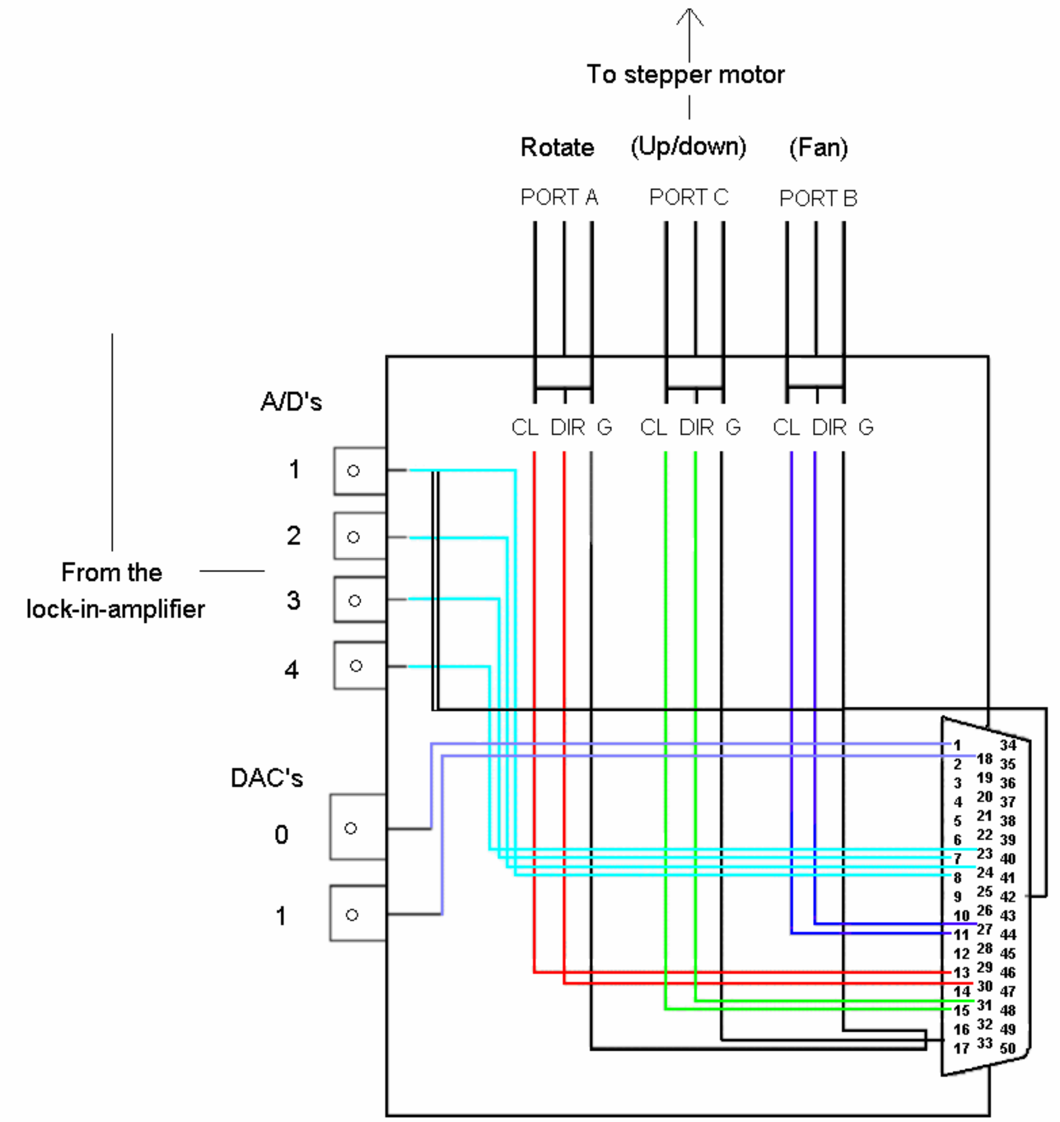

Figure [4-7] Schematic of the conversion box used to convert electrical signals between the computer and the optical scanner. The stepper motor turning rate is controlled by the CL input, the direction by the DIR input, all of which are grounded (G) to pin 17 on the D type connector used. BNC type connections are provided for both A/D and DAC data conversion inputs. The 50-way D-connector provides the capability to add further connections if required from the available pins.

The three stepper motors were controlled *via* Port A (Rotation), B (Fan beam) and C (Up/Down), from which the specific direction (DIR) and stepper motor clock speed (CL) was determined. The connections were grounded (G) to pin 17 on the 50 way D-connector, see Figure [4-8]. The detected voltage signals were transferred from the lock-in-amplifier *via* the BNC connectors 1, 2, 3 and 4 and transferred to the PC-30/D acquisition board *via* pins 7, 8, 23, and 24 respectively. Additional DAC controlled peripheral systems could be driven *via* extra BNC connectors. The 50 way connector is shown in more detail in Figure [4-8].

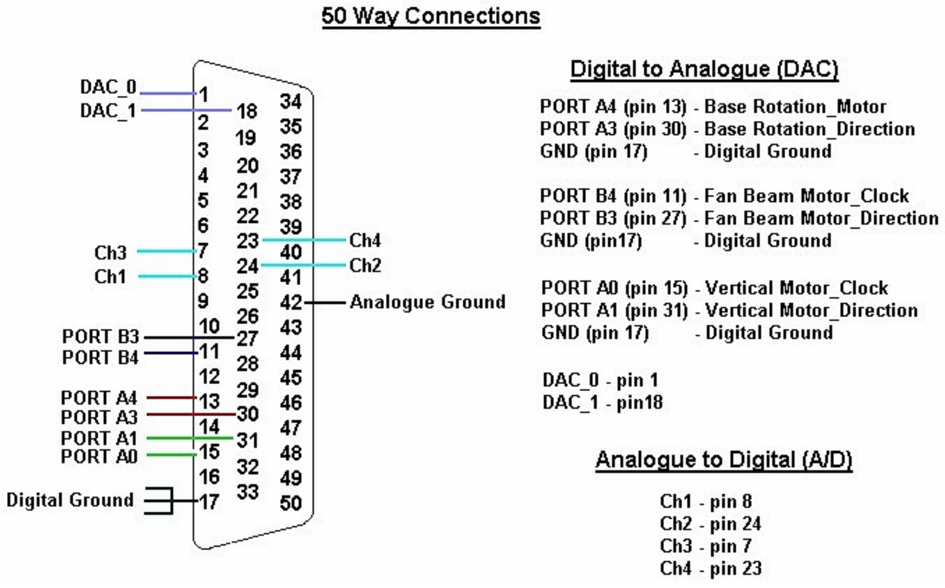

Figure [4-8] Schematic showing the 50 way pin D-connector and pins used to transfer data between the control PC, data conversation box, lock-in-amplifier and optical scanner.

The computer programs that were used to control the data flow between instruments was written in BASIC. The syntax is detailed in Appendix B.

4.2 Instrument Development

The concept was to use a cylindrical geometry for the scanner in order to have a convenient imaging device that would be portable and could accommodate, for example, a head and neck phantom.

As mentioned in the previous chapter, all early optical tomography scanners were based on the first generation conventional X-ray CT machines in which the laser and detector are positioned either side of the object to be scanned and move in unison together (Webb, 1988; Gore *et al*., 1996; Kelly *et al*., 1998). To successfully reconstruct a two dimensional attenuation map of a gel flask, the spatial and *Radon* space have to be sufficiently sampled (this is analogous to fitting spokes within a bicycle wheel). The data projections acquired form the sinogram in *Radon* space (see section 3.6.1.2 in the previous chapter).

There are a number a software packages available to assist with reconstructing tomographic (OCT) images. Matlab (The Mathworks Inc) has an excellent image processing toolbox that provides the required imaging functionality to allow data to be converted *via* the *Radon* transforms and by the inverse *Radon* transform. The *Radon* transform and the *Iradon* transform data sheets are detailed in Appendix C.

A conscious effort was made to design and manufacture an optical tomography scanner that would provide the raw sinogram data sets (projections) that the *Iradon* transform could be used to directly reconstruct as images using Matlab. Using the *Iradon* function reduced the complexity inherent in developing a tomography scanner and all the in-house programming that would be required to reconstruct the images from the raw data. In addition the functionality of Matlab would allow other users to operate the scanner and reconstruct the tomographic scans with relative ease.

The final scanner design and geometry can be seen in section 4.1.1. The following sections will provide details of the developmental issues and problems that were specific to obtaining the required projection data sets. These include the non-repeatable nature of the data collection equipment (backlash), the volumetric scattering issues with the various glassware used i.e. gel flasks and waterbaths and the careful ray consideration requirement of the path used. The final sections describe the scanning methodology and reconstruction processes and laser safety considerations related to the scanning system.

4.2.1 Sampling of the Spatial Domain ($\mu(x, y)$)

The majority of early optical scanners were based on first generation CT scanners. In this configuration, both the source and detector moved either side of the object (gel phantom), and data was collected from parallel projections from differing rotations around the phantom. These systems and data acquisition methods (developed by a number of scientists) were under computer control. Thus, a large number of data points within each projection could be collected allowing both the spatial and frequency (*Radon*) domains to be fully sampled. This of course provides the raw data to allow accurate two dimensional images to be reconstructed.

From initial work, a manual approach in which the data would be collected from points within the projection arc (i.e. 1, 2, 5 and 10 degrees) was adopted. This is shown in Figure [4-9]

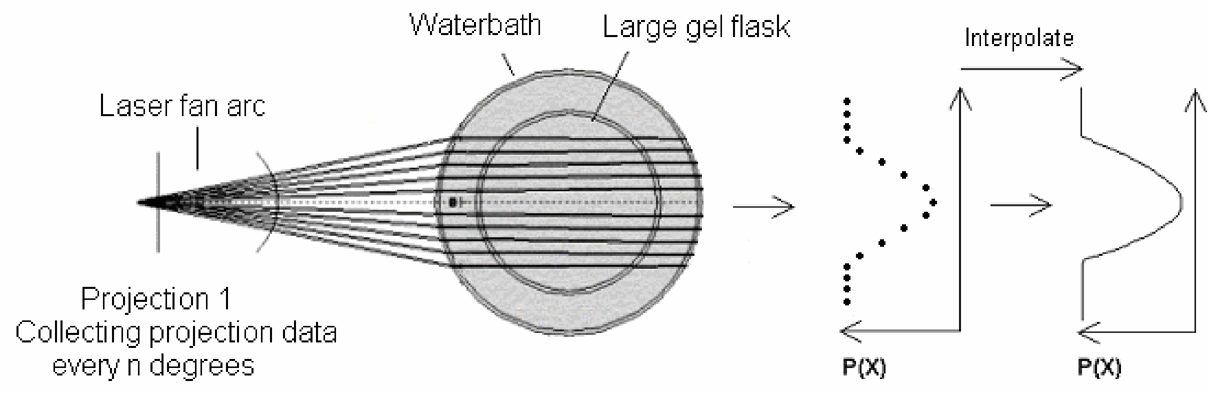

Figure [4-9] schematic diagram of the proposed initial manual method to collect limited projection data sets (discrete points) and to interpolate between them to form a continuous distribution. The P(X) axis refers to the transmitted intensity of the laser beam, and is related to the corresponding radiation dose induced attenuation values.

The collection of 10 to 20 data points within the projection was deemed to be insufficient in providing the required sampling to allow a true reconstructed representation of the attenuation coefficients, ($\mu(x,y)$), within the gel. The degree of the interpolation required would severely limit the accuracy of reconstructed image if the dose delivered varied significantly due to high dose gradients between the parallel projections shown in Figure [4-9].

The introduction of computer controlled stepper motors (see Figure [4-1]) allowed the scanner to be operated and orientated more conveniently and efficiently than manual scanning. The height of the scanning arm was controlled by vertical stepper motor. The second motor controlled the rotation of the brass base plate between acquiring each projection data set. Finally a third stepper motor was added to the scanning arm to control the laser diode and create the fan beam motion required to scan the gel flasks. This increased the amount of data captured and thus enhanced the available image resolution following image reconstruction (see Figures [4-1] and [4-3]). The laser could now be programmed to sample the projection data to a much higher level. A typical scan could then be initiated, collecting data on every step over a total of 600 which allows the attenuation data to be collected from the gel flask very accurately. For example for a gel flask 100 mm in diameter, 600 data points could be collected providing data every 167 μm i.e. with sub-mm resolution.

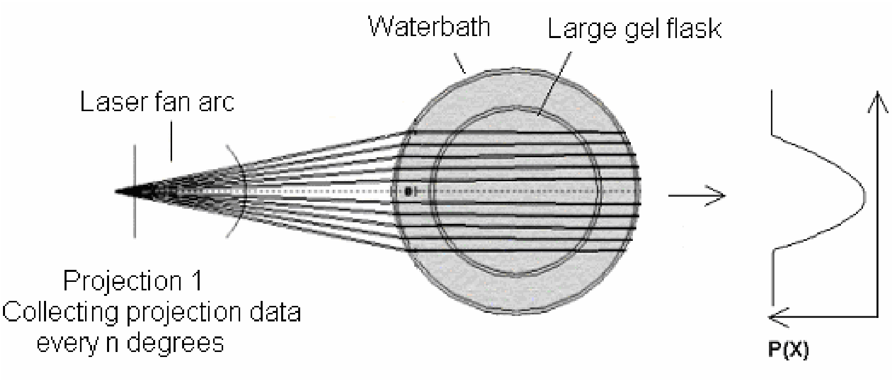

Figure [4-10] The computer controlled laser beam fan arc method of collecting 2D projection data. The gel flask can be sampled with sub mm resolution i.e. 600 elements within 1 projection during the 100 projection required for the full scan. The P(x) axis refers to the transmitted intensity of the laser beam, and indicates the corresponding radiation dose related attenuation values.

4.2.2 Scanning Non-Repeatability

The addition of a third stepper motor to drive the data acquisition was required to provide the necessary sampling of both the spatial and *Radon* space for accurate image reconstruction. Transmitted light was collected by the photodiode detector from every step taken by the stepper motor. However, the fan beam translation (see Figure [4-10]) was found to be inconsistent within repeated 2D scans and in collecting sequential projection data sets.

The platform on which the laser diode was positioned was driven *via* two gears with differing teeth dimensions (see the outline area in Figure [4-11]).

Figure [4-11] Photograph showing the stepper motor gears used to drive the laser beam fan arc required for gel scanning. The area circled shows the problematic fan beam scanning pivot and source of the scanning jitter.

The integration of the two cogs was achieved by fixing them in position whilst touching one another. This provided a good contact and resulted in a working motorised translation allowing the laser to be orientated during data acquisition. However, on occasion, after a return sweep, the gears would remain stationary for an interval and not respond to the stepper motor drive instruction i.e. backlash. During this time, the attenuation data collected by the photodiode detector would not correspond to the true value due to the positional error. This directly affected the data collection and provided erroneous data within the sinogram.

The solution to this fundamental problem concerning accurate data acquisition was to replace the drive gears with comparable teeth dimensions and to fix damping springs within the scanning arm of the scanner. This is shown in Figure [4-12].

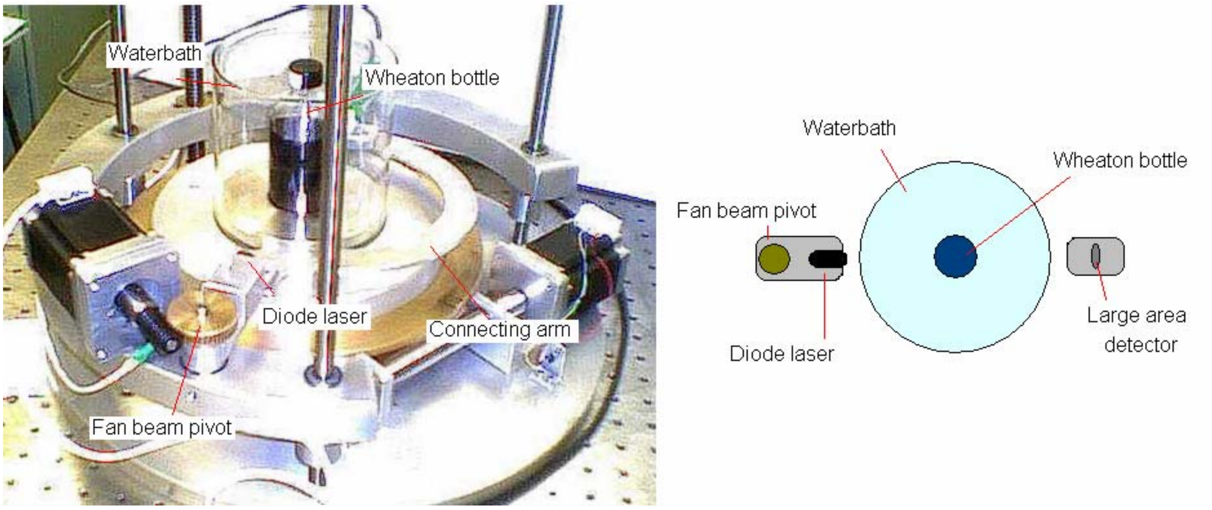

a) b)

Figure [4-12] Photograph showing a) the corrected gear assembly and the laser pivot point from which accurate projection data could be collected and b) a schematic diagram for clarity showing the laser diode and large area detector.

4.3 Opto-Mechanical Development

A crucial difference between X-ray CT and optical CT scanning is that optical light is reflected and refracted to a much higher degree than X-rays. The lowest orientation from which reflection is observed is at normal incidence where Snell's law shows that the coefficient of reflection is 0.04. For typical optical glasses or liquid surfaces in air the Fresnel reflection loss amounts to a few % at normal incidence.

Due to the refraction of the laser light at the various interfaces in the scanner, a specialised beam tracing software package was utilised to predict the required angles of incidence needed to achieve the beam trajectories within the polymer gel for satisfactory sampling.

It is also of great importance to calculate where the emerging beam would be within 3D geometry so that precise detector positioning could be achieved. The software package was used to determine the geometry of the system with and without the addition of the waterbath. The beam calculations were performed by the Beam2.

4.3.1 Glassware Considerations

In X-ray computerised tomography, the radiation beam is not reflected or refracted during the imaging sequence. This however is not the same for optical systems due to the reflective and refractive nature of visible light. Thus, a different set of scanning considerations are required in order to acquire accurate and useful projection attenuation data prior to a successful 2D reconstruction. From the schematic diagram of the scanner arrangement shown in Figure [4-2], it can be seen that the heart of the device is composed of both a series of concentric glass interfaces and regions with varying refractive index acting in effect like a compound lens arrangement. Therefore, in any optical scan the laser beam undergoes various multiple reflections and refractions during its three dimensional translation though the waterbath glass walls and the gel phantom glass walls. It finally emerges from the external waterbath glass wall and then converges onto the detector port of the integrating sphere.

For early gel calibration investigations, 125 ml bottles from Wheaton Scientific were purchased in bulk quantities. The method used for the mass manufacture of bottles is to bring together two halves and fuse them together on a base. When used in optical tomography this has the undesired effect of introducing two vertical joins in the bottle that scatter the laser light. In addition, the optical finish on the walls was sufficiently imperfect that they could refract the laser beam away from the intended optical path.

At this early stage of the optical scanner development MRI was used to determine whether a linear relationship existed between the radiation dose delivered to the bottles and the resulting T_1 and T_2 relaxation times (see Chapter 3 and Appendix A). The optical finish (quality of the bottle walls) of the calibration bottles was not a concern in the MRI imaging technique that utilise the emission of radio frequencies from the gel phantoms under investigation. However the optical finish of the calibration and indeed all glassware bottles used in conjunction with the scanner was an important and limiting factor that required careful consideration. As indicated earlier, the laser beam undergoes volumetric forward scattering at the interfaces between the source and detector (glass surfaces and gel). The refractive index of the gel increased in proportion to the increase in dose absorbed. This relationship and expected degree of refraction could be anticipated in advance. The laser beam is incident upon the glass first and therefore can be refracted or reflected away from the intended path within the scanning projection. Furthermore, it was observed that the laser beam was being refracted three dimensionally during the laser beam scanning motion. This made it extremely difficult when considering the optical pathlength, to arrange the apparatus to accurately collect the attenuated transmitted laser beam. This is illustrated in Figure [4-13].

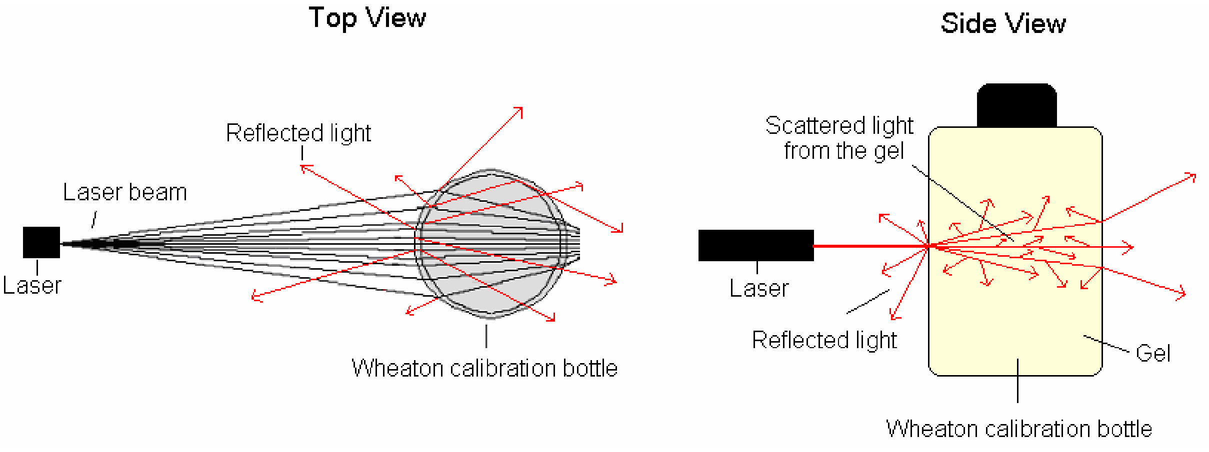

a) b)

Figure [4-13] Illustration showing a) the top view of possible reflection and refraction at the interfaces from the imperfect glass finish of the calibration bottles and scattering effects from the internal gel structure resulting from the fan beam scanning motion. Scattering in the horizontal and vertical plane is emphasised in b), here the location of the detector becomes an important factor in accurately collecting representative projection data due to the beam spread and subsequent loss of spatial resolution.

Although these bottles proved adequate for calibration purposes (using MRI) the bottle wall qualities were not of the required standard for accurate optical image reconstruction. It was found that the varying degree of laser beam scatter during the acquisition of the projection data severely reduced the reconstructed image quality, in effect producing streaking effects and ghosting artefacts. For example if a small speck of dirt was located within the gel flask, the laser beam would be completely deflected from the integrating sphere detector and the resultant intensity recorded for that particular data point within that projection, within the sinogram, would be zero. This would continue throughout the scanning procedure yielding an unwanted image artefact. The same was observed with mass manufactured glassware.

The solution was to have the gel dosimeter flasks purpose made with optical friendly (OF) glass cylinders with high quality finishes on all surfaces. The individual flasks were cut from drawn out glass cylinders (i.e. not joined from two halves) and fitted onto a glass base. A comparison between the glassware evaluated during these investigations is illustrated in Figure [4-14].

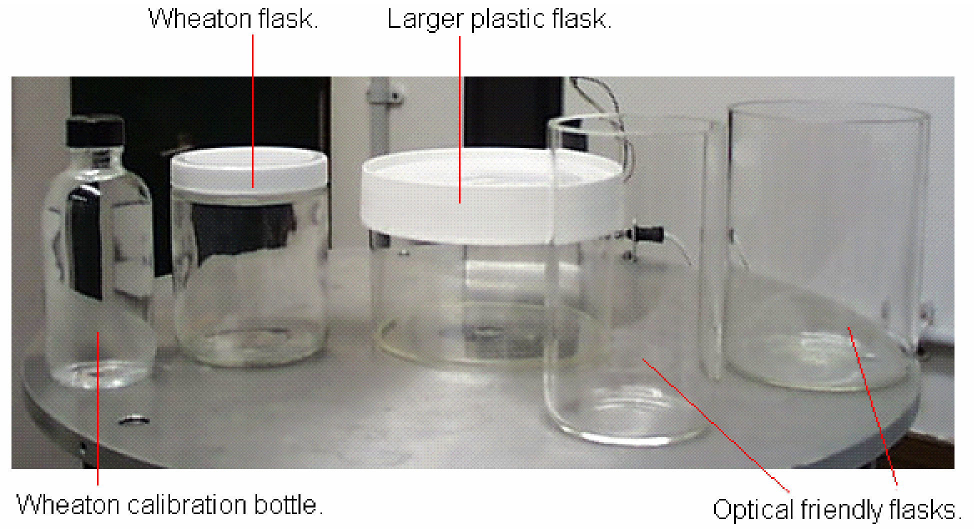

Figure [4-14] A photograph of the glassware available for scanning tomography, showing the differing sizes, volumes and optical finish. The Wheaton calibration bottle, larger diameter gel flask and the plastic container (higher permeability to oxygen than glass) were unsuitable for optical tomography due to their overall imperfect glass finish. The OF flasks provided improved though not perfect beam transmission quality.

The resulting beam transmission using OF glass during scanning provided line integrated attenuation data that closely corresponded to the true line integral expected i.e. reduced beam refraction and scattering. This had the positive effect of reducing the variation in the laser beam focusing post transmission onto the detection port of the integrating sphere.

4.3.2 Beam2 – Ray Tracing Software

At this point of the scanner development it was still felt that reconstruction could be achieved using the fan beam method with the *Radon* transform theorem. A fan beam data collection method was developed for use with third generation CT scanners, collecting multiple transmission data points from a single un-collimated X-ray pulse. In this system the scanning times were reduced by collecting fan beam projection data from the whole field of view (FOV) with an array of xenon detectors (Webb, 1988).

Use of a basic optical design software package, Beam2, allowed a realistic interpretation of the scanning geometry and scanning system in terms of laser reflection and refraction from source to detector. Beam2 also allowed the effects of the varying levels of high energy radiation delivered and absorbed by the gel flask to be investigated and characterised. The gel polymerisation and consequent levels of visible gel opacity grow with increased dose absorbed and therefore have varying effects on the refractive indices of the gel, and more importantly, the probing laser beam path behaviour. Beam2 proved to be a useful tool in this respect for analysing the effects of both varying absorbed doses and the refractive index change during ray path simulations. The basic method of simulating the scanning system is described in the next section.

4.3.2.1 Optical Ray Tracing Method

In this section the method used to simulate the optical scanner is presented, detailing the optical arrangement of the surfaces, the required ray paths and orientations and resulting simulations are reported.

The first thing to determine was the optical surfaces which the ray paths traverse. The system operates within an XYZ Cartesian coordinate system (we are only concerned with XZ here), where Z denotes the optical axis and X the distance from the optical axis. The screen capture from Beam2 shown in Figure [4-15] gives, in this particular example, the number of surfaces, the refractive index of the media, the position of the surface on the optical axis (Z), the degree of curvature, what specifically is the surface, the diameter of the optical components and media and finally any related comments.

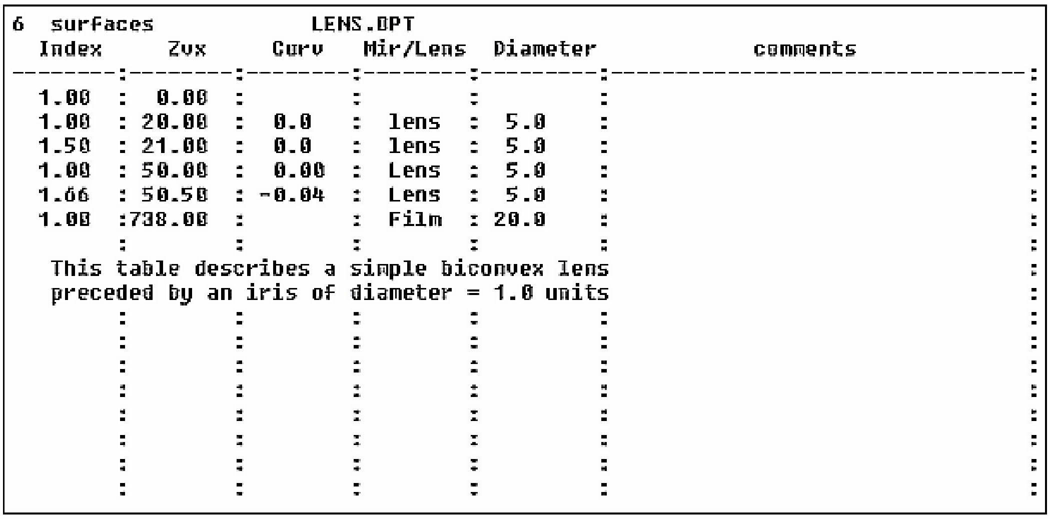

```
6  surfaces            LENS.OPT
  Index     Zvx     Curv   Mir/Lens  Diameter            comments
--------:--------:--------:--------:---------:--------------------------------:
  1.00  :  0.00  :        :        :         :                                :
  1.00  : 20.00  :  0.0   :  lens  :  5.0    :                                :
  1.50  : 21.00  :  0.0   :  lens  :  5.0    :                                :
  1.00  : 50.00  :  0.00  :  Lens  :  5.0    :                                :
  1.66  : 50.50  : -0.04  :  Lens  :  5.0    :                                :
  1.00  :738.00  :        :  Film  : 20.0    :                                :
        :        :        :        :         :                                :
   This table describes a simple biconvex lens                                :
   preceded by an iris of diameter = 1.0 units                                :
        :        :        :        :         :                                :
        :        :        :        :         :                                :
        :        :        :        :         :                                :
        :        :        :        :         :                                :
        :        :        :        :         :                                :
        :        :        :        :         :                                :
        :        :        :        :         :                                :
        :        :        :        :         :                                :
```

Figure [4-15] A screen capture from Beam2 showing the optical setup workspace. Here the optical surfaces which the rays pass through are specified including the refractive index, distance on the z-axis (units in cm), curvature of the interface and the diameter (units in cm).

The ray path details are input onto a separate worksheet (shown in Figure [4-16]. The number of rays is input first in the top left hand corner of the spreadsheet; here 15 rays are used in the simulation. The process of entering data is facilitated by occasionally running the simulation to determine if there are any ray path errors.

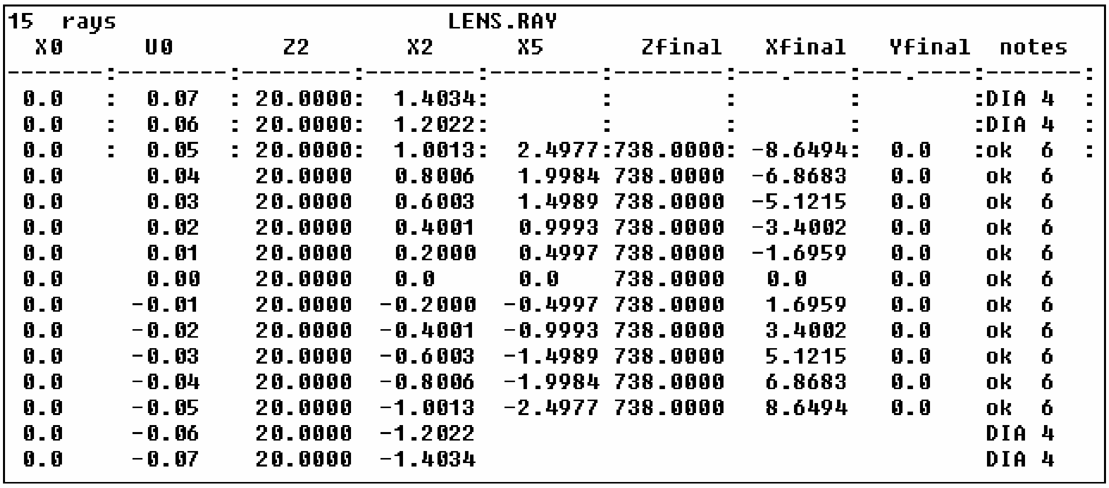

```
15  rays                        LENS.RAY
  X0      U0        Z2       X2       X5       Zfinal    Xfinal    Yfinal  notes
-------:--------:--------:--------:--------:--------:---.----:---.----:-------:
 0.0   :  0.07  : 20.0000:  1.4034:        :        :        :        :DIA 4  :
 0.0   :  0.06  : 20.0000:  1.2022:        :        :        :        :DIA 4  :
 0.0   :  0.05  : 20.0000:  1.0013:  2.4977:738.0000: -8.6494:  0.0   :ok   6  :
 0.0      0.04    20.0000   0.8006   1.9984 738.0000  -6.8683   0.0    ok   6
 0.0      0.03    20.0000   0.6003   1.4989 738.0000  -5.1215   0.0    ok   6
 0.0      0.02    20.0000   0.4001   0.9993 738.0000  -3.4002   0.0    ok   6
 0.0      0.01    20.0000   0.2000   0.4997 738.0000  -1.6959   0.0    ok   6
 0.0      0.00    20.0000   0.0      0.0    738.0000   0.0      0.0    ok   6
 0.0     -0.01    20.0000  -0.2000  -0.4997 738.0000   1.6959   0.0    ok   6
 0.0     -0.02    20.0000  -0.4001  -0.9993 738.0000   3.4002   0.0    ok   6
 0.0     -0.03    20.0000  -0.6003  -1.4989 738.0000   5.1215   0.0    ok   6
 0.0     -0.04    20.0000  -0.8006  -1.9984 738.0000   6.8683   0.0    ok   6
 0.0     -0.05    20.0000  -1.0013  -2.4977 738.0000   8.6494   0.0    ok   6
 0.0     -0.06    20.0000  -1.2022                                     DIA 4
 0.0     -0.07    20.0000  -1.4034                                     DIA 4
```

Figure [4-16] Screen capture of the ray workspace in which the number, orientation and position within the XZ coordinate system during translation from X_0 to X_{final} are presented. U0 refers to the sine of the angle ϕ the ray makes with the optical axis. The distance (units in cm) of the individual surfaces along the optical axis (Z_{n+1}, Z_{n+2} etc) and away from the optical axis (X_n) is given. The final status of all the input rays is shown in the notes column.

Data can be collected from the XZ plane at every interface in the simulation. Figure [4-16] shows that the initial beam angle with respect to the optical axis, can be varied ray to ray. The negative values indicate positions of the rays below the optical axis. The success of individual rays completing the simulation is given from the notes column i.e. ok 6 (referring to the 6 surfaces within the simulation). The data in the column shows that the two rays with the greatest angles with respect to the optical axis did not complete the simulation and did not meet surface number four. This can be seen in the ray trace in Figure [4-17].

Once the data values for both the optics and ray paths have been completed in the respective worksheets, the simulation details can be calculated *via* the layout function. This will allow the user to assess the initial input details. The simulation is illustrated in Figure [4-17].

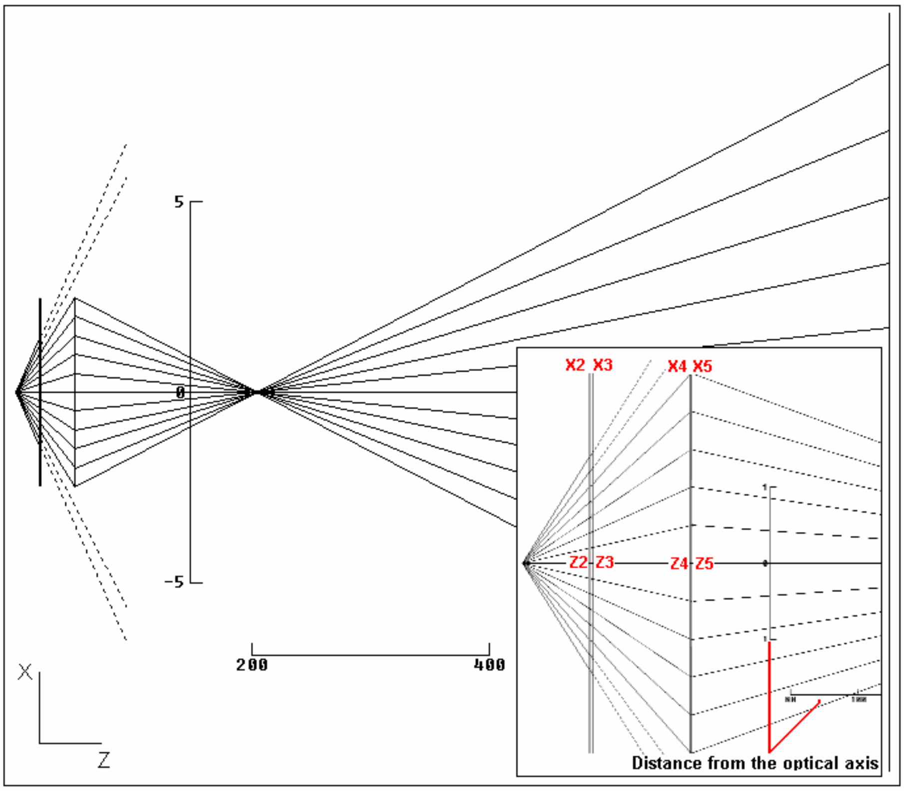

Figure [4-17] A schematic showing the simulation output from the data shown in Figures [4-15] and [4-16]. Initially the simulation shows that 15 rays leave the origin point at the left hand side. Under the interactions detailed in the optics spreadsheet, (Figure [4-16]), proceed along the optical axis to the right and final surface. The inset shows the magnified positions of the X and Z interfaces with respect to the optical axis. The units in X and Z are in cm.

The use of a basic optical design software package such as Beam2 provides an insight into the scanning geometry and scanning system in terms of laser reflection and refraction between the various surfaces between the source and detector. Beam2 provides a relatively convenient method for simulating an optical system prior to its practical implementation. Providing all input data is correct i.e. refractive indices, glass thicknesses and surface curvatures, the simulations provide a good description of the ray paths within that optical system.

The main use for the software was to determine the required fan beam arc angles, the path lengths and the level of refraction expected from the glassware, including the laser beam refraction at the bottle extremes where the curvature increases. It was also found to be extremely useful for simulating the ray behaviour in a three dimensional optical system that had a variety of interfaces between the laser and the detector. In the next section various optical systems of differing levels of complexity are described in the quest to produce fan beams suitable for direct reconstruction using the Matlab fan beam function (modified *Iradon* function).

4.3.3 Development of the Fan Beam Acquisition Method

Initially the diode laser and the photodiode detector were positioned on the same connecting arm (see Figure [4-18]), allowing the movement of the detector to correspond with movement of the pivoted diode laser.

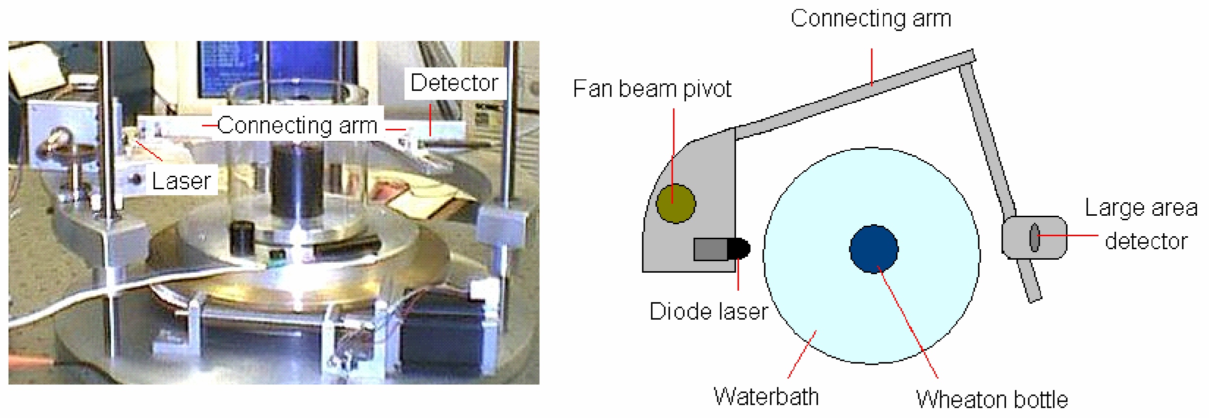

a) b)

Figure [4-18] Photograph showing, a) the diode laser and the photodiode detector connected on the same scanning arm and, b) a schematic diagram for clarity.

This direct approach of having the detector motion coupled to the laser relies heavily upon the beam path through the scanning system (glass interfaces and gel) and the accumulative refractive effects between the source and the detector. Figure [4-19] below, illustrates the beam paths through a 45 mm Wheaton calibration bottle filled with water off refractive index, *n* = 1.33.

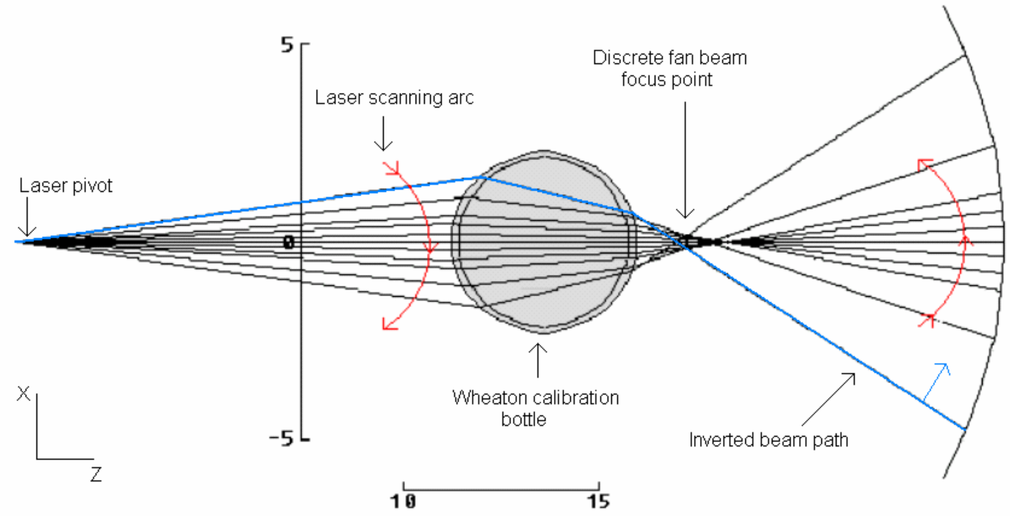

Figure [4-19] Beam2 simulation of the effect of refraction at the optical interface. The laser beam is inverted after passing through the calibration bottle and is analogous to an object image after passing light through a lens. All units are in cm.

The simulation in Figure [4-19] shows that the laser diode and coupled detector move in the opposite direction to the output (refracted) laser beam. This can be seen from the red and blue arrows and can be followed by tracing the ray paths. The data could be corrected in the post data acquisition processing by transforming the data set to match up line paths and relevant integrated data points. However, the relatively inexpensive Wheaton bottles used for the calibration had considerable optical defects that introduce both 2D and 3D scattering of the laser beam during projection acquisitions. It was therefore considered reasonable to modify the existing setup and use another approach that would incorporate optical impedance matching and alter the refraction effects experienced by the laser beam.

The Beam2 simulation of the system shown in Figure [4-19] confirmed experimental observations that at the extremes of the gel bottle, the refraction inverted the laser beam to the opposite side of the scanning motion.

The solution was to use a cylindrical waterbath and position the gel flask centrally within it. The refractive index of the glass was taken to be n = 1.5 and water n = 1.33. This significant change in index compared to air ($n_{air} \approx 1$), greatly reduced refraction and unwanted reflection at the flask boundary. There was reduced spot wander on the active area of the detector, thus improving the overall accuracy of the line integrals with the projection data sets and, in general, the repeatability from scan-to-scan.

Again by using Beam2 as a ray path simulator, the addition of a waterbath could be seen to have an immediate and beneficial effect on the ray paths in the sample. The results for a waterbath of approximately 13 cm in diameter with a 5 cm diameter calibration bottle centred within are seen in Figure [4-20].

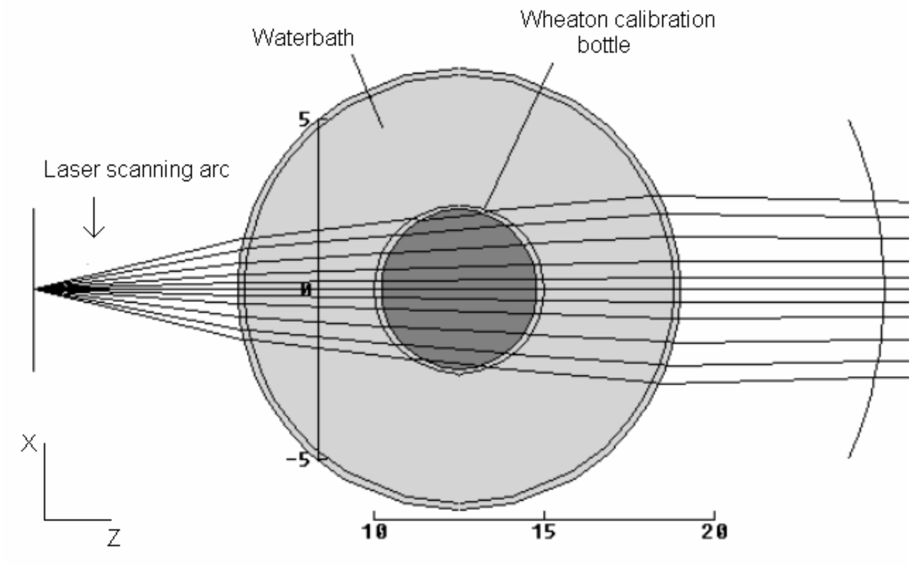

Figure [4-20] Beam2 ray trace for the optical system where a waterbath of 13 cm diameter has a 5 cm diameter calibration (gel) bottle located centrally. All units are in cm.

In general, the limit to useful data acquisition was restricted to 90 % of the overall diameter of the gel flask or vessel, as reported by Gore (Gore *et al*., 1996). Using Beam2, the laser beam fan arc was set to keep the ray path within the calibration bottle. This was achieved by varying the ray orientations and by incorporating the refractive effects of the air-water and water-glass interfaces on the laser beam. This constraint was set by the Beam2 software requirement in that all ray paths must interact with all the surface interfaces presented in the optic spreadsheet (see section 4.3.2.1).

The angular diversion of the ray paths are greatly reduced in this way, which is particularly evident at the extremes of the ray paths. Whereas for the geometry in Figure [4-19], rays would undergo refraction-induced inversion, from Figure [4-20] it is evident that here the paths are only very slightly affected on passing from the water – glass – gel – glass – water interfaces. The level of ray divergence through the optical system is relatively constant, until the final glass – air boundary where the ray paths can be seen to exhibit a very slight convergence to a distant focus. This focus point for all converging rays would occur well outside of the scanner geometry and fixed detector location.

However, the laser fan beam and detector motion could be in tandem, moving together in the same clockwise direction. This would allow representative data to be collected that would correspond to the unique ray path taken through the gel flask. A further possibility arising from Figure [4-20] is that acquisition of line integral data could be obtained using a 2D linear detector array at a stationary position. Depending on the available resolution of the detector (i.e. pixel width of comparable dimensions to the laser beam width post transmission) the data acquisition could be obtained as the fan beam arcs fall onto each individual pixel elements in the detector array. This could in principle, reduce data acquisition times though it may be prone to effects in which scattered light passing through neighbouring regions within the gel flask, contributed an undesirable background signal. This would lead to inaccurate line integral attenuation values.

Two Beam2 optical simulations were performed (in which the laser beam paths and resulting beam foci were compared) between an un-irradiated calibration bottle and an irradiated bottle positioned centrally in the waterbath. For the simulations the refractive index change in the gel resulting from the absorbed radiation dose was estimated and set at n =1.40, and that in the un-irradiated sample set to n =1.35. These refractive indices have been estimated using values given in other literature (Gore *et al*., 1996 and Kelly *et al*., 1998). The full input parameters including the initial ray angles, surface position along the optical axis and the resulting simulation results are shown in Figures [4-21 – 4-26]. The input parameters correspond to the scanner dimensions along the source to detector path.

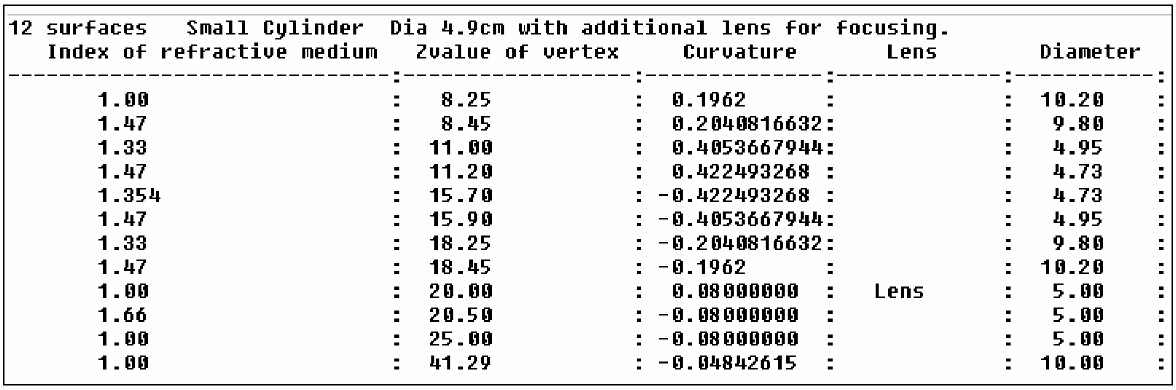

```
12 surfaces   Small Cylinder  Dia 4.9cm with additional lens for focusing.
   Index of refractive medium   Zvalue of vertex     Curvature       Lens        Diameter
----------------------------:------------------:--------------:-------------:-----------:
       1.00                 :   8.25           :  0.1962      :             :  10.20    :
       1.47                 :   8.45           :  0.2040816632:             :   9.80    :
       1.33                 :  11.00           :  0.4053667944:             :   4.95    :
       1.47                 :  11.20           :  0.422493268 :             :   4.73    :
       1.354                :  15.70           : -0.422493268 :             :   4.73    :
       1.47                 :  15.90           : -0.4053667944:             :   4.95    :
       1.33                 :  18.25           : -0.2040816632:             :   9.80    :
       1.47                 :  18.45           : -0.1962      :             :  10.20    :
       1.00                 :  20.00           :  0.08000000  :   Lens      :   5.00    :
       1.66                 :  20.50           : -0.08000000  :             :   5.00    :
       1.00                 :  25.00           : -0.08000000  :             :   5.00    :
       1.00                 :  41.29           : -0.04842615  :             :  10.00    :
```

Figure [4-21] Screen capture for 12 surfaces from the Beam2 simulation showing the results from an un-radiated calibration bottle. The input parameters for the optical surfaces between the laser diode source and the post transmission beam focus point are given. The parameters include the refractive indices of the input surfaces, position along the optical Z axis (Zvalue of vertex) and the curvature and diameter of the waterbath and calibration bottle.

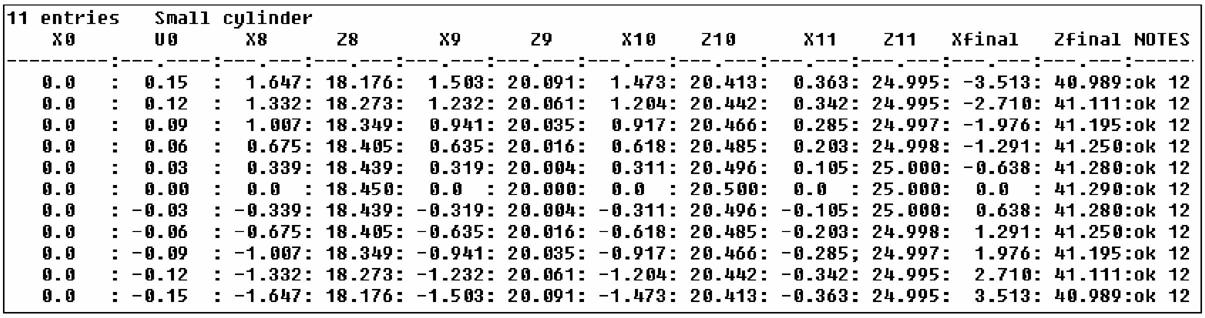

```
11 entries   Small cylinder
   X0        U0       X8       Z8       X9       Z9       X10    Z10      X11    Z11   Xfinal   Zfinal NOTES
---------:---.----:---.---:---.---:---.---:---.---:---.---:---.---:---.---:---.---:---.---:---.---:-----
   0.0   :  0.15  :  1.647: 18.176:  1.503: 20.091:  1.473: 20.413:  0.363: 24.995: -3.513: 40.989:ok 12
   0.0   :  0.12  :  1.332: 18.273:  1.232: 20.061:  1.204: 20.442:  0.342: 24.995: -2.710: 41.111:ok 12
   0.0   :  0.09  :  1.007: 18.349:  0.941: 20.035:  0.917: 20.466:  0.285: 24.997: -1.976: 41.195:ok 12
   0.0   :  0.06  :  0.675: 18.405:  0.635: 20.016:  0.618: 20.485:  0.203: 24.998: -1.291: 41.250:ok 12
   0.0   :  0.03  :  0.339: 18.439:  0.319: 20.004:  0.311: 20.496:  0.105: 25.000: -0.638: 41.280:ok 12
   0.0   :  0.00  :  0.0  : 18.450:  0.0  : 20.000:  0.0  : 20.500:  0.0  : 25.000:  0.0  : 41.290:ok 12
   0.0   : -0.03  : -0.339: 18.439: -0.319: 20.004: -0.311: 20.496: -0.105: 25.000:  0.638: 41.280:ok 12
   0.0   : -0.06  : -0.675: 18.405: -0.635: 20.016: -0.618: 20.485: -0.203: 24.998:  1.291: 41.250:ok 12
   0.0   : -0.09  : -1.007: 18.349: -0.941: 20.035: -0.917: 20.466: -0.285; 24.997:  1.976: 41.195:ok 12
   0.0   : -0.12  : -1.332: 18.273: -1.232: 20.061: -1.204: 20.442: -0.342: 24.995:  2.710: 41.111:ok 12
   0.0   : -0.15  : -1.647: 18.176: -1.503: 20.091: -1.473: 20.413: -0.363: 24.995:  3.513: 40.989:ok 12
```

Figure [4-22] A screen capture of the computed ray path data from the simulation.

The interface data points sampled throughout the XZ plane provide a theoretical standpoint from which scanner modifications can be made. Here the total beam envelope used was approximately 17 degrees (2x ($\sin^{-1}$(0.15)).

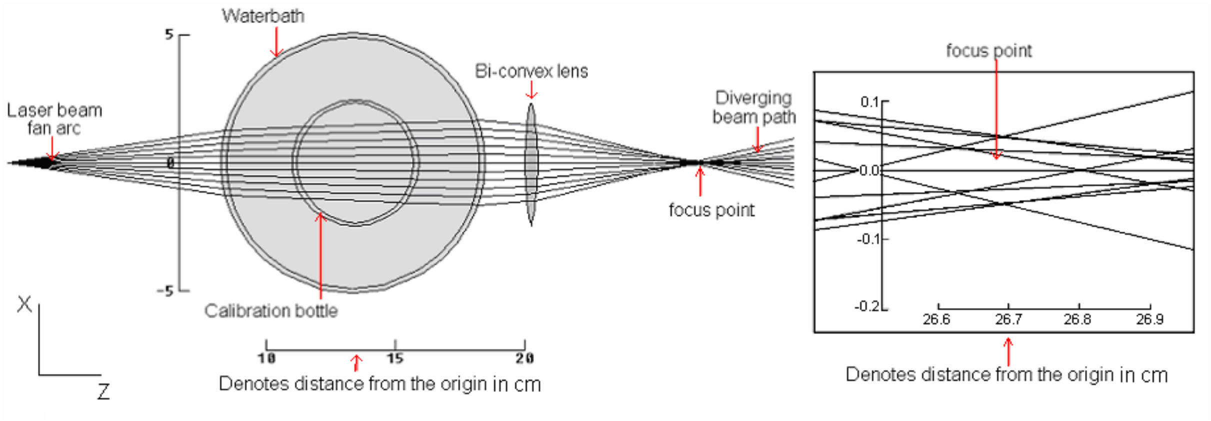

a) b)

Figure [4-23] a) The resulting ray path simulation for an un-irradiated Wheaton calibration bottle with a 5 cm diameter, positioned centrally in the waterbath. The output ray paths were focused by a 2 inch diameter bi-convex lens with a 5 cm focal length. b) The focus point showing that the focal spot diameter is approximately 0.15 cm and occurs 26.7 cm from the beam origin. All units are in cm.

The ray path simulation shows the ray paths are not parallel during the central transition through the calibration bottle and would diverge upon exit of the waterbath. A lens was therefore used to focus the rays to a point within the scanner geometry. Under theses conditions the detector would ideally be placed 26.7 cm from the beam origin at the beam focal point. The next logical simulation would be to incorporate a dosed region in the calibration bottle. The input parameters for this simulation are shown in Figure [4-24] and indicate that 14 surfaces were required to fully simulate the ray paths.

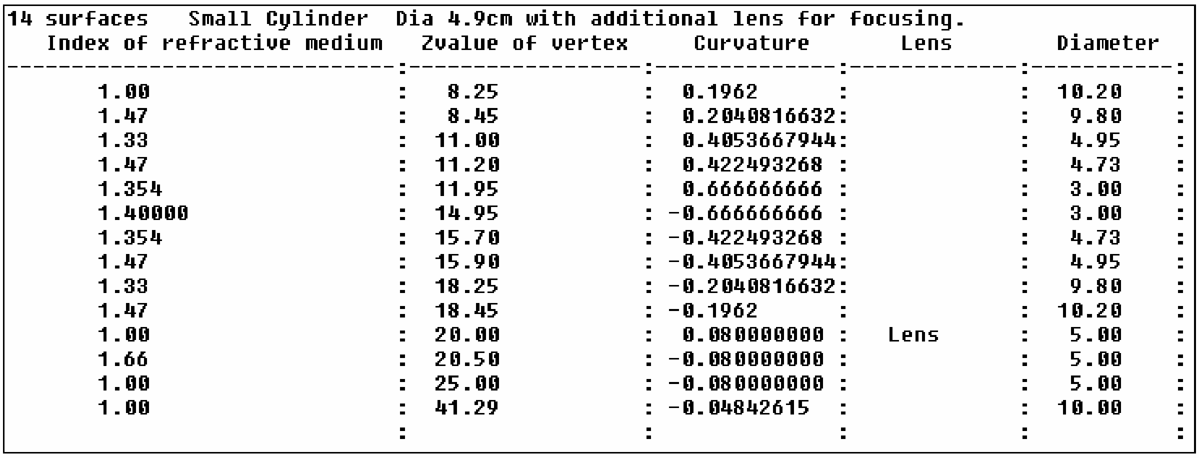

```
14 surfaces   Small Cylinder  Dia 4.9cm with additional lens for focusing.
   Index of refractive medium   Zvalue of vertex     Curvature       Lens       Diameter
-----------------------------:-----------------:--------------:-------------:-----------:
       1.00                  :   8.25          :  0.1962      :             :  10.20    :
       1.47                  :   8.45          :  0.2040816632:             :   9.80    :
       1.33                  :  11.00          :  0.4053667944:             :   4.95    :
       1.47                  :  11.20          :  0.422493268 :             :   4.73    :
       1.354                 :  11.95          :  0.666666666 :             :   3.00    :
       1.40000               :  14.95          : -0.666666666 :             :   3.00    :
       1.354                 :  15.70          : -0.422493268 :             :   4.73    :
       1.47                  :  15.90          : -0.4053667944:             :   4.95    :
       1.33                  :  18.25          : -0.2040816632:             :   9.80    :
       1.47                  :  18.45          : -0.1962      :             :  10.20    :
       1.00                  :  20.00          :  0.080000000 :   Lens      :   5.00    :
       1.66                  :  20.50          : -0.080000000 :             :   5.00    :
       1.00                  :  25.00          : -0.080000000 :             :   5.00    :
       1.00                  :  41.29          : -0.04842615  :             :  10.00    :
                             :                 :              :             :           :
```

Figure [4-24] Screen capture from the Beam2 simulation showing the results for an irradiated calibration bottle. The dose absorbed by the gel and the subsequent increase in refractive index (*n* =1.4) was estimated and incorporated into this simulation. The input parameters of the optical surfaces between the laser diode source and the post transmission beam focus point are given. The parameters include the refractive indices of the input surfaces, position along the optical axis and the curvature and diameter of the waterbath and calibration bottle.

The resulting ray paths are shown in Figure [4-25] and show the ray path distances, in centimetres, from both axis during the simulation. The diverging fan beam has been set to interact with the whole calibration bottle diameter to assess the possible ray response.

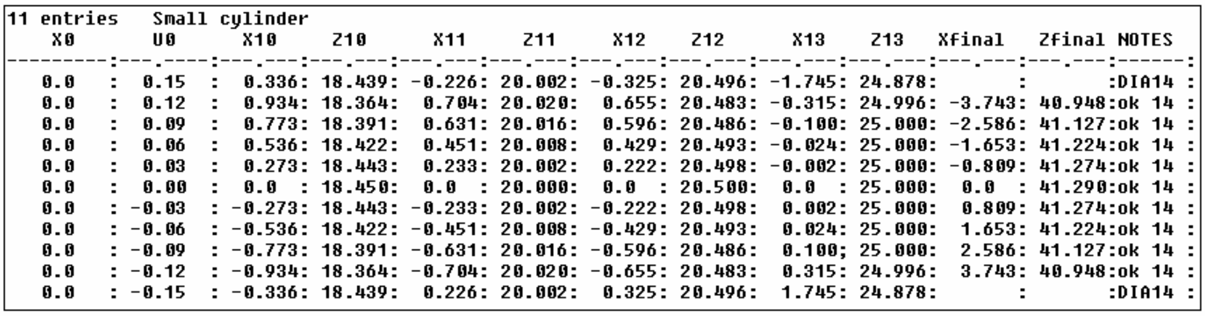

```
11 entries   Small cylinder
   X0        U0       X10      Z10       X11      Z11       X12      Z12       X13      Z13    Xfinal    Zfinal NOTES
---------:---.----:---.---:---.---:---.---:---.---:---.---:---.---:---.---:---.---:---.---:---.---:------:
   0.0   :  0.15  :  0.336: 18.439: -0.226: 20.002: -0.325: 20.496: -1.745: 24.878:        :       :DIA14 :
   0.0   :  0.12  :  0.934: 18.364:  0.704: 20.020:  0.655: 20.483: -0.315: 24.996: -3.743: 40.948:ok 14 :
   0.0   :  0.09  :  0.773: 18.391:  0.631: 20.016:  0.596: 20.486: -0.100: 25.000: -2.586: 41.127:ok 14 :
   0.0   :  0.06  :  0.536: 18.422:  0.451: 20.008:  0.429: 20.493: -0.024: 25.000: -1.653: 41.224:ok 14 :
   0.0   :  0.03  :  0.273: 18.443:  0.233: 20.002:  0.222: 20.498: -0.002: 25.000: -0.809: 41.274:ok 14 :
   0.0   :  0.00  :  0.0  : 18.450:  0.0  : 20.000:  0.0  : 20.500:  0.0  : 25.000:  0.0  : 41.290:ok 14 :
   0.0   : -0.03  : -0.273: 18.443: -0.233: 20.002: -0.222: 20.498:  0.002: 25.000:  0.809: 41.274:ok 14 :
   0.0   : -0.06  : -0.536: 18.422: -0.451: 20.008: -0.429: 20.493:  0.024: 25.000:  1.653: 41.224:ok 14 :
   0.0   : -0.09  : -0.773: 18.391: -0.631: 20.016: -0.596: 20.486:  0.100; 25.000:  2.586: 41.127:ok 14 :
   0.0   : -0.12  : -0.934: 18.364: -0.704: 20.020: -0.655: 20.483:  0.315: 24.996:  3.743: 40.948:ok 14 :
   0.0   : -0.15  : -0.336: 18.439:  0.226: 20.002:  0.325: 20.496:  1.745: 24.878:        :       :DIA14 :
```

Figure [4-25] Screen capture from Beam2 showing the calculated ray path data from the simulation. For this simulation 11 rays were required to adequately sample the calibration bottle and detail the focal point of the emanating ray paths. All but 2 rays converged in the common focal point at 24 cm from the beam origin.

The simulation from the input parameters detailed in Figures [4-24] and [4-25] are shown in Figure [4-26].

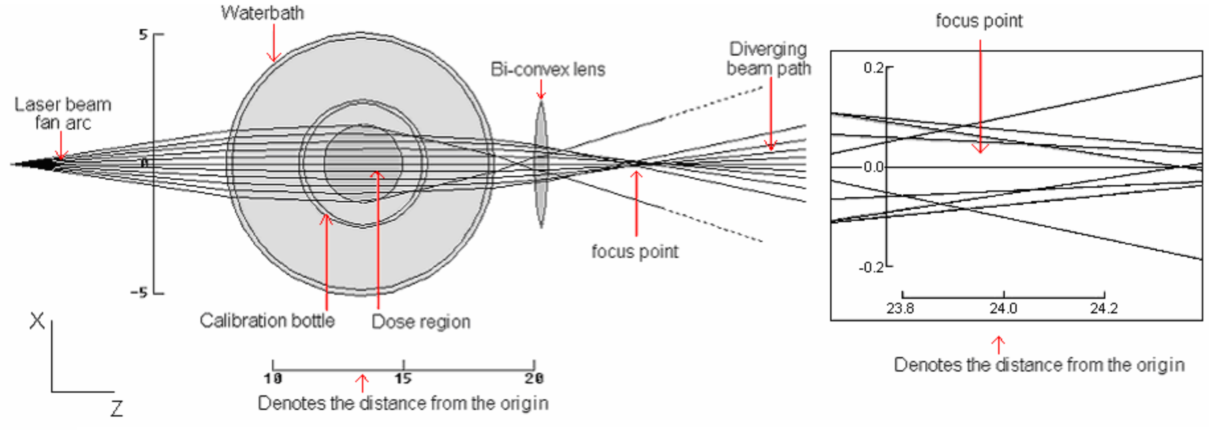

a) b)

Figure [4-26] The resulting ray path simulation for an irradiated calibration flask positioned centrally in the waterbath. The output of the approximately parallel ray paths were focused by a 2 inch diameter bi-convex lens with a 5 cm focal length. b) The focus point showing that the focal spot diameter is approximately 0.2 cm and occurs 23.5 cm from the beam origin. All units are in cm.

4.3.3.1 Fan Beam Versus Parallel Beam

Calculations using the Beam2 ray tracing software predicted that an initially diverging fan beam geometry would in effect become parallel due to refraction within the gel phantom in the waterbath arrangement. Using Beam2 it was possible to vary the refractive indices of the system with the goal of producing an arrangement that would produce an accurate parallel transition through the gel phantom. This led to the discovery that using a larger 13 cm diameter waterbath with the same calibration bottles, the resulting ray paths could be rendered parallel. This suggested that the projection data collected from the scanner could be directly reconstructed using the basic inverse *Radon* computation method that requires data sets to be acquired from parallel projections. The simulation of the fan beam in a geometry producing parallel projections is shown in Figure [4-27].

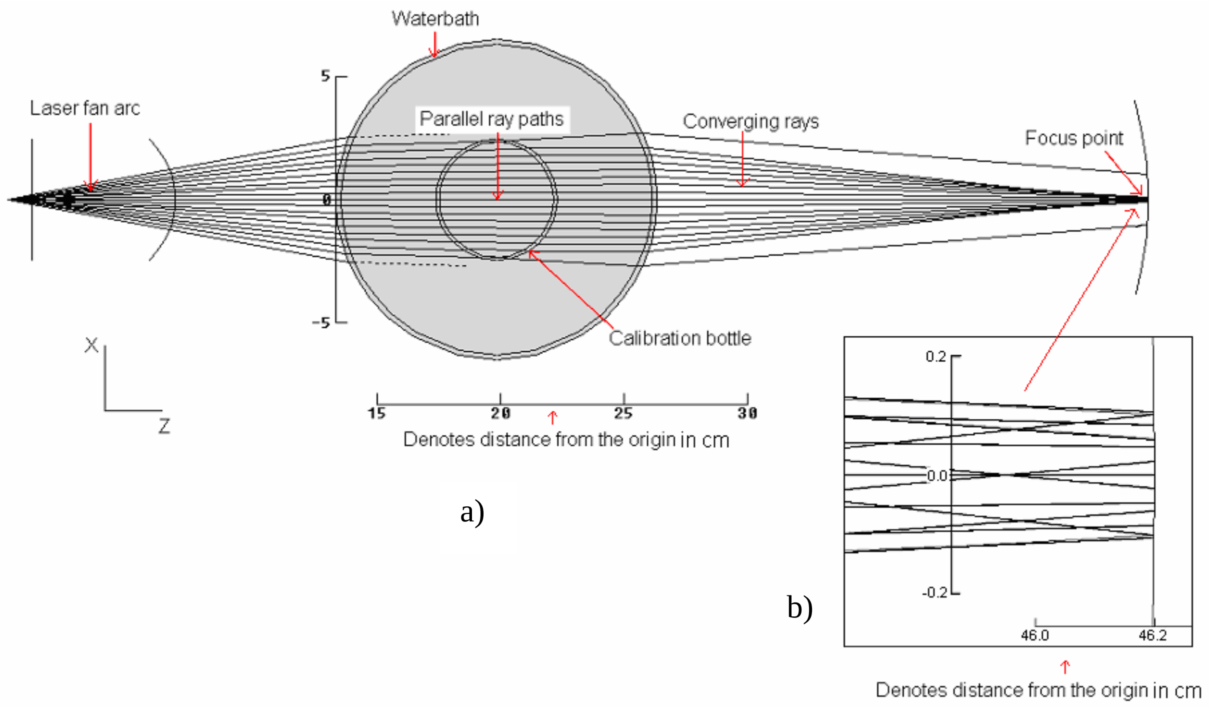

Figure [4-27] The simulated Beam2 transition of the laser beam transition through the scanning geometry showing the parallel ray paths in the central gel flask. The addition of a larger diameter waterbath produced parallel rays through the central region as required for the *Iradon* reconstruction algorithm. The removal of the lens increased the focal distance from the waterbath from approximately 25 cm to 46 cm. All the units are in cm.

The ray path details are shown in Figure [4-28].

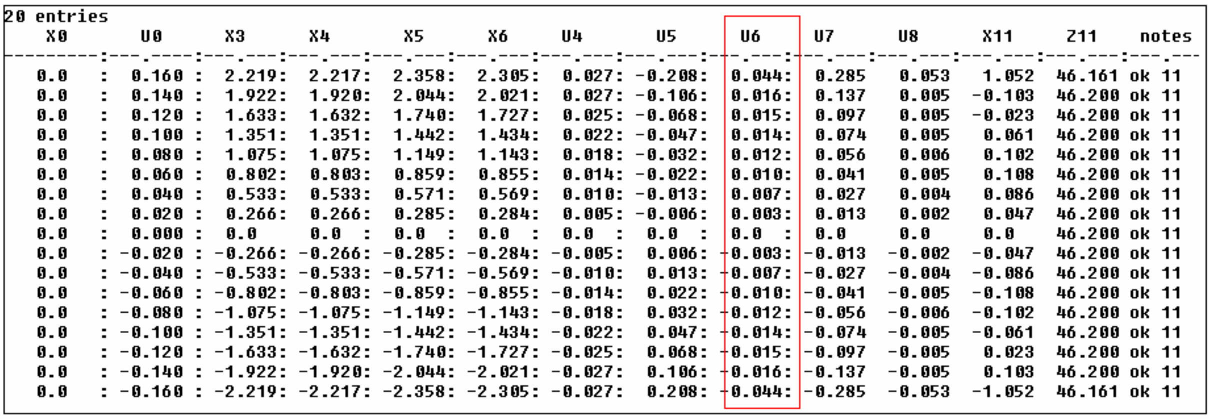

```
20 entries
   X0        U0       X3       X4        X5       X6       U4       U5       U6       U7       U8       X11      Z11     notes
---------:---.----:---.---:---.---:---.---:---.---:---.---:---.---:---.---:---.---:---.---:---.---:---.---:---.---
   0.0    :  0.160 :  2.219:  2.217:  2.358:  2.305:  0.027: -0.208:  0.044:  0.285    0.053    1.052   46.161 ok 11
   0.0    :  0.140 :  1.922:  1.920:  2.044:  2.021:  0.027: -0.106:  0.016:  0.137    0.005   -0.103   46.200 ok 11
   0.0    :  0.120 :  1.633:  1.632:  1.740:  1.727:  0.025: -0.068:  0.015:  0.097    0.005   -0.023   46.200 ok 11
   0.0    :  0.100 :  1.351:  1.351:  1.442:  1.434:  0.022: -0.047:  0.014:  0.074    0.005    0.061   46.200 ok 11
   0.0    :  0.080 :  1.075:  1.075:  1.149:  1.143:  0.018: -0.032:  0.012:  0.056    0.006    0.102   46.200 ok 11
   0.0    :  0.060 :  0.802:  0.803:  0.859:  0.855:  0.014: -0.022:  0.010:  0.041    0.005    0.108   46.200 ok 11
   0.0    :  0.040 :  0.533:  0.533:  0.571:  0.569:  0.010: -0.013:  0.007:  0.027    0.004    0.086   46.200 ok 11
   0.0    :  0.020 :  0.266:  0.266:  0.285:  0.284:  0.005: -0.006:  0.003:  0.013    0.002    0.047   46.200 ok 11
   0.0    :  0.000 :  0.0      0.0   :  0.0   :  0.0   :  0.0   :  0.0   :  0.0   :  0.0      0.0      0.0     46.200 ok 11
   0.0    : -0.020 : -0.266: -0.266: -0.285: -0.284: -0.005:  0.006: -0.003: -0.013   -0.002   -0.047   46.200 ok 11
   0.0    : -0.040 : -0.533: -0.533: -0.571: -0.569: -0.010:  0.013: -0.007: -0.027   -0.004   -0.086   46.200 ok 11
   0.0    : -0.060 : -0.802: -0.803: -0.859: -0.855: -0.014:  0.022: -0.010: -0.041   -0.005   -0.108   46.200 ok 11
   0.0    : -0.080 : -1.075: -1.075: -1.149: -1.143: -0.018:  0.032: -0.012: -0.056   -0.006   -0.102   46.200 ok 11
   0.0    : -0.100 : -1.351: -1.351: -1.442: -1.434: -0.022:  0.047: -0.014: -0.074   -0.005   -0.061   46.200 ok 11
   0.0    : -0.120 : -1.633: -1.632: -1.740: -1.727: -0.025:  0.068: -0.015: -0.097   -0.005    0.023   46.200 ok 11
   0.0    : -0.140 : -1.922: -1.920: -2.044: -2.021: -0.027:  0.106: -0.016: -0.137   -0.005    0.103   46.200 ok 11
   0.0    : -0.160 : -2.219: -2.217: -2.358: -2.305: -0.027:  0.208: -0.044: -0.285   -0.053   -1.052   46.161 ok 11
```

Figure [4-28] The corresponding Beam2 screen capture showing the ray path simulation data illustrated in Figure [4-27]. The highlighted ‘U6’ column shows that the central ray paths are approximately parallel to one and another. Parallel lines would be simulated by 0.000 values.

From Figure [4-27], the simulation predicts the ray paths exiting the waterbath would eventually converge at a point 20 cm beyond the final interface of the waterbath and ray path emergence. The focal point for the rays can be seen in Figure [4-27] and shows that at 46.2 cm from the origin all but two rays converge within a 0.20 cm diameter. Therefore in this idealised situation and assuming that no scattering occurs within the system, a detector with a 0.25 cm^2 active area could be used to record the attenuated laser beam during the fan beam scanning motion.

However, in a real situation where the scattering effects discussed in section 4.3.1 arise, the detection area required would exceed the idealised dimensions. In practice the focal point for all the rays would vary in both their position on the optical axis and the converging diameter at the focal point. This can be understood when comparing Figures [4-23] and 4-26] that illustrate the change in focal points for the ray paths in the XZ planes from following refraction in the system. The additional scattering and refraction that would be present in the imperfect glassware, would exaggerate this problem (see section 4.3.1).

At this point only simulations using a centralised calibration bottle inside a waterbath have been considered. For gel dosimetry investigations larger diameter gel flasks would be required and a two dimensional dose fixed within the gelatin matrix (see Chapter 3). It was therefore important to try and simulate the possible effects of using larger flasks with 90 mm diameters and the resulting refractive change the dosed gel would have on the light paths between the source and photodiode detector. To further improve the simulation quality, 1 mm collimated rays were incorporated. The Beam2 parameters are detailed in Figures [4-29] and [4-31].

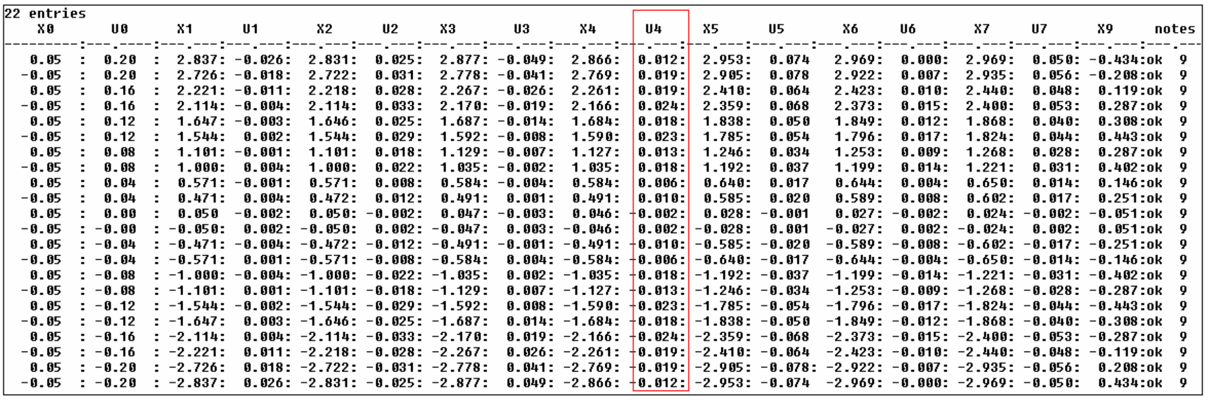

```
22 entries
   X0       U0      X1      U1       X2      U2      X3       U3      X4      U4      X5      U5       X6      U6       X7      U7      X9     notes
---------:---.----:---.---:---.---:---.---:---.---:---.---:---.---:---.---:---.---:---.---:---.---:---.---:---.---:---.---:---.---:---.---:---.---
   0.05  :  0.20  :  2.837: -0.026:  2.831:  0.025:  2.877: -0.049:  2.866:  0.012:  2.953:  0.074   2.969:  0.000:  2.969:  0.050: -0.434:ok  9
  -0.05  :  0.20  :  2.726: -0.018:  2.722:  0.031:  2.778: -0.041:  2.769:  0.019:  2.905:  0.078   2.922:  0.007:  2.935:  0.056: -0.208:ok  9
   0.05  :  0.16  :  2.221: -0.011:  2.218:  0.028:  2.267: -0.026:  2.261:  0.019:  2.410:  0.064   2.423:  0.010:  2.440:  0.048:  0.119:ok  9
  -0.05  :  0.16  :  2.114: -0.004:  2.114:  0.033:  2.170: -0.019:  2.166:  0.024:  2.359:  0.068   2.373:  0.015:  2.400:  0.053:  0.287:ok  9
   0.05  :  0.12  :  1.647: -0.003:  1.646:  0.025:  1.687: -0.014:  1.684:  0.018:  1.838:  0.050   1.849:  0.012:  1.868:  0.040:  0.308:ok  9
  -0.05  :  0.12  :  1.544:  0.002:  1.544:  0.029:  1.592: -0.008:  1.590:  0.023:  1.785:  0.054   1.796:  0.017:  1.824:  0.044:  0.443:ok  9
   0.05  :  0.08  :  1.101: -0.001:  1.101:  0.018:  1.129: -0.007:  1.127:  0.013:  1.246:  0.034   1.253:  0.009:  1.268:  0.028:  0.287:ok  9
  -0.05  :  0.08  :  1.000:  0.004:  1.000:  0.022:  1.035: -0.002:  1.035:  0.018:  1.192:  0.037   1.199:  0.014:  1.221:  0.031:  0.402:ok  9
   0.05  :  0.04  :  0.571: -0.001:  0.571:  0.008:  0.584: -0.004:  0.584:  0.006:  0.640:  0.017   0.644:  0.004:  0.650:  0.014:  0.146:ok  9
  -0.05  :  0.04  :  0.471:  0.004:  0.472:  0.012:  0.491:  0.001:  0.491:  0.010:  0.585:  0.020   0.589:  0.008:  0.602:  0.017:  0.251:ok  9
   0.05  :  0.00  :  0.050  -0.002:  0.050: -0.002:  0.047: -0.003:  0.046: -0.002:  0.028: -0.001   0.027: -0.002:  0.024: -0.002: -0.051:ok  9
  -0.05  : -0.00  : -0.050:  0.002: -0.050:  0.002: -0.047:  0.003: -0.046:  0.002: -0.028:  0.001  -0.027:  0.002: -0.024:  0.002:  0.051:ok  9
   0.05  : -0.04  : -0.471: -0.004: -0.472: -0.012: -0.491: -0.001: -0.491: -0.010: -0.585: -0.020  -0.589: -0.008: -0.602: -0.017: -0.251:ok  9
  -0.05  : -0.04  : -0.571:  0.001: -0.571: -0.008: -0.584:  0.004: -0.584: -0.006: -0.640: -0.017  -0.644: -0.004: -0.650: -0.014: -0.146:ok  9
   0.05  : -0.08  : -1.000: -0.004: -1.000: -0.022: -1.035:  0.002: -1.035: -0.018: -1.192: -0.037  -1.199: -0.014: -1.221: -0.031: -0.402:ok  9
  -0.05  : -0.08  : -1.101:  0.001: -1.101: -0.018: -1.129:  0.007: -1.127: -0.013: -1.246: -0.034  -1.253: -0.009: -1.268: -0.028: -0.287:ok  9
   0.05  : -0.12  : -1.544: -0.002: -1.544: -0.029: -1.592:  0.008: -1.590: -0.023: -1.785: -0.054  -1.796: -0.017: -1.824: -0.044: -0.443:ok  9
  -0.05  : -0.12  : -1.647:  0.003: -1.646: -0.025: -1.687:  0.014: -1.684: -0.018: -1.838: -0.050  -1.849: -0.012: -1.868: -0.040: -0.308:ok  9
   0.05  : -0.16  : -2.114:  0.004: -2.114: -0.033: -2.170:  0.019: -2.166: -0.024: -2.359: -0.068  -2.373: -0.015: -2.400: -0.053: -0.287:ok  9
  -0.05  : -0.16  : -2.221:  0.011: -2.218: -0.028: -2.267:  0.026: -2.261: -0.019: -2.410: -0.064  -2.423: -0.010: -2.440: -0.048: -0.119:ok  9
   0.05  : -0.20  : -2.726:  0.018: -2.722: -0.031: -2.778:  0.041: -2.769: -0.019: -2.905: -0.078: -2.922: -0.007: -2.935: -0.056:  0.208:ok  9
  -0.05  : -0.20  : -2.837:  0.026: -2.831: -0.025: -2.877:  0.049: -2.866: -0.012: -2.953: -0.074  -2.969: -0.000: -2.969: -0.050:  0.434:ok  9
```

Figure [4-29] Screen capture detailing the required ray path input data that would provide collimated rays to fully sample the larger gel flask. Particular attention should be drawn to the U4 column showing how parallel the ray paths are prior to crossing the gel flask. For the example shown on Figure [4-31], the data suggests for the input optical parameters used (see Figure [4-30]) the rays are approximately parallel.

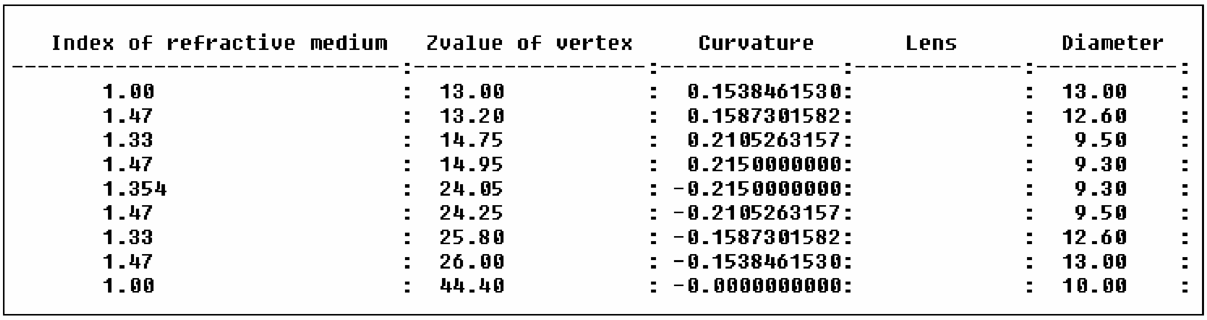

```
  Index of refractive medium   Zvalue of vertex     Curvature       Lens        Diameter
------------------------------:------------------:--------------:-------------:-----------:
       1.00                   :  13.00           :  0.1538461530:             :  13.00    :
       1.47                   :  13.20           :  0.1587301582:             :  12.60    :
       1.33                   :  14.75           :  0.2105263157:             :   9.50    :
       1.47                   :  14.95           :  0.2150000000:             :   9.30    :
       1.354                  :  24.05           : -0.2150000000:             :   9.30    :
       1.47                   :  24.25           : -0.2105263157:             :   9.50    :
       1.33                   :  25.80           : -0.1587301582:             :  12.60    :
       1.47                   :  26.00           : -0.1538461530:             :  13.00    :
       1.00                   :  44.40           : -0.0000000000:             :  10.00    :
```

Figure [4-30] Showing the optical system parameters used in the larger flask simulation. Units are in cm.

The resulting Beam2 simulation for the input parameters detailed in Figures [4-29] and [4-30] are shown in Figure [4-31].

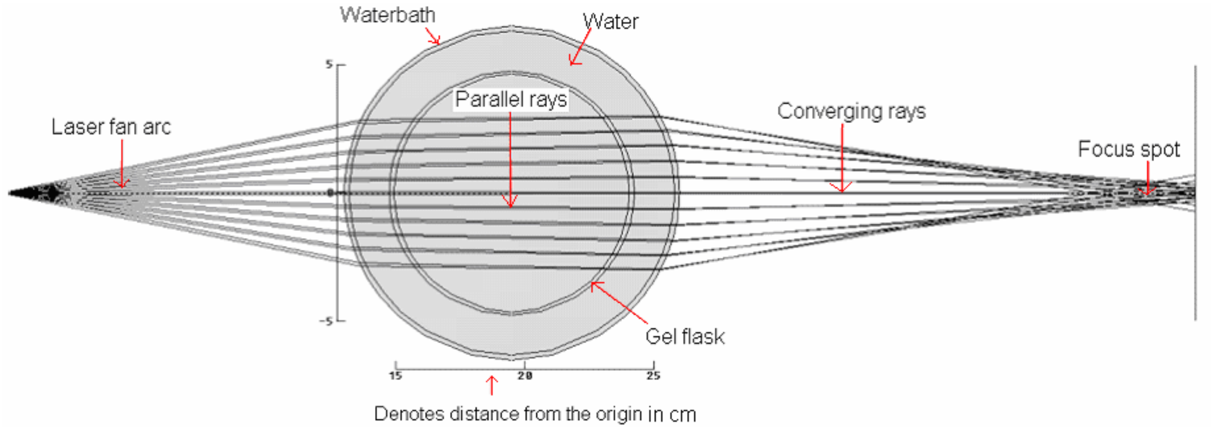

Figure [4-31] Beam2 ray trace of the complete laser to detector path showing the parallel transmission of the collimated rays through the flask and the successful convergence of the laser fan beam to a fixed focal point along the optical axis. The calculated ray paths and input parameters are detailed in Figures [4-29] and [4-30] respectively. All units are in cm.

The increased flask diameter and subsequent divergence of the laser arc required to probe it had the effect of increasing the common focal point on the axis. A larger diameter detector was therefore required to collect all the transmitted beams during optical scanning. The solution to successful data collection was achieved by using an integrated sphere (see Figure [4-3]) with a large optical collection port to collect the transmitted laser beam, shown above in Figure [4-31].

This approach using an integrating sphere removed the previous requirement of directly coupling a scanning photodiode detector to the laser arc scan (see Figure [4-18]). It is important to note, however, that at this stage no attempt had been made to reconstruct a 2D image of a solid object with the optical scanner.

It is relevant to consider how different detector arrangements might be used to speed up scanning times. Fundamentally, the scanning accuracy is directly proportional to the degree of sampling required and conversely the duration of scanning. A method of splitting the laser beam could be considered by the use of a simple cylindrical glass rod vertically orientated in front of the laser beam. This would effectively replace the need to produce a scanning arc from the laser pivot and could lead to a fixed laser source. A 2D linear array detector, fixed at some distance from the waterbath could be used to record the transmission intensities. The approach would be to instruct the data acquisition card to acquire data sequentially along the fixed 2D array detector or in one instance in a linear snap shot of the attenuated laser field. It was also suggested that a web camera could be used to image the transmitted laser line directly onto the 2D detector. The use of a web camera could allow data to be transferred across intranets and allow increased efficiency in data reconstruction and peer analysis.

4.4 Experimental Safety of the Scanner

The predominantly forward scattering nature of the radiosensitive polymer gels is illustrated schematically in Figure [4-32]. It is important to recognise that the scattering occurs in three dimensions during the scanning operation.

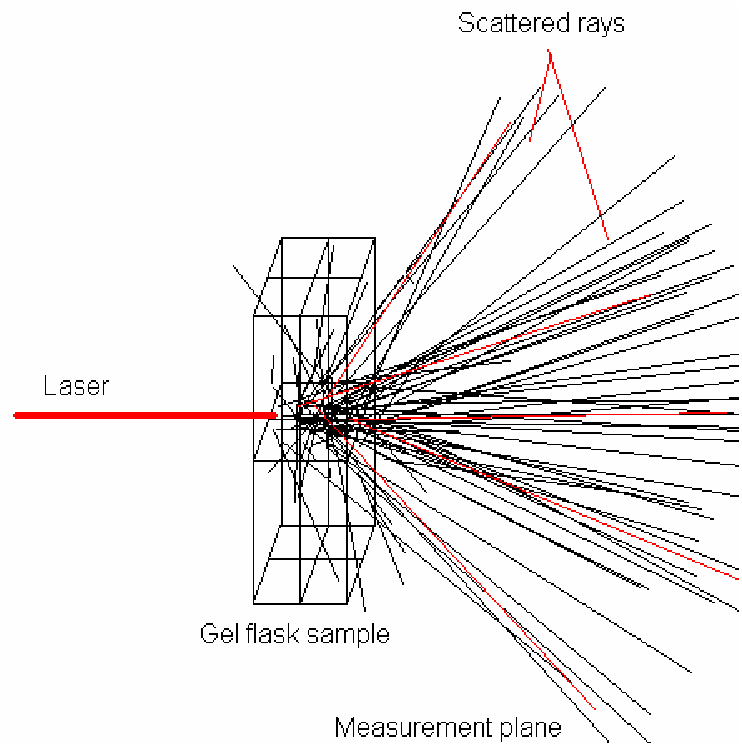

Figure [4-32] Schematic diagram of the inherent 3D scattering from a tissue equivalent volume.

To deal with unavoidable external 3D reflection and scattering of the laser beam during typical scanning translations a protective cabinet was constructed to enclose the scanner (Figure 4-33]). This enclosure thus prevented the possibility of ocular exposure and the risk of eye damage from the laser beam.

Figure [4-33] Photograph of the scanning system enclosed by a blacked-out protective cabinet (the front face has been removed). The enclosure is required to eliminate the possibility of ocular exposure to the scattered or reflected laser beams.

In addition to the requirement to wear laser safety glasses when working around the scanner, micro-switches were fitted to the base of the front plate closure panel and connected to the laser power supply unit. This ensured that the laser would be deactivated if the front panel was raised during optical scanning and therefore added an additional level of protection during scanning operations.

4.5 Optical Scanning Methodology

The following sections will outline the method to optically scan and reconstruct a tomographic image using the optical scanner. This will include the pre-scanning calibration, experimental data acquisition, and the methodology developed to manipulate the raw data into a format compatible with Matlab. A summary is then given of the reconstruction of data with the *Iradon* function within the image processing toolbox (program syntax explanation is given in Appendix C). Finally, details of the MRI protocols used to similarly image the irradiated gel flasks are presented.

4.5.1 Pre-Scanning Calibration

The basic method used to calibrate the scanning of all three stepper motors was to specify a number of degrees of rotation and a distance in mm and determine how many steps were required to complete the intended movement. This would allow a specific ratio of steps per distance and rotation to be calculated and inserted into the software control programs (see Appendix B). However the motor gears used to drive both the fan beam motion and the rotation of the scanner base plate were different. This meant that the gears would turn by differing amounts per number of steps input. For example the number of steps for one complete revolution i.e. 360 degrees was found to be 111,000 steps. This value was then divided by 360 to give the number of steps per degree turned through i.e. 308.333 steps per degree of rotation and this value was then inserted into the computer program as a multiplication factor. The fan beam calibration was achieved by first describing an accurate geometrical representation of a bottle within the Beam2 ray tracing software. Then knowing the diameter of an opaque object at a known distance the number of steps required to cross the diameter could be calculated, giving the number of steps per unit distance translated. For example the number of steps required to translate a 5 cm diameter 125 ml bottle at a known distance allowed the angle/steps ratio to be determined, e.g. 380 steps ~ 13.8 degrees, 1 degree ~ 27.57 steps. The same method was again used for the vertical scanning motion. The number of steps required to raise the scanning arm 14 mm was 1000. Thus, 1 mm increments equated to 71.42 steps in the scanning software.

4.5.2 Experimental Data Acquisition

The method of obtaining a 2D cross section or planar image through the gel flask is as follows:

1) The laser was positioned directly on the optical axis (see section 4.1) with the laser aperture at the same distance to that entered into the Beam2 software (See section 4.3.3.1).

2) The starting position for the scanner was set by user and depended on the size of the gel bottle or flask to be scanned. A computer program for controlling the scanner was written in BASIC. The program was used to manually control three stepper motors. One motor was used to drive the rotating platform on which the gel platform was situated; one was used to increment the scanner arm holding the diode laser and the third motor allowed changes in the vertical orientation of the scanner arm and height of the data acquisition.

3) At user determined points of the rotation, the transmitted laser beam signal recorded on the BPX-65/integrating sphere detector was output to the computer *via* the data conversion box. The value obtained was stored in an array. The array also showed the corresponding angle of rotation and the scanning height relative to the acquired voltage and the start position.

4) After the planar scan had been completed the projection data stored in the array was automatically saved prior to being transferred as an M-file to Matlab for reconstruction. Once the first planar scan had been acquired the second vertical stepper motor was instructed to vertically increment the scanning arm by a determined amount. The level of rotational sampling and this vertical increment determine the resolution of the scan. For example 1 mm slices are obtainable such is the resolution of the stepper motor and the size of the transmitted laser beam.

5) The laser was then re-positioned to enable data acquisition from projections within the user defined fan beam envelope.

6) The first stepper motor was again instructed to rotate the gel phantom and acquired more projection data for the same rotating sampling points the initial scan slice. Data was again stored in an array and saved to an array in Matlab.

7) The data arrays containing all the required fan beam projections were then combined to form one single array containing all the projection information from all the beam envelopes at each selected point of the rotation.

8) A Matlab program then reconstructed a 2D image of the optical density distribution within the phantom using the inverse *Radon* transform function from Matlab by applying the method of filtered back-projection.

The objective was to eventually ‘stack’ the 2D images and interpolate them to form a 3D volumetric representation of the dose distribution with good accuracy and resolution.

9) The process for obtaining 2D scans was repeated for a suitable number of vertical increments to fully characterise the polymer gel region of interest.

10) The 2D planar scans were then stacked together to form a 3D image of the dose distribution within the gel phantom.

4.5.3 Software Control

A program was written in BASIC to provide the capability for both manual and automated scanning options (see Appendix B).

In an ideal system both data acquisition and image reconstruction would be performed on the same computer system. This system was limited due to the aged PC30/D data acquisition card available and required the DOS operating system to function. This system was limited by the lack of computing power, processor speed and available memory required for the complex nature of data reconstruction using the Matlab image processing toolbox. The solution was to use the DOS computer for data acquisition and a more modern PC (Hewlett Packard (HP Compaq)) for image reconstruction and data analysis. Data was transferred from one PC to the other by means of 1.44 inch floppy discs.

4.5.3.1 Raw Data Manipulation

Once the scan was completed, the scanned data file, which was essentially a single column of data, was transformed into a 2D array (R) (see the Filconv program syntax given in the appendix) and exported to Matlab. The columns of (R) correspond to parallel-beam projection data. This raw 2D array represents the raw sinogram of the scanned cross-section of the radiosensitive gel or object under investigation. Within Matlab the 2D data array (R) is manipulated to determine the attenuation coefficients (*via* Beer's law). The 2D array is then reconstructed with the Matlab function *Iradon*. The *Iradon* function reconstructs the sinogram by using the filtered back projection algorithm to perform the inverse *Radon* transforms (see and Appendix C). The *Iradon* function provides the capability to reconstruct images from a variety of interpolation methods, namely: nearest neighbour, linear and spline interpolation. In conjunction with the interpolation options there is a selection of filtering provided including Ram-Lak, Cosine, Hanning and Hann filters. This is an important aid that can remove unwanted noise within the data obtained from the scanning process and which subsequently produces an enhanced reconstructed 2D image slice of the gel/object scanned. A differential image is then produced by subtracting the reconstructed reference image from the scanned image.

4.5.3.2 Image Reconstruction in Matlab

It was intended that the utilisation of the optical tomography scanner to collect data and the method of reconstructing planar images should be straightforward and not overly complicated. With that in mind the linear data array was converted into the 2D matrix of attenuation values using the Filconv program (see section 4.5.3.1). This data, stored in text file format (.txt) was then imported into the Matlab workspace for further data manipulation and processing.

Two methods were used for reconstructing the raw projection data collected by the scanner that used the *Iradon* function. The only difference between Method ‘A’ and Method ‘B’ was the additional data processing that was required for B. The matlab syntax for the methods is briefly described here showing the simple steps of importing, processing and reconstructing the data. For reference, examples of the *Radon* and *Iradon* functions are presented in Appendix C, and show how the projection sinogram is produced for the commonly used Shepp-Logan phantom and then reconstructed.

The raw projection data file (Gel.txt) is imported into the Matlab workspace by the following syntax:

```
Load Gel.txt – Ascii;
```

The *Iradon* function now required that a 1D matrix be created and assigned that corresponded to the data collection parameters e.g. data collected from 0 to 180 degrees at 1 degree intervals would be expressed as

```
[theta] = 0:1:180;
```

Now the *Iradon* function can be used to reconstruct the basic 2D image (used for method ’A’ and here assigned to the variable IR) from the input sinogram and the 1D matrix.

```
IR = iradon(Gel, theta);
```

This method can be used to reconstruct solid objects that provide a binary projection data set i.e. signal or no signal.

Method ‘B’ is used for reconstructing images obtained from varying attenuation values i.e. a dosed gel flask, and requires additional data processing. The process of taking logarithms of the projection data enhances the available information and therefore usefulness of the reconstructed images. It is described as follows:

```
Load Gel.txt – ASCII;

[theta] = 0:1:180;

A = log(Gel/100);
```

The degree of image detail can be varied by changing the value of the denominator i.e. 1 – 100.

The image can be padded (500 by 500 pixels) and filtered, for example, using the Hann window to reduce high frequency components to the images and is produced by:

```
IR = iradon(A, theta, 500, ‘hann’);
```

The image can be displayed in various colour maps and displayed by:

```
imshow (IRx-100), colormap(jet), colorbar;
```

The image contrast can be varied by changing the multiplication factor, for example, from -1 to -1000.

Results using both methods are reported in Chapter 5.

4.6 MRI Imaging Protocols

All MR imaging was performed on a 1.5 Tesla GE Signa scanner using a commercial radio-frequency (RF) head coil. Following initial sagittal localiser images, a T_2-mapping protocol was acquired as described in previous work (Liney 1996).

The sequence used to image gel batches manufactured with 9 % Methacrylic acid (MAA) was a dual-echo fast spin echo (FSE) pulse sequence with four echoes acquired over two acquisitions (T_E/T_R = 24,109 & 60,145 ms). Only when deviating away from the nominal 9 % batches was it required to vary these values. In all cases a field of view of 240 mm was used with an image matrix of 256 x 256, giving an in-plane resolution of 0.9 mm. Images were obtained throughout the entire volume of the Wheaton calibration bottles and the gel flask in the coronal plane, with a slice thickness of 5 mm and an interslice gap of 1.5 mm. The total scan time for each FSE sequence was approximately 3 minutes, giving a total examination time for calibration and verification of 15 minutes. Regions of interest (ROI) were defined in each of the calibration vessels at each slice location using Advantage Window Software (GE Medical Systems).

Mean values of signal intensity were recorded at each echo time and the logarithm of the signal intensity determined (see Figure [4-34]. These values were fitted to the following equation using linear regression.

$$\ln S(T_E) = \ln S_0 - R_2(D).T_E \qquad (4\text{-}1)$$

where $S(T_E)$ is the measured MR signal intensity at a given echo time, (T_E), S_0 is the signal at $T_E = 0$, and $R_2(D)$ is the transverse relaxation rate, being a function of dose. A calibration was established by plotting the estimated R_2 for each known dose value.

The method used to calibrate the gel batches is summarised below:

After a period of time, the radio frequency (RF) induced magnetism within the gel flasks begins to decay. This free induction decay (FID) occurs when the aligned magnetic spins within the gel flask begin to relax and de-phase with one and another (see Figure [4-34]). The intensity of the signal decay is recorded by an appropriate RF receiver. For the experiments presented here, a head and neck coil receiver was used to obtain signal intensities at the echo times detailed above.

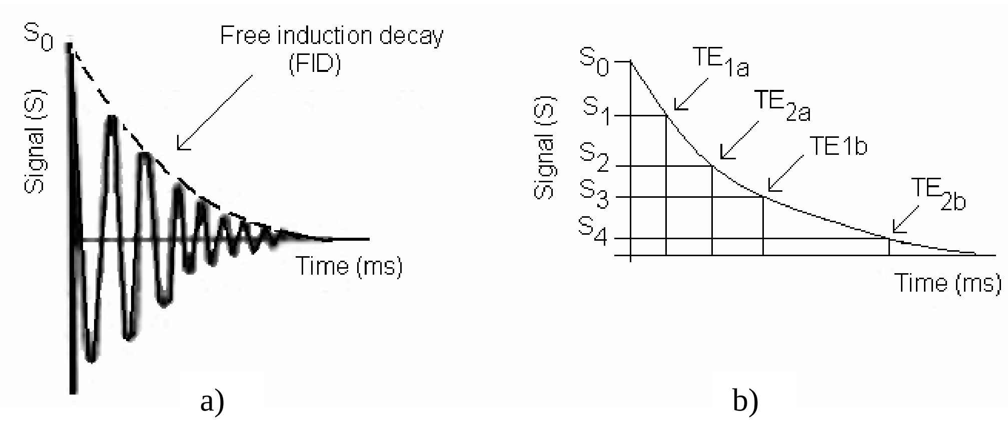

a) b)

Figure [4-34] Illustration of a) the free induction decay (FID), a consequence of the de-phasing spin-spin magnetism and b) the R_2 signal intensities (S) at the associated echo times (TE). Here TE_{1a}, TE_{2a}, TE_{1b} and Te_{2b} were collected at 24, 60, 109 and 145 ms respectively.

The signal data used for this example is shown in Table [4-1]. In order to produce the calibration curve for the batch, the gradient of each FID from the gel flasks (dose at (6, 12, 18 and 24 Gy) has to be found. The gradient allows the corresponding R2 value to be obtained for the particular dose level delivered to the flask.

Time	Dose (Gy)							
(ms)	6		12		18		24	
	Signal (S)	Ln(S)	Signal (S)	Ln(S)	Signal (S)	Ln(S)	Signal (S)	Ln(S)
24	1709	7.444	1446	7.277	1205	7.094	1223	7.109
60	1321	7.186	1007	6.915	725	6.586	626	6.439
109	1152	7.049	690	6.537	412	6.021	325	5.784
145	916	6.800	529	6.271	279	5.631	189	5.242

Table [4-1] Data showing both the signal intensity (S) and the natural logarithms of the signal (Ln(S)) collected at different times during the free induction decay (FID). The R2 values corresponding to the 6, 12, 18 and 24 Gy level are then calculated.

The dose dependant gradients are obtained from the Ln(S) versus time are shown in Figure [4-35].

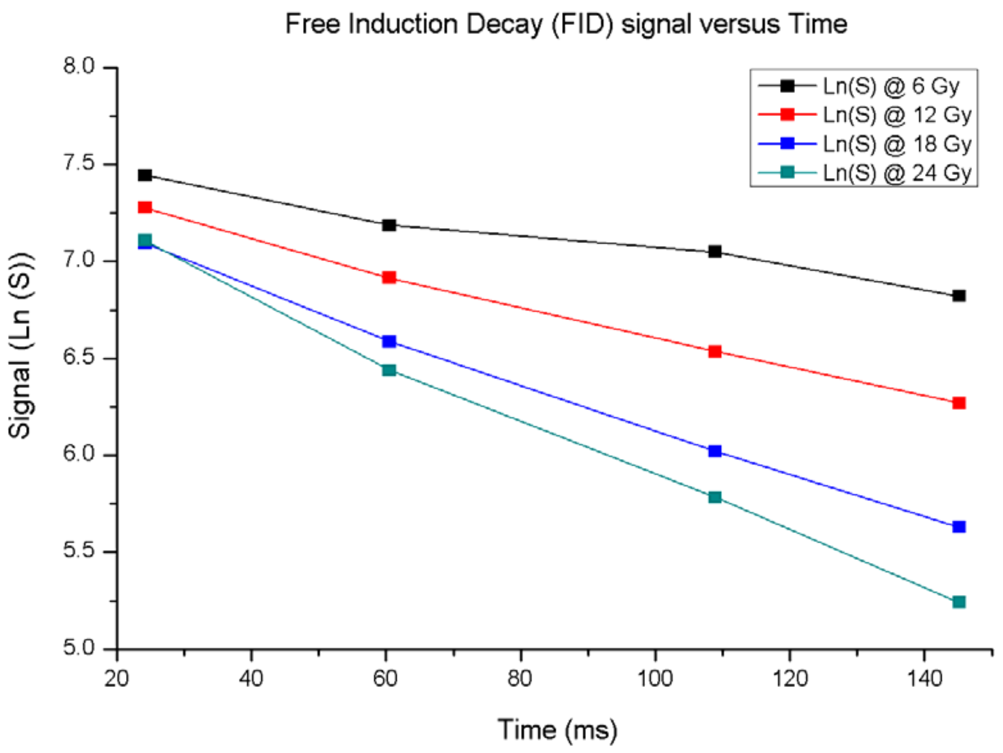

Figure [4-35] Plot of the natural logarithms of the signal intensity versus time (ms). The data shows that the signal intensity is reduced for both increasing time and increasing dose values.

Once the gradient has been calculated for each dose level, the value is multiplied by -1000 to produce the corresponding R2 value in s^{-1}. This is shown in Table [4-2].

Dose (Gy)	Gradient (G)	R2 (G*-1000)
6	-0.00483	4.83
12	-0.00824	8.24
18	-0.01203	12.03
24	-0.01553	15.53

Table [4-2] Data showing the R2 (s^{-1}) value corresponding to the dose (Gy).

The calibration curve for this example is shown in Figure [4-36].

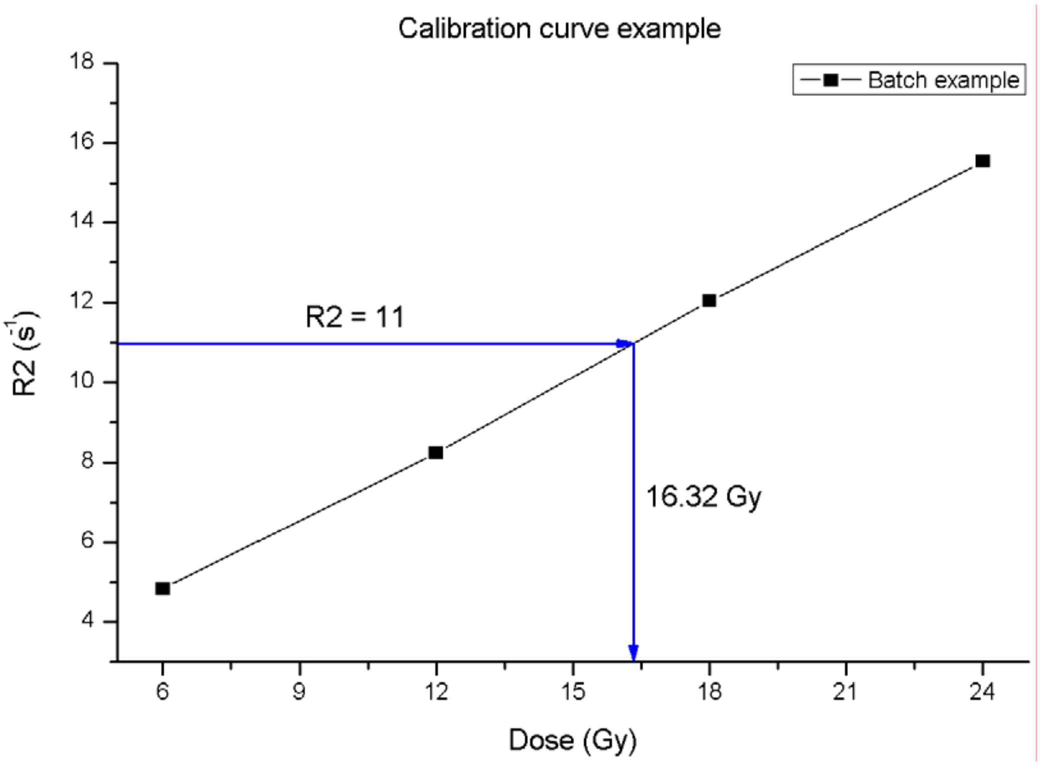

Figure [4-36] Plot of R2 (s^{-1}) versus dose (Gy) showing how the unknown dose value is obtained from the calculated R2 value.

Once the calibration curve has been produced for a particular gel batch, unknown dose regions can be inferred from it. This is achieved by following the process detailed above and producing a R2 value for the irradiated gel flask. The R2 value (y-axis value) shown in Figure [4-36], is then referenced to the previously calculated calibration curve from which the corresponding x-axis dose level (16.32 Gy) is then revealed.

4.7 Dosing the Calibration Flasks

The gel dosing experiments were performed at the Princess Royal Hospital in Sutton, East Hull. A 2100C linear accelerator delivering 6 MV X-rays was used to dose the gel calibration bottles and larger gel flasks. Throughout the experimental series, the dose rate was maintained for all gel dosing, with only the radiation field size, required dose to be delivered and desired dose distribution/volume being varied (‘cross’ and ‘quadrant’ volumes). To calculate the dose delivered to the gel flask using either MRI or OCT, a series of calibration bottles were irradiated to specific values to provide a relationship between dose delivered and the imaging signal response. The calibration studies used 8 x 125 ml bottles of 50 mm diameter filled with MAGIC radiotherapy gel manufactured in the laboratory. For the calibration studies, the bottles were irradiated from 0 to 28 Gray (Gy) with 4 Gy dose increments. A bottle was always left un-irradiated as a control so the background level of pre-polymerisation from free radicals within the gel flask without dosing could be accounted for, see Chapter 3.

Table [4-3] displays the dose delivered to the calibration bottles.

Bottle	1	2	3	4	5	6	7	8
Dose (Gy)	4	8	12	16	20	24	28	0 (Control)

Table [4.3] A standard calibration experiment dosing the bottles with 0 to 28 Gy.

The method used to uniformly dose the calibration bottles is outlined in the following pages. Figure [4-37] shows the experimental arrangement used to irradiate both the calibration bottles and gel flasks. Initially bottles 1 – 4 were positioned on the treatment table and centralised in a straight line equally at the iso-centre with centre of the bottle positioned at 1 m from the X-ray source.

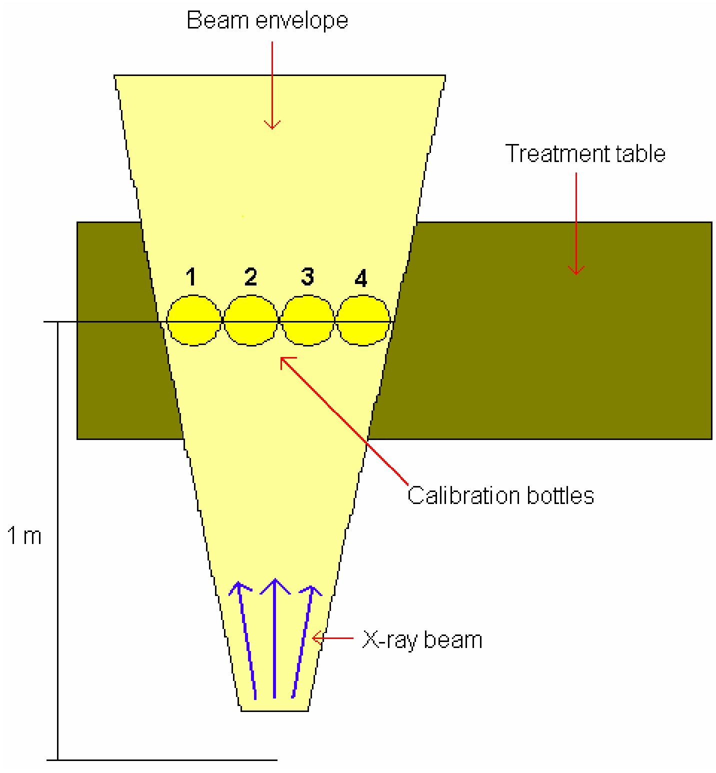

Figure [4-37] Schematic plan view of the initial gel radiation dosing setup.

The 2D field sizes (generally 22 cm wide by 5 cm high) were created to completely encompass all the 5 cm Wheaton calibration diameter bottles when in position, thus uniformly delivering equal levels of radiation to all the bottles at the iso-centre. This is shown in Figure [4-38].

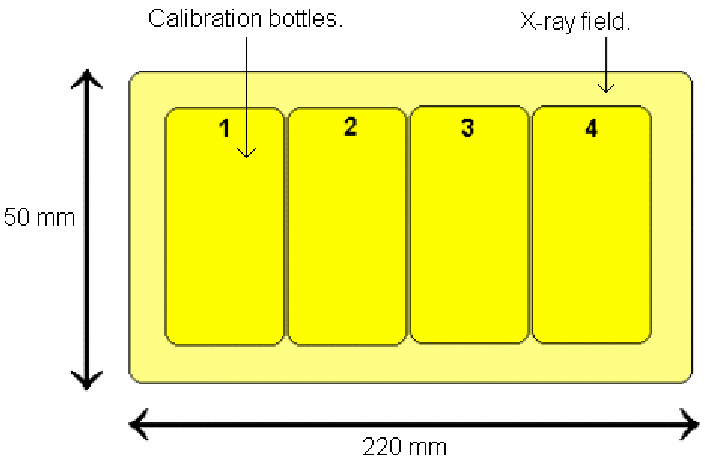

Figure [4-38] Lateral view of the X-ray field bathing the calibration bottles at the 1 m iso-centre (not to scale).

All field sizes and subsequent monitor units (MU's) delivered are calculated from a 10 x 10 cm field size and a corresponding conversion factor. Changes in the radiation field size require that the MU's are recalculated to provide the required dose to be delivered. For example, to deliver 2 Gy to a depth of 2.5 cm, 189 MU's would be required. The MU value would increase for the same field if required at a greater depth due to a larger flask and gel volume.

The method for delivering uniform radiation to the calibration bottles was as follows:

1) Bottles 1-4 were simultaneously irradiated with the desired dose. For example delivering a dose of 2 Gy at a depth of 2.5 cm with a field size of 22 x 5 cm requires 189 monitor MU's.

2) Bottle 1 was removed and the remaining three then irradiated with a further 2 Gy accumulating 4 Gy in total for bottles 2, 3, and 4.

3) Bottle 2 was removed and the remaining two bottles further irradiated with 2 Gy.

4) Bottle three was removed and the final bottle again irradiated with 2 Gy.

This procedure is summarised in Figure [4-39].

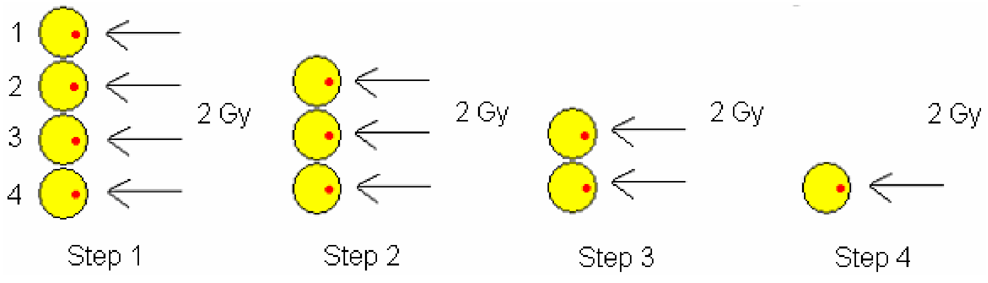

Figure [4-39] Illustration of the dosing Steps 1 to 4 as outlines in the text.

The total radiation delivered and therefore accumulative absorbed dose for the particular radiation field is summarised in the Table [4-4].

Bottle	1	2	3	4
Dose (Gy)	2	4	6	8

Table [4-4] Summary of the final accumulated absorbed dose for each bottle.

To deliver a uniform dose distribution to the gel bottles, steps 1 – 4 were repeated with all the bottles rotated by 180 degrees as shown in Figure [4-40].

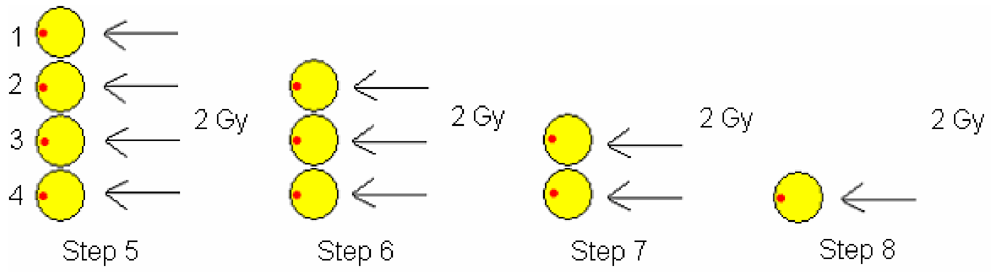

Figure [4-40] Steps required for a uniform dose delivery.

The accumulative dose absorbed after step 8 is summarised in Table [4-5].

Bottle	1	2	3	4
Dose (Gy)	4	8	12	16

Table [4-5] Total uniform dose absorbed for each bottle after step 8.

The following steps describe the method used to dose the remaining bottles 5-7 with 20 to 28 Gy and is shown in Figure [4-41].

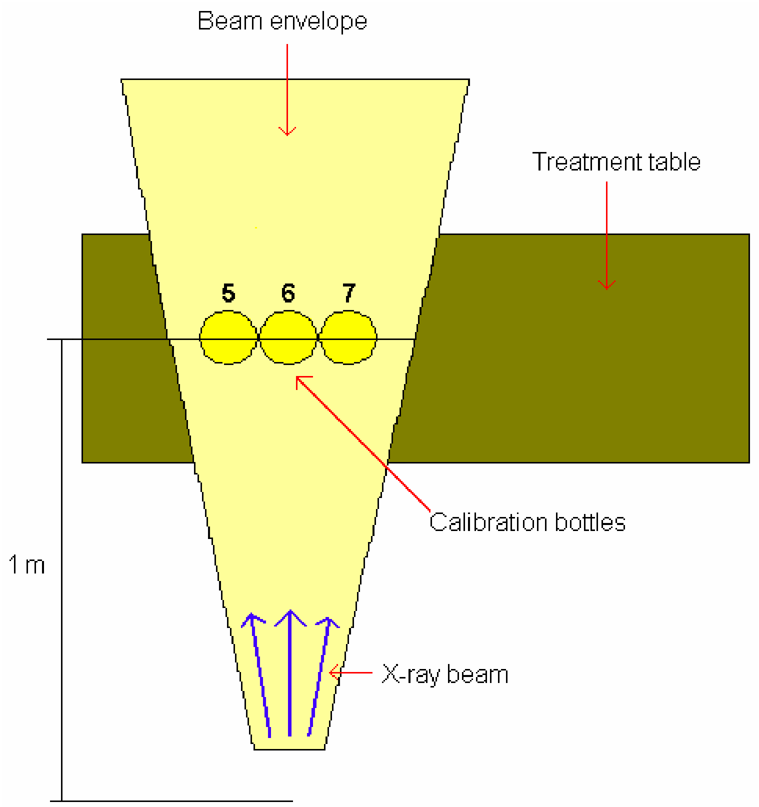

Figure [4-41] Bottle positioning for doses of 20 to 28 Gy.

9) A dosing 'boost' of 10 Gy was delivered to the remaining bottles (5, 6 and 7). Again based on the field sizes this equated to 945 MU's.

10) Bottle 5 was then removed and the remaining bottles further irradiated with 2 Gy (189 MU's).

11) Bottle 6 was removed and bottle 7 irradiated with a further 2 Gy.

This sequence can be summarised in Figure [4-42].

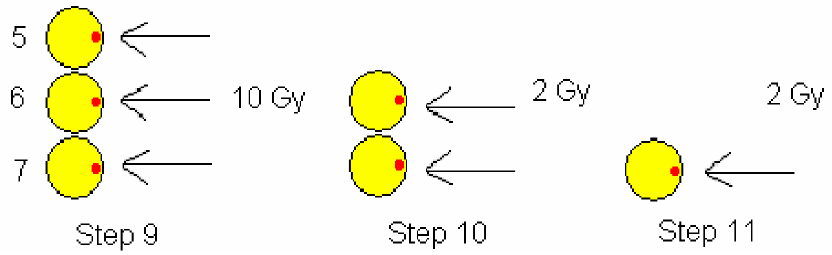

Figure [4-42] The 'Boost' dose and final dose delivery steps.

The total dose absorbed by bottles 5, 6 and 7 is summarised in Table [4-6].

Bottle	5	6	7
Dose (Gy)	10	12	14

Table [4-6] Total dose absorbed at step 11.

Bottles 5, 6 and 7 were replaced, rotated through 180 degrees and then steps 9, 10 and 11 repeated exactly, see Figure [4-43].

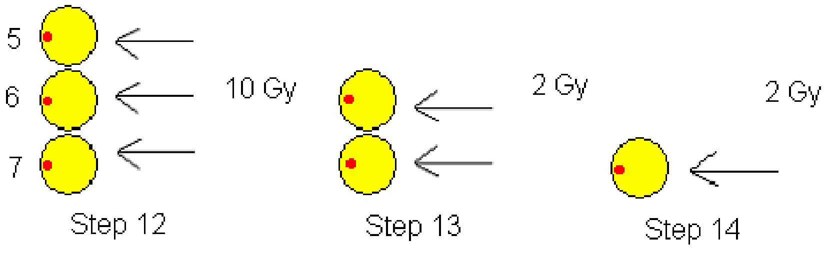

Figure [4-43] Illustration of the final steps to complete the dosing method.

Table [4-7] gives the final total dose delivered to the bottles 5, 6, and 7.

Bottle	5	6	7
Dose (Gy)	20	24	28

Table [4-7] Final dose absorbed from steps 12 to 14 (repeats of 9 -11).

It is important to note that the method described here of sequential exposure of both sides of the bottles and larger gel flasks holds for all irradiations designed to produce uniform absorbed doses in this thesis.

4.7.1 Generating Dose Distributions

There are a number of benefits to producing different types of dose distribution in terms of e.g. strips, crosses and quadrants.

1. Optical scanner performance in terms of reconstruction accuracy and resolution can be assessed from how well it deals with these patterns.

2. Gel properties such as linearity of dose response can be investigated.

3. How gel chemistry is governed by bulk polymerisation effects by varying exposure geometries.

This section describes the various methods used to produce strip, cross and quadrant exposure regions in the gel flasks.

4.7.1.1 Dose ‘Strip’ Distribution

Three large flasks with 7 cm diameters were initially irradiated with a 22 x 9 cm field delivering 5 Gy (470 MU’s) to the centre of the flasks. Two larger calibration flasks were prepared to test out the gel response to a ‘strip’ distribution and a more complex distribution in the form of a cross.

This basic dosing experiment was used to test the resolving ability of the optical scanner in reconstructing the dose distributions delivered. To achieve a uniform dose distribution the gels were irradiated with 2.5 Gy from both 0 and 180 degrees as illustrated in Figure [4-44].

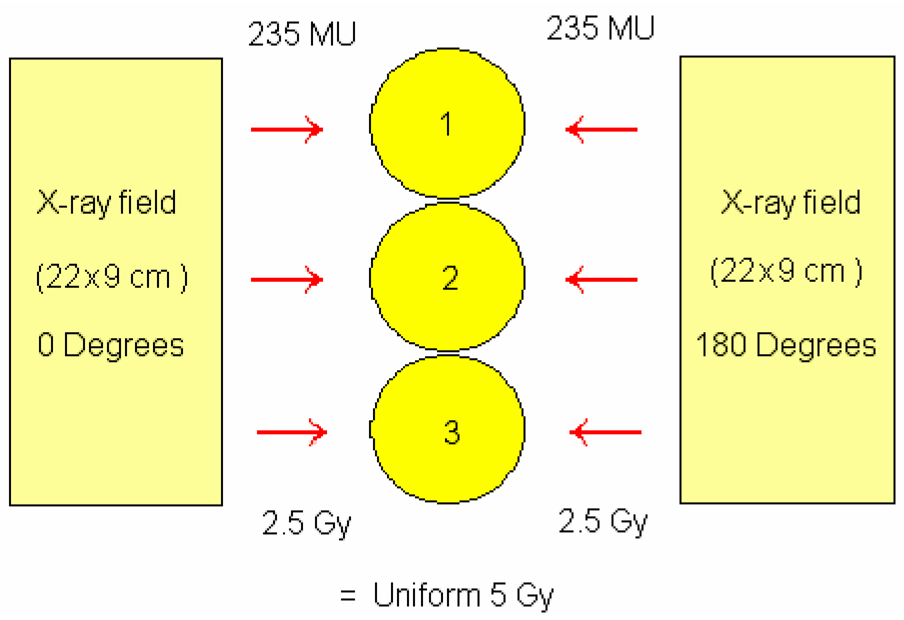

Figure [4-44] Diagram showing the 22 by 9 cm radiation field used to deliver a uniform 5 Gy dosing to the 7 cm diameter gel flasks from opposite sides.

A further 10 Gy was delivered uniformly to flask 2 as shown in Figure [4-45]. This was achieved using a smaller field size (7 cm wide by 9 cm high), delivering a calculated 488 MU (5 Gy) from opposing delivery angles equalling 10 Gy in total.

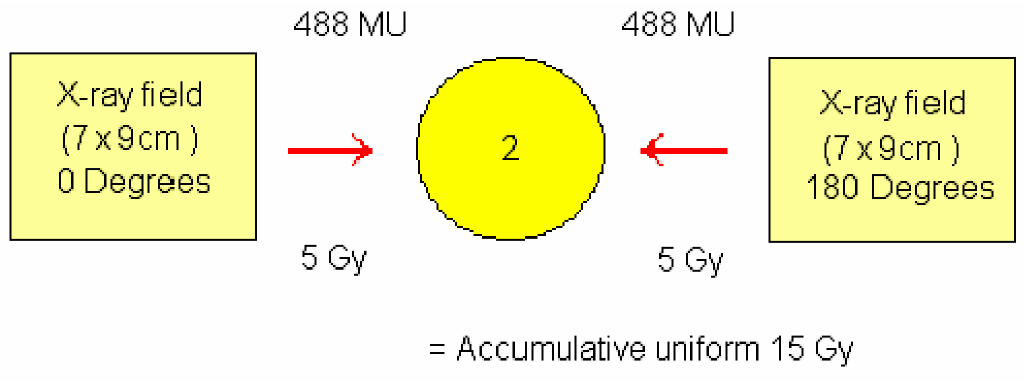

Figure [4-45] Diagram showing the additional exposure required to boost gel flask 2 to a uniform 15 Gy dosing.

The final 7 cm diameter flask was then irradiated with a narrow beam of 5 Gy X-ray radiation (507 MU's), from opposing directions. This produced a region of higher dose level of dose within the distribution and therefore additional spatial structure the optical scanner would need to resolve. This 'strip' distribution is shown In Figure [4-46].

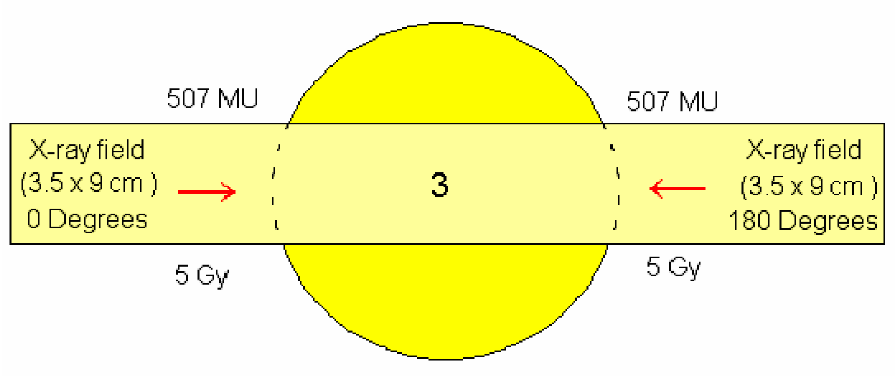

Figure [4-46] Illustration of the uniform single strip distribution in gel flasks.

The uniformly dosed 5 and 15 Gy calibration flasks and the third 'strip' flask can be evaluated using MRI to determine the effectiveness in accumulating the overlaying dose areas within this 'strip' distribution. The results, shown in Table [4-8], indicated that regions (above the strip, in the strip and below the strip) had differing levels of absorbed dose based on comparison with MRI results for the calibration bottles.

	Gel Flask 1	Gel Flask 2	Above strip	Below strip	Strip
Dose	6.95	13.92	7.97	7.74	13.77
Planned Dose	5	15	5	5	15
Percentage Error (%)	+ 39	- 7.2	+ 59	+ 55	- 8.2

Table [4-8] MRI results for the deduced dose from the 'Strip' distribution performed on the MAGIC gel Batch number 6.

The results in table [4-8] indicate that flask 1 was significantly over dosed whilst flask 2 was somewhat under dosed. This can also be seen in the corresponding 5 and 15 Gy areas in Figure [4-46]. However, it should be noted that the calibration bottles have different volumes and hence differing bulk chemical polymerisation reactions, glass and dimensions. The difference between measured and planned doses led to subsequently preparing both calibration and gel distribution flasks from glassware with of the same dimensions and volumes. It was hoped that this approach would further reduce the differences observed from values obtained using the smaller Wheaton calibration bottles to the 90 mm diameter gel flasks. Thus 90 mm flasks were used for calibrating the gel batch dose responses produced from the same radiation fields.

4.7.1.2 Dose ‘Cross’ Distribution

Figure [4-47] illustrates a three-dimensional cross delivered to an optical friendly 90 mm diameter flask in the following steps:

1) The flask was dosed with a 3.5 cm by 9 cm X-ray field delivering 253 MU’s (2.5 Gy) from 0 degrees.

2) The Gel was rotated 180 degrees and irradiated again with the same dose and field size, thus delivering a uniform 5 Gy strip.

3) The Gel was then rotated through 90 degrees and irradiated with 507 MU (5 Gy).

4) Finally the gel was again rotated through 180 degrees and irradiated with a 507 MU again delivering a uniform 10 Gy strip normal to the previously irradiated 5 Gy strip. The accumulated absorbed dose in the central cross over region was then 15 Gy.

This method provided 0, 5, 10 and 15 Gy regions of interest within the gel flask for OCT and MRI evaluation.

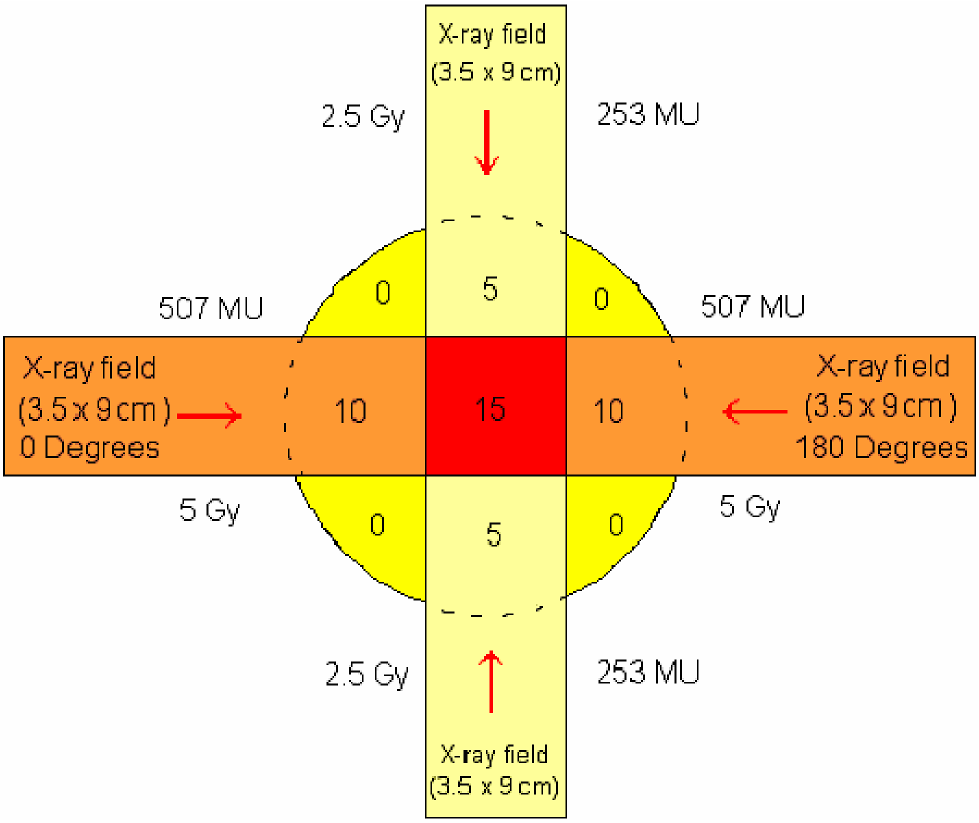

Figure [4-47] Illustration of the 3D 'Cross' dose distribution from the MAGIC gel Batch number 6.

	Gel Flask 1	Gel Flask 2	Left of cross	Right of cross	Top of cross	Bottom of cross	Centre region
Dose	6.95	13.92	9.87	11.92	6.96	8.44	13.73
Planned Dose	5	15	10	10	5	5	15
Percentage Error (%)	+ 39	-7.2	-1.3	+ 19.2	+ 39.2	+ 68.8	- 8.47

Table [4-9] MRI results obtained for the dose cross distribution obtained from Batch 6. The regions of interest are, specifically the 5 areas forming the cross (5, 10 and 15 Gy regions).

The data shown in Table [4-9] illustrates again that there seems to be both over and under dosing of the gel flask compared to that planned. The absorbed doses are again calculated from the calibration bottles ranging from 0 to 15 Gy, specifically from the decay signals relating known dose values and used to infer unknown (planned) dose regions from the signals obtained from the cross distribution. This is made possible because the same gel batch and response characteristic made up both the calibration bottles and the gel flasks. Within the gel flask, regions of polymerisation will vary and thus influence the monomer reservoirs required for additional polymerisation. Regions of dose gradients will also develop due to the radiation absorbed within the gel flask. So in general, there exists a complex series of unknown quantities with regards to the gel chemistry and the effect of non-uniform radiation on them.

4.7.1.3 Dose ‘Quadrant’ Distribution

The method of obtaining MRI cross-sectional images from the gel flasks is briefly detailed in section 4.6. Essentially, areas from the images are sampled to provide the signal values required to calculate the dose delivered to the gel flask. The gel distribution (strip, cross and more complex distributions) can therefore limit the areas from which signal data can be taken from in the reconstructed MRI image. To compound this limitation, the gels exhibit a heterogeneous quality best described as polymer strands. The ideal flask would contain homogeneous gel from which a true dose signal could be collected. The level of polymer strands present in the gels varied between gel batches and attempts to adjust the manufacture process were continually made to do this. The heterogeneous nature of the gel, and image examples are detailed below. In an attempt to enlarge areas from which data can be sampled, compared with the cross-distribution, quadrant distributions were produced as follows.

The method of delivering the dose distribution is illustrated in Figure [4-48] which indicates the step by step procedure. Again it was important that the final doses delivered were linear and uniform. The method used was analogous to that of delivering the ‘cross’ distribution and consisted of turning the various gel flasks through 180 and 90 degrees in between beam-on deliveries. The individual steps are detailed in Figure [4-48] and were as follows:

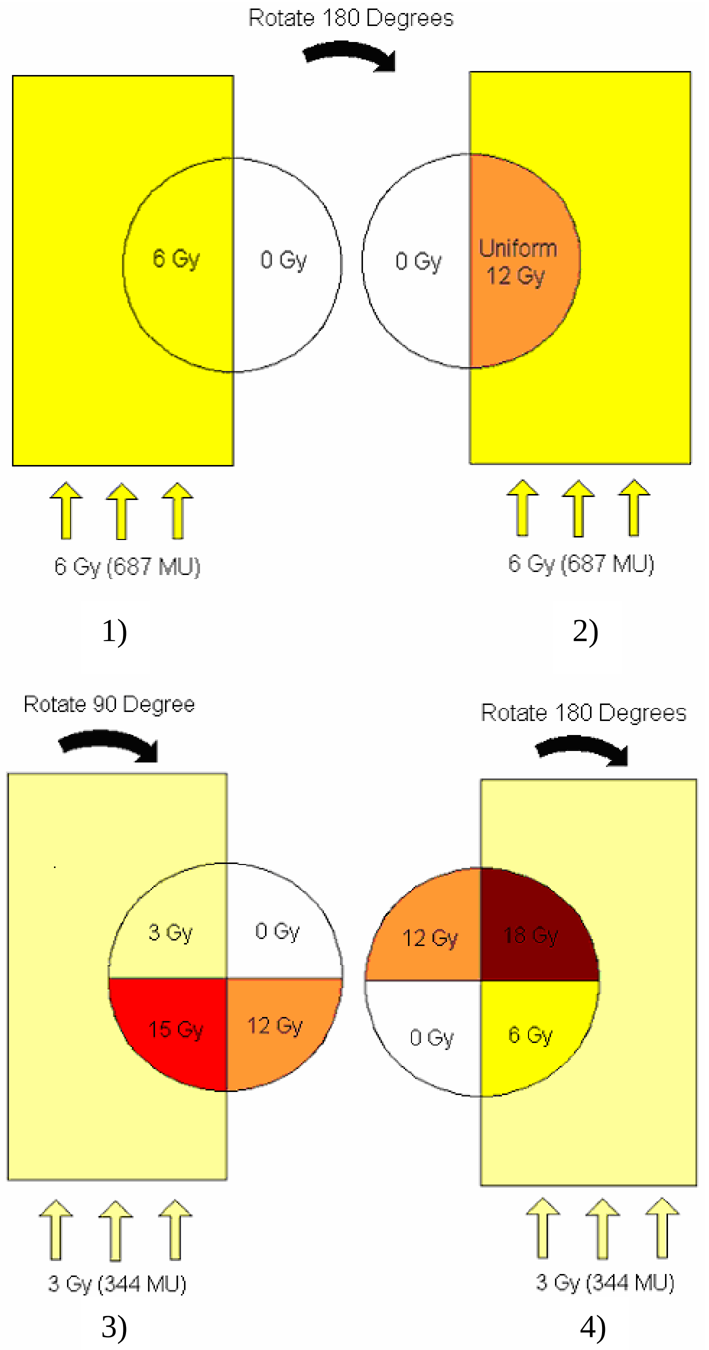

Figure [4-48] Outline for the procedure for delivering a quadrant distribution to a 90 mm gel flask.

1) Initially 6 Gy or 687 MU's (10 x 10 cm field) was delivered to the gel flask on the left hemisphere.

2) The gel flask was then turned through 180 degrees and irradiated again for a further 6 Gy hence resulting in a uniform 12 Gy (orange region) dose having been delivered to the flask.

3) The gel flask was then turned through 90 degrees and a further 3 Gy or 344 MU delivered to the flask.

4) To complete the gel dosing, the flask was turned through 180 degrees and a final 3 Gy was delivered to dose a uniform 6 Gy onto the previous 0 and 12 Gy regions.

Therefore the resulting distribution consisted of final doses of 0, 6, 12 and 18 Gy being delivered to the individual quadrant of the 90 mm diameter gel flask.

The next chapter describes the results of using the optical tomography scanner to assess these various dose distributions.

Chapter 5 Tomographic Imaging Results

5.1 Optical Tomography Scanning Results

In order to generate accurate 3D gel images using the optical scanner, the optical scanner itself was evaluated to determine its ability to scan and reconstruct solid objects of known dimensional complexity. This yielded simplified binary reconstructed images (i.e. black and white), in contrast to that expected for varying degrees of attenuation (i.e. from a MAGIC gel flask). This method also allowed the physical mechanisms involved in acquiring projection data from the optical scanner to be assessed.

5.1.1 Single Absolute Cylinder Attenuator

The details of the scanning process given in the previous chapter provided experimental information regarding the reflective and refractive nature of light at optical interfaces. As a reminder, Figure [5-1] summarises the scanning geometry for acquiring projection data from an object of interest, for example a cylinder.

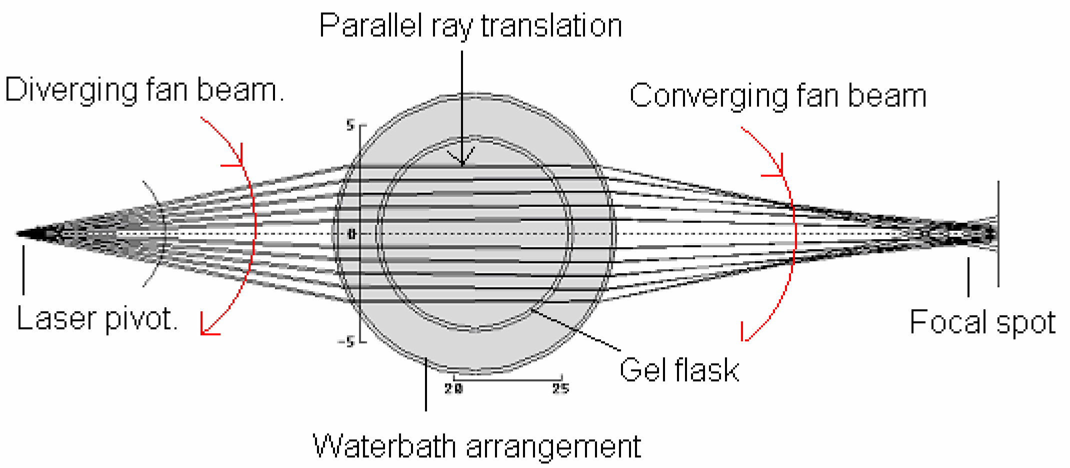

Figure [5-1] Scanning geometry showing the optical ray paths from the laser source to the detector when the laser is rotated through a range of angles. The rays make a parallel translation through the waterbath and sample vessel and converge to a focus on emerging. All units are in cm.

The ray tracing software allowed extensive modelling of the ray paths within the waterbath arrangement. This allowed all the system parameters to be varied and ultimately refined enabling accurate assessment of the main parameters to be made. Thus the desired ray path was derived for varying interface curvatures, impedance matching solutions, glass thickness, and component diameters.

It should be understood that at present all optical tomography scanners developed for gel dosimetry have the same rectangular scanning geometry, unlike the cylindrical configuration presented in this thesis. Both scanner geometries and the resultant reconstruction accuracies are limited by reflection and refraction effects inherent in the optical interactions of the probing laser beam with the glass interfaces in the system. In the original optical scanner developed by Gore (Gore *et al.*, 1996) the useful region of a cylindrical vessel that could be scanned was limited to 90 % of its diameter. Obtaining projection data from beyond this would yield artefacts and reconstructive flaws due to acute beam loss at high incident angles on curved interfaces at the flask extremes. This effect is shown in section 4.3.3 in Figure [4-19].

To accurately reconstruct a tomographic image, both real and Radon space must be accurately sampled between 0-180^0. The level of interrogation within the 0 – 180^0 range will ultimately determine the fine detail of the reconstructed tomographic image. For example, projection data might be obtained from 1, 2, 5 or 10 degree intervals.

The following describes the experimental arrangement, the metallic cylinder used as the object to be reconstructed and the subsequent projection traces of a gel flask with and without the cylinder present.

The metallic cylinder used for the initial experimental validation exercise is shown in Figure [5-2]. Here the 15 mm diameter cylinder was positioned centrally within a large optical friendly gel flask and waterbath arrangement.

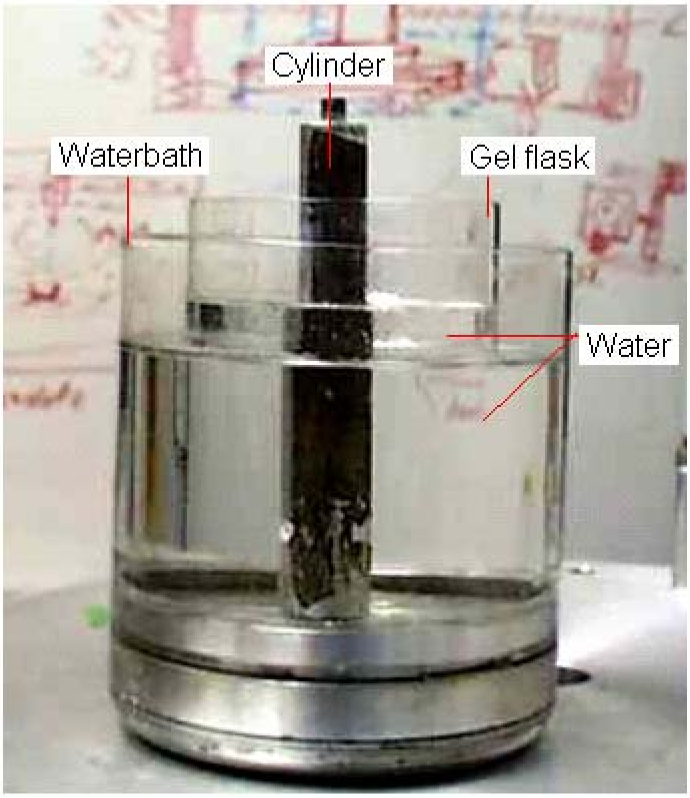

Figure [5-2] A photograph showing the waterbath, gel flask and cylinder used to evaluate the reconstruction methodology. A metallic cylinder was imaged to provide a binary data set and therefore a black and white reconstructed image.

The positioning of the waterbath within the optical scanner and the peripheral instruments are shown below in Figure [5-3]. For this early experiment a large area photodiode detector (S-2387-1010R, Hamamatsu) with a 10 mm^2 active area was used prior to being replaced by an integrating sphere, as discussed in the previous chapter. The directly transmitted and scattered laser light was focused onto the active area of the detector to provide the required attenuation data for tomographic reconstruction of the cylinder.

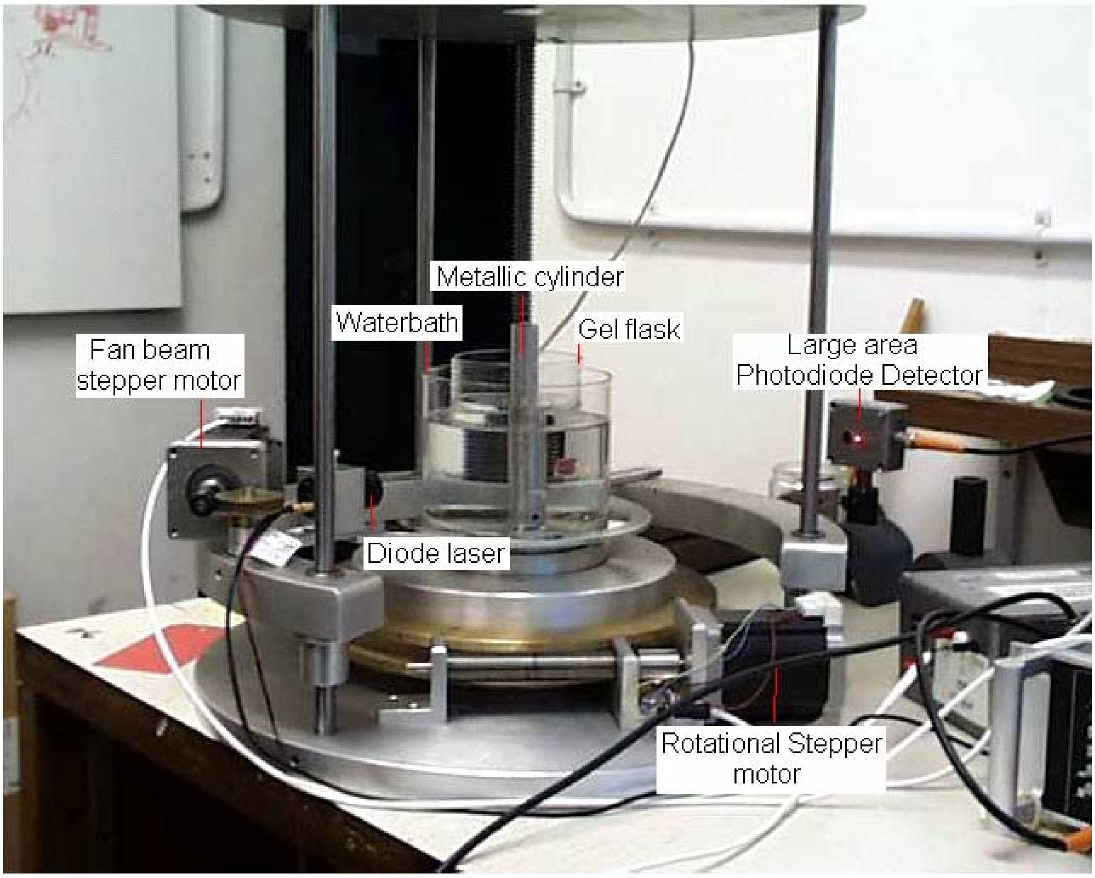

Figure [5-3] Photograph of the experimental setup showing the waterbath and metal cylinder *in situ* prior to image acquisition.

To assist the operator during scanning operation, the photodiode detector signal was displayed simultaneously on a computer screen. The software control program for this is described in Appendix B. A screen capture is shown in Figure [5-4] that shows the precise orientation of the scanner in terms of the scanning height (mm), scanning rotation (degrees) with respect to the start position (0 degrees), exact fan beam sweep orientation (no. of steps) and the optical detector output voltage (Data). An unattenuated fan beam projection (i.e. no cylinder present in the waterbath arrangement) is shown as is a ‘top hat’ distribution.

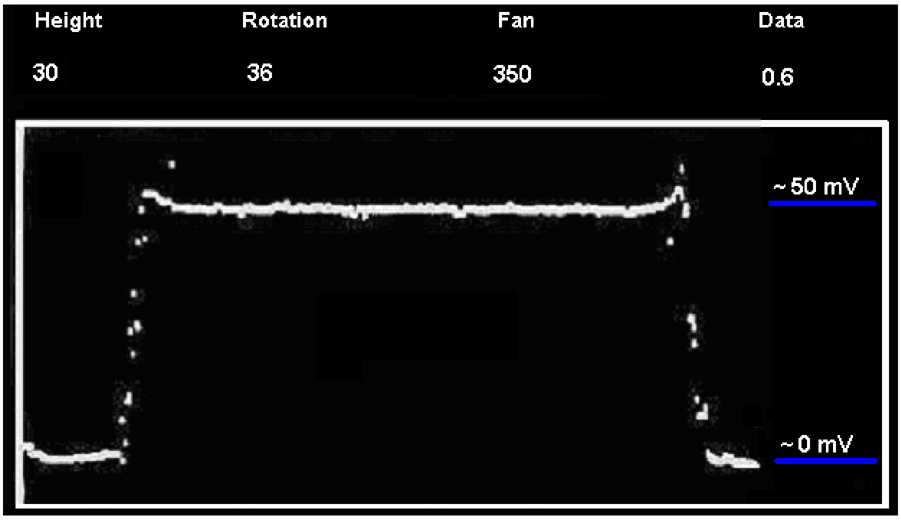

Figure [5-4] A typical display screen image showing a scanning projection of a gel flask containing water only. The fan beam scanning is shown moving left to right on the screen display. The unattenuated (upper plateau) voltage values are approximately 50 mV compared to the attenuated values of approximately 0 mV. The readings did however fluctuate around the zero value with 0.6 mV shown here corresponding to the far right reading.

The unattenuated readout trace shown in Figure [5-4] specifies that the scanner is at 30 mm above the zero start height, is collecting projection data from 36^0 with respect to the start position and the detector signal recorded at the end of the 350 step projection trace is 0.6 mV.

The low voltage regions that can be seen at the scanning extremes are due to the finite size of the detector that was used for the initial data collection. The photodiode detector in these early scanning experiments was positioned at the effective beam focal point to the right of the scanner as shown in Figure [5-3]. A large area photodetector with a long response time was used to collect the transmitted laser beam. The detector was positioned centrally on the optical axis and the laser beam can be seen clearly on the active area. Due to the cylindrical nature of the scanning design the refractive and reflective properties of the system produce an imperfect spot that under certain conditions can exhibit a degree of spot wander during the scanning motion of the laser beam. This can be visualised by considering that at the beginning of the scan the beam spot is just to the left of the active area, and during scanning moves very slightly to the right of the detector. Therefore the laser beam is not incident upon the detector's active area at the extremes and as a result, low voltage values are recorded. This can be corrected to some extent by varying the detector distance from the source and in essence positioning the detector at an improved focus. This however could never really be fully achieved because of the imperfections in the glassware of the system together with the small area detector used. Hence, certain trade offs had to be made.

Figure [5-5] shows the resulting laser beam attenuation when the cylindrical metallic object seen in Figure [5-2] was placed in the gel flask.

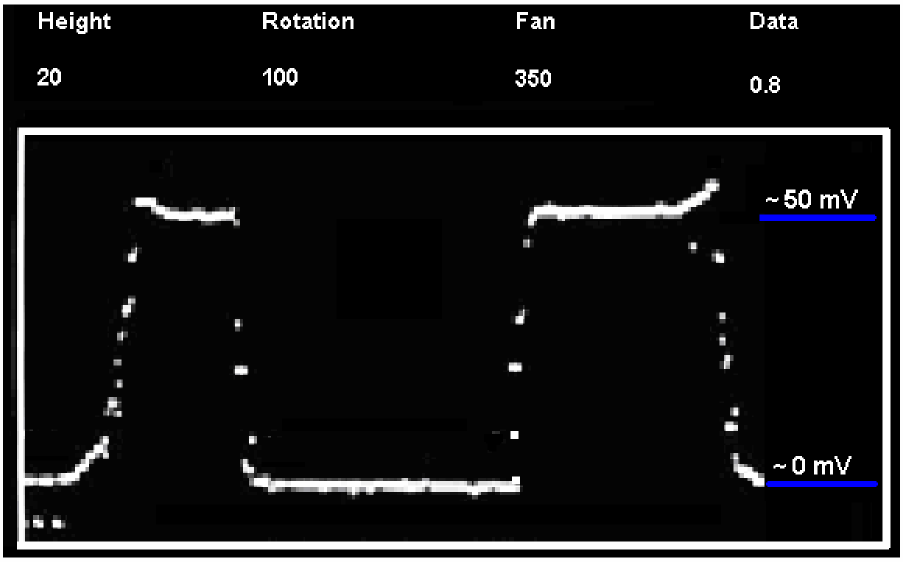

Figure [5-5] Attenuated data projection with the steel cylinder as the object in the gel flask. The trace illustrates that the passage of the laser beam is blocked by the cylinder so the detector does not record a corresponding signal voltage. The detected voltage values for the upper unattenuated region shown here is approximately 50 mV compared to 0 mV (0.8 mV shown above) at the baseline.

The method of data acquisition and subsequent data manipulation used to deal with these scans was described in the previous chapter. To successfully reconstruct a 2D image from a series of 1D projections, a 2D Fourier space has to be sufficiently sampled prior to image reconstruction. This is achieved by acquiring projection data from 0 to 180 degrees.

The scanner was designed and developed to fully sample (user’s discretion) the 2D Fourier domain during the scanning process. The collection of 2D projection data sets acquired is called a sinogram and can be visualised in a 3D mesh graph produced in Matlab. Figure [5-6] shows the full experimental projection data set obtained from an optical scan of the metal cylinder. Projection data was acquired from scanning between 0 to 360 degrees. The x axis (elements within the projection) and y axis (period of projection rotation) represents the physical dimensions of the scanned field of view (250 elements per projection were sampled) and the z axis (transmission intensity) indicates the transmitted laser light detected during scanning. Note here the sinogram was produced from another scan of a cylinder that was positioned off centre. This is to emphasise the sinusoidal structure of the data projection set. If the cylinder was positioned centrally on the scanning axis, the subsequent sinogram would be a straight edged trough that would be repeated during the scanning data acquisition. The physical dimension of the cylinder used determines the trough width.

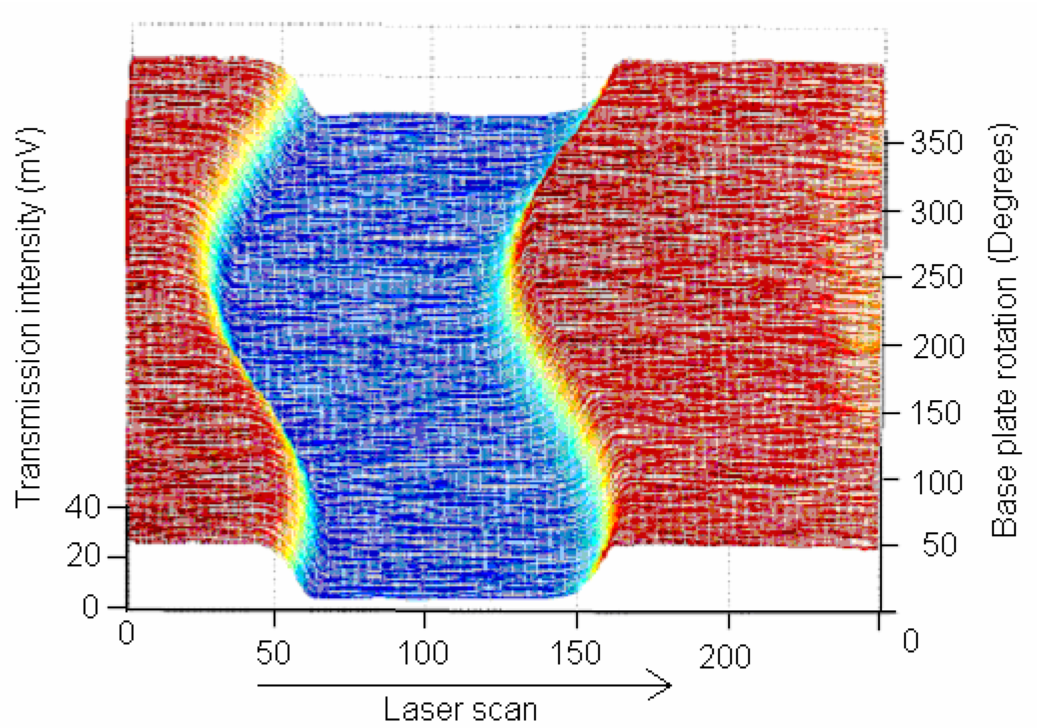

Figure [5-6] A 3D mesh figure showing the full sinogram projection data obtained from optically scanning the metal cylinder shown in Figure [5-2]. The laser scan was set to acquire 250 elements per projection (x-axis) whilst scanning through one revolution i.e. between 0 and 360 degrees (y-axis). The base plate was rotated at 10-degree intervals shown on the right hand side. The differences in transmitted intensity are shown on the z-axis on the left indicating both attenuated and unattenuated values ranging from 0 to 40 mV respectively.

A single projection taken from the sinogram shown in Figure [5-6], (i.e. projection 1 at the bottom of the image) represents the same data shown in the screen capture in Figure [5-5]. Here the red plateau represents zero signal attenuation and the blue trough the attenuated signal caused by the metal cylinder. The sinogram is built up during the accumulation of projection data obtained at advancing degrees of scanning rotation.

Figure [5-7] illustrates an alternative image representation of the sinogram clearly indicating the cross-sectional dimension of the cylinder. This therefore represents the full projection data set obtained from the optical scanner.

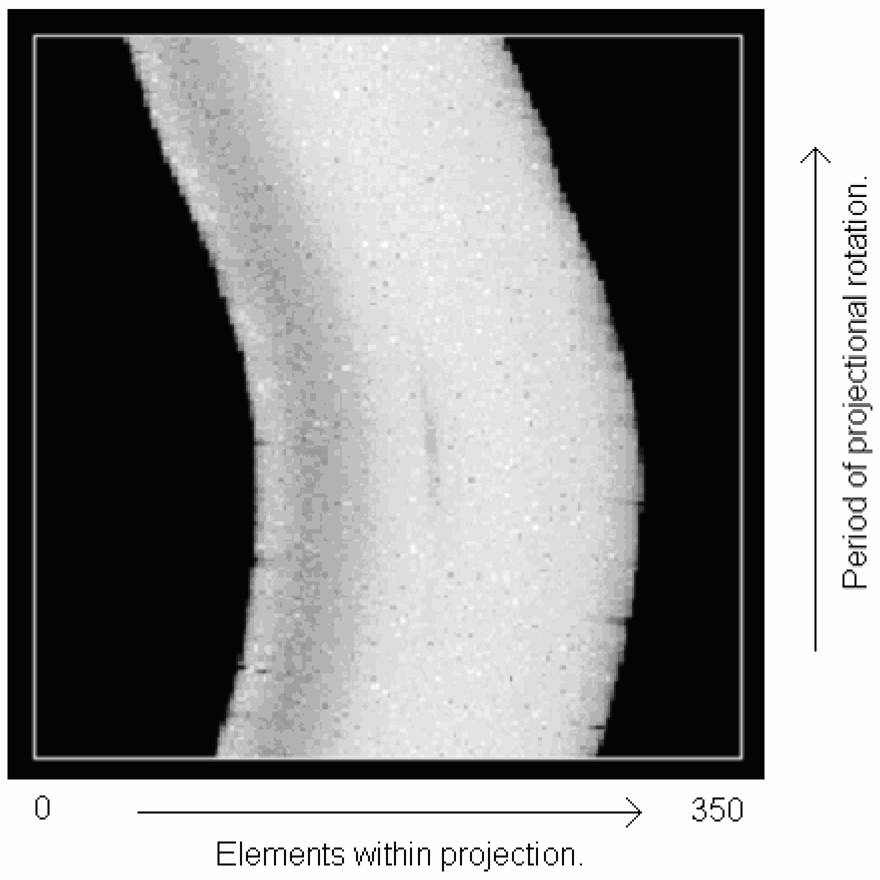

Figure [5-7] Alternative sinogram obtained from a cylinder projection data set showing the corresponding elements within the projection and the period of rotation during scanning. Here the image has been inverted showing the unattenuated voltage signal in white and the attenuated signal in black.

The 2D data set was then reconstructed within Matlab using the *Iradon* function (detailed in Appendix C) using the approach discussed in Chapter 3.

Figure [5-8] shows the reconstructed cross section of the cylinder.

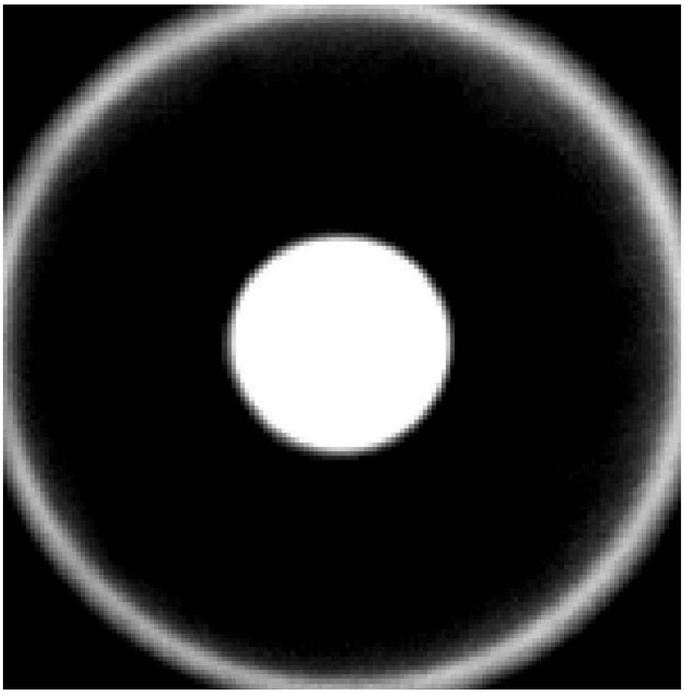

Figure [5-8] The 2D cross section of the 15 mm diameter cylinder reconstructed from the scanner data using the Iradon function within Matlab.

The cross sectional image shown in Figure [5-8] demonstrates capability of the optical scanner in reconstructing images from data collected from total attenuators.

However, useful as it is to analyse 2D image planes, it is the ability to acquire a full 3D projection data set over a region of interest that is required for a full assessment in gel dosimetry. In this circumstance, once a 2D scan has been completed, the scanner is instructed to vertically reposition the diode laser and acquire another 2D data set. The vertical increment is user defined and here system-limited by the laser beam diameter to 1 mm increments. However, in practice 5 mm increments are generally used initially to limit the time for full 3D data set acquisition and also to limit the amount of data captured. Considerations have to be made regarding the data storage capabilities of the dedicated scanning computer, the ease of manipulating the matrix data (possibly 500 by 180) and transferability of this data into Matlab in a form that provides the maximum efficiency in reconstruction.

The simplest method found to reconstruct 3D images of the scanned object was to export 2D planar images from Matlab into IRIS, a 3D rendering software package. The 3D image shown in Figure [5-9] was created in this way by interpolating between 2D planar images reconstructed from data acquired from the optical scanner. IRIS allows the user to re-orientate the 3D image and allow a full assessment of the volume to be made. It is also evident that a good representation of the cylinder has been obtained using data obtained from the optical scanner.

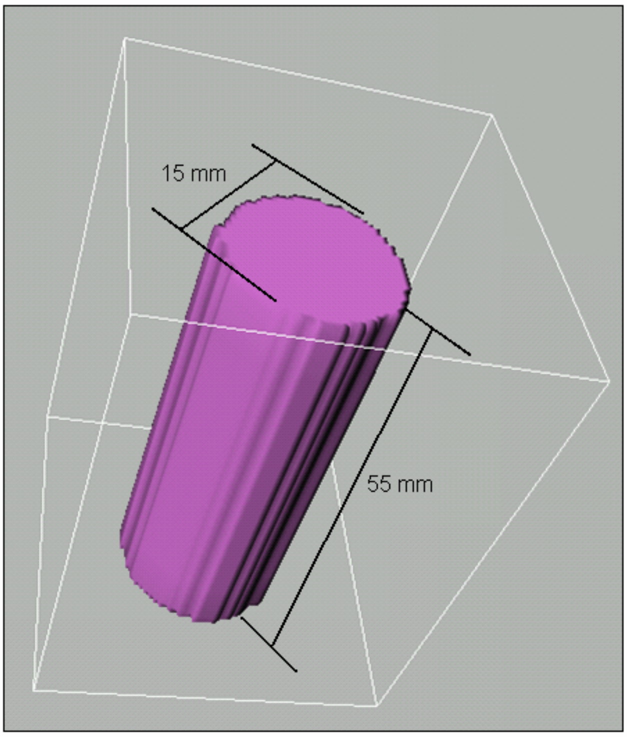

Figures [5-9] A 3D representation constructed from a series of 2D planar attenuation maps acquired from the 15 mm diameter steel cylinder over a 55 mm vertical region of interest. The 3D image was formed by interpolating the 2D data sets with the IRIS image rendering software.

This early capability to image absolute attenuators was the first pre-requisite achievement required before fully investigating an optically scanned volumetric treatment plan with varying attenuation levels. This remains the goal of this research.

5.1.2 Tomographic Imaging Capabilities

The scanning and image reconstruction methods were successfully tested on a steel cylinder as demonstrated in the previous section. To further assess the reconstructive ability of the optical scanner, investigations were then carried out on various objects of more complicated form. These took the form of a 2 mm Allen key and a 9 volt battery, the latter providing a test of reconstructing a non-symmetrical object. A further test was made on reconstructing the cylinder and 9 volt battery placed in close proximity to one another

5.1.2.1 Scanner Resolution

The resolution of the scanner is limited by a number of factors. These include the laser beam diameter, the number of elements per projection, the number of projections, the photodetector response, the acquisition speed of the lock-in-amplifier, the scanning software controlling the data acquisition and the software driving the reconstruction method within Matlab. Therefore the resolution of reconstructed tomographic images will tend to be limited by the largest of these contributing factors.

In theory the laser beam should resolve objects that are of the same order of magnitude as the collimated 1 mm beam diameter. However the beam undergoes an inevitable expansion during its passage through the optical system due to phase front degradation produced by imperfect optical surfaces of the glassware and spatially varying refractive index regions in the exposed gel.

The ability of the scanner to resolve and reconstruct small sized objects was performed using a 2 mm hexagonal Allen key positioned centrally within the waterbath arrangement. Due to the small cross section dimensions of the Allen key the number of projections was reduced to a value that would provide a comfortable buffer to the attenuated region. This also had the advantage of speeding up the scanning time due to the reduced number of projections. The Allen key was scanned from 0 to 180 degrees with 250 elements per fan beam projection. The resulting sinogram obtained in this way is given in Figure [5-10].

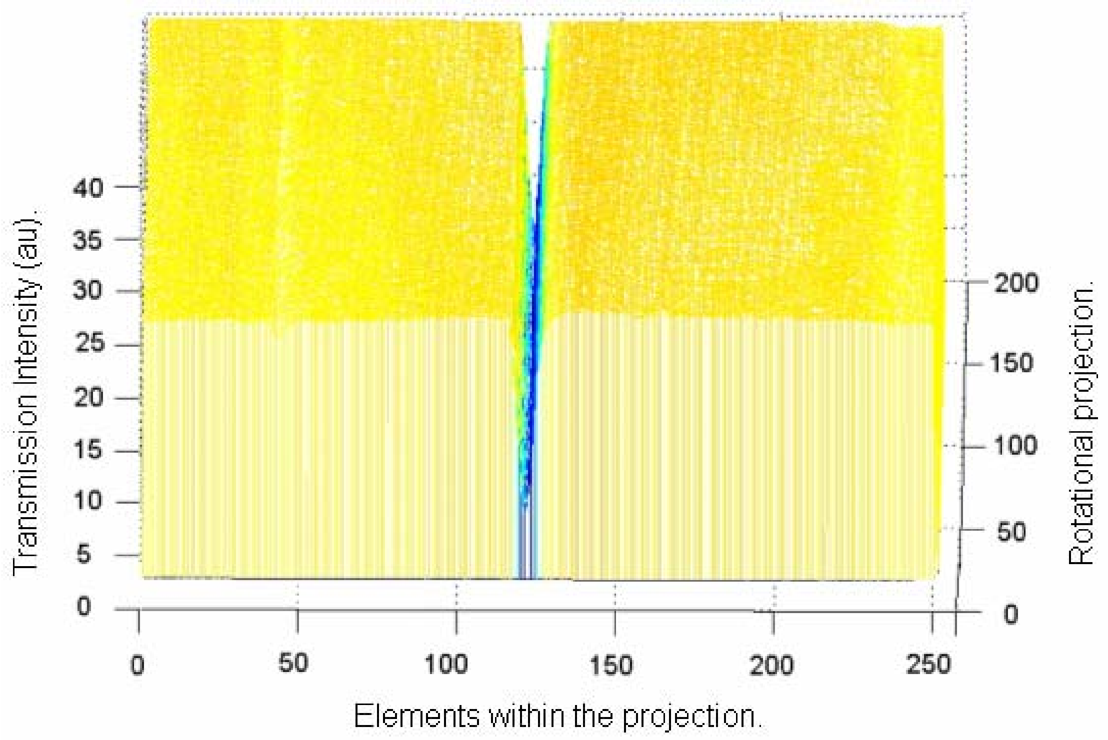

Figure [5-10] The three-dimensional sinogram produced from the attenuated laser light from the centred Allen key.

It is of interest to note that because the Allen key was centred within the projection, the sinogram varies very little unlike the steel cylinder illustrated previously where a more recognisable sinusoidal tracing was formed because it was placed off-axis.

The two dimensional data array captured by the optical scanning was reconstructed *via* the method described above using the *Iradon* transform function within Matlab.

The reconstructed image of the Allen key and the degree of imaging accuracy available from the scanner is illustrated in Figure [5-11]. The resolution of the scanner is such that the hexagonal shape of the Allen key cross-section can be recognised.

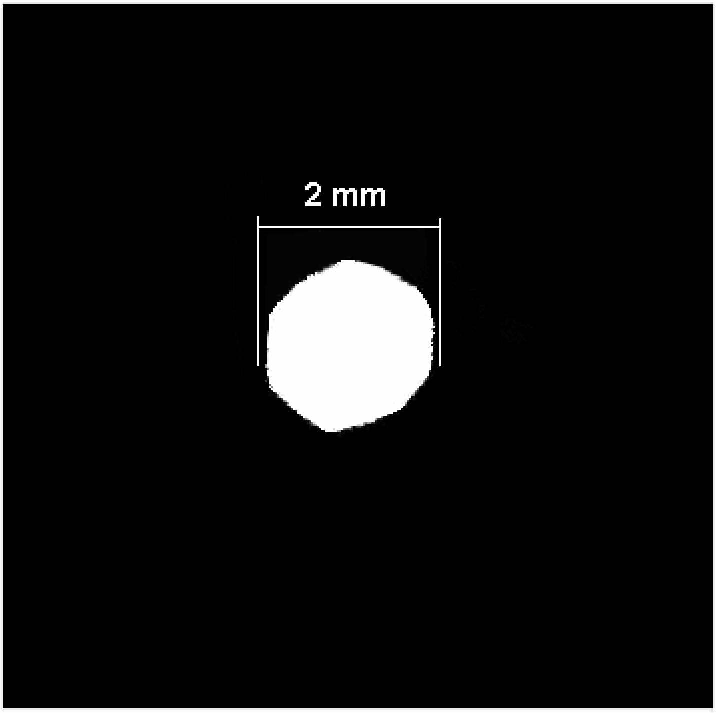

Figure [5-11] A cropped 2D reconstruction of a 2 mm Allen key clearly revealing its hexagonal cross-section.

To test the scanner ability to reconstruct other non-circular cross sections a rectangular 9 V (10 x 20 mm) battery was positioned within an optical flask filled with water. The scanner was set to acquire projections from 0 to 180 degrees with rotation intervals of 1.8 degrees, thus providing 181 projections for image reconstruction. The reconstructed raw image of the battery is given in Figure [5-12].

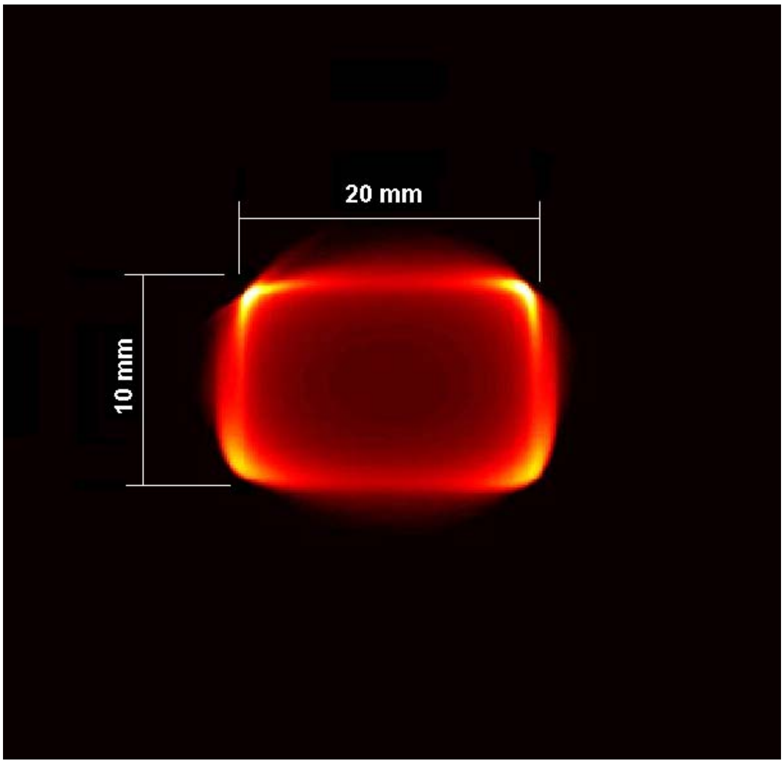

Figure [5-12] An unprocessed reconstructed tomographic 2D image of a 9 volt rectangular battery.

It can be seen that the cross-section is essentially rectangular though the image has certain flaws, notably that the opposite sides are not quite straight and parallel. Although this type of battery does have rounded corners, these are somewhat exaggerated by the reconstructed scan.

Although the ability of the scanner to resolve single objects was successfully tested, the next logical test was to assess the scanner's ability to reconstruct two solid objects positioned in the waterbath in close proximity. This was tested using both the previously imaged battery (see Figure 5-12]) and metallic cylinder (see Figure [5-8]). Figure [5-13] shows a) the positioning of the objects, b) the resulting sinogram, c) the reconstructed cross-section using the basic imaging method and d) the cross-section obtained from the method used to show small changes in detected signals. The reconstruction methods used are described in section 4.5.3.2 and syntax described in Appendix C.

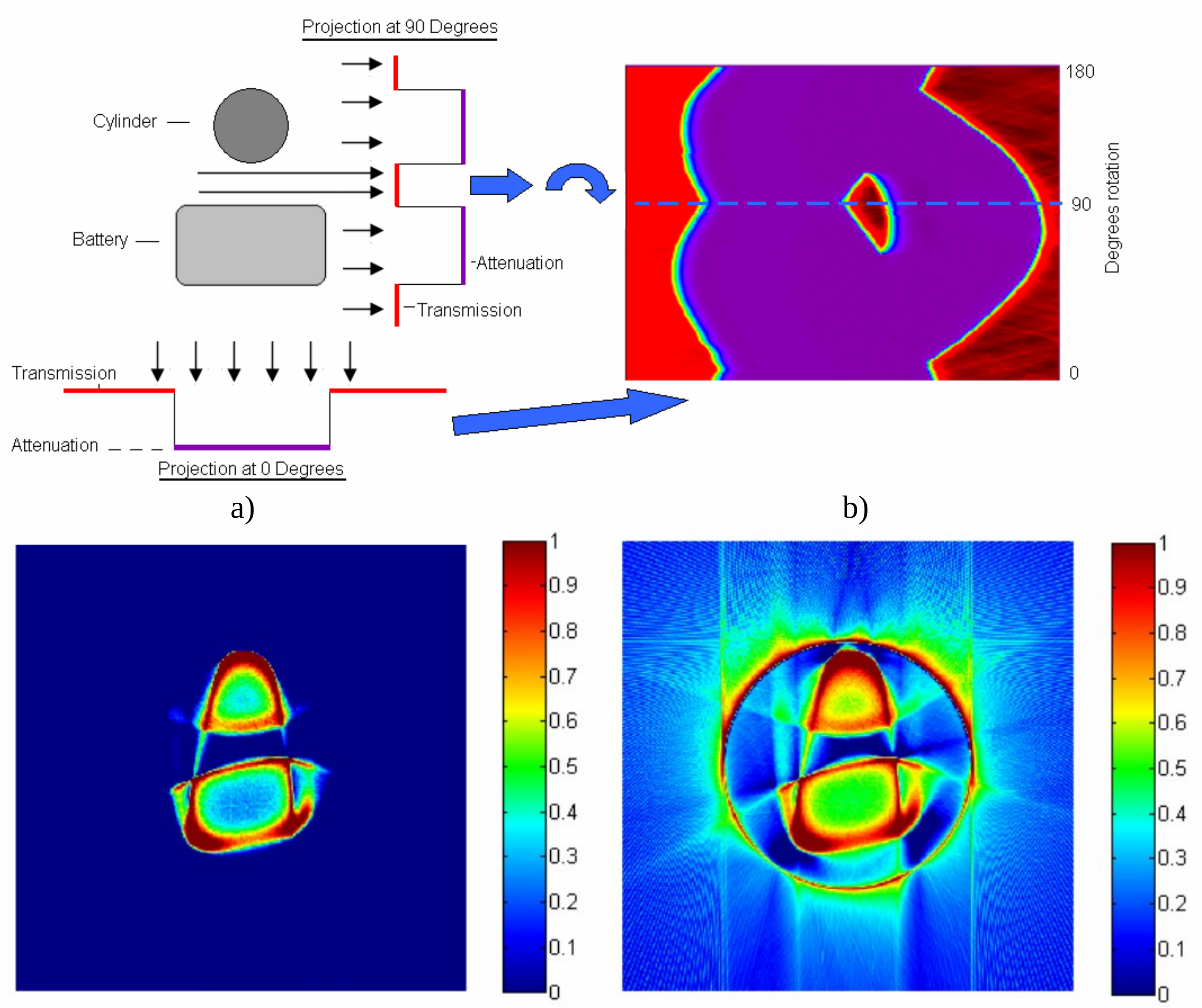

a) b)

c) d)

Figure [5-13] A sketch of both the cylinder and battery cross-sections with their corresponding projections at 0 and 90 degrees are shown in a), the resulting raw data sinogram from the 0 to 180 degree image scan is shown in b), the reconstructed images produced by method A and method B are shown in c) and d) respectively.

It was found that taking logarithms of the raw data provided greater fine detail in the reconstructed images unlike the basic method of back-projecting the raw data with the *Iradon* transform without further data manipulation. However it was found there was no clear advantage to using either method when reconstructing solid objects. This is shown in c) and d) in Figure [5-13] whereby both methods have produced the same basic cross-sectional images. Additional data manipulation is required when reconstructing data obtained from objects with varying attenuation values other than the binary result from solid objects. However, both methods are unable to accurately separate both objects and reconstruct the sketch shown in a). To overcome this, a larger data set with additional interrogation may be required to improve image resolution on reconstruction. In addition, further data manipulation could be required to improve the accuracy of the image.

5.1.2.2 Image Artefacts

Figures [5-14] and [5-15] provide examples of possible image artefacts that may arise in optical tomographic reconstruction as a direct consequence of beam wandering leading to undetected laser light. Here a pencil was scanned and its cross-section reconstructed. Figure [5-14] shows, a), the projection sinogram obtained from the scanner whilst using the 10 mm^2 large area detector (S-2387-1010R, Hamamatsu), and variation to the projection data (b - d) taken during the sinogram acquisition.

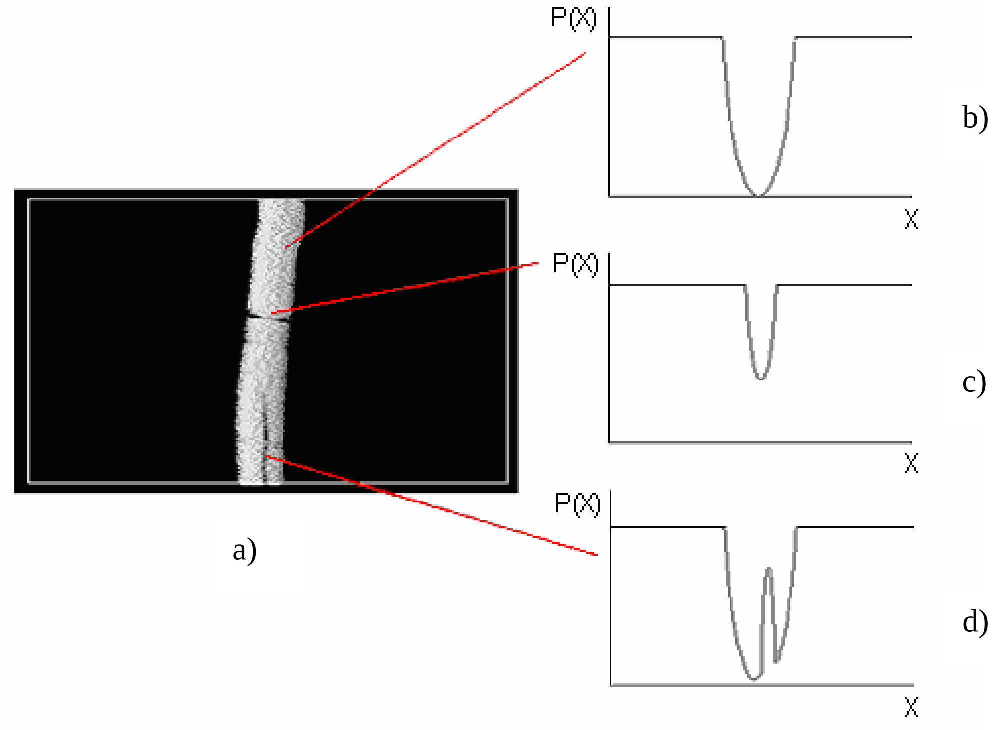

Figure [5-14] Illustration of a) the projection sinogram of the pencil with inherent artefacts and b-d) a representation of the possible attenuation profiles produced by beam wander during the scanning process.

The pencil should, like a metal cylinder, act as a total attenuator of the laser beam, therefore producing a binary reconstructed image. In the sinogram shown in Figure

[5-14] there are regions of varying attenuation shown as darkened regions that imply that light has been detected during this period of scanning. This could be due to a combination of both scattering and refraction of the laser beam around the pencil cross-section within the water or possibly *via* the glass interfaces of the waterbath and gel flask essentially trapping the light and transferring it to the rear of the scanner where it is detected. Three elements of the sinogram have been selected and their corresponding projection distributions shown on the right hand side of Figure [5-14]. The top image, b), shows a satisfactory projection indicating the total attenuation of the laser beam during the fan beam translation. The central projection, c), shows a small region where there is higher transmission than expected; this may be a result of processes previously described including beam wander and refractive processes within the water phantom arrangement. The final image, d), shows an extended region where the transmission within the scan has been increased due to the beam wander possibly due to glassware imperfections. The reconstructed image with inherent artefacts is illustrated in Figure [5-15].

Figure [5-15] Reconstructed cross section of a 7 mm diameter pencil illustrating the possible image artefacts originating from optical tomography.

The correctly reconstructed cross-section of the pencil is shown in Figure [5-16] obtained from the same optical scan whilst using the integrating sphere and BPX-65 detector combination. This method widens the effective detection port from 10 mm^2 to a 25 mm diameter aperture and thus reducing the effect of beam wander.

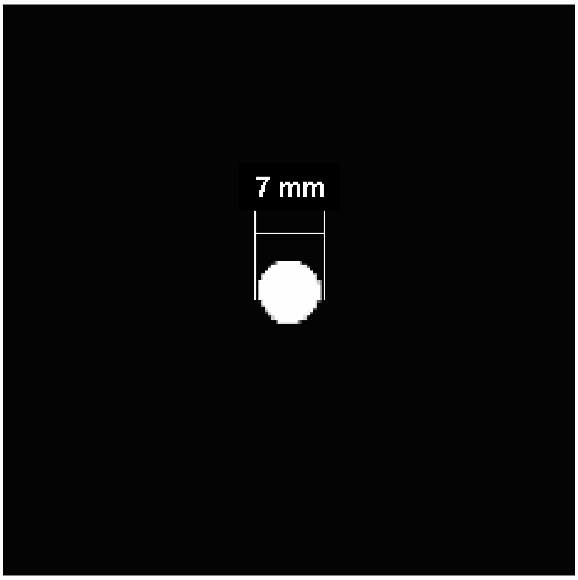

Figure [5-16] Reconstructed cross-sectional image of a pencil obtained by replacing the 10 mm^2 detector (S-2387-1010R, Hamamatsu) with the integrating sphere and BPX-65 detector combination. Here the effect of beam wander and loss of transmission signal is reduced. This therefore allows a representative image to be reconstructed.

5.1.3 Optical Tomographic Gel Images

The examples in the previous section essentially validate the method for reconstructing 2D attenuation images of solid objects. The following results illustrate the natural progression from total attenuators to dosimeter gels where varying levels of absorbed dose produce a graded variation in the opacity. Initially these optical tomography experiments were limited in their usefulness by the poor optical quality of the glassware used for the gel flasks as discussed in Chapter 4.

The following images show the reconstructed gel cross-sections obtained from data collected by the optical scanner. A number of images are provided from a number of gel batches all having been irradiated with the cross distribution (see section 4.7.1.2). The distributions produced exhibit varying dose regions, unlike the previous total attenuation examples. Both Matlab methods with differing amounts of data manipulation will be compared. Figure [5-17] shows the reconstructed ‘cross distribution' from Batch 13 obtained from using the basic gel flasks with optical imperfections (see section 4.3.1). The distribution contained three regions of differing absorbed dose 5, 10 and 15 Gray (Gy).

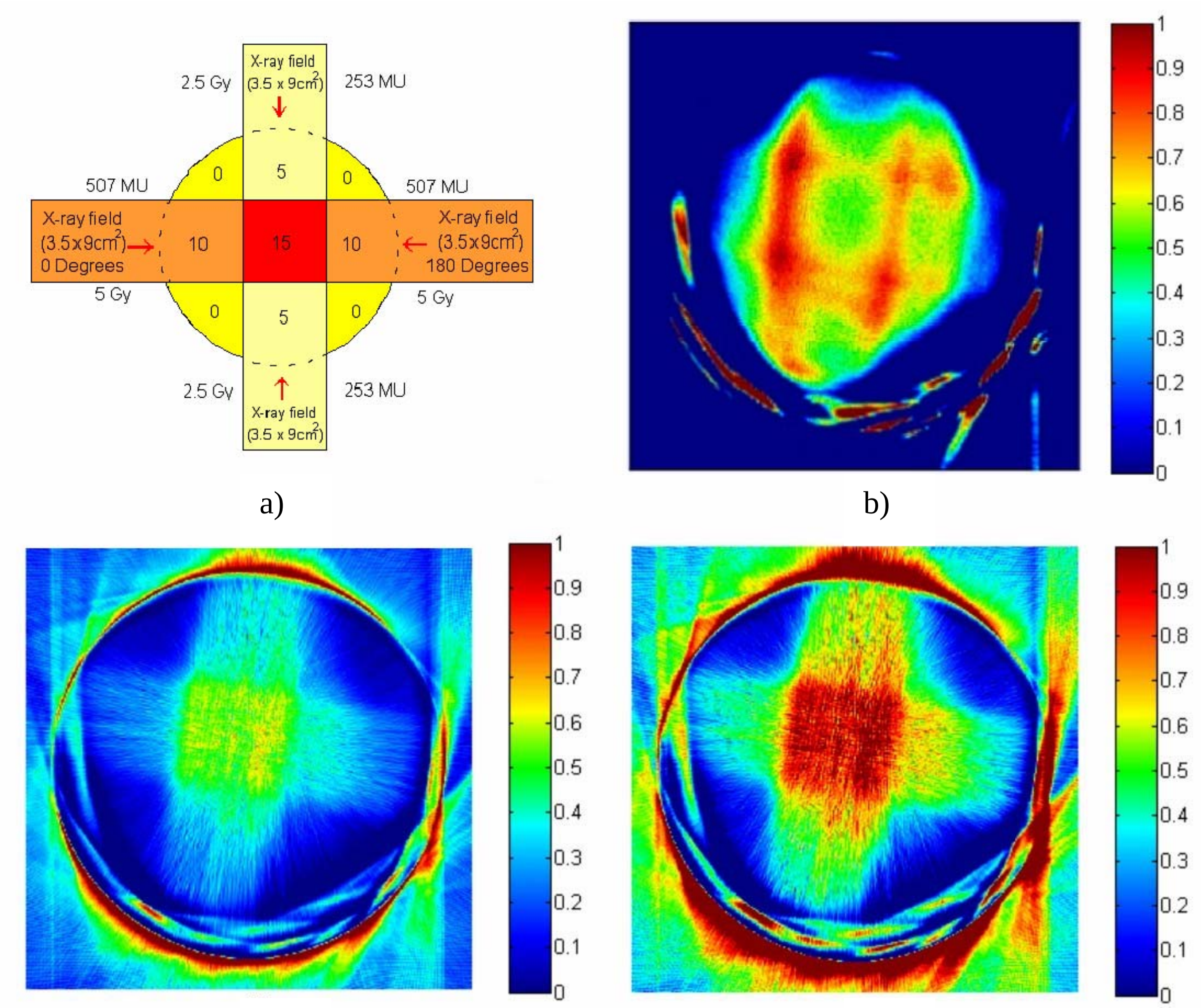

a)

b)

c)

d)

Figure [5-17] Optical tomography reconstruction of the 'cross' distribution produced from dosing Batch 13 as shown in a). The basic reconstruction obtained from the basic method is shown in b) and is accompanied by a legend indicating the relative dose absorbed within the gel flask. Both c) and d) show the reconstructions obtained from using the method that required further data manipulation. Here the details of the 'cross' distribution are discernable when compared to b), but are sill somewhat un-defined. The degree of image intensity can be varied by choosing a different multiplication factor in the Matlab syntax used. Here different values have been chosen to further enhance the central 15 Gy region.

The anomalous result in Figure [5-17b] illustrates the imaging limits of using the simple 'Method A' approach in conjunction with the Iradon function to reconstruct a gel with varying dose levels. Here the reconstructed image bares little resemblance to the cross distribution shown in both c) and d). The central 15 Gy dosed region has been primarily reconstructed at the expense of the fine detail surrounding it at lower dose levels. Thus by taking natural logarithms (‘Method B’) of the projection data effectively rescales the intensity values and allows additional fine structure to be visualised.

The incorporation of optical friendly flasks greatly reduced the amount of scattering experienced by the laser beam during scanning experiments. This reduced variations in the spot size and limited the spot wandering on the active area of the detector. Thus attenuation values obtained for the corresponding line integrals in the gel were more representative of the local dose than obtained in the experiments using the lower quality glass vessels.

The most successful optical reconstruction is seen in Figure [5-18] and was produced from Batch 11 using optical friendly gel flasks. This very clearly shows the ‘cross’ distribution within the gel showing the 5, 10 and 15 Gy regions. In addition when the optical tomography images were compared with the corresponding results obtained by MRI for Batch 11 they were seen to be in good agreement.

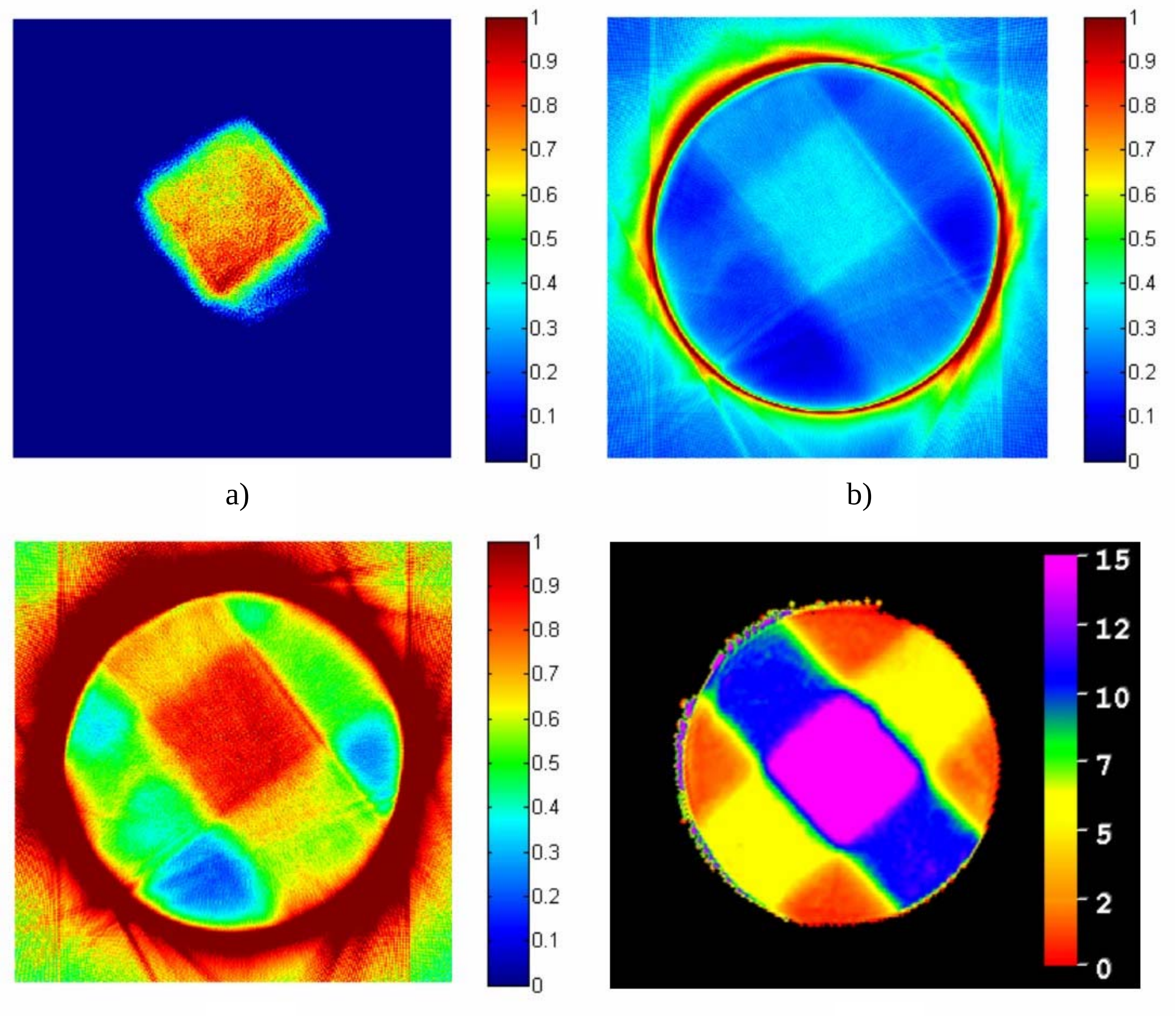

a) b)

c) d)

Figure [5-18] a) showing the reconstructed image obtained from using the less exhaustive method A (see section 4.5.3.2); the central 15 Gy square region can be seen with no indication that a cross distribution was delivered to the flask. b) and c) show the reconstructed images obtain using method B (see section 4.5.3.2) whereby the 5 and 10 Gy areas of the distribution can be distinguished from one another. The full ‘cross’ distribution can be clearly seen. Additional image contrast can be produced by changing the scaling factors used in the Matlab syntax. Here the lower dose regions of the cross can be clearly seen above the un-irradiated background. d) shows the corresponding MRI image with the legend showing the calibrated dose absorbed from 0 to 15 Gy.

The reconstructed 2D cross sections were then interpolated and rendered to form a 3D dose distribution using the IRIS software. The results are seen in Figure [5-19].

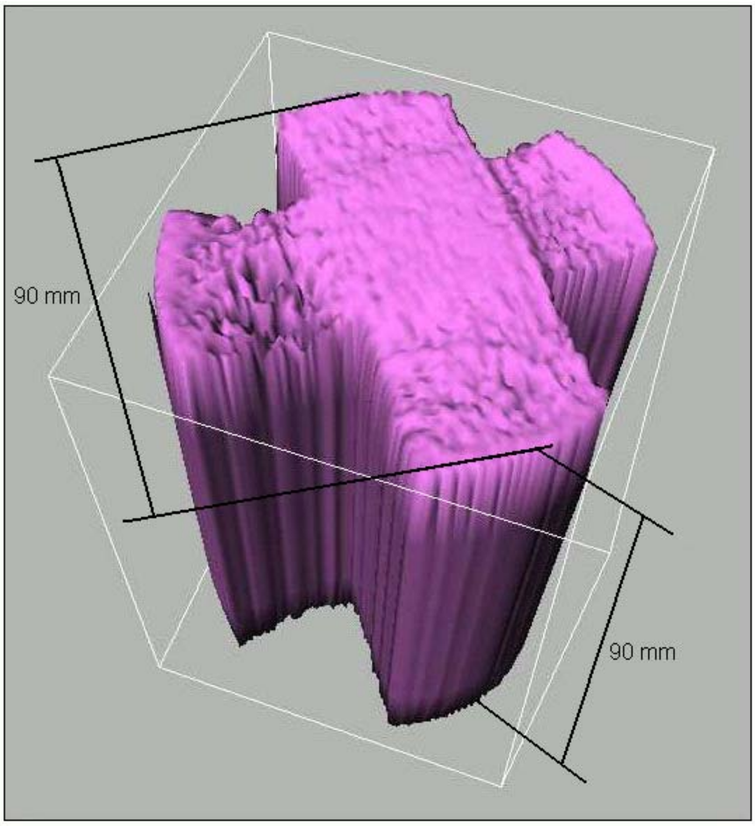

Figure [5-19] The 3D representation of the dose varying ‘cross’ distribution formed in Batch 11 gel from a 90 mm diameter optical friendly gel flask. 2D optical tomography images were collected from over 90 mm within the flask, stacked and interpolated with imaging software IRIS to render the 3D image.

These early attempts to obtain optically reconstructed gel images that could be effectively compared with MRI imaging were encouraging. However the fundamental inability of the scanner to image gels containing regions of high dose (opacity) over large path lengths within large gel flasks was a limiting factor. A number of scanning parameters like the scanning speed of the laser beam, the detection rate of the lock-in-amplifier and the degree of projection sampling can affect the outcome of tomographic reconstruction. Varying the rate of data capture can have a significant influence on the image clarity and resolution. Figure [5-20] illustrates this effect.

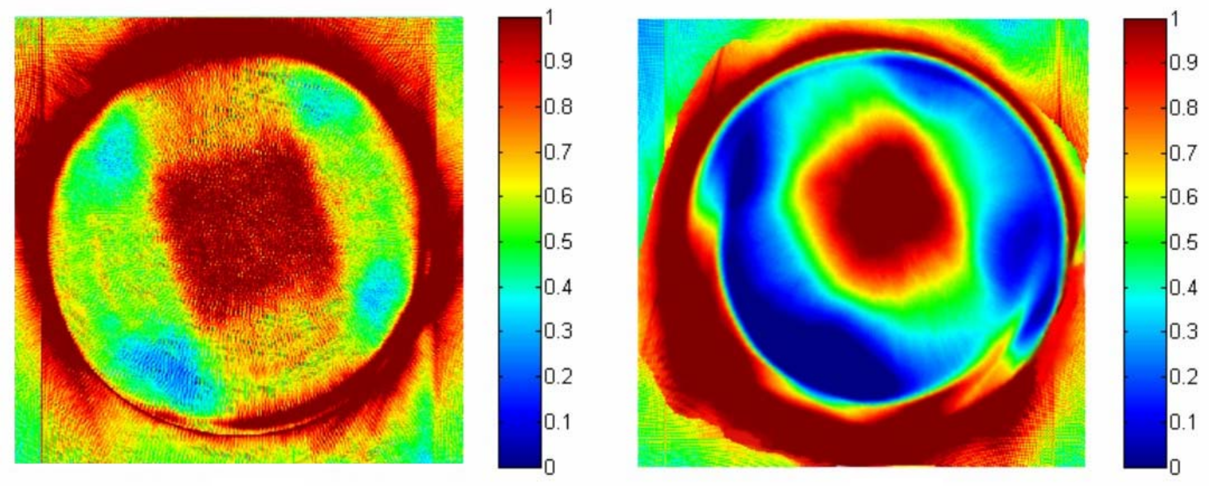

a) b)

Figure [5-20] Reconstructed images of the 'cross' showing how the rate of data capture influences the quality of the image. a) The fast data capture rate collected data every 3 ms and shows the cross details. b) shows the blurred reconstructed image produced from the data collected from the slower data capture rate of 100 ms.

Acquiring data every 100 ms had the effect of smoothing the image and therefore having the effect of losing image resolution. This is due to the slow capture rate of the lock-in-amplifier with respect to the motion of the probing laser beam i.e. the acquisition rate was to slow to collect the required accuracy from the scan. Conversely, the high sampling rate of 3 ms produced images with improved detail but to a higher degree of granularity.

5.1.4 Limitations to Optical Imaging

The following images highlight a limiting factor in using optical tomography for gel dosimeter that related to the exponential attenuation in the Beer-Lambert law. The four uniformly dosed gel flasks (90 mm diameter) shown in Figure [5-21] were irradiated with 4, 8, 12 and 16 Gy doses. The reconstructed images show that with this combination of gel volume and the corresponding attenuation the laser beam was subjected to due the path length, the scanner cannot distinguish doses above 8 Gy from one and another.

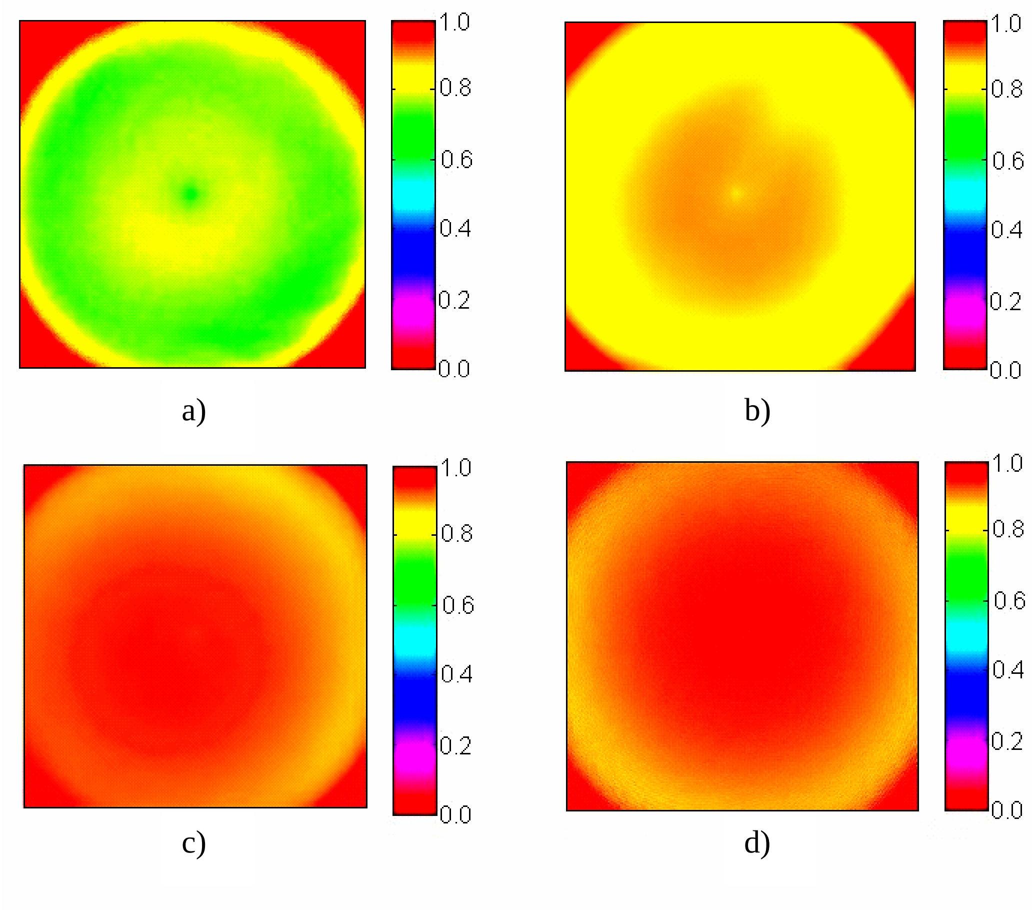

Figure [5-21] Reconstructed optical tomographic images of uniformly irradiated large gel flasks with a) = 4 Gy, b) = 8 Gy, c) = 12 Gy and d) = 16 Gy. The 90 mm diameter flasks attenuate the laser beam to such a degree that when reconstructed, doses above 8 Gy cannot be distinguished from one another. Here, optically, there are no perceivable differences between c) the 12 Gy and d) the 16 Gy gel flasks.

The inability of the optical scanner to accurately reconstruct doses above 8 Gy for this particular dosing experiment, illustrates the limits of the scanning system at present. It is important to consider that the optical scanner had been purposely restricted to a class 1 laser system design. This had the effect of limiting all optical scanning to a laser power output of ≤ 4 mW. Therefore to successfully interrogate large gel flasks when irradiated with uniform doses, see Figure [5-21], a system with a higher laser output power would be required. However in radiotherapy treatments, doses above 5 – 10 Gy would realistically never be required and therefore the need to reconstruct them with optical techniques would be redundant. Realistically, treatments using small radiation doses are more common place requiring doses of the order of 1 – 5 Gy to be delivered.

It is of further interest to have the capability to resolve small dose increments of 0.1 Gy, for example. The optical images previously shown have demonstrated that the scanner can resolve 2 mm objects (see Figure [5-11]) and reconstruct ‘cross’ distributions up to 15 Gy (see Figure [5-18]) and with further research the primary requirement to resolve treatments with small dose increments could be achieved with the optical tomography scanner and the current class 1 system.

To assess this scanning limitation, a measurement of optical opacity of Batch 13 versus dose was made using the 655 nm red diode laser from the scanner. The optical density (OD) was calculated from the ratio of input to transmitted beam intensity I_0 / I using

$$OD = \log_{10}\left(\frac{I_0}{I}\right) \tag{5-1}$$

This is shown in Figure [5-22].

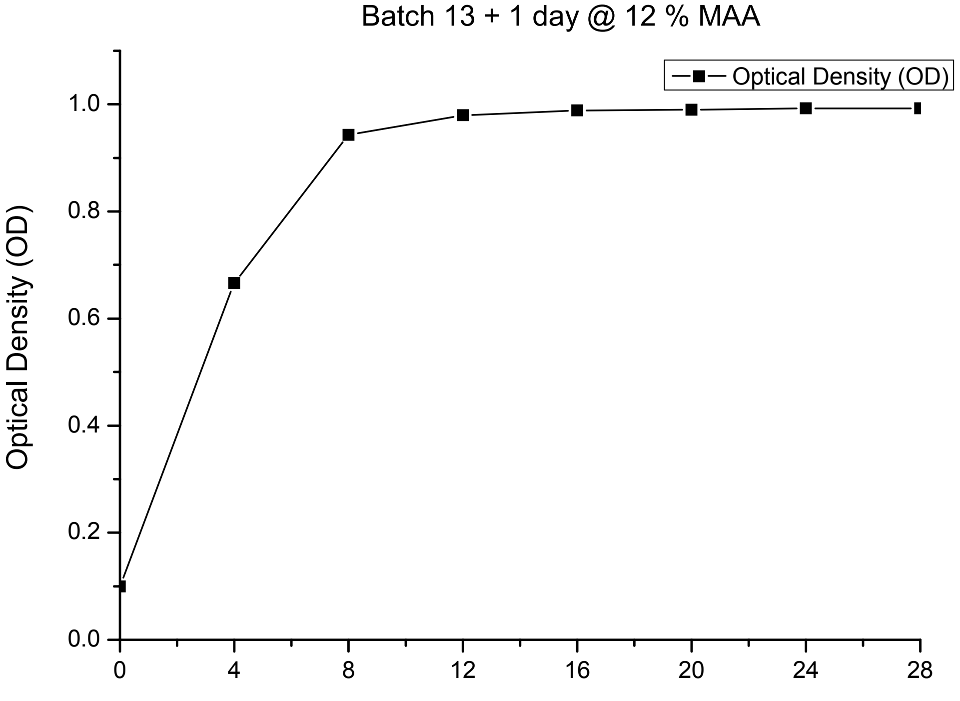

Figure [5-22] The optical density (OD) response of gel Batch 13 versus dose. The plot compares well to the optically reconstructed images illustrated in Figure [5-21]. There is an initial strong response to OD for the dose regions between 0 and 8 Gy. Beyond the 8 Gy region the dose response is negligible and the OD curve forms a plateau.

Figure [5-22] shows that initially there is a good response to the absorbed dose until a plateau level is formed at around 8 Gy. This plateau region indicates that the combination of the dose absorbed and the path length in the gel was sufficient to reduce the transmitted signal to effectively zero. However from a clinical stand-point, it is extremely unlikely that a clinical treatment would require dose levels approaching 8 Gy. Much smaller dose levels are delivered to the patient over a number of weeks. This therefore indicates the optical scanning technique could be utilised for dose levels less that 8 Gy.

5.2 Investigation of MAGIC Gels with MRI

The initial gel dosimetry experiments used the BANG® gel formulations based on the production methods detailed in other papers (Maryanski *et al*., 1994, 1996). However all gel investigations reported within this thesis are for MAGIC gels (Fong *et al.,* 2001) as described in Chapter 3.

Running parallel with the development of the optical scanner for gel imaging was Magnetic Resonance Imaging (MRI) studies provided by Dr G Liney at the Hull Royal Infirmary, Hull, UK. Repeatability measurements allowed a consistent trial and error program of study that enabled MRI protocols to be refined and realised. The majority of the results described in this chapter are fundamentally MRI based and obtained from an established imaging modality.

It was the intention that with further research and development optical tomography could provide a quick and relatively easy method of treatment verification that would alleviate the over-worked MRI facilities.

5.2.1 Gel Repeatability Studies

Running parallel with the development of an optical tomography scanner was the investigation into whether MAGIC gels could be routinely manufactured in a regular laboratory environment then irradiated with a radiation treatment plan and having the capability to successfully reconstruct the dose delivered to the gels with both OCT and MRI. To achieve this goal gel batches were produced on a weekly basis for calibration studies that investigated the gel response to X-ray radiation.

These gel repeatability studies were in effect quantitative feasibility studies into the batch-to-batch properties including baseline opacity, colour, viscosity, gel response, longevity, and gel homogeneity. These gel properties can be significant when considering the nature of imaging the gels with both MRI and especially with OCT as described previously. The repeatability results have been principally derived from MRI imaging with some corresponding OCT examples of the gel batches. The goal was that of routinely producing gel batches with consistent properties that when imaged with both MRI and OCT would provide comparable dose information that would complement one another.

In gel dosimetry there are many variables that contribute to the gel properties and their response to radiation. The manufacture process followed that of Fong (Fong *et al.,* 2001), and although every attempt was made to maintain sample consistency, degree of batch-to-batch variability remained as is reported in the results that follow. Only when unexpected or poor results were obtained was a variable from the process changed in an attempt to improve the gel performance i.e. variability in the baseline polymerisation of the gels (opacity of the gel), the sensitivity of the gel batches and the overall linearity of the dose response of the gels. Additional investigations were also performed on the effect of ageing on the gel sensitivity and response. The change in opacity and copper colouration of the gel (wavelength related optical attenuation) and varying levels of the monomer methacrylic acid (MAA) was assessed to see if this could improve the gel sensitivity and therefore response to X-ray radiation.

Earlier work (Fong *et al*., 2001) had shown that varying the MAA concentration in a gel batch alters its response to radiation via the varying reservoir of MAA available for the polymerisation reaction initiated by the radiolysis of water. During the period of the present investigations the most common quantity of MAA used in gel research was 9 % by batch weight. A concentration of 9 % was therefore selected as the baseline level for repeatability studies. Further to this 12 % and 15 % concentrations of MAA were also investigated.

The ideal properties of a gel dosimeter would be a high response to irradiation and a low level of initial gel opacity, as measured by the intercept on the y-axis of a R2 (s^{-1}) versus dose plot. A ratio that conveniently characterises a gel batch can be sought that effectively relates the batch response to increasing levels of radiation dose (Fong *et al*., 2001); this is essentially the ratio of the gradient to the intercept. Thus the optimum gel batch would have a low intercept and a high gradient providing a high ratio value.

Overall in excess of twenty batches of 9 % MAA MAGIC gels were investigated over an 18 month period. The overall aim, as explained above, was to routinely manufacture gel in a non-specialised laboratory, irradiate them, interrogate the resulting dosing and finally accurately reconstruct the tomographic images showing the initially basic dose distributions leading to more complex treatments.

Figure [5-23] shows the results of the gross repeatability studies for gel batches with 9 % methacrylic acid (MAA). Each batch was consistently imaged with MRI by the method summarised in Chapter 4. Here the ordinate axis gives the spin-spin relaxation rate R2 (s^{-1}) and the abscissa the level of irradiation delivered to the gel batches in Grays (Gy).

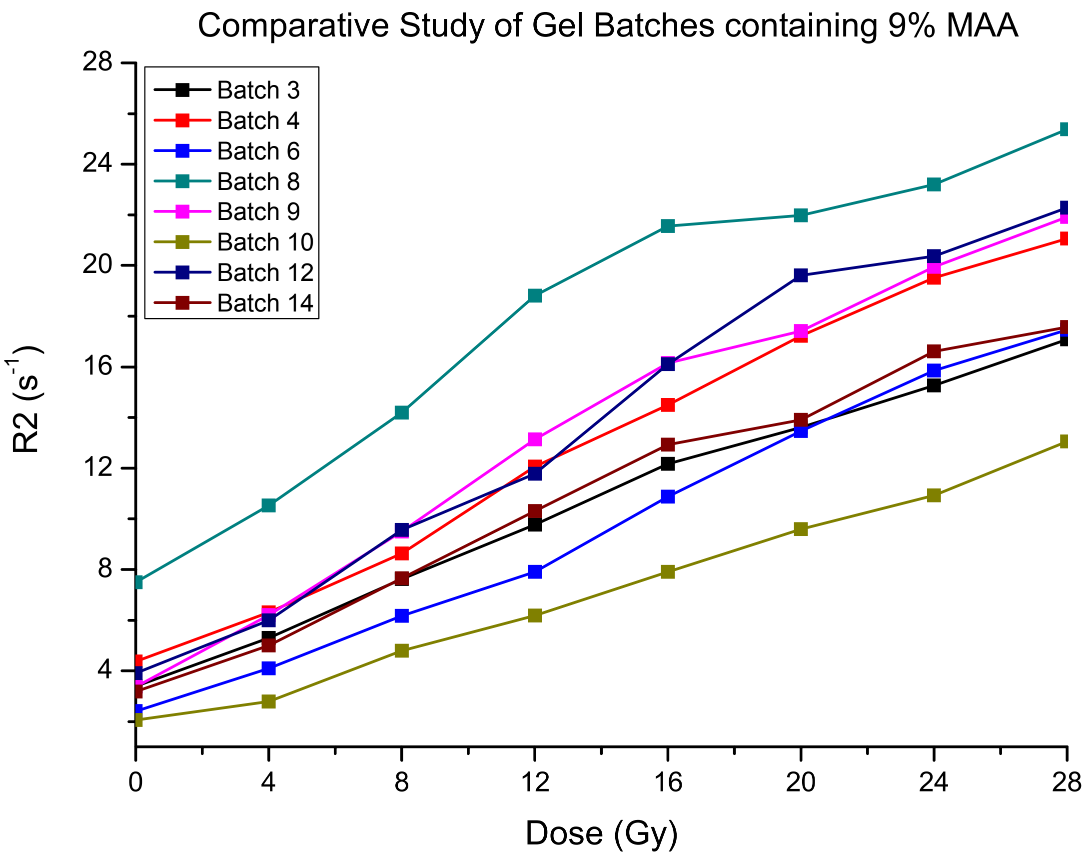

Figure [5-23] Comparative study of Gel batch repeatability using 9 % MAA per batch volume.

Figure [5-23] indicates that the base level spin-spin relaxation rate (R2) for the un-irradiated MAGIC gels (i.e. zero dose) lies in the region 2 - 4 s^{-1}. The values reflect the general level of viscosity in the gel with respect to the decay response after the radiofrequency (RF) excitation of the gel. All batches were dosed up to 28 Gy with the same dose rate delivery of 250 monitor units per minute.

Although the same manufacturing process and concentrations of MAA were consistent, from Figure [5-23] it is evident that the dose response of the gel batches varied from one and another. This was most likely attributable to the small unavoidable variations in the manufacture process e.g. contaminates on the internal walls of the flasks used, difference in water pH, ambient temperature, the frequency of the magnetic stirrer used to mix the gels and the length of time for temperature equalisation to 37 ^{0}C.

Figure [5-24] was produced to extract further information from the results shown in Figure [5-23] and shows the individual batch values for the gradient, intercept and the figure-of-merit (FOM).

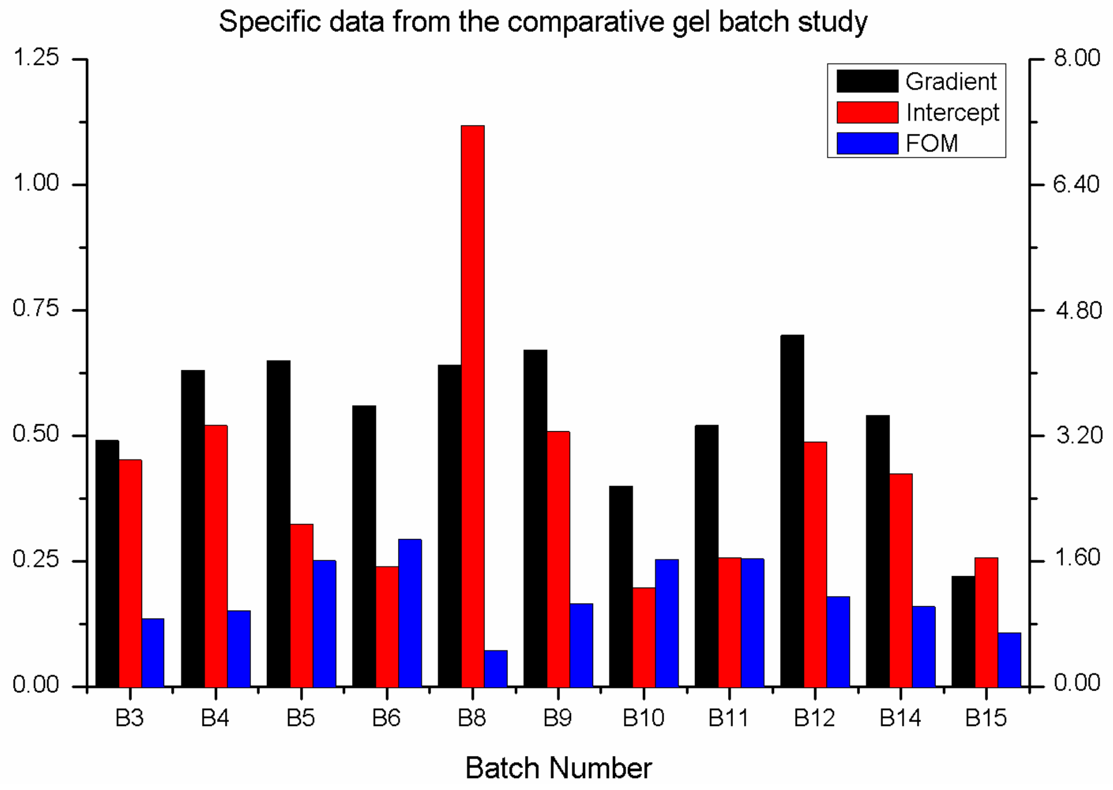

Figure [5-24] Graph showing batch-to-batch repeatability in terms of the R2-dose line gradient, R2 intercept at zero dose and the figure of merit for the individual batches. The graph shows that all the batches with the highest sensitivity values (B6, B10 and B11) have intercept values ≤ 2 s^{-1} and that the intercept value is the limiting factor to sensitivity. The units of the first y axis are s^{-1} Gy^{-1} for gradient and Gy^{-1} for the FOM. The second y-axis has units s^{-1} for the intercept.

To provide an indication of the errors inherent in the batches, the standard deviation, σ, was taken from the batch data set and is shown in (5-2). The standard deviation is a measure of how widely values are dispersed from the average value (the mean).

$$\sigma = \sqrt{\frac{1}{N}\sum_{i=1}^{N}(x_i - \bar{x})^2} \qquad (5\text{-}2)$$

Table [5-1] details the average gradient, intercept and FOM as well as their standard deviation values for the batch data shown in Figure [5-23] and Figure [5-24].

	Average	Standard Deviation
Gradient	0.58	0.10
Intercept	3.90	2.20
FOM	0.18	0.13

Table [5-1] details the average gradient, intercept and FOM as well as their standard deviation values for the batch data shown in Figure [5-23] and Figure [5-24].

The results show that the error in the intercept count is much larger, 57%, than the error in the slope, equal to 17%. This implies that more work is needed to ensure that the gels maintain a consistent background before irradiation. The calibration equation, R2 = slope*dose +c, is to be used to obtain the dose applied to the gel phantoms from measurements of R2. The errors indicated in table 5-1 provide an indication on how reliable the calibration is.

A further relationship was also observed between the batch-to-batch intercept values on the R2 (s^{-1}) graphs to the degree of gel whitening. The gel opacity will significantly affect the optical transmission properties of the batches especially for the larger volume flasks with increased integral line paths between laser and detector. The 9 % MAA batches show a linear relationship between dose and response to approximately 16-20 Gy but beyond this the R2 value no longer increases significantly and the curve flattens off. A possible explanation for this plateau, is the depletion of the MAA reservoir available at high doses and therefore it is unable maintain the linear response seen for lower dose values. Thus the plotted batch data can effectively be spilt into two gradient regions that more accurately describe the initial steep linear gradient in the gradient achieved at the plateau region. However when one wishes to determine the gradient, a linear regression plot must be produced that essentially provides the line equations for the individual batches. This led to low R^2 values, which can provide misleading information about the batch properties. This is emphasised in Figure [5-25] where the R^2 values for both regions are inserted i.e. the 0 to 16 Gy region (blue line) and the 16 to 28 Gy range (red line) from Batch 8.

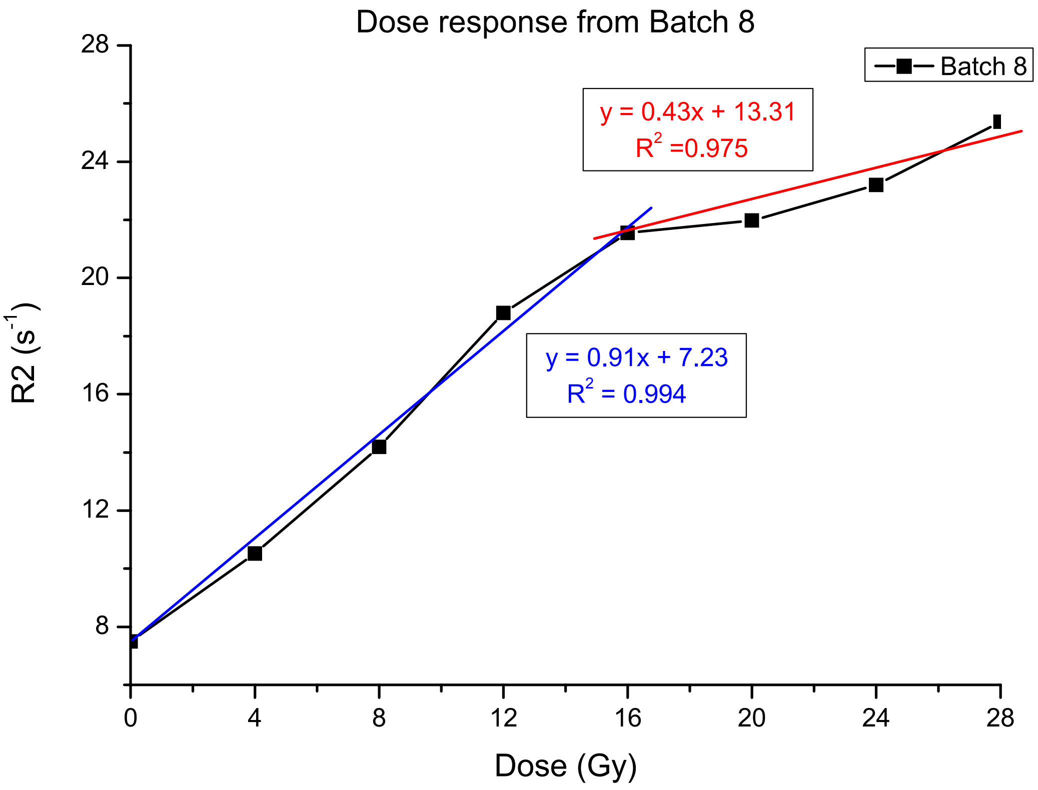

Figure [5-25] Graph showing the dose response (R2 (s^{-1}) versus dose for both the 0 - 16 Gy and 16 - 28 Gy regions. The linear regression fits for both the blue line (0-16 Gy range) and the red line (16 - 28 Gy range) are shown. The corresponding fit data is inserted adjacent to both lines and indicates that the initial gradient and therefore response to the radiation absorbed is approximately double that of the higher dosed region.

Batch 8 has been chosen for this example to indicate the high intercept value on the y-axis. This high baseline (0 Gy) value reduces the effective sensitivity/FOM of the batch to the lowest calculated throughout the investigation series. The highest sensitivity was calculated for Batch 6 at approximately 0.30 compared to 0.10 for Batch 8.

5.2.2 Monomer Concentration Studies

Experimentally it has been shown (Fong *et al*., 2001) that varying the percentage by volume of MAA within a gel batch has a variety of outcomes, the most significant being the higher the concentration the greater the response of the gel to the absorbed radiation. The vast majority of research papers that have undertaken normoxic gel studies with 3 %, 6 % and 9 % MAA samples have revisited a 9 % MAA concentration level for gel dosimetry studies.

In the present work higher levels of MAA concentrations were investigated in a hope of obtaining increased sensitivity to the radiation as a direct result of the increased availability of the MAA reservoirs in the gel. In terms of gel chemistry, this increase of monomer concentration will increase the acidity of the gel and alter its properties e.g. gelation processes and the general response/sensitivity to radiation.

The number of flasks available for producing a calibration study is limited to the total volume of gel manufactured. In general, 2 litre batches were prepared and evenly distributed to five optically friendly flasks with 90 mm diameters. Therefore to produce the 0 - 24 Gy dose range each flask was uniformly irradiated by 6 Gy increments whilst one remained a control i.e. 0 Gy.

It was found that the additional concentration of methacrylic acid on going from 9 to 12 % increased the viscosity of the gel. The gel became visibly more solid in appearance than previous 9 % batches. When the gels were probed with the usual MRI protocols, the RF signal response decayed much faster as a consequence of the higher viscosity. This prompted the use on longer echo times during MRI interrogation in an attempt to extract higher RF signals and therefore collect comparable data to previous 9 % MAA gel batches that exhibited lower viscosities.

Figure [5-26] illustrates the response of Batch 13 in terms of the relaxation rate (T_R) and two different echo times (T_E) of 90 and 180 ms.

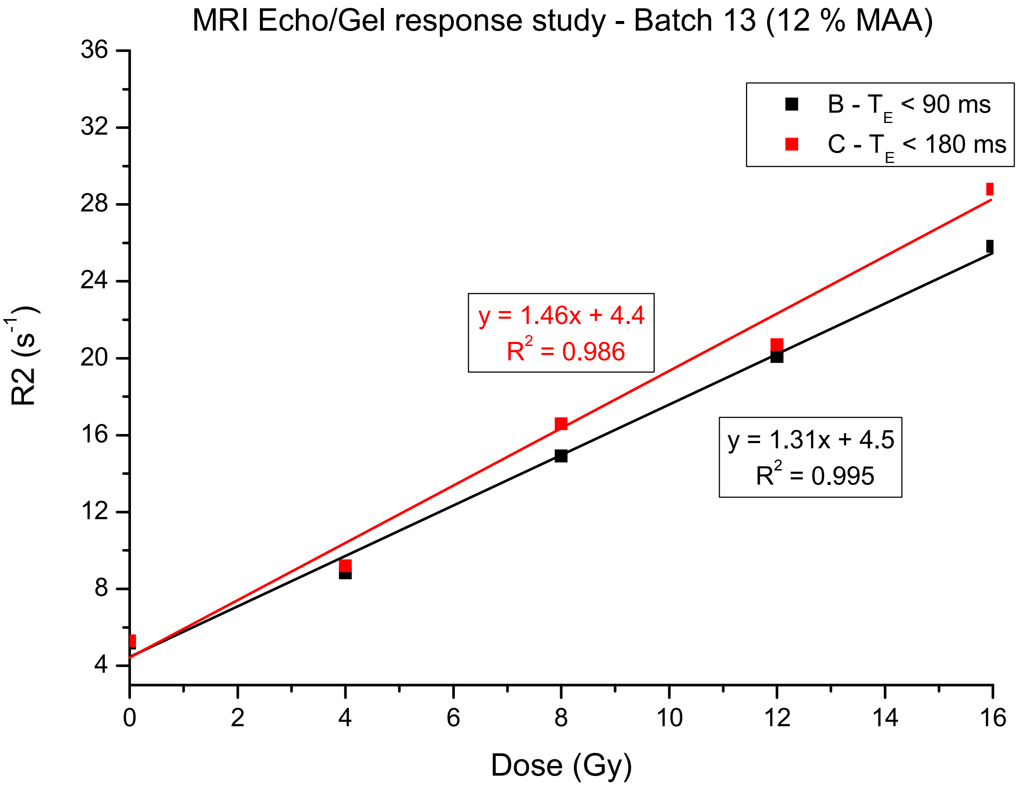

Figure [5-26] Graph of R2 (s^{-1}) versus dose from Batch 13 (12 % MAA) showing the differing MRI signal readouts from using different echo times (T_E) during the gel interrogation. A higher response to dose was observed from the longer 180 ms echo time than the 90 ms echo. Linear regression lines (hashed) and corresponding values have again been inserted that show the line details in terms of gradient, intercept and the R^2 value indicating to what degree the lines are linear.

The different echo time yielded slightly different gradient responses with the 180 ms echo time giving a sensitivity of 0.33 compared to the value 0.29 derived for the 90 ms echo time. The intercept value was found to be just above the range reported above in Figure [5-24] i.e. an R2 (s^{-1}) value between 2 and 4 s^{-1}. This slightly elevated baseline level would be expected due to the increase amount of MAA available for spontaneous polymerisation due to impurities and available free radicals prior to irradiation.

A second result for a MAGIC gel with 12 % MAA per volume is shown for comparison in Figure [5-27].

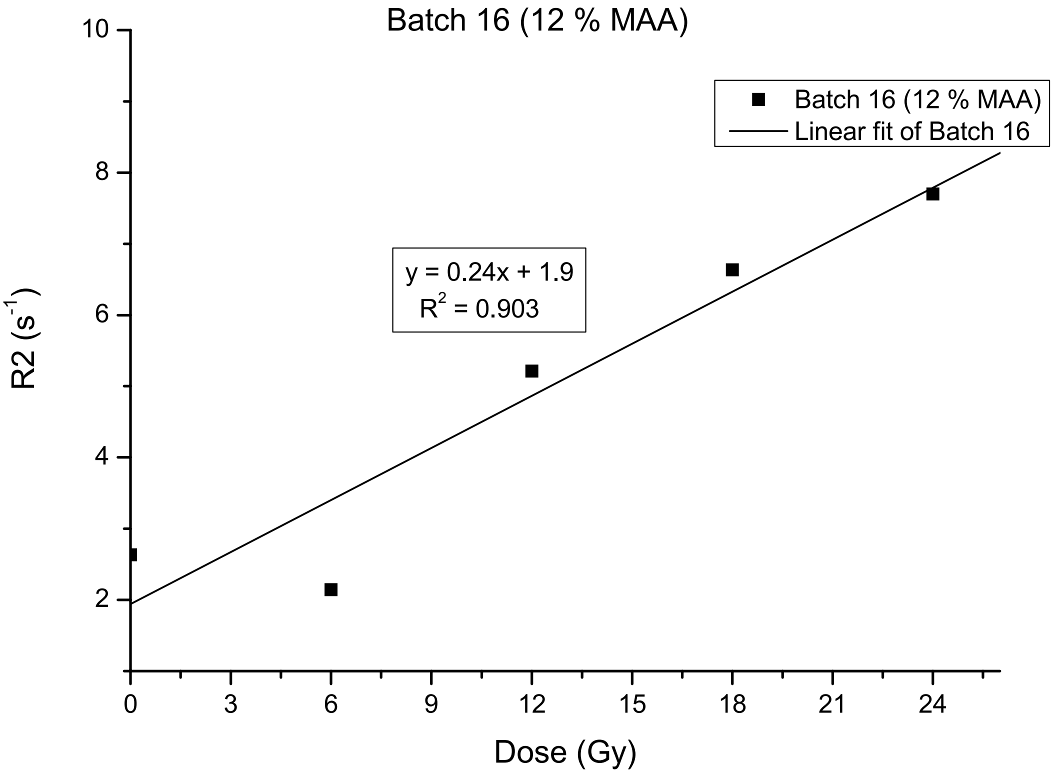

Figure [5-27] Graph of R2 (s^{-1}) versus dose from Batch 16 (12 % MAA) obtained from MRI readout using 180 ms echo times (T_E). A linear regression has been fitted; the resulting line data has been inserted adjacent to the line and from which the low gradient indicates the batch responded poorly to the dose absorbed.

This batch differs from Batch 13 in Figure [5-26]. The linear regression suggests that the overall linearity of the data has been reduced when compared to Batch 13 as is indicated by the poor R^2 value of 0.903. However if the 6 Gy data point was deemed erroneous and removed, the remaining data point appears very linear. The low gradient value obtained also indicates that for this particular batch the dose response was poor when compared to Batch 13. A further point is that the fit intercept gives a value of 1.96 whilst it is clear that the actual value for an un-irradiated control gel is nearer to 2.7. This is a consequence of the poor linearity of the response.

Again it is noted that the manufacturing method for manufacturing the MAGIC gels remained unchanged from all previous 9 % and 12 % MAA batches.

To further investigate the effects of increasing MAA concentrations, Batch 17 was manufactured with 15 % MAA by weight. The results for the highest level of MAA of 15 % used for producing a gel are shown in Figure [5-28].

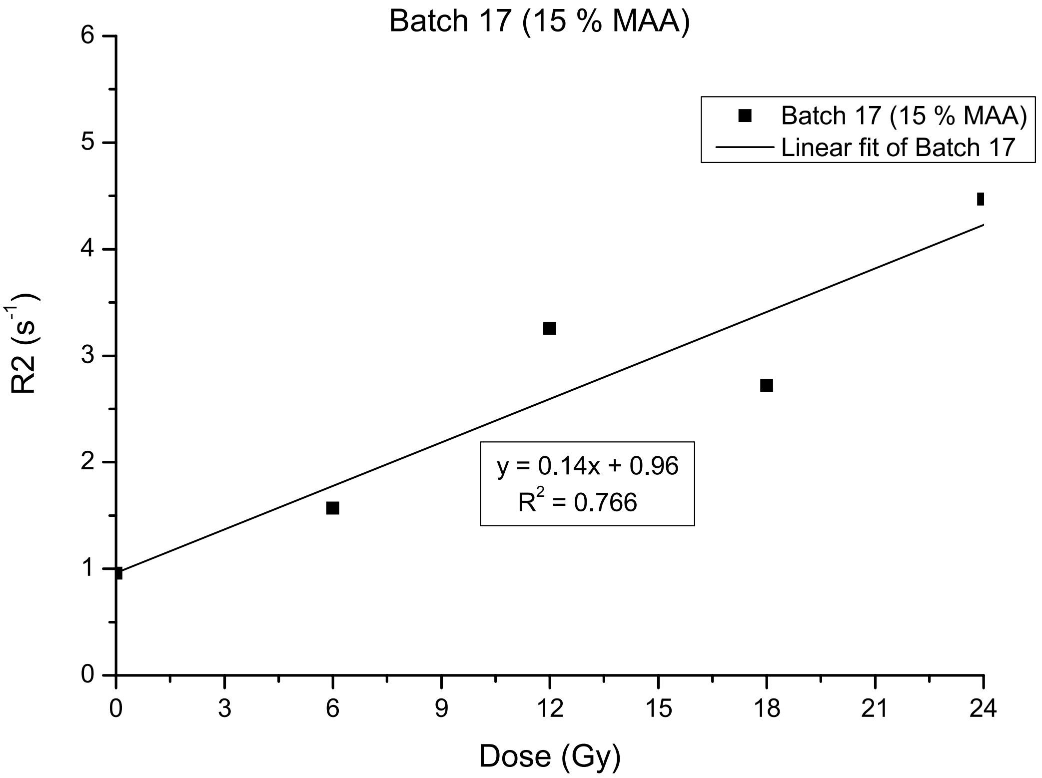

Figure [5-28] R2 (s^{-1}) versus dose plot for Batch 17 containing 15 % MAA by volume. The 90 mm diameter gel flasks were irradiated at 6 Gy intervals from 0 – 24 Gy. A linear regression was fitted and the corresponding data inserted adjacent to the line.

Compared to all previous batch data, the immediate observation from Batch 17 is the poor linearity of the dose response, the low sensitivity response (gradient) of the gel and low extrapolated R^2 intercept. The planned dose, calculated dose and the percentage errors within the gel are summarised in Table [5-2].

Gel Flask	1	2	3	4
Calculated Dose	1.57	3.26	2.72	4.47
Planned Dose	6	12	18	24
Percentage Error (%)	-73.80	-72.80	-84.90	-81.40

Table [5-2] Data taken from the resulting 0 to 24 Gy irradiation of a batch of MAGIC gel manufactured with 15 % MAA by weight. The dose values for the distribution was calculated from the 0 -24 Gy calibration flasks that provide the R2 (s^{-1}) and dose delivered relationship.

Figure [5-28] and Table [5-2] clearly indicate the limited usefulness that an additional MAA concentration will have on the gel response. Although the gels were allowed to form temperature equilibrium with the surrounding environment prior to irradiation, the gel viscosity did appear somewhat reduced from previous batches. This in effect would reduce the propagation of the polymerisation reactions within the gel volume and produce MRI signals comparable to lower dosed flasks i.e. with less polymer to polymer structure. Both points could suggest why poor dose response results were collected from Batch 17. In addition, the acidity per unit volume due to the MAA concentration could be attributed to this effect resulting from structural and chemical denaturing of the protein based (bovine skin) gelatin. This could limit the formation of polymer strands in the denatured dose fixing gelatin matrix.

5.2.3 Investigation of Gelation Methods

In general, radiosensitive gels are constantly undergoing chemical and physical changes between their initial preparation and the time they are actually irradiated and analysed. During the gelation process the liquid gel mixture slowly solidifies into a viscous gel as the temperature of the liquid falls from 37 ^{0}C to ambient storage temperatures of approximately 15-20 ^{0}C. During this phase change there will be a continuous volumetric diffusion flow within the gel imparted from the magnetic stirrer used to mix the gel ingredients during manufacture. Here the rate of cooling can determine the distribution and homogeneity of the gel constituents i.e. monomer concentrations. If the gel properties were non-uniform within the flask the spatial response to complex spatial patterns and therefore the related degree of polymerisation could differ from region to region. A further point to consider is that spontaneous polymerisation reactions occur in the gel, a consequence of free radicals being present, prior to irradiation. The degree of polymerisation prior to irradiation could also be a limiting factor for optical tomography in terms of base level gel opacity. The ideal gel would exhibit a very low opacity prior to irradiation that would be instantly discernible from dosed regions within the flask.

In MAGIC gel dosimetry there are many variables than can influence the gel properties and performance. These include the quality and longevity of the gel constituents i.e. the shelf life of the methacrylic acid, the quality of gelatine as well as possible microscopic impurities in the gel flasks and slight variations in the water content (80 % by volume) of the gel. During the gel investigations it was found that the homogeneity of the gel batches varied from batch-to-batch even though the same method of manufacturing these was used.

This section describes non-homogeneities revealed in gels by MRI imaging. It is suggested that this occurs because during the normal gelation processes, localised regions within the gel contain higher levels of MAA and thus are susceptible to polymerisation at higher rates than neighbouring regions.

The problem of localised polymer strands is illustrated in Figure [5-29]. The MRI scan here is based on the spin-spin T_2 weighted image of several gel flasks. The localised polymer strands can be seen to be darker than the base line gel levels. The level of absorbed dose is proportional to the degree of darkening of the image. The darkness of the image gives a direct indication of the dose absorbed within the gel.

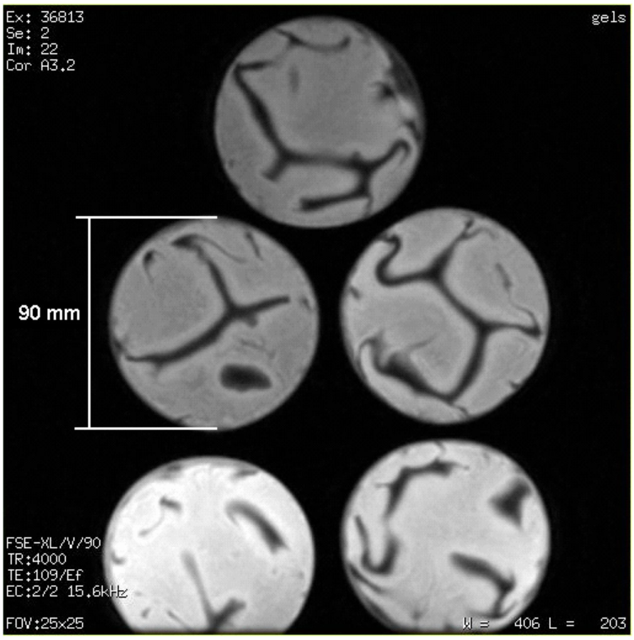

Figure [5-29] Planar MRI image taken from a 9 % MAA MAGIC gel showing the unwanted polymer strands produced by the polymerisation processes initiated by free radicals present within the gel prior to irradiation. The scan protocols are shown in the bottom and top left hand side of the image.

It is desirable when taking data from MRI to sample the largest region of interest (ROI). This gives the most accurate account of that area of the gel flask. This is illustrated in Figure [5-30] showing both a uniform gel distribution without polymer strands and an example with polymer strands.

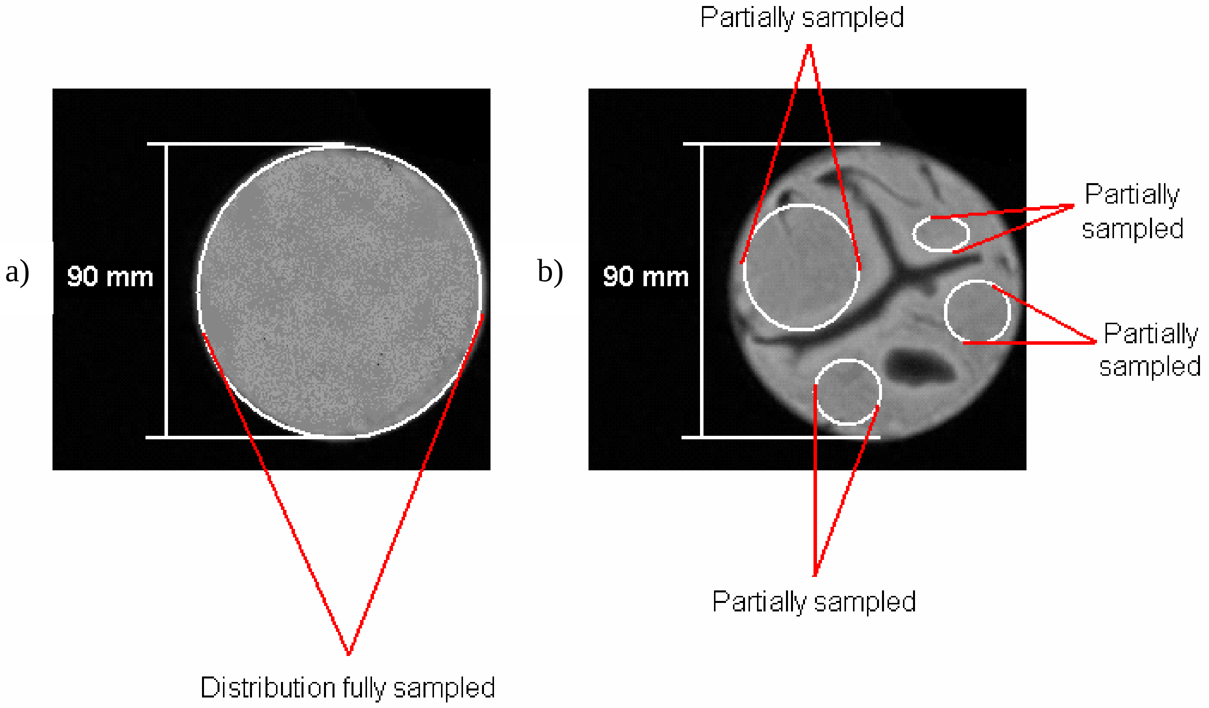

Figure [5-30] Showing the optimal situation of a) collecting signal data from the whole region as opposed to b) collecting decay signals from restricted spatial regions of the sample.

If MRI decay signals were collected from the complete cross-section of a gel flask containing polymer strands the resulting data would over estimate the absorbed dose. The additional signal from the polymer strands would increase the signal obtained from the region of collection hence providing incorrect dose values. Thus, smaller areas are sampled that produce results that are limited and prone to increased statistical variability and reduced accuracy.

5.2.4 Gel Cooling Investigations

Varying the environmental conditions the gel batches are subjected to during the gelation phase was attempted in an effort to reduce, if not remove, the presence of undesired polymer strands prior to irradiation. For this simple investigation into the effects, the rate of change of gel cooling would have on the gelation processes, the same manufacturing process was followed up until the point of gel transfer to the flasks. Under normal conditions, the gels are transferred from the mixing vessel into the gel flasks at 37 ^{o}C and left to cool. They subsequently reach the storage temperature naturally. Here the process was changed using waterbaths, ovens and fridges, a batch volume being distributed among both the Wheaton calibration bottles and the 90 mm flasks and each cooled differently. Thus differing rates of gelation could be investigated in this way.

The methods used were:

1. Air cooling – The normal process under which the gels would be allowed to cool at room temperature.

2. Refrigeration cooling – In this case, the gels were cooled at a faster rate due to using an increased temperature gradient i.e. 37 ^{0}C to 4 ^{0}C.

3. Iced water cooling – A general concern was that oxygen was perfusing into the sealed gel flasks through the glass walls during the gelation processes in open aerated conditions. It was hoped that placing the gel flasks within iced water (with less molecular oxygen absorbed within the water) could improve the final gel results.

4. Oven treatment – A Wheaton calibration bottle and a 90 mm flask was placed into an oven set to 37 ^{0}C. It was conjectured that this quasi-steady state method of gelation would gradually allow the gel to set homogeneously i.e. evenly distributing the MAA within the flasks rather than forming regions of higher MAA concentration that were presumed to form polymer strands.

5. Storage in differently sized vessels to determine if volumetric effects influenced the gelation process i.e. the convection currents imparted by the magnetic stirrer distributing the gel components within the gel flask.

MRI images of the various flasks prepared in these different ways are presented in Figure [5-31]. The smaller diameter Wheaton bottles were uniformly irradiated to 15 Gy whilst the larger flasks received a uniform 15 Gy strip dose. Thus the batch had two dose regions 0 and 15 Gy.

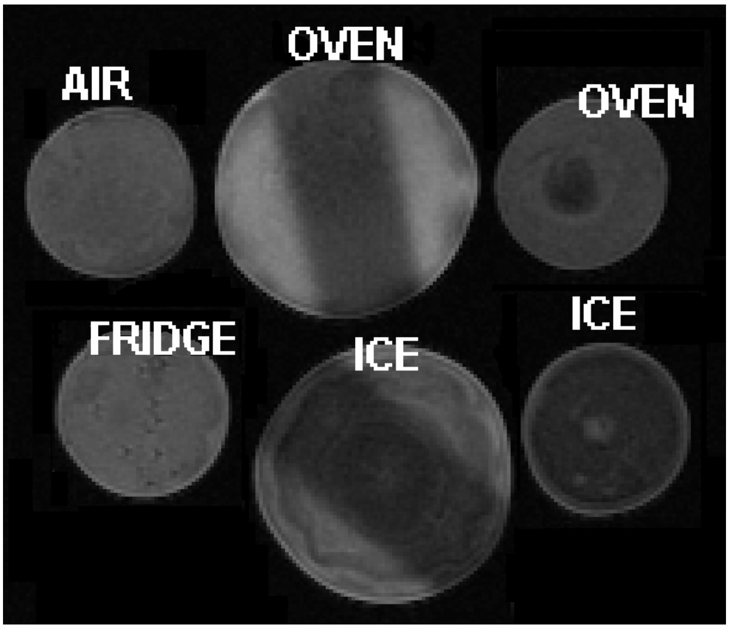

Figure [5-31] MRI images of the differing vessels and cooling methods from the gelation investigations. Both the 50 mm diameter Wheaton bottles and the 90 mm flasks were cooled and set by the refrigeration, ice method and *via* an oven at 37 ^{o}C.

The MRI images indicate the absence of polymer strands in the gels despite the various cooling methods tried. The regular ‘Air’ cooled method shows a homogeneous distribution whilst the ‘Fridge’ cooled bottle shows trace polymer speckles along a central belt. The ‘Oven’ gels display a surface dose above 0 Gy in the large flask and an over-dosed central column in the smaller bottle. The ‘Ice’ cooled gels show similar artefacts to the oven method showing both an inner surface wave irregularity and a central column that appears under-dosed i.e. light colour in the small bottle. In conclusion, the regular method of gelation provides, in general, the most homogeneous gel when compared to the other cooling methods. There continued to be a batch-to-batch variance in the homogeneous finish of the gels produced in the method described by Fong (Fong *et al.*, 2001), requiring further investigations.

The MRI image R_2 versus dose data for the cooling investigation are shown in Figure [5-32].

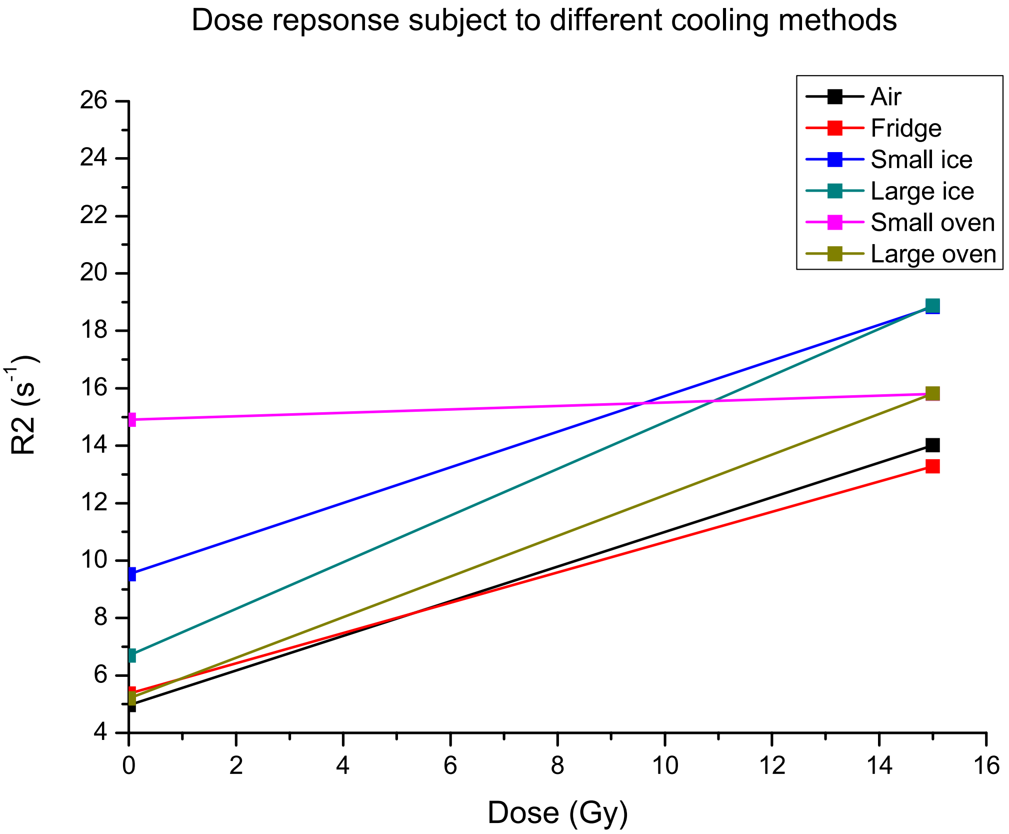

Figure [5-32] R2 (s^{-1}) versus dose results taken from the various cooling methods investigated showing the large variation of the dose response of the gels.

The data in Figure [5-32] shows that the gradients produced from the individual methods were comparable with the exception of the Wheaton bottle that used the oven to set the gel. This suggests that the combination of the small volume and oven rendered the gel unresponsive to radiation unlike the larger flask. The graph also shows differences in the intercept values from all the gels. Therefore further gel investigations are required to determine the cause of the polymer strands.

The iced method of increasing the rate of gelation was used for a number of subsequent batches using the ‘Quadrant’ distribution (see section 4.7.1.3). Although this produced flasks free of polymer radicals, there still existed, a batch to batch variability in dose response and large differences in the expected-to-calculated doses absorbed in the gels. The MRI images, for Batch 17 (9 % MAA) and the corresponding dose values, are shown in Figure [5-33].

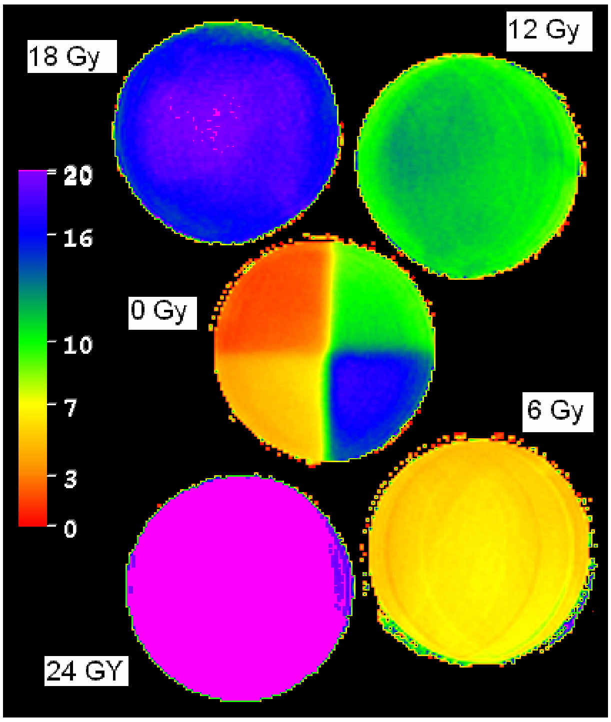

Figure [5-33] MRI images showing the 90 mm calibration flasks uniformly irradiated between 0 and 24 Gy and the quadrant distribution with 0 to 18 Gy regions.

The dose values for Batch 17 were obtained from MRI and are shown in Table [5-3]. The calculated dose values in the quadrant distribution have been obtained from the calibration curve, produced from the uniformly dose flasks. Thus, the R2 (s^{-1}) signals taken from different regions within the flask, have been corrected to the corresponding calibration values at known doses i.e. between 0 and 28 Gy. The % errors have been calculated from the ratio between the calculated-to-expected dose values.

Gel Flask (Gy)	Dose (Gy)		
	Expected	Calculated	% Error
0	0	2.4	/
6	6	4.9	-18
12	12	10.7	-11
18	18	17	-5.5

Table [5-3] Showing the under estimated doses delivered to the flask within the quadrant distribution. The percentage errors vary from -18 % (6 Gy) to -5.5 % at the higher 18 Gy dose region.

The data shown in Figure [5-33] and Table [5-3] show some of the better batch results obtained from MRI analysis. The percentage errors, between expected and calculated values, are always higher from regions with lower doses than regions with higher doses. This is a common element in all batches irrespective of dose distribution. The results obtained from Batch 17, show some of the better results from the gel investigations. Batches in general, show percentage errors far higher than the values shown in Table [5-3]. To emphasise both the variability in percentage errors and therefore the further investigations required, Table [5-4] shows dose results obtained from Batch 19 (9 % MAA) with the same quadrant distribution delivered to Batch 17.

Gel Flask (Gy)	Dose (Gy)		
	Expected	Calculated	% Error
0	0	-0.2	/
6	6	1.9	-67.6
12	12	7.6	-36.5
18	18	12.3	-31.5

Table [5-4] Showing the expected, calculated and corresponding percentage dose error from the quadrant distribution delivered to Batch 19. The percentage errors vary from -67.6 % (6 Gy) to - 31.5 % at the higher 18 Gy dose region.

The explanation for these large percentage errors have been considered at length despite the following points:

1) The calibration and distribution flasks have the same dimensions.
2) The energy rate, field size etc were maintained throughout the dosing.
3) All the gels were kept at the same temperature and were from the same batch.
4) The gels were irradiated in succession (i.e. no significant delay between dosing).

The possible source of these large errors could be attributed to the overlaying of dose onto areas previously irradiated and therefore under chemical flux and polymerisation reactions.

5.2.5 Longevity Studies

The properties of the gel batches were investigated over a three week interval during which the irradiated gel batch would be kept at a constant temperature and re-imaged with MRI. This was to establish what effect ageing would have on the gel sensitivity to radiation. Ideally, the R2 (s^{-1}) versus dose plots obtained would show high gradients combined with low intercept values; this would indicate a batch with a high sensitivity to radiation.

Figures [5-34] and [5-35] below, show the R2 (s^{-1}) versus dose response, for batches 10 (9 % MAA) imaged with MRI immediately after manufacture and then 3 weeks later.

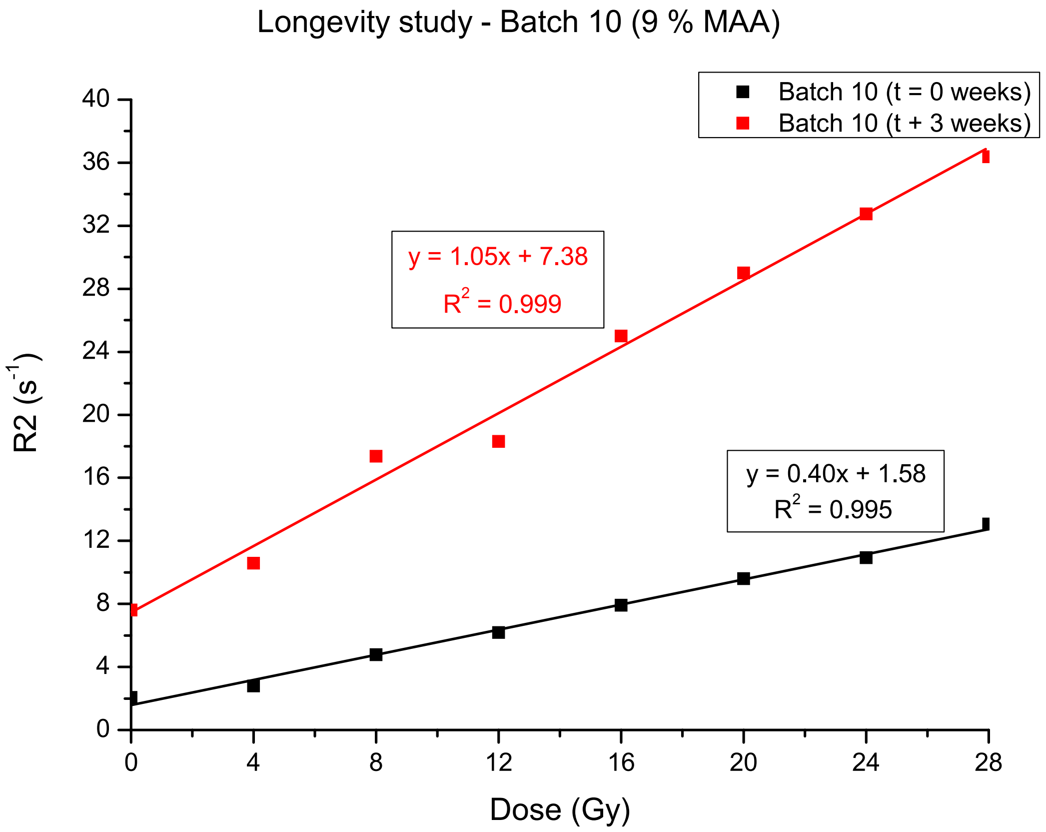

Figure [5-34] The R2 (s^{-1}) versus dose response for Batch 10 (9 % MAA), comparing results obtained immediately after dosing and again after a 3 week period. Linear regression fits have been plotted in bold along side the MRI data points to indicate the linearity of gel response and gradient and intercept values. The linear regression data for both data sets are inset adjacent to the relevant plot.

Figures [5-34] shows that both the gradient and intercept values increased after a period of 3 weeks. A direct consequence of this is that the gel sensitivity was reduced from 0.25 to 0.14 by taking the ratio of gradient to intercept values from both t = 0 and t = 3 weeks. This therefore indicates the opposite effect to what is required for the gel responses.

To provide additional ageing data Batch 11 (shown in Figure [5-35]) was also imaged immediately after dosing and again after a period of 3 weeks. This batch was manufactured using large flasks as opposed to the Wheaton bottles used for Batch 10 shown in Figure [5-34].

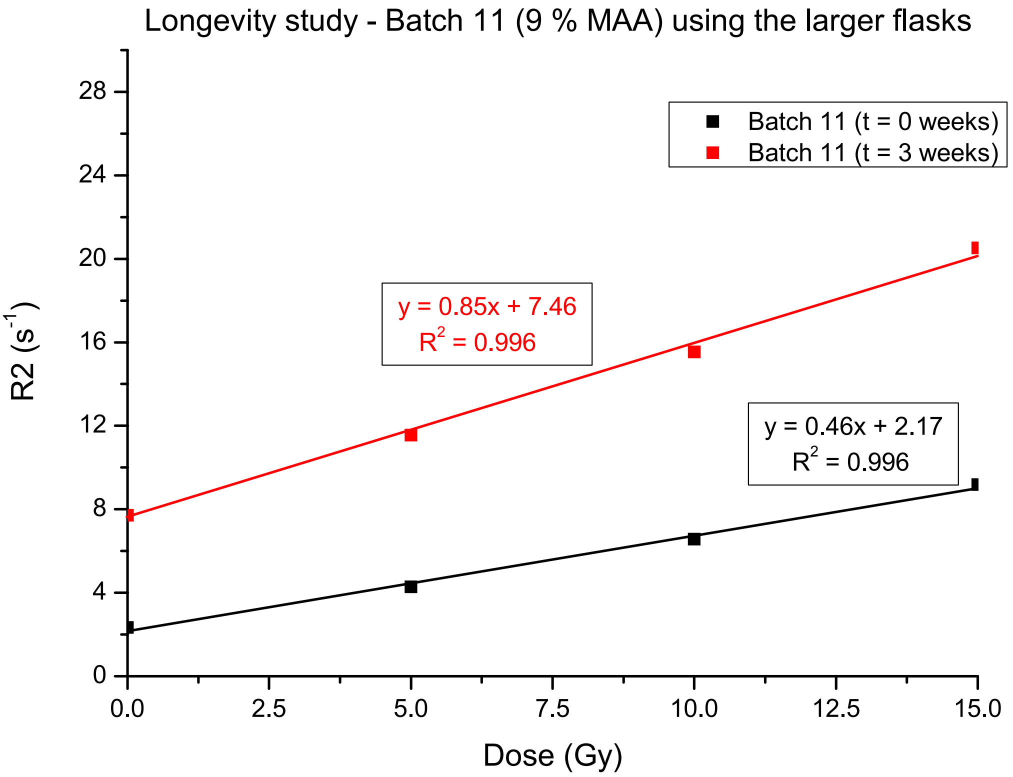

Figure [5-35] The R2 (s^{-1}) versus dose response for Batch 11 (9 % MAA), comparing results obtained immediately after dosing and again after a 3 week period. Here, the larger 90 mm diameter flasks were irradiated from 0 to 15 Gy. Linear regression fits have been plotted in bold along side the MRI data points to indicate the linearity of gel response and gradient and intercept values. The linear regression data for both data sets are inset adjacent to the relevant plot.

Both Figures [5-34] and [5-35] show that the ageing effects observed for both the small bottles and larger flasks were very similar. The sensitivity from Batch 11, like Batch 10, was also reduced from 0.21 to 0.11 over the 3 week period. The temporal effects observed during these ageing studies showed that both Batches 10 and 11 (manufactured with 9 % MAA by concentration), exhibited both elevated gradients and baseline y-axis intercept levels. This dual increase, especially from the intercept, in effect nullified any possible increase in the sensitivity attributable to the increase in gradient.

As mentioned earlier, the ability to increase the available dynamic response of gels would in particular be desirable for complex treatments that utilise low doses delivered by small dose increments. This can be achieved by simply increasing the gradient and response of the gels whilst keeping the intercept (baseline polymerisation) minimised, therefore providing the highest available gel performance ratio (gradient/intercept). Although the ageing experiments did show increased gradients and response to X-ray radiation, the accompanying rise in intercept values nullified this increase. The additional baseline polymerisation (optically detrimental to optical scanning over larger gel volumes and line integral distances) limits the usefulness of replacing (in some instances) freshly prepared gels with aged gels.

In addition to the longevity investigation into batches containing 9 % MAA by concentration, the ageing effects of Batch 13 with 12 % MAA was investigated and shown in Figure [5-36].

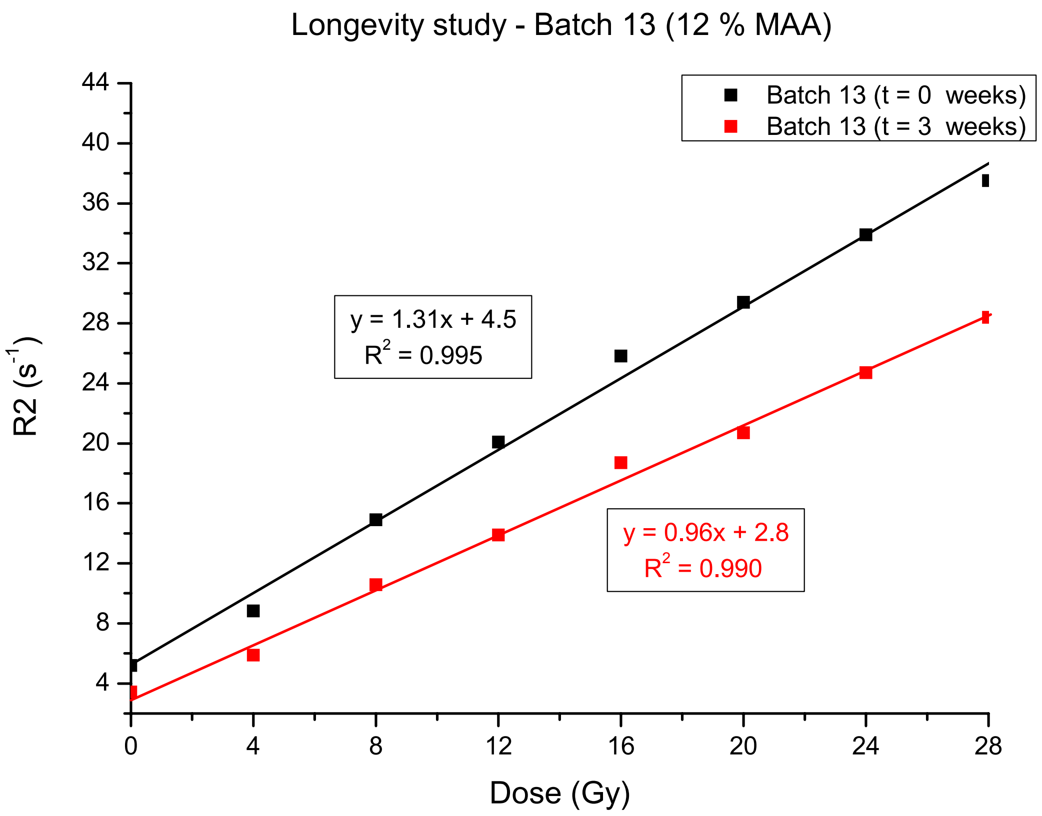

Figure [5-36] The R2 (s^{-1}) versus dose response for Batch 13 (12 % MAA), comparing results obtained immediately after dosing and again after a 3 week period. The Wheaton bottles flasks irradiated from 0 to 28 Gy. Linear regression fits have been plotted in bold along side the MRI data points to indicate the linearity of gel response and gradient and intercept values. The linear regression data for both data sets are inset adjacent to the relevant plot.

The results in Figure [5-36] show the opposite ageing response when compared to the 9 % MAA batches described earlier. The sensitivity was increased from 0.29 to 0.34. It is possible that the increased concentration of MAA reduces the strength of the structural lattice within the gel (polymerisation strands produced from irradiation) and lengthens the spin-spin decay time thus reducing the relaxation rate of the gel.

5.2.6 *In situ* Gel Investigations

Unlike most other dosimetry systems, the gel dosimetry method is non-invasive. As the gel itself forms the phantom, there is no need to introduce a probe, nor is it necessary to remove parts of the irradiated material for analysis. The site of measurement and the spatial resolution are determined almost entirely by the measuring system (MR scanner), which is, in principle, capable of scanning the complete 3D dose distribution. A complete quality assurance test object, including anatomically related compartments and markers for measuring image distortion was developed (Moore *et al*., 2003). In this preliminary study, the applicability of a MAGIC gel phantom for the verification of complex treatment plan was assessed. The treatment plan showing the intended dose delivery and radiation contour map and the resulting treatment outcome is shown in Figure [5-37].

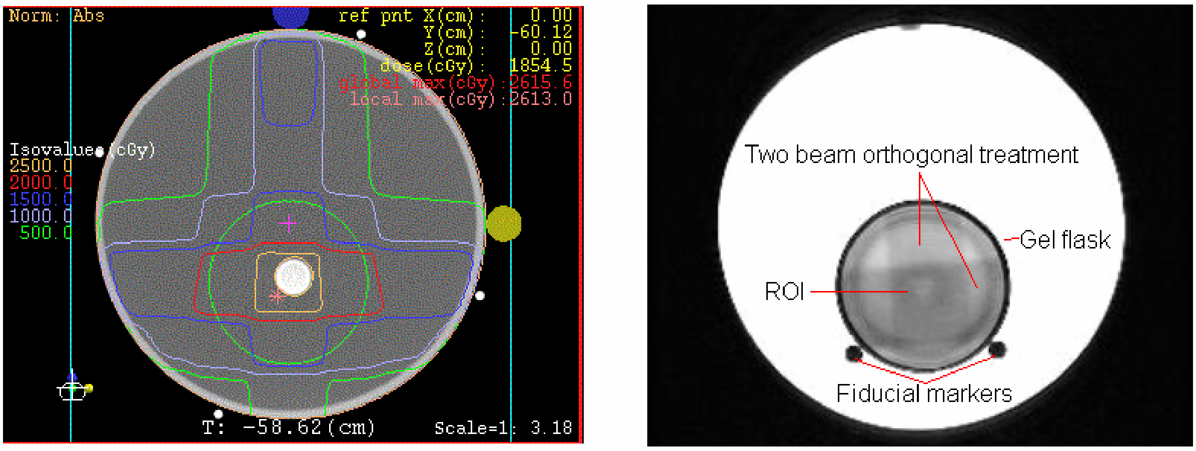

a) b)

Figure [5-37] a) The IMRT beam configuration showing the transversal view of a proposed treatment. The central white region is the target and a series of beam deliveries are considered that would minimise the dose delivered to the surrounding regions. The coloured lines (dose envelopes) indicate what dose would be delivered to the areas surrounding the central white region. b) MRI image taken inside a head coil of the gel phantom *in situ* showing the resulting dose delivered to the phantom. The lower black circles are fiducial markers and are used to indicate the orientation of the gel flask from intended treatment plan with respect to the IMRT plan in a).

Figure [5-37] shows that although simple beam profiles can be reproduced, there is a large error in calculating the absolute dose received by the gels as the analysis in section 5.2.1 shows. Currently MRI can be used to show the outcome of intended basic treatment plans. However, without continued research into gel chemistry, the application of 3D gel dosimetry into oncology centres for routine 3D radiotherapy verification will be severely limited.

Chapter 6 Discussion and conclusion

6.1 Scanner Development and Optical Imaging

The prototype hybrid CT scanner was designed to be a self containable instrument that could be used to accurately image 3D gel dosimetry in both university laboratories and hospital environments. The cylindrical design and internally positioned waterbath arrangement was an important consideration for minimising the size of the instrument and thus facilitating the movement of the scanner between different locations.

In general, OCT systems are rectangular in design and are based on the 1st generation CT scanners that use the raster and rotate method for collecting parallel projection data. The scanner designed at the University of Hull, is a hybrid design that uses elements from both the 1st and 3rd generation CT scanners. The fan beam to parallel data interrogation method was designed to collect 2D attenuation maps that could be reconstructed by the Matlab *Iradon* function. Whilst developing the optical tomographic scanner, it was important to consider the level of complexity that would be required to reconstruct images from raw projection data. The system was therefore configured in such a way that non-technical personnel, with a limited familiarity with optical tomography could operate it.

A significant part of the work reported herein involved the system development and in particular generating the ray path simulations using the ray tracing software package Beam2. Scanning parameters, including the laser orientation and required scanning fan beam, the position along the optical axis of all interfaces (including the glassware diameters), curvatures (including wall thicknesses) and the refractive indices of the interfaces were input into Beam2. The detailed simulations allowed the system properties to be varied, thus providing information on the ray path transitions and ultimately on their end points i.e. focal point along the optical axis.

From the simulations, it was found that the scanner would only successfully produce parallel beams through the gel flasks under certain conditions. Accurate image reconstruction was dependent on the combinations of dose absorbed (refractive index variability) and the waterbath and gel flasks diameters. This relationship effected the ray transitions through the system due to the changing optical properties. This, therefore, was found to be a fundamental limitation to the scanner geometry and therefore its ability to accurately scan flasks with diameters above 90 mm.

However, as discussed previously, the optical scanner is a class 1 laser system that used a 4 mW laser diode operating at 655 nm. It has been shown that under certain conditions a combination of the dose absorbed and related path lengths between the laser and detector renders the scanner unable to accurately reconstruct tomographic images. In addition, the requirement to reconstruct dose distributions exceeding the 90 mm diameter flask would be unlikely. Future work to meet this requirement would involve increasing the laser power above 4 mW and possibly changing to infra red (IR) wavelengths to reduce the laser beam attenuation *via* Rayleigh scattering for example. The required parallel ray paths could be engineered by impedance matching the solutions that surround the larger gel flasks. Further ray path control manipulation could be gained from using additional optics to allow additional beam manipulation.

6.1.1 Data Acquisition and Reconstruction

The PC-30/D interface card used for the data acquisition required the use of a computer with the operating system DOS. This lacked the windows functionality required for an efficient scanning system. The reliance on both acquiring and reconstructing the projection data on separate systems could prove laborious and is an important factor relating to the ease of application and using the scanner. An ideal system would use a single PC with sufficient performance to control the scanner, collect and process the data and finally reconstruct the large matrix data sets in Matlab.

A 3D rendering routine could be produced in Matlab that could take the reconstructed 2D tomographic images and produce 3D images without requiring an additional program. A fully automated scanning system could be configured that would scan a gel flask, obtain projection data with sufficient sampling and reconstruct images in both 2D and 3D.

6.1.2 Optical Scanning Results

The optical scanning performance and successful methodology of 2D and 3D image reconstruction was validated by the accurate reconstruction of the metal cylinder shown in Figures [5-9] and [5-10]. Other aspects of scanning performance, including scanning resolution (2 mm Allen key, see Figure [5-12]) and the ability to reconstruct multiple objects (metal cylinder and the 9 Volt battery, see Figure [5-14]) in close proximity was also achieved. Immediate issues regarding the level of interrogation and sampling required, the data manipulation necessary prior to being imported into Matlab, and the subsequent processing required to accurately reconstruct an accurate tomographic image was assessed from these fundamental investigations.

The scanning system was developed to provide raw projection data that could be imported directly into the Matlab workspace and easily reconstructed using a few lines of code incorporating the *Iradon* image processing function. The Matlab toolbox also provides numerous sub-functions that allow further image processing i.e. image padding, filtering and a variety of colour-maps that can aid the image contrast.

6.1.3 Optical Imaging of Gels

Tomographic images were also successfully reconstructed from gel flasks using data obtained from the optical scanner. The results varied according to the optical setup, specifically the quality and dimension of glassware used, dose delivered and the line integral path length under which the beam intensity would be attenuated. In its current state, the scanner remains a class 1 system that uses a 4 mW laser producing modulated light at 655 nm. Thus, further advances in optical reconstruction would be made with higher power lasers, for example. The higher power would also improve upon the current signal to noise ratio that in some instances were limiting.

The different dose levels delivered to flasks with the cross distribution could be clearly discerned in Figure [5-19] showing the 5, 10 and central 15 Gy regions. This indicates that the scanner can reproduce 2D images from gels that can be compared, to 1st order, to MRI images. Additional research is required to further develop this technique if optical scanning is to become both a valid and complementary imaging modality to MRI.

6.1.4 Summary of the MRI Gel Investigations

The main application and development of an OCT scanner was to complement the work provided by MRI centres. The MAGIC gels, also under development alongside the scanner, were investigated using MRI primarily as it is an established imaging modality. The optical scanner, whenever appropriate and possible, would produce comparable tomographic images to the MRI images.

The primary reason for gel investigations was to establish if a gel dosimeter could be manufactured in an ordinary laboratory on a routine basis, and whether or not it exhibited both repeatable and expected responses to X-ray radiation. The batch properties of some 9 % MAA gels are summarised in Table [6-1].

Batch No.	Line Equation	R^2 Value	Figure of Merit
Batch 3	$Y = 0.49x + 3.60$	$R^2 = 0.995$	0.136
Batch 4	$Y = 0.63x + 4.16$	$R^2 = 0.994$	0.151
Batch 6	$Y = 0.56x + 1.91$	$R^2 = 0.994$	0.293
Batch 8	$Y = 0.91x + 7.23$	$R^2 = 0.994$	0.126
Batch 9	$Y = 0.67x + 4.06$	$R^2 = 0.985$	0.165
Batch 10	$Y = 0.40x + 1.58$	$R^2 = 0.994$	0.253
Batch 11	$Y = 0.51x + 2.10$	$R^2 = 0.994$	0.243
Batch 12	$Y = 0.70x + 3.91$	$R^2 = 0.981$	0.179
Batch 14	$Y = 0.54x + 3.39$	$R^2 = 0.988$	0.159

Table [6-1] Results from the comparative repeatability batch studies.

The results show that although the linear regression values (R^2) are comparable between batches, the individual gradients and intercept varied between batches. The batches sensitivities varied between 0.126 and 0.293 at the extremes. The goal of gel manufacture would be to reproduce the same dose response i.e. steep gradient and low intercept values whilst maintaining high linearity between points. In addition, the dose response could be customised to specific treatment requirements by varying the MAA concentration.

Although the manufacturing process described by Fong (Fong *et al.,* 2001) for producing Magic gels is less complicated when compared with the PAG gel process, it still requires the addition of components in small amounts. For example, 0.02 g of copper sulphate is added to 30 ml of water during the process. Therefore, unintended errors in weight and measures could have contributed to the batch-to-batch variance in dose response. In addition, other aspects, including water composition and possible trace elements on the inner glass walls could have influenced the outcome.

MRI was used to investigate these gels as it was an established imaging modality. Initially, 8 Wheaton calibration bottles were irradiated from 0 to 28 Gy in 4 Gy intervals. The gel response (R2 (s^{-1}) versus dose delivered) was derived and used to estimate the dose delivered to larger gel flasks from a number of different dose distributions i.e. strip, cross and quadrant. However, large percentage errors were found between what dose was delivered to the flasks and what dose was calculated by using the 0-28 Gy calibration data. The errors varied between 5 and 80 %, which is a significant figure for accurate dosimetry.

6.1.5 Improving Gel Response

Improvements to gel response were investigated by changing the concentration of the monomer Methacrylic acid used for gel manufacture and a number of longevity studies. It was reported that the gel response to radiation could be varied by changing the concentration of MAA in the gel (Fong *et al.,* 2001). The gradient of the R2 (s^{-1}) versus Dose graphs, indicated higher gradients were obtained by increasing levels of MAA from 3 to 9 %. The most commonly used concentration of MAA was

9 %. Studies were therefore performed on gel batches with both 12 and 15 % MAA. The results obtained proved inconclusive in showing that the gel response increased by increasing the MAA concentration. The batches showed both increases of gradient and intercept values. Therefore, the representative gel performance ratio of gradient/intercept showed no clear improvement over previous 9 % MAA batches. In addition, the gel batches with 15 % MAA were largely liquid gels i.e. not set like other batches with less MAA. The increased acidity within the gel could therefore have limited the initial gelation process attributable, possible to the denaturing of the bovine protein in the gelatin. Thus polymer binding was to some degree inhibited. The gels upon irradiation produced very weak polymerisation reaction to the radiation. This is shown by their very low and varied R2 (s^{-1}) values shown in Figure [5-30].

The prospect of an increased gel dose response was investigated by re-imaging gel batches after a period of 3 weeks. By this time the polymerisation reaction would be steady-state and therefore would represent the dose absorbed more accurately. It was found that the sensitivity decreased for batches containing 9 % and increased for batches with 12 % MAA concentrations over the 3 week period. It was shown that, for the 9 % MAA batches, the intercept value would increase by a factor of 4 and was accompanied by an average 1.35 fold increase in the gradient over the 3 weeks. In the 12 % batches, the intercept value was reduced by a factor of 2 whilst the gradient was increase by a factor of 1.35. This therefore increased the sensitivity. This raises the question as to why the intercept value increased for 9 % MAA gels and reduced for 12 % MAA gels. The answer could be that the polymerisation reactions continue to take place in the 9 % gel due to the available MAA reservoirs from the un-irradiated ‘control’ bottle. Conversely, the higher acidity in the 12 % batches could have, over the 3 week period, broken down the spontaneous polymerisation occurring in the gel prior to X-ray dosing, and therefore the reducing the gel viscosity.

6.1.6 Gel Viscosity

The anti-oxidant used for oxygen scavenging in these gel investigations was ascorbic acid (vitamin c). A study of alternative scavengers (De Deene *et al.,* 2002) and more recently by Senden (Senden, 2006) identified tetrakis (hydroxymethyl) phosphonium chloride (THP) as having an improved ability to remove molecular oxygen from the gel *via* the organo-metallic reaction. The reduction of the initial polymerisation and degree of gel fogging prior to irradiation of the flask could be achieved by replacing the ascorbic acid with THP. This modification of the gel manufacture would have been investigated if the current repetitive studies had proved more successful.

The batch-to-batch results also indicated a variability in the viscosity of the gels before and after irradiating them. It was thought this could directly affect the ability of the gel matrix to 'fix' the dose delivered to the gel and as such to produce an expected dose distribution. The gels were manufactured consistently with 80 % per batch weight of gelatin. To try and improve variability in the viscosity levels, agarose was considered to be a viable replacement for gelatin due to its previous usage in fixing dose distributions in radiotherapy gels. Further, both hydrogels and cryogels were considered for future investigations.

6.1.7 Homogeneity of the Gels

A recurring problem with the gel studies was the presence of polymer strands in the gel flasks. These strands, when compared to the surrounding homogeneous gel, were polymerised to a higher degree. This effect was evident in the darker regions, i.e. different signal responses, when reconstructed using MRI. Therefore, a series of cooling experiments were implemented to try and increase the rate of gelation and hopefully improve the homogeneity of the gels. It was thought that during slow gelation processes, localised volumes of MAA monomers could congregate and therefore become more susceptible to polymerisation at a higher rate during irradiation of the gel than other regions. This could explain the localised polymer strands.

6.1.8 Comparison of Measured to Planned Dose

It was found that although the majority of gel batches exhibited linear dose responses, the doses calculated from distributions compared very poorly to the expected dose values. For example, errors approaching 80 % were observed for dose regions containing 6 Gy in flasks with the quadrant distributions. In an attempt to reduce this error, the Wheaton bottles were replaced with the same flasks used for dose distributions i.e. the same gel volumes. Therefore, the same radiation fields, dose rates, storage environments and time of dosing were consistent with both the calibration and distribution flasks. Unfortunately, the large percentage errors and underestimates for the dose delivered within the distribution remained. Other contributing factors, including the accumulative method of overlaying dose onto previously dosed gel regions, could be attributable to the errors. The initial dosing and subsequent polymerisation processes could, to some degree, heavily reduce the ability of additional polymers forming in that dosed region due to chemical fluxing. Specialised research was therefore required to attempt to correct this observation. In an attempt to resolve theses issues, the MAGIC gels were later manufactured in the University of York's chemistry department. Although early results indicated a reduction in the occurrence of polymer strands the overall errors in delivered samples to calculate gel dose still continued.

In conclusion, the ability to reconstruct both simple and complex dose distributions (see Figure [6-1]) is somewhat redundant if unaccompanied by accurate dose values leading to acceptable treatment verification.

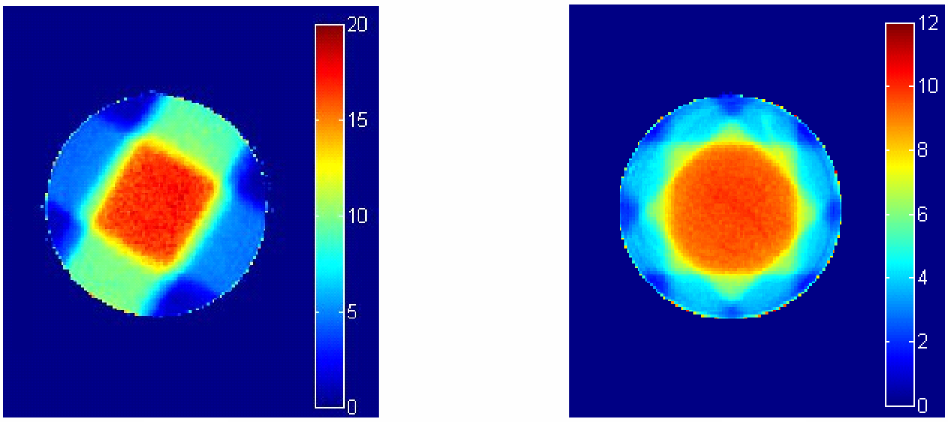

a)　　　　　　　　b)

Figure [6-1] Illustrates a) a familiar 2D MRI image of a 'cross' distribution within a radiotherapy gel flask, b) MRI image of a complex dose distribution using multiple beams to irradiate a central region.

6.2 Future Work

In addition to improving the optical properties of the radiotherapy gels for optical interrogation, there may be other technical improvements relating to improving the scanning methodology. The 3D scanning time could be reduced considerably by modifying the scanner to collect data in a fashion that is analogous to tomotherapy systems. Until the existing limitations to both scanning and reconstructed image quality are resolved this requirement is unimportant. However, considerable improvements can be made to the quality of projection data collected from the optical scanner. The existing 4 mW laser diode could be replaced with a laser system that can deliver laser pulses in the femtosecond regime. This significant upgrade to the light source and the detection system could allow time gated tomography to be developed.

6.2.1 Time Resolved Tomography

Getting optical tomography to work for radiosensitive gels is a big challenge, for the associated mathematical problem is by its nature very difficult to model accurately. Imaging in X-rays is a relatively straightforward matrix inversion, since the radiation is assumed to have travelled along the straight line between the source and detector. Under these circumstances it is a formidable problem to retrieve the ‘optical’ image by computed tomography. Radiosensitive gel dosimeters are highly scattering media, causing the photons to take lengthy and highly irregular paths such that the optical pathlength is usually several times the geometric distance between the input and output.

Ideally, a laser pulse of finite width, when introduced to the gel flask, would be maintained during its passage through the gel and maintain comparable properties upon its exit and detection. However, due to scattering and absorption mechanisms inherent within the gel, the laser pulse length is lengthened and the photon pathlengths will be highly randomised with multiple scattering events and therefore different path directions during the translation. The time taken for these individual photons to traverse the gel flask will consequently vary greatly.

Time resolved investigations use pulse imaging techniques to collect gated information from a system. Here time resolved tomography could be utilised by using pulsed laser light to probe the scattering media (gel dosimeter). A schematic of a possible arrangement illustrating both early and late arriving photon trajectories is shown in Figure [6-2].

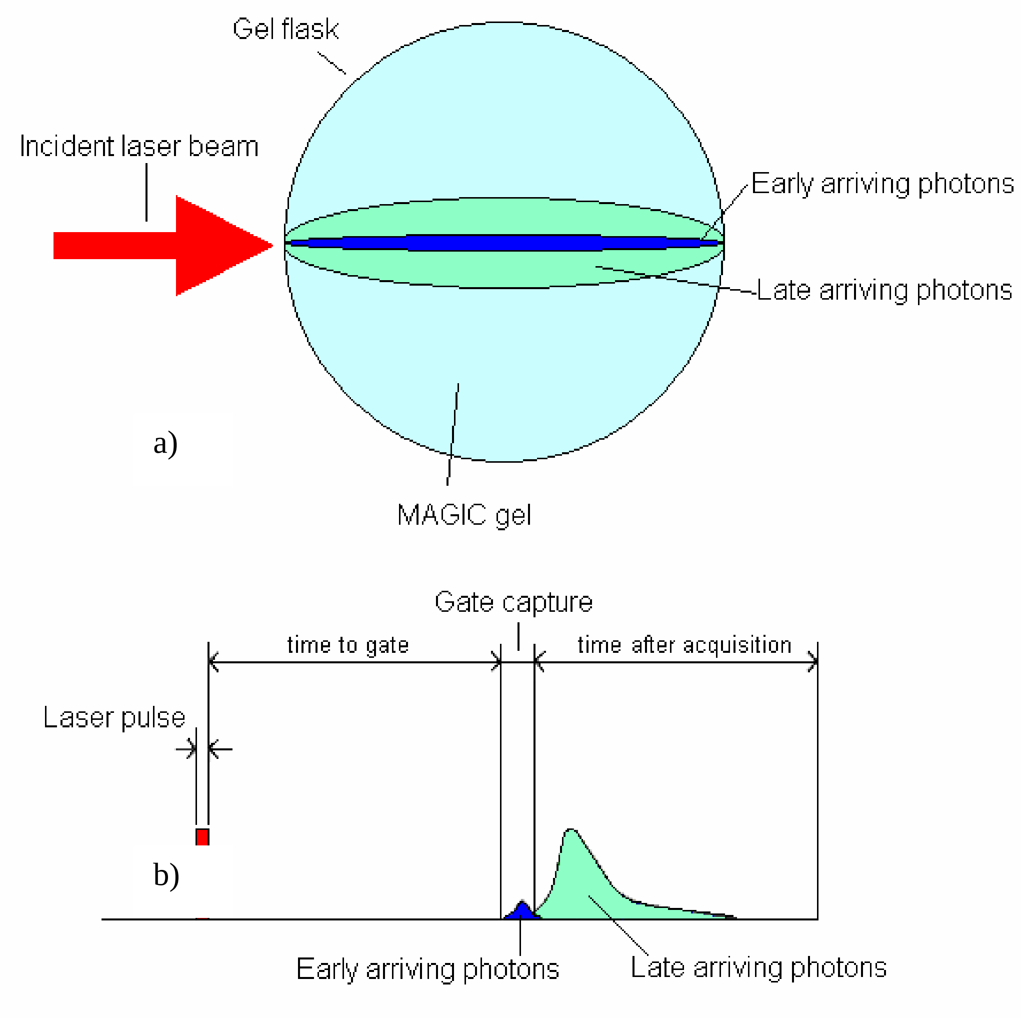

Figure [6-2] Schematic showing a) both early and late arriving photons passing through the highly scattering gel medium and b) the corresponding gated time acquisition required to collect the early arriving photons and neglect the pulse width broadened late arriving photons.

Of particular interest is the time range when the ballistic photons have completely traversed the gel flask. The photons would have followed an approximate straight line through the gel i.e. with minimal scattering effects.

For example, if we assume the refractive index of the gel flask has been averaged to *n* = 1.354 (used in Beam2 simulations) which would suggest the speed of light to be approximate to 2.22×10^8 ms^{-1}. If the diameter of the gel flask is approximately 0.1 m, the time taken for the light to traverse the diameter is calculated to be 451 ps. Therefore, to utilise the early arriving photons a detection window would be used that would only acquire data from t = 485 ps to t = 535 ps. To optimise the line integral data detected, the time window should be minimised to effectively gate the data acquisition. The scattered photons require a longer period of time to arrive at the detector than the ballistic photons and therefore will not be collected within the selected time gated detection window.

Appendix A Magnetic Resonance Imaging (MRI)

A.1 MRI Machine

The basic components of a MR unit are a very strong magnet, a radio transmitter, a radio frequency receiver coil, and a computer.

Most magnets have a magnetic field orientated parallel to the long axis of the patient, shown in Figure [A-1].

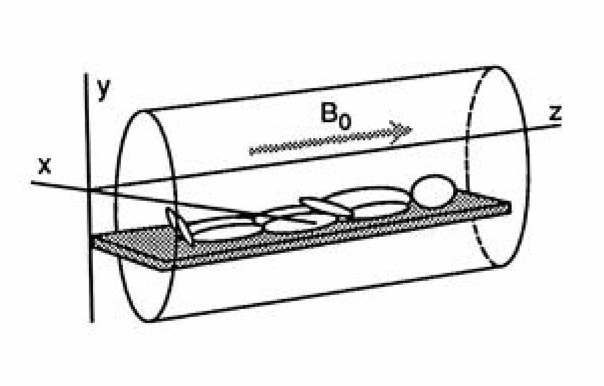

Figure [A-1] The MR magnet. Most magnets are electromagnets with a horizontal magnetic field (B_0). During imaging, the patient lies in the tunnel-shaped interior of the magnet. The z, x, and y co-ordinates are shown. Reproduced from http://www.medcyclopaedia.com/library/radiology/chapter04.

The magnetic field of the strong magnet is designated B_0, and is represented by a vector, i.e., an arrow whose orientation shows the direction of the magnetic field. The orientations within the magnet are shown by means of an imaginary frame of reference with three co-ordinates, z, x, and y. The z-direction is always the direction of the magnetic field, B_0, and when this field is parallel to the long axis of the patient, the horizontal axis perpendicular to z is named x, and the vertical axis is named y. The plane through x and y (the x-y plane) is thus orientated perpendicular to the magnetic field, B_0. The strength of the magnetic field is measured in tesla (T) of which values ranging bewteen 0.1 and 3.0 T are most commonly used.

A.1.1 Basic Physics

Magnetic resonance imaging exploits the fact that hydrogen nuclei, in this context often named protons, are tiny magnetic dipoles with a north pole and a south pole. Under normal circumstances these moments have no fixed orientation and so there is no overall magnetic field. However, when nuclei are placed in an external magnetic field, for example a patient placed in the MRI scanner, they begin to align in given directions dictated by the laws of quantum physics. For a hydrogen nucleus (a single proton with a spin quantum number, I = ½) two discrete energy levels (2I +1) are created; a higher energy level where the magnetic moments are opposing the external magnetic field, and a lower energy level in which the nuclei are aligned with the magnetic field (B_0). Under normal circumstances, a tiny majority of spins are in the latter energy state thereby creating a *net magnetisation* in the direction of the main magnetic field. The population difference, and therefore the sensitivity of the technique, can be altered by reducing the temperature or increasing the field.

In terms of classical physics, when the spin is placed in a magnetic field it precesses about that field in a motion analogous to a spinning top. The frequency of precession is governed by the Larmor equation:

$$\omega_0 = \gamma B_0 \tag{A-1}$$

where B_0 is the magnetic field and the frequency ω_0, depends on the gyromagnetic ratio, γ, of the particle. This ratio (ω_0/B_0) is specific to each type of magnetic atomic nucleus, and for the hydrogen nucleus, the ratio is equal to 42.58 MHz/Tesla. This means that at the magnetic field strengths used in MRI, the Larmor frequency of the hydrogen nucleus is in the radio frequency range (42.58 MHz at 1.0 Tesla).

This relationship is shown in Figure [A-2].

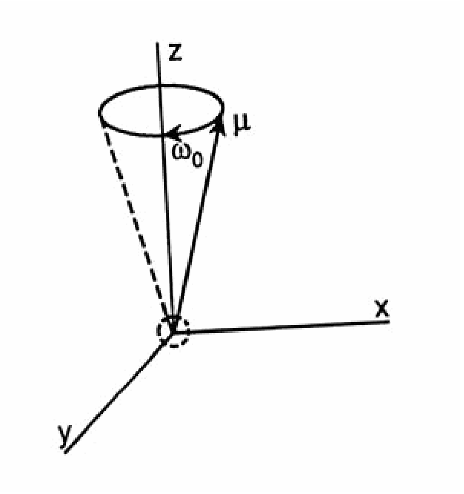

Figure [A-2] The magnetic moment of one proton is illustrated as a vector (μ). The vector indicates the direction of the proton magnetic field from south to north (the magnetic axis). In a strong, external magnetic field (B_0), the magnetic axis of the proton will rotate (precess) around the B_0 (z) direction, describing a cone-shaped figure. (The circle in the origin of the frame of reference indicates the proton.). Reproduced from http://www.medcyclopaedia.com/library/radiology/chapter04.

At first, the tissue magnetism has no precessional motion. Although the individual protons all precess, they are evenly distributed around the B_0 direction, leaving no magnetic component in the x-y plane. The surplus of parallel protons is proportional to the external magnetic field strength and determines size of **M**, the tissue magnetism. This is shown in Figure [A-3].

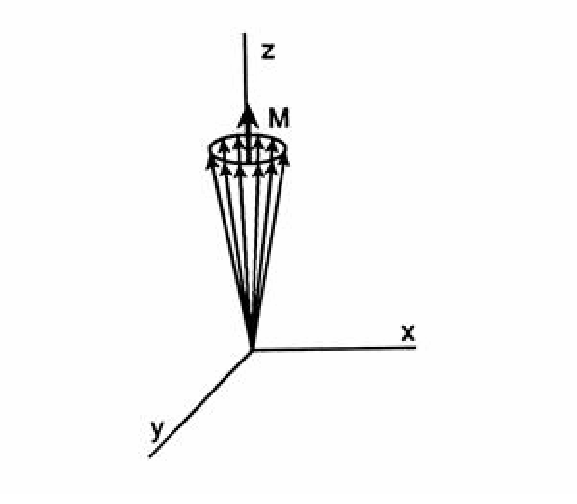

Figure [A-3] The tissue magnetism (**M**) is created by a surplus number of "parallel" protons. The magnetic vectors of the individual protons (thin arrows) are evenly distributed around the z-axis, and **M** is therefore oriented exactly in the z-direction.
Reproduced from http://www.medcyclopaedia.com/library/radiology/chapter04.

When the surplus parallel protons are rotated away from the B_0 direction, **M** must follow. The protons will continue to precess around the z-axis (they are forced to do so by the B_0 magnetic field), and **M** will consequently also start to precess around the z-axis (see Figure [A-4]). The strength and duration of the radio frequency pulse determine how many degrees **M** is rotated away from the B_0 direction, and the pulse is named accordingly.

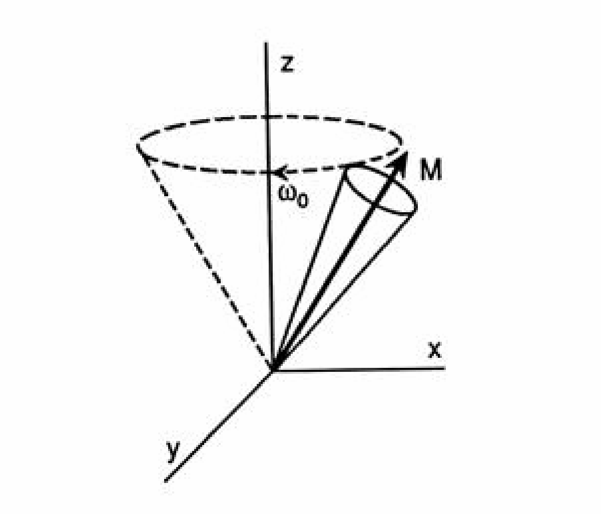

Figure [A-4] A 30° radio frequency pulse has rotated all x protons and **M** 30° away from z, in the clockwise direction. The continual proton precession around the z-axis results in the precession of **M** around the z axis also. Reproduced from http://www.medcyclopaedia.com/library/radiology/chapter04.

The result of a 90° pulse is thus that **M** (for a short period of time) will rotate in the x-y plane, perpendicular to the B_0 direction is shown in Figure [A-5].

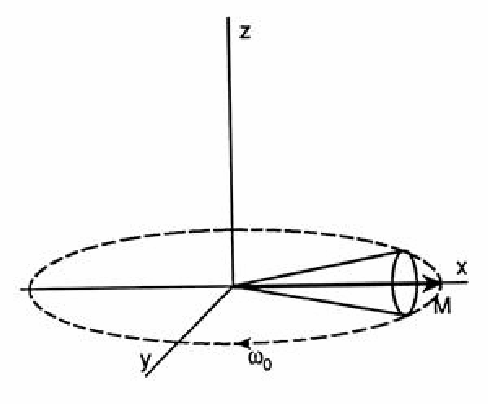

Figure [A-5] The result of a 90° pulse: **M** is precessing around z in the x-y-plane. Reproduced from http://www.medcyclopaedia.com/library/radiology/chapter04.

A.1.2 The MR Signal

Radio-frequeny (RF) waves contain both an electric and a magnetic field and are used to induce a current in a coil from the magnetism, **M**. When a short electromagnetic radio frequency pulse is transmitted into the tissue along the y-axis, for example, the magnetic field of the radio waves will force the magnetic moments of all the protons to rotate in a clock-wise direction around the y-axis. For this to happen, the frequency of the radio waves must be exactly equal to the Larmor frequency of the protons. This is the phenomenon termed magnetic resonance.

A receiver coil is placed on the outside of the anatomical region with its bore oriented towards the patient, perpendicular to the B_0 direction. When **M** rotates in the x-y plane, it will induce an electric current in the coil, and this electric current is called the MR signal (see Figure [A-6]). These (or similar) signals are used for reconstruction of sectional MR images.

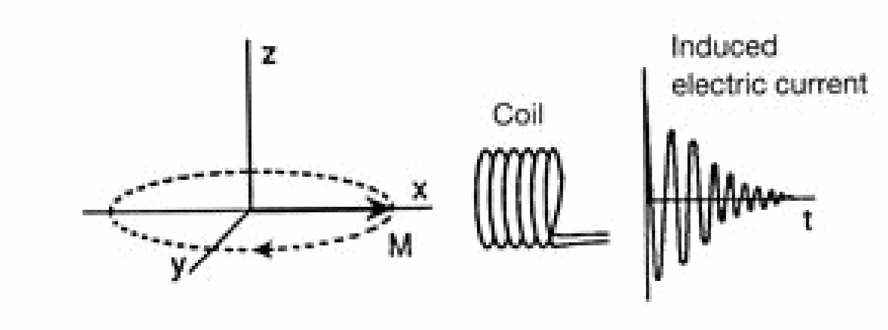

Figure [A-6] After the transmission of a 90° pulse, the tissue magnetism (**M**) is inducing an electric current (MR signal) in the receiver colt. The signal strength determines the shade of grey of the corresponding area in the final image.
Reproduced from http://www.medcyclopaedia.com/library/radiology/chapter04.

A.1.3 Image contrast: Proton Density, T_1, and T_2 Weighting

Contrast in MR images is determined by differences in tissue magnetisms, or more precisely, by the different strengths of magnetism that rotate in the x-y plane and induce currents in the receiver coil. Tissue magnetism is first of all determined by the proton density. Anatomic areas containing very few protons, such as air, will always induce very weak MR signals and therefore always appear dark in images. Water and other fluids, on the other hand, having a very high proton density, presumably should always appear bright in MR images. This is not completely true, as the contrast is also determined by other importasnt factors such as the T_1 and T_2 parameters.

To reconstruct an image, several MR signals are needed, and several RF pulses must therefore be transmitted. Between the pulse transmissions, the protons undergo both T_1 and T_2 relaxation processes.

The rapid decay of the induced signal seen in Figure [A-6], is partly the result of T_2-relaxation. The decay is a consequence of the gradual disappearance of the magnetism in the x-y plane, **Mxy**, caused by small differences in the local magnetic field strength. This loss of net magnetism in the x-y plane is called T_2 relaxation, and T_2 is defined as the time until **Mxy** has lost 63 % of its original, maximum value. Fluid and fluid-like tissues typically have a long T_2 (**Mxy** and the MR signal disappear slowly), and solid tissues and substances have a short T_2 (**Mxy** and the MR signal disappear rapidly).

T_1 relaxation is a slower process than T_2 relaxation, and involves the gradual alignment of the individual protons with the B_0 direction, thus restoring the situation prior to the 90° pulse (Figure [A-3]). During this process, the net magnetic moment along the z-axis, **Mz**, will increase from zero with ever decreasing speed until its maximum value, determined by the proton density in the tissue, is reached. T_1 is defined as the time until **Mz** has regained 63 % of its original, maximum value. The T_1 value is largely determined by molecular size and mobility. Generally, T_1 is shortest in tissues having molecules of medium size and mobility. Smaller, more mobile molecules (as in fluids) and larger, less mobile molecules (as in solids) have longer T_1 values.

By adjusting the time period between the RF pulses transmitted, the operator of a MR unit may decide whether image contrast should be determined mainly by proton density, T_1 or T_2. A certain time interval between the pulses is needed to allow regaining of **Mz**. The longer the time interval (up to a certain point), the larger the **Mz** to be rotated into the xy-plane by the next 90° pulse, and the stronger the MR signal induced. If the next 90° pulse is transmitted before completion of T_1 relaxation in the tissues, the size of **Mz** in the tissues will depend upon their T_1 values. This is shown in Figure [A-7].

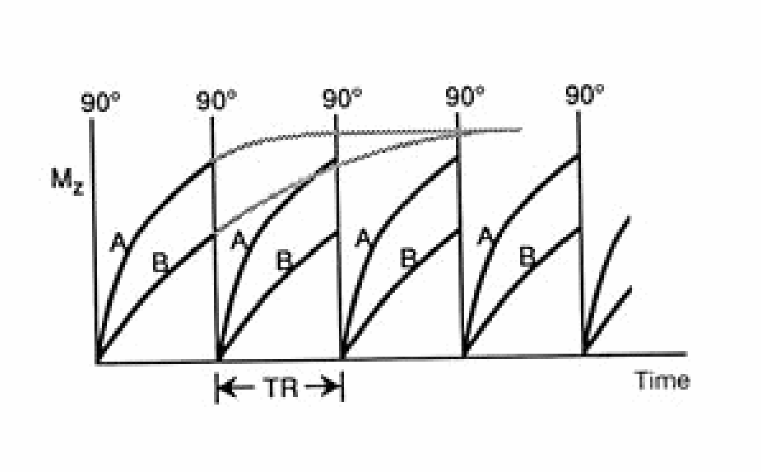

Figure [A-7] T_1 relaxation curves showing how the magnetism in the z-direction (**M**) in two different tissues (A and B) increase from zero after repetitive 90° pulses. The shaded parts of the first two relaxation curves indicate how **Mz** would have increased until maximum if the next 90° pulse had not been transmitted. The **Mz**'s of tissue A and B would have levelled out at the same maximum value, indicating similar proton densities in the two tissues. The repetition time (T_R) is so short; however, that T_1 relaxation is not completed when the next pulse is transmitted. At pulse transmission, tissue A, having the shortest T_1, will have regained a larger **Mz** than tissue B, and tissue A will therefore induce a stronger signal in the receiver coil after each 90° pulse. The difference in signal strength is caused by differences in T_1, hence the term T_1-weighted image.
Reproduced from http://www.medcyclopaedia.com/library/radiology/chapter04.

These tissues will therefore appear bright in the final image. Tissues with the longest T_1 will similarly induce the weakest signals. MR images where contrast is largely determined by differences in T_1, are called T_1-weighted images. The time interval between the radio frequency pulses is named repetition time (T_R), and T_1-weighted images are acquired with relatively short TRs.

By increasing the T_R, it is possible to achieve alternative T_2-weighted images. In T_2-weighted images, the brightest tissues are those having the longest T_2. For both types of contrast long TRs are needed to eliminate the effect of differences in T_1 on image contrast.

T_2-weighted contrast is achieved by introducing a time interval (called echo time, T_E) between the 90° pulse and the signal measurement. During this time interval, the size of **Mxy** is gradually reduced due to T_2 relaxation; slowly in tissues having a long T_2, more rapidly in tissues having a short T_2. The amplitudes of the induced MR signals recorded at the end of the echo time, will therefore reflect the differences in T_2 in the tissues. Thisd is shown in Figure [A-8].

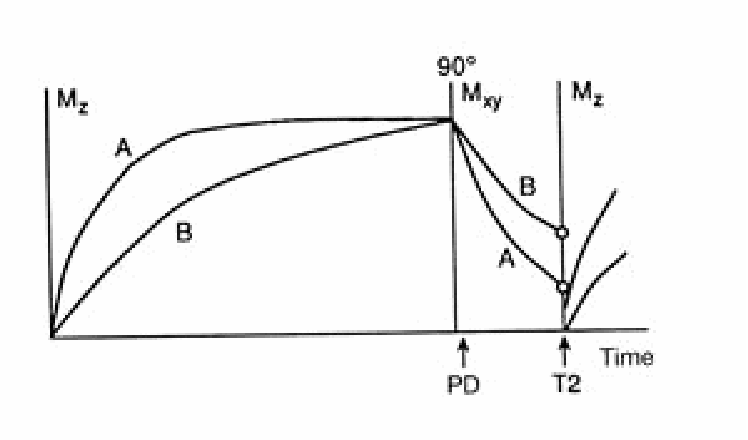

Figure [A-8] The increase of **Mz** and reduction of **Mxy** are shown for two tissues (A and B) having short T_1 and T_2 (A), and long T_1 and T_2 (B), respectively. After having recorded the MR signals, the waiting time until the next 90^o pulse is sufficiently long to complete T_1 relaxation in both tissues. The possible effect on contrast by differences in T_1 is thereby eliminated. Early signal registration provides proton density weighting (PD); late registration gives T_2-weighting (T_2). Reproduced from http://www.medcyclopaedia.com/library/radiology/chapter04.

It should be clear from the above that image contrast in MR imaging can be made much more variable than image contrast in alternative modalities such as computed tomography and ultrasonography. Image contrast is determined by operator-dependent parameters such as repetition time and echo time, and by tissue-dependent parameters such as proton density, T_1, and T_2. A basic knowledge of these parameters is necessary for proper evaluation of MR images.

A.1.4 Slice Selection, Magnetic Field Gradients

RF pulses will cause induction of MR signals only when the pulse frequency is exactly equal to the proton Larmor frequency. This fact makes it possible to collect MR signals from a predetermined thin slice of tissue. The first step towards slice selection is to create a magnetic field gradient through the ROI to be imaged. This is shown in Figure [A-9].

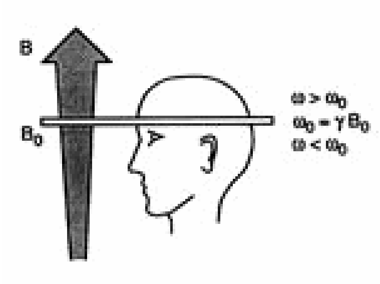

Figure [A-9]. By means of gradient coils, the external magnetic field increases linearly in the z-direction. Planes perpendicular to this magnetic field gradient have uniform magnetic field strength. Reproduced from http://www.medcyclopaedia.com/library/radiology/chapter04.

Special coils (gradient coils) create small additional magnetic fields with the result that the strength of the B_0 magnetic field increases linearly in one direction. The Larmor frequency of the protons is proportional to the magnetic field strength (see the Larmor equation), and the Larmor frequency will therefore increase linearly in the gradient direction. By transmitting radio frequency pulses having a predetermined narrow frequency range, MR signals will be recorded from only the thin slice of tissue that has a Larmor frequency range corresponding to the pulse frequency range. The orientation of the magnetic field gradients and therefore also the slice directions, are freely selectable.

A.1.5 Reconstruction of the MR Image

The tissue slice to be imaged, may be considered as consisting of several equally large volume elements, voxels. After each 90° pulse, every voxel has its own tissue magnetism (**Mxy**) which induces a signal in the receiver coil. The amplitude of the individual voxel signal is determined by the size of the voxel tissue magnetism, which again is determined by voxel dependent factors such as proton density, T_1, and T_2, and choice of repetition time and echo time. Each voxel corresponds to a picture element, pixel, in the final two-dimensional image. The brightness (shade of grey) of the pixel is determined by the signal amplitude induced by the magnetism in the corresponding voxel.

The MR signal recorded from a slice of tissue, is a composite signal induced by all the individual voxel magnetisms simultaneously. The MR computer needs to differentiate between the various voxel signals to assign the correct brightness to each pixel. To enable the computer to do so, each voxel signal must be given a unique and recognisable code. The code being used, is the frequency and phase of the voxel signal, which is determined by the frequency and phase of the rotating voxel magnetism (**Mxy**), The encoding is done by two magnetic field gradients, applied in the y- and x-direction, respectively (for axial slices). The gradients affect the rotation of the voxel magnetisms in such away that the resulting voxel signals are given a phase determined by the voxel location along the y-axis, and a frequency determined by the voxel location along the x-axis (see Figure [A-10]). As a result, each voxel is given a unique code of phase and frequency.

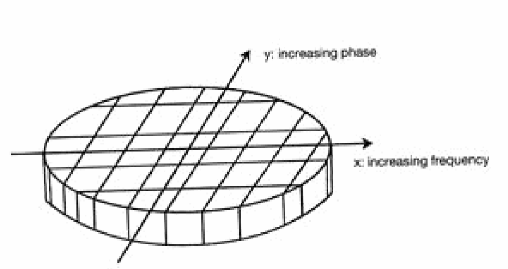

Figure [A-10] Part of a tissue slice in the x-y plane (axial slice) is shown with voxels. A brief magnetic field gradient in the y-direction applied between pulse transmission and signal registration provides the voxel signals with phases determined by the voxel locations in the y-direction. A magnetic field gradient in the x-direction applied during measurement of the MR signal provides the voxel signals with frequencies determined by the voxel locations in the x-direction. Reproduced from http://www.medcyclopaedia.com/library/radiology/chapter04.

To extract the various frequencies and phases contained in the composite MR signal, a complicated mathematical analysis termed two-dimensional Fourier transform is used. This method is dependent upon the information contained in numerous repetitive signals derived from the same slice, and this is the reason why "conventional" MR imaging is relatively time-consuming.

Appendix B   Software Control Programs

B.1   Scanning Program for Fan Beam Projection Data Acquisition

 # System Initialisation #

This initialises the PC30/D interface card and allocates the memory address used for data acquisition and storage in the DOS computer.

```
cls
dim limit as integer '181
%BASEADDR = &H700
%ADDATL   = &H700
%ADDSR    = &H701
%ADCCR    = &H702
%ADMDE    = &H703
%TMRCTR   = &H707
%PORTA    = &H708      ' Rotation
%PORTB    = &H709      ' Up/Down
%PCONTROL = &H70b
Dim  store(181)  as single
Dim  phia(181)  as single
Dim  heighta(181) as single
' Next counters holding absolute positions of all motors
shared FanCounter,HeightCounter,RotCounter
Shared FileName$
Fancounter=0
Rotcounter=0
HeightCounter=0
? " Data Logger Demo "
```

 # Initial scanner setup under manual control #

This allows the uses to manually position the scanner with respect top the size of flask to be imaged and degree of scanning interrogation required.

```
? " First move all stages to a starting point"
? " To adjust Height motor Press 'H'  "
? " To adjust Rotation motor Press 'R' "
? " To adjust Fan motor Press 'F'      "
?" Press 'G' to go on to data collection "
do
a$= ucase$(inkey$)          ‘Sets the on screen display parameters
   if a$ = "H" then
   locate 12,4:input;"Height steps + or -";Hstpe%
   moveheightmotor(hstpe%)
```

```
    a$ = "2"
    end if
  if a$ = "R" then
    locate 12,4:input;"Rotation steps + or -";Hstpe%
    moverotmotor(hstpe%)
    a$="2"
    end if
  if a$ = "F" then
    locate 12,4:input;"Fan steps + or -";Hstpe%
    moveFanmotor(hstpe%)
    a$="2"
    end if
    locate 12,4:?"                                  "
loop until a$ = "G"
cls
input;" Name of Data File ";FileName$
?
cls
? " Running......."
? " Press 'Q' to quit without losing data "
open "o",1,FileName$
```

 # Initialisation of the PC30/D data ports used for data acquisition #

```
 init_card

 initialize_ports_for_output
```

 # The individual projection settings required for the scan are input #

```
' moveheightmotor(300)
' moverotmotor(-200)
' move height 20 steps, do fan reading with 200 steps
for g% = 1 to 100            'projections at 1.8 degree increments
 for t% = 1 to 200
 a$=ucase$(inkey$)
 if a$ ="Q" then
  close
  cls
  ?" Aborted, data saved in ";Filename$
  end
  end if

 movefanmotor(1)             'Data is collected every step during fan beam motion'
 a$ =str$(read_adc)
 print #1,str$(heightcounter)+" , "+str$(FanCounter)+" , "+a$
 locate 4,4
 ? heightcounter,fancounter
```

```
 next t%
 movefanmotor(-200)
 moveheightmotor(20)
 next g%

 close
end

sub     initialize_ports_for_output()

          out %PCONTROL,&H080
end sub

sub MoveRotMotor(NumberofSteps)
   if Numberofsteps<0 then stp%=-1 else stp% =1
   if stp% = -1 then
   for T% = -1 to NumberofSteps step stp%

     out %PORTA,&H10     'Returns the base plate to the start point’
     dwell(1)
     out %PORTA,&H00
     dwell(1)
   decr RotCounter
   next t%
   else
 for T% = 1 to NumberofSteps step stp%
     out %PORTA,&H18      'Increments the base plate to the next projection point’
     dwell(1)
     out %PORTA,&H08
     dwell(1)
   incr RotCounter
   next t%
   end if

end sub

Sub MoveHeightMotor(NumberofSteps)
   if Numberofsteps<0 then stp%=-1 else stp% =1
   if stp%=-1 then
   for T% = -1 to NumberofSteps step stp%

     out %PORTA,&H18     'Returns the scanner to the vertical start point’
     dwell(4)
     out %PORTA,&H08
     dwell(4)
   decr HeightCounter
   next t%
   else
 for T% = 1 to NumberofSteps step stp%
     out %PORTA,&H01     'Increments the scanner to the next vertical scan point’
```

```
      dwell(4)
      out %PORTA,&H00
      dwell(4)

      incr HeightCounter
    next t%
    end if
end sub

Sub MoveFanMotor(NumberofSteps)
    if Numberofsteps<0 then stp%=-1 else stp% =1
     if stp% = -1 then
    for T% = -1 to NumberofSteps step stp%
      out %PORTB,&H18      'This returns the laser to the start point’
      dwell(4)
      out %PORTB,&H08
      dwell(4)
    decr FanCounter
    next t%
    else
 for T% = 1 to NumberofSteps step stp%
      out %PORTB,&H10       'This increments the laser for scanning’
      dwell(4)
      out %PORTB,&H00
      dwell(4)
    incr FanCounter
    next t%
  end if
end sub
```

 # Function for AD/DA conversion #

```
function read_adc() as single


  'chan=chan*16
  call init_adc()
  out %ADCCR,&H32
  out %ADCCR,&H33
  out %ADCCR,&H32
  do
  a% =inp(%ADDSR)
  loop until a% and &H40<>0
  a%=inp(%ADDSR)
  a%=a% and &H0f
  a%=a%*&H100
  b%=inp(%ADDATL)
  b%=a%+b%
  read_adc=(b%-2047)/(409.4)
```

```
  end function

sub init_adc()

   out %ADMDE,&H92
   out %ADCCR,&H02
   a%=inp(%ADDATL)
   do

   a%=inp(%ADDSR)
   loop until a% and &H40<>0
    for a% = 1 to 2000
    next a%
    a%=inp(%ADDATL)
    a%=inp(%ADDATL)
end sub

sub init_card()

  out %ADMDE,&H92
  out %TMRCTR,&H34
  out %TMRCTR,&H74
  out %TMRCTR,&Hb6
  out %ADCCR,&H02
  for t% = 1 to 9000
  next t%
  t%=inp(%ADDATL)
  t%=inp(%ADDSR)

end sub
sub dwell(x%)
do
    for t% = 1 to 20000
    next t%
    decr x%
loop until x% <0
    end sub
```

B.2 FILCONV Program

This program is used to restructure the single 1D array of raw data acquired from the PC30/D data acquisition card and is converted into a compatible two dimensional array for exportation into Matlab. The 2D matrix of projection data is then imported prior to the data processing and image reconstruction.

```
$huge
cls
locate 2,2
input;"Input data filename";filnam$
locate 4,2
input;"Output rearranged dat filename";ofil$


open "i",1,filnam$
first%=0
datcount% =0
blockcount% = 0
while not eof(1)
input#1,a$
if a$="" then
 incr blockcount%
 if first% = 0 then
   first%=1
   DataCount%=datcount%
 end if
 datcount% =0
else
 incr datcount%
end if
wend
close

?
? "Block Count = ";blockcount%
? "Data Count  = ";datacount%
bb%=blockcount%
dd% = datacount%

dim datapl(blockcount%,datacount%)

first%=0
datcount% =0
blockcount% = 0

open "i",1,filnam$
first%=0
```

```
datcount% =0
blockcount% = 0
while not eof(1)
input#1,a$
if a$="" then
 incr blockcount%
 if first% = 0 then
    first%=1
    DatCount%=dd%
 end if
 datcount% =0
else
 datapl(blockcount%,datcount%) = val(a$)
 incr datcount%
end if
wend
close


open "o",1,ofil$

for td% = 0 to dd%
for tb% = 0 to bb%
print #1,datapl(tb%,td%);" ";
next bb%
print #1,""
next td%
close
?
? " Program Finished "
end
```

Appendix C Image Processing Functions

C.1 Radon transform

Syntax

- R = radon(I,theta)
- [R,xp] = radon(...)

Description

R = radon(I,theta) returns the Radon transform R of the intensity image I for the angle theta degrees.

The Radon transform is the projection of the image intensity along a radial line oriented at a specific angle. If theta is a scalar, R is a column vector containing the Radon transform for theta degrees. If theta is a vector, R is a matrix in which each column is the Radon transform for one of the angles in theta. If you omit theta, it defaults to 0:179.

[R,xp] = radon(...) returns a vector xp containing the radial coordinates corresponding to each row of R.

The radial coordinates returned in xp are the values along the *x'*-axis, which is oriented at theta degrees counterclockwise from the *x*-axis. The origin of both axes is the center pixel of the image, which is defined as

- floor((size(I)+1)/2)

For example, in a 20-by-30 image, the center pixel is (10,15).

Class Support

I can be of class double, logical, or any integer class. All other inputs and outputs are of class double.

Example

- iptsetpref('ImshowAxesVisible','on')
- I = zeros(100,100);

- I(25:75, 25:75) = 1;
- theta = 0:180;
- [R,xp] = radon(I,theta);
- imshow(R,[],'Xdata',theta,'Ydata',xp,...
- 'InitialMagnification','fit')
- xlabel('\theta (degrees)')
- ylabel('x''')
- colormap(hot), colorbar

References

Bracewell RN, Two-Dimensional Imaging. Prentice Hall, Englewood Cliffs, NJ, 1995.

Lim JS, Two-Dimensional Signal and Image Processing. Prentice Hall, Englewood Cliffs, NJ, 1990.

Algorithm

The Radon transform of an image is the sum of the Radon transforms of each individual pixel, the superposition principle.

C.2 Iradon Transform

Compute inverse Radon transform

Syntax

- I = iradon(R,theta)
- I = iradon(R,theta,interp,filter,frequency_scaling,output_size)
- [I,H] = iradon(...)

Description

I = iradon(R,theta) reconstructs the image I from projection data in the two-dimensional array R. The columns of R are parallel beam projection data. iradon assumes that the center of rotation is the center point of the projections, which is defined as ceil(size(R,1)/2).

theta describes the angles (in degrees) at which the projections were taken. It can be either a vector containing the angles or a scalar specifying D_theta, the incremental angle between projections. If theta is a vector, it must contain angles with equal spacing between them. If theta is a scalar specifying D_theta, the projections were taken at angles theta = m*D_theta, where m = 0,1,2,...,size(R,2)-1. If the input is the empty matrix ([]), D_theta defaults to 180/size(R,2).

iradon uses the filtered back-projection algorithm to perform the inverse Radon transform. The filter is designed directly in the frequency domain and then multiplied by the FFT of the projections. The projections are zero-padded to a power of 2 before filtering to prevent spatial domain aliasing and to speed up the FFT.

I = iradon(P,theta,interp,filter,frequency_scaling,output_size) specifies parameters to use in the inverse Radon transform. You can specify any combination of the last four arguments. iradon uses default values for any of these arguments that you omit.

interp specifies the type of interpolation to use in the back projection. The available options are listed in order of increasing accuracy and computational complexity. The default value is enclosed in braces ({}).

Value	**Description**
'nearest'	Nearest-neighbour interpolation
{'linear'}	Linear interpolation
'spline'	Spline interpolation

Filter specifies the filter to use for frequency domain filtering. filter can be any of the strings that specify standard filters. The default value is enclosed in braces ({})

Value	**Description**
{'Ram-Lak'}	Cropped Ram-Lak or ramp filter. The frequency response of this filter is | f |. Because this filter is sensitive to noise in the projections, one of the filters listed below might be preferable. These filters multiply the Ram-Lak filter by a window that deemphasizes high frequencies.
'Shepp-Logan'	Multiplies the Ram-Lak filter by a sinc function
'Cosine'	Multiplies the Ram-Lak filter by a cosine function
'Hamming'	Multiplies the Ram-Lak filter by a Hamming window
'Hann'	Multiplies the Ram-Lak filter by a Hann window

Frequency_scaling is a scalar in the range (0,1] that modifies the filter by rescaling its frequency axis. The default is 1. If frequency_scaling is less than 1, the filter is compressed to fit into the frequency range [0,frequency_scaling], in normalized frequencies; all frequencies above frequency_scaling are set to 0.

output_size is a scalar that specifies the number of rows and columns in the reconstructed image. If output_size is not specified, the size is determined from the length of the projections.

- n = 2*floor(size(R,1)/(2*sqrt(2)))

If you specify output_size, iradon reconstructs a smaller or larger portion of the image but does not change the scaling of the data. If the projections were calculated with the radon function, the reconstructed image might not be the same size as the original image.

[I,H] = iradon(...) returns the frequency response of the filter in the vector H.

Class Support

R can be double or single. All other numeric input arguments must be of class double. I has the same class as R. H is double.

Example

- `P = phantom(512); % Shepp-Logan image`
- `imshow(P)`

- `theta = 0:179;    % projection angles`
- `[R, xp] = radon(P, theta);`

We can now display the resulting sinogram:

- `figure, imagesc(theta3,xp,R3); colormap(hot); colorbar`
- `xlabel('\theta'); ylabel('x\prime');`

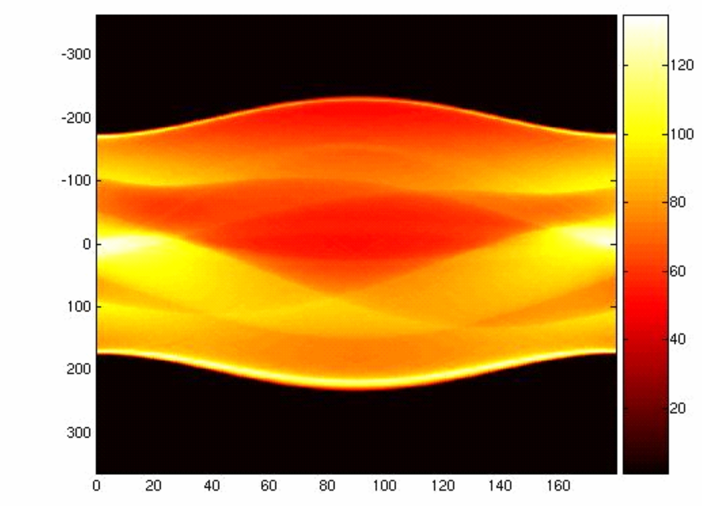

- `I = iradon(R,0:179,'nearest','Hann');`
- `imshow(P), figure, imshow(I)`

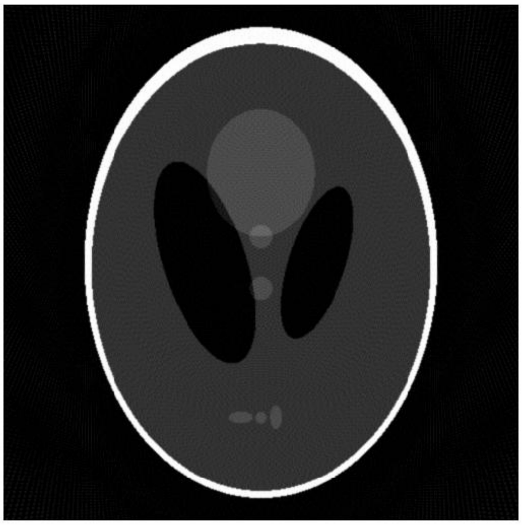

Algorithm

`iradon` uses the filtered back projection algorithm to perform the inverse Radon transform. The filter is designed directly in the frequency domain and then multiplied by the FFT of the projections. The projections are zero-padded to a power of 2 before filtering to prevent spatial domain aliasing and to speed up the FFT.

References

Kak, A. C., and M. Slaney, Principles of Computerized Tomographic Imaging. IEEE Press, New York, 1988.

Appendix D

Absolute Radiation Dose Verification using Magnetic Resonance Imaging I: Feasibility Study

Gary P. Liney PhD, Alan Heathcote BSc[*], Alan Jenner PhD*, Lindsay W. Turnbull MD, Andrew W. Beavis PhD[^].

Centre for MR Investigations, Hull Royal Infirmary, [*]Department of Physical Sciences, University of Hull, & [^]Department of Radiation Physics, Princess Royal Hospital, Hull, England.

Short Title: Dose Verification using MRI
Keywords: IMRT, Gel Dosimetry, MRI

Corresponding Author:
Dr Gary P. Liney
Centre for MR Investigations
Hull Royal Infirmary
Hull
England
HU3 2JZ
(01482) 674078
g.p.liney@hull.ac.uk

This work has been funded by a grant from Yorkshire Cancer Research

Abstract

This work describes the feasibility of using a polymer-based tissue equivalent gel for measuring radiation doses in situ. The gel is based on the MAGIC formulation thereby enabling it to be manufactured under normal atmospheric conditions. Its composition has been altered to achieve a similar sensitivity to the more widely used, but technically more difficult to produce, PAG gels. Irradiation of the gel material causes polymerization of the molecular structure resulting in a shortening of transverse relaxation time (T_2), which can be imaged using Magnetic Resonance Imaging (MRI). This work calibrates the radiation response in terms of transverse relaxation rate (R_2) and uses this information to provide absolute dose verification in a separate gel, which has been previously irradiated to a known configuration. Results demonstrate that this technique is able to verify radiation doses to within a few percent of delivered intent in three dimensions and with high spatial resolution. This work may be followed by anyone with an interest in the quality assurance of advanced conformal radiotherapy delivery methods.

Introduction

In conformal therapy an increase in the therapeutic ratio is sought; this can be achieved by an increase in control of the disease or by a reduction in the adverse affects to proximal normal tissues. The radiotherapy community is witnessing a revolution in radiotherapy technology whereby commercial planning and delivery solutions are enabling advanced conformal techniques such as Intensity Modulated Radiotherapy (IMRT) [1] to become more widely utilised. However, these advanced approaches to treatment delivery, with beams that dynamically change during their delivery, have rendered traditional quality control solutions inadequate. Currently, dose verification and quality assurance of IMRT is typically performed using appropriate x-ray film. This methodology is not ideal, due to its inherent two-dimensional limitations. Furthermore, the film has a much higher density than tissue and so very careful calibration techniques are required to gain accurate results [2]. Three-dimensional distributions can be measured by using phantoms incorporating a stack of films positioned at various planes, thereby recording doses with improved coverage. A true three-dimensional solution requires the ability to make measurements at much greater through-plane spatial resolution without the need to specifically construct test objects.

The use of tissue-equivalent gels to provide these dose measurements has been of interest to various research groups over the last few years. The gels are irradiated and subsequently characterised using some three-dimensional imaging modality, which in the vast majority of cases, has been Magnetic Resonance Imaging (MRI). Initially much work focused on so-called Fricke gels, which were comprised of an aqueous gel infused with Fricke ferrous sulphate solution [3]. The gel worked by producing free radicals from the radiolysis of water, which oxidised ferrous ions into ferric ions. The change in magnetic susceptibility caused by this process enabled the dose distributions to be demonstrated on MRI and these could be calibrated from the resulting change in T_1 relaxation time. Unfortunately these gels suffered from ferric ion diffusion following irradiation, which effectively blurred the dose distributions and limited their usefulness. This is especially important in modern IMRT delivery, where high spatial gradients can exist ‘everywhere’! Solutions to this problem have been to either reduce the diffusion mechanism by using PVA-based formulations [4] or acquiring much faster MRI measurements using calibrations based on relative signal changes rather than absolute T_1 measurements [5].

In 1994 Maryanski et al [6] introduced a new generation of polymer gels composed of acrylamide set in gelatin (referred to here and in the literature as PAG). These gels contain acrylic monomer units, which polymerise during irradiation and can be interrogated with MRI due to the resulting relaxation time shortening. These gels have several advantages over Fricke gels. Firstly, they are inherently more stable and can be used to produce calibration curves, which demonstrate little change in the slope or intercept over time [7]. Secondly, the gels are more sensitive to radiation than Fricke gels. Thirdly, the radiation-induced polymers are insoluble and the altered optical density of the gel permits a visual inspection of the irradiation and opens up the possibility of using a cheaper optical based scanning technique [8]. However, much of the work to date has investigated their use in conjunction with MRI. In MRI, both T_1 and T_2 relaxation times are affected, causing hyper- and hypointensity in the irradiated region respectively, although the latter effect is more pronounced. The radiation changes can be demonstrated with both MR imaging and spectroscopy [9] though our own experience has found that the dynamic range of the spectroscopy changes to be disappointing, with only a 10 % difference in spectral profile between 0 and 10 Gy [10].

The use of PAG gels is not without their own difficulties. Commonly used ingredients such as bis and acrylamide (BANG^{TM} gels) need careful handling, as the constituents are neurotoxins and carcinogens. Manufacturing and storage has to be in a strictly oxygen-free environment. This is to prevent the oxygen inhibition of the polymerisation process and has ultimately led to their limited clinical application as dosimeters. In order to simplify the production and reduce the sensitivity to oxygen new generations of polymer gels have been devised. Fong et al [11] introduced the first 'normoxic' gel in which a bivalent metal (copper) complexes with ascorbic acid in the presence of oxygen to generate free radicals which then initiates the polymerization process. In this case oxygen is required and the gels can be made and used without the earlier restrictions. This gel is known as MAGIC (Methacrylic acid, Ascorbic acid, Gelatin Instigated by Copper) and is the basis of the work described here. Fong et al showed that by altering the concentrations of methacrylic acid some alteration in the calibration characteristics could be observed.

This study has adapted Fong's work and produced a simple gel-dosimeter with improved sensitivity and extended linearity compared to PAG gels. A calibration has been obtained and this has been used to verify doses in a separate flask, which had been previously irradiated with a parallel pair of opposing beams. Results demonstrate the accuracy of the technique and the feasibility of using MRI for providing dose mapping at high spatial resolution. The intention of this paper is to illustrate the ease with which gel dosimetry may be performed and to stimulate interest in this field.

Methods

The MAGIC gel was prepared using the following ingredients: gelatin 300 bloom), 80 grams per litre (~ 8% by weight); hydroquinone, 1.8×10^{-2} M; ascorbic acid, 2.0×10^{-3} M; copper (II) sulphate pentahydrate 99.9%, 8.0×10^{-5} M; methacrylic acid 99%. The manufacturer of 1 litre of the gel (at a strength of methacrylic acid (MAA) of 9 %) can be summarized as follows. Firstly, 700 ml of water is heated to 50 °C and the gelatin added. Two grams of hydroquinone in 48 ml of distilled water is added at this stage and the mixture is allowed to cool. At 37 °C, 0.352 g of ascorbic acid in 50 ml of water and 0.020 g of copper sulphate in 30 ml of water is added. Finally 90 g of methacrylic acid is added and the mixture is transferred to suitable containers, which are then sealed and permitted to cool to room temperature and set into a translucent gel. While the quality of the glassware used is not important from the MR imaging point of view, we have chosen to use bottles from a specialized glass-blower rather than mass produced containers which are produced in two halves and as a result are of poor quality with vertical defects. This becomes a crucial consideration if an optical scanning technique is to be used, as is the case in a study we are running in parallel to this work. We have investigated various concentrations of MAA from 3 to 12 % in an attempt to reproduce the sensitivity of PAG gels.

It is crucial that both the calibration and verification stages use gel from the same batch. For the calibration step the gel is poured into several 125 ml bottles

(Wheaton Science Products, NJ, USA) with diameter × height of 48 × 112 mm. One of these is the control and is left unirradiated, while the remaining bottles were irradiated uniformly, using a parallel pair, to receive incremental doses from (typically) 4 to 30 Gy. The radiation was delivered using 6 MV x-ray beams from a Varian 600C Series Linear Accelerator. A separate large 500 ml glass flask ('test distribution flask' with diameter × height of 91 × 95 mm) filled with gel from the identical batch was irradiated using a parallel pair of 3 cm wide opposing beams to obtain a uniform dose of 5 Gy in the flask. The flask was then rotated through 90° and a second dose of 10 Gy. The combined effect produced a 'crossfire' of irradiated gel such that the centre of the cross received 15 Gy.

All MR imaging was performed on a 1.5 Tesla GE Signa scanner using a commercial radio-frequency head coil. Following initial sagittal localiser images, a T_2-mapping protocol was acquired as described in our previous work [12]. The sequence used was a dual-echo fast spin-echo (FSE) pulse sequence with four echoes acquired over two acquisitions (T_E/T_R = 30,105 & 60,180 ms). In the case of the 12 % MAA mixture this protocol was altered to make use of shorter echo times with T_E values of 20, 30, 70 and 90 ms. This was to account for the increased attenuation at the longer echo times and at doses greater than 20 Gy. In all cases a field-of-view of 24 cm was used with an image matrix of 256 × 256, giving an in-plane resolution of 0.9 mm. Images were obtained throughout the entire volume of the calibration vessels and the test distribution flask acquired in the coronal plane, with a slice thickness of 5 mm and an interslice gap of 1.5 mm. The total scan time of each FSE sequence was approximately 3 minutes, giving a total examination time for calibration and verification of 15 minutes.

Regions-of-interest (ROI) were defined in each of the calibration vessels at each slice location using Advantage Windows software (GE Medical Systems). Mean values of signal intensity were recorded at each echo time and the logarithm of the signal intensity determined. These values were fitted to the following equation using linear regression.

$$\ln S(T_E) = \ln S_0 - R_2(D) \cdot T_E \qquad [1]$$

where $S(TE)$ is the measured MR signal intensity at a given echo time, TE, S_0 the signal at TE = 0, and $R_2(D)$ is the transverse relaxation rate, being a function of dose. A calibration was established by plotting the estimated R_2 for each known dose value.

Images of the test distribution flask were then transferred to a Sun Workstation whereby in-house software was utilized to re-arrange the order of the image data and produce absolute dose maps. Pixel intensity values were used in the manner described above to determine R_2. These values were then used to infer dose, D, from the above calibration data as follows:

$$R_2(D) = R_2^0 + \frac{\Delta R_2}{\Delta D} \cdot D \qquad [2]$$

where R_2^0 is the intercept and $\frac{\Delta R_2}{\Delta D}$ is the slope of the fitted line to the calibration data respectively. As an indication of the sensitivity of each gel as a dosimeter the ratio of the slope of the fitted line to the intercept value was made [11].

After a period of three weeks a calibration was once again established in order to examine the stability of the gel. This was used to re-calculate the dose distributions in the test flask.

Results

Figure 1 illustrates the typical results obtained from the calibration of the dose response. Figure 1 (a) shows a T_2-weighted coronal image of the calibration vessels demonstrating the increased signal attenuation, which is observed with incremental dose. Figure 1 (b) gives example calibration plots of transverse relaxation rate (R_2) against known radiation dose for three batches of the MAGIC type gel dosimeter made with different concentrations of MAA. For comparison, our previously obtained data using a PAG-type gel [12] is also displayed on the same plot. In contrast to the PAG gel, which only demonstrates a linear dose-R_2 relationship below 10 Gy, the MAGIC gels have an effective range of up to 30 Gy. When linear regression was performed on each of the data (excluding the 10 Gy value for PAG) this gave R^2 = 0.98, 0.99 and 0.99 for the MAGIC gels and R^2 = 0.97 for the PAG gel. The equations of best fit gave the following values for slope and intercept; 0.26 and 4.08 (3 % MAA); 0.56 and 1.91 (9 % MAA); 1.19 and 5.25 (12 % MAA); 0.32 and 1.25 (PAG).

The plot also demonstrates the degree to which the dose response of the gel can be altered by varying the concentration of methacrylic acid. The ratio of the slope to intercept of each line was 0.06, 0.29 and 0.23 for the MAGIC gels using concentrations of 3.0 %, 9.0 % and 12 % respectively. The corresponding value for the PAG gel sample was 0.26.

Figure 2 demonstrates T_2-weighted coronal images acquired in the large test flask. The images correspond to echo times of (a) T_E = 30 ms, (b) 60 ms, (c) 105 ms and (d) 180 ms respectively. The actual dose values of each region are shown in Figure 2 (a). At the longer echo times, the relative doses can be discriminated (in the grey scales) due to the increased signal attenuation caused by the relaxation shortening effects of radiation-induced polymerisation. The signal-to-noise in all images was excellent, and even in the worst case (longest echo time, highest dose) it was three times that of the background signal enabling a good fit to the pixel data.

In Figure 3 the actual dose map is demonstrated using a colour scale with a minimum and maximum set at 0 and 15 Gy. This was calculated by fitting pixel intensity values to equation [1] and using the predicted R_2 values to infer the dose from equation [2]. The calibration in this particular batch (9 % MAA) revealed a value for the gradient and intercept of 0.51 and 2.06 respectively. Regions of interest were drawn in each of the areas corresponding to actual doses of 0, 5, 10 and 15 Gy and the corresponding calculated values were 0.7, 4.7, 9.1 and 15.4 Gy respectively. Figure 4 plots the dose profiles taken from regions of interest drawn in the map in Figure 3 across the 0 to 5 Gy, 0 to 10 Gy and 5 to 15 Gy boundaries respectively. The resolution of the dose edges (taken as the FWHM of the differentiation of the profile) is approximately 4.5 pixels (≈ 4 mm) in each case. After three weeks the calibration and verification flasks were re-scanned. The characteristics of the gel had changed considerably (slope and intercept equal to 1.04 and 7.3) and resulted in a decrease in verification accuracy; the agreement was only accurate to 20 %.

Discussion

This study has demonstrated the efficacy of using MRI gel dosimetry to accurately verify delivered intent. A technique, which is able to accurately verify radiation doses and demonstrate high dose gradients over a small distance, is essential if the full potential of advanced conformal treatments is to be realised. Much of the work in this area to date has used PAG gels to demonstrate dose distributions. Promising results have been obtained, although the majority of studies have only been able to show relative dose measurements with any degree of accuracy and have overestimated absolute values by between 18 and 24 % [9, 14]. In our own studies we have been able to demonstrate quite a wide range of accuracy with PAG gels (typically between 2 and 30 %) and ultimately decided to pursue other dosimeters due to their inherent difficulty in manufacture and the resulting poor reproducibility. Results shown here with MAGIC gels have improved on the sensitivity of PAG gels and also offer the advantage of the simplified manufacturing process and ease of use. These results, examining three dose regions, suggest an accuracy of at least 9 %. Furthermore the MAGIC gels provide an extended useful dose range compared to PAG gels. The stability of MAGIC gels also appears to be good with an optimum imaging time of 30 hours following irradiation being reported in one study [15]. We have shown that considerable changes occur in the MAGIC gel after three weeks, which reduced the verification accuracy even when a new calibration was acquired at this time.

Crucial to the success of this technique is the accuracy of the T_2 mapping sequence used as the basis of both the calibration and the verification. A study of some the various MRI sequences has been examined comparing the accuracy over a range of T_2 values between 140 – 700 ms [16]. This study assumed the dosimeter was PAG-based, but the T_2 values corresponding to MAGIC gels are somewhat smaller (see Figure 1). The reliability of the T_2 measurements will depend on the choice of pulse sequence and the range of echo times used to sample the signal decay. In this work we had to modify our echo times for the 12 % MAA gel in order to accommodate the rapid signal attenuation observed at high dose levels. We have previously demonstrated the accuracy of our FSE sequence in a clinical situation although it is important to ascertain the best sequence on each particular system. Assuming an expected T_2 measurement accuracy of 10 % and considering a gel sensitivity of 0.29 (M_9 in Figure 1 b), a dose resolution of approximately 0.5 Gy should be possible. Certainly, the FSE sequence provides inherently fast T_2-weighted images and can be used efficiently over a large volume coverage. For example, in our protocol up to 22 slices can be acquired in less than six minutes, which may be reduced to three minutes if a two-point calculation is required.

An important consideration in this work is the attainable spatial resolution. In this study an in-plane resolution of 0.9 mm was used in both the calibration and verification process. This has provided adequate signal to noise even for T_E = 180 ms and the highest dose values. By using a true 3D image acquisition (compared to multi-slice 2D imaging) a more isotropic resolution (typically 1 mm in each direction) could be realized albeit with a slight increased time penalty.

While the gels in their current formulation seem to provide excellent accuracy and reproducibility there is a great deal of potential for exploiting the Chemistry still further. For example the increased concentration of MAA has increased the slope of the calibration curve but at 12 % MAA this has also lead to an increased background polymerization, increasing the value of the intercept and therefore having a detrimental effect on sensitivity. This would therefore imply that there is an optimal value of MAA concentration, between 9 % and 12 %, in which the sensitivity is maximized. In addition there may be more suitable anti-oxidants to use rather than copper, which will further simplify the preparation and usefulness of these gels [17]. The rate of cooling needs further attention to minimise the inhomogeneities in the mixture that arise near the top of the containers. These can be seen in Figure 1 as irregular hypointense streaks in the gel and will result in tiny areas of artificially high dose in the final map. We are presently investigating the use of ice-cooling as a method of preventing these artefacts.

In our on-going work we are developing a complete quality assurance test object, including anatomically related compartments and markers for measuring image distortion [18]. It will also incorporate a removable gel flask for dose verification in the manner described above. In the future the current trend to move towards higher magnetic field strength will see further improvements in image signal-to-noise and therefore spatial resolution. This seems certain to extend the role of MRI in radiotherapy practice from treatment planning to dose verification.

Acknowledgements

The authors would like to express their gratitude to Yorkshire Cancer Research for providing a grant to fund this work.

References

1) Webb S. *Intensity Modulated Radiation Therapy* (Bristol: IOP Publishing), 2000.

2) Beavis AW, Weston SJ, Whitton VJ. Implementation of the Varian EDW into a commercial RTP system. *Phys. Med. Biol.* **41**(9):1691-704, 1996.

3) Gore JC, Kang YS, Schulz RJ. Measurement of radiation distribution by nuclear magnetic resonance (NMR) imaging. *Phys. Med. Biol.* **29**:1189-1197, 1984.

4) Chu KC, Jordan KJ, Battista JJ, Van Dyk J, Rutt BK. Polyvinyl alcohol-Fricke hydrogel; and cryogel:two new gel dosimetry systems with low Fe3+ diffusion. *Phys. Med. Biol*; **45**: 955-969, 2000.

5) Chu WC, Guo WY, Wu MC, Chung WY, Pan DHC. The radiation induced magnetic resonance imaging intensity change provides a more efficient three-dimensional dose measurement in MRI-Fricke-agarose gel dosimetry. *Med. Phys.* **25**: 2326-2332, 1998.

6) Maryanski MJ, Schulz RJ, Ibbott GS. Magnetic resonance imaging of radiation dose distributions using a polymer-gel dosimeter, *Phys. Med. Biol.* **39**:1437-1455, 1994.

7) Cosgrove VP, Murphy PS, McJury PS et al. The reproducibility of polyacrylamide gel dosimetry applied to stereotactic conformal radiotherapy. *Phys. Med. Biol.* **45**; 1195-1210, 2000.

8) Gore JC, Ranade M, Maryanski MJ, Schulz RJ. Radiation dose distributions in three dimensions from tomographic optical density scanning of polymer gels:I. Development of an optical scanner. *Phys. Med. Biol*. **41**: 2695-2704, 1996.

9) Murphy PS, Cosgrove VP, Schwarz AJ, Webb S, Leach MO. Proton spectroscopic imaging of polyacrylamide gel dosimeters for absolute radiation dosimetry, *Phys. Med. Biol.* **45**:835-845, 2000.

10) Liney GP, Manton DJ, Hutton J, Beavis A, Turnbull LW. MRI and MRS of radiation distributions using a polymer-gel dosimeter. *Proceedings 9th Meeting of the International Society for Magnetic Resonance in Medicine*; 903, 2001.

11) Fong PW, Keil DC, Dose MD, Gore JC. Development of “normoxic” polymer gels for MRI dosimetry. *Proceedings of DOSGEL 2001*, ISBN: 1 86435 549 2; 95.

12) Liney GP, Knowles AJ, Manton DJ, Turnbull LW, Blackband SJ, Horsman. Comparison of conventional single echo and multi-echo sequences with a fast spin-echo sequence for quantitative T_2 mapping: Application to the prostate. *J. Magn. Reson. Imag.* **6**:603-607, 1996.

13) Liney GP**,** Beavis AW, Goodby JW, Turnbull LW, Calibrating Radiotherapy Doses using MRI. *Magnetic Resonance Materials in Phys. Biol. Med.*; **15** (S1): 480, 2002.

14) Meeks SL, Bova FJ, Maryanski MJ. Image registration of BANG gel dose maps for quantitative dosimetry verification. *Int. J. Radiat. Oncol*. **43**:1135-1141, 1999.

15) De Deene Y, Venning A, Hurley C, Healy BJ, Baldock C. Dose-response stability and integrity of the dose distribution of various polymer gel dosimeters. *Phys. Med. Biol.* **47**:2459-2470, 2002.

16) Baustert IC, Oldham M, Smith TAD, Hayes C, Webb S, Leach MO. Optimised MR imaging for polyacrylamide gel dosimetry. *Phys. Med. Biol.* **45**: 847-858, 2000.

17) De Deene Y, Hurley C, Venning A et al. A basic study of some normoxic polymer gel dosimeters. *Phys. Med. Biol.* **47**:3441-3463, 2002.

18) Moore CS, Liney GP, Beavis AW. Quality assurance of CT and MR registration for radiotherapy planning of head and neck cancers. *Clin. Oncol*. **15**:S8, 2003.

Figure Legends

Figure 1 (a): A T_2-weighted image (T_E = 105 ms) of the calibration vessels. The control flask is left unirradiated (indicated by a marker) and the rest have received incremental doses in steps of 4 Gy (anticlockwise and inwards).

Figure 1 (b): Calibration plot of delivered radiation dose (Gy) against transverse relaxation rate (R_2) for different types of gel dosimeter. Results illustrate the difference in the linearity range of PAG gels (P; circles) compared to the MAGIC gels (M_3, M_9, and M_{12}; triangles corresponding to 3 %, 9 % and 12 % MAA (first three points only shown) respectively). The figure alongside each plot is the ratio of the slope to the intercept, which is an indication of sensitivity; the highest sensitivity of MAGIC gel was achieved using 9 % concentration of MAA.

Figure 2: A T_2-weighted image (T_E = 105 ms) acquired in a MAGIC gel sample which has been irradiated with two 5 Gy and 10 Gy beams to produce a cross configuration giving an isodose of 15 Gy at the centre of the sample. The images are acquired with increasing echo times (T_E = (a) 30 ms, (b) 60 ms, (c) 105 ms & (d) 180 ms) and demonstrate increased signal attenuation with increasing dose. These separate echo images enable the transverse relaxation rate to be measured on a pixel-by-pixel basis ($R_2 = 1/T_2$).

Figure 3: A calculated dose map from the data in Figure 2. By fitting to the signal decay shown in Figure 2 and obtaining a map of R_2, the calibration data can be used

to infer a map of absolute radiation dose. A colour scale from 0 to 15 Gy is also shown.

Figure 4: A plot of dose profiles taken across the image in Figure 3 (indicated by insert) illustrating dose changes from 0-5 Gy, 0-10 Gy and 5 –15 Gy. The dashed line indicates values within ± 10 % of each isodose.

Figure 1

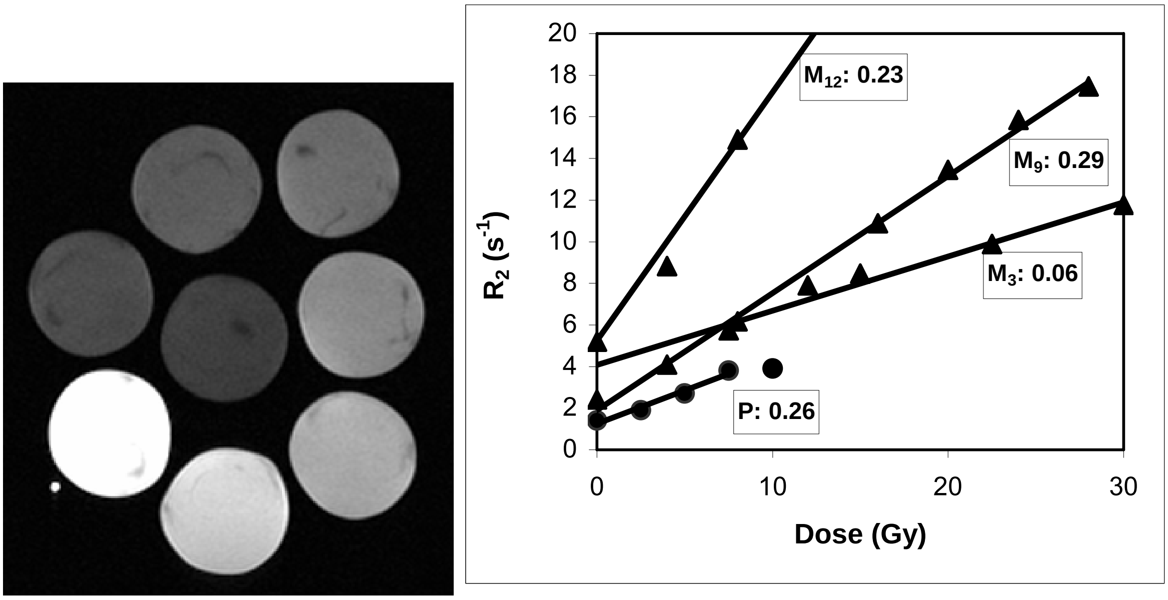

Figure 2

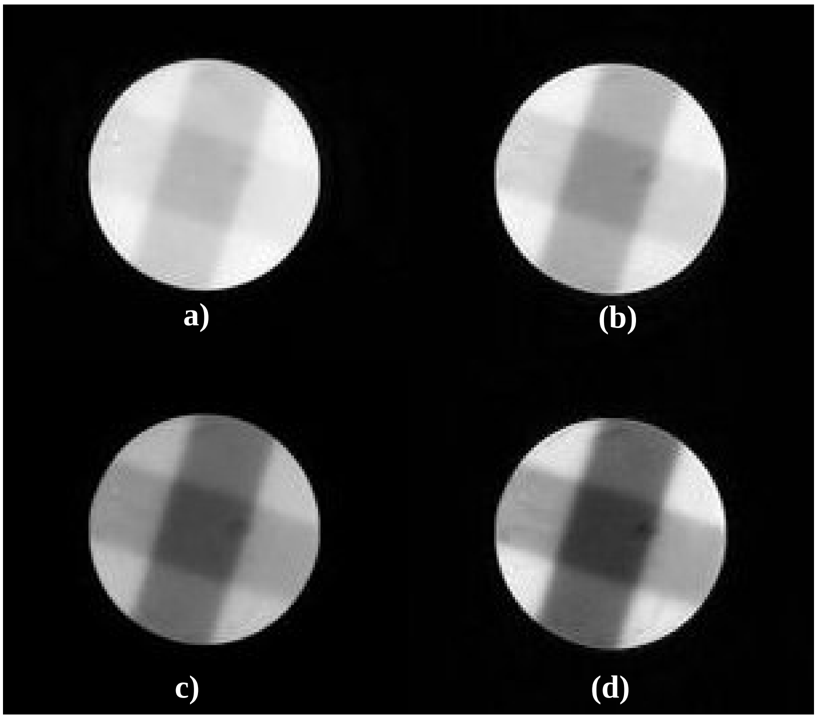

Figure 3

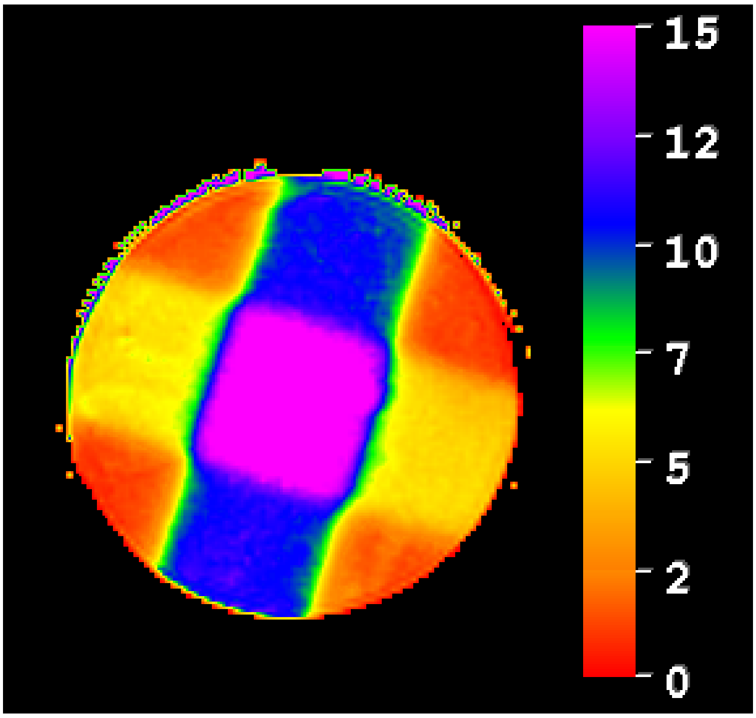

Figure 4

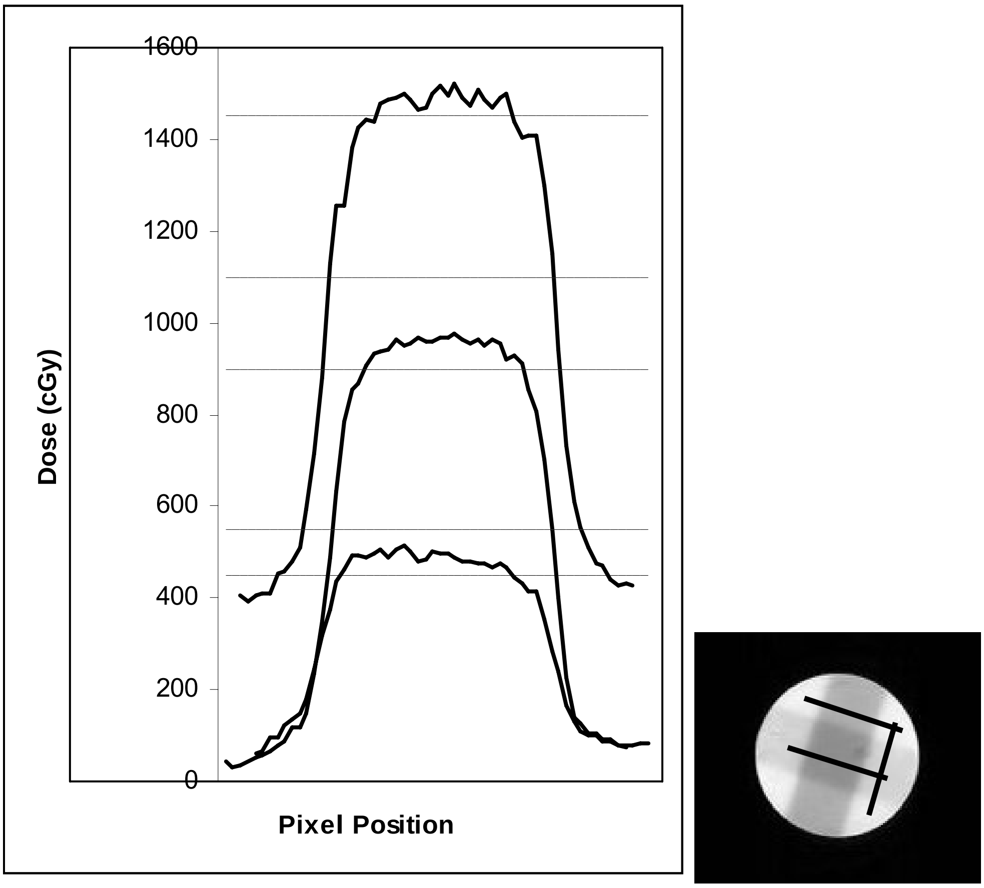

References

Adamovics J. and Maryanski MJ, New 3D radiochromic solid polymer dosimeter from leuco dyes and a transparent polymeric matrix. *Med. Phys.* **30** 1349, 2003.

Alexander P, Charlesby A and Ross M. The degradation of solid polymethylmethacrylate by ionizing radiations. *Proceedings of the Royal Society* **A223** 392, 1954.

Allen AO, The radiation chemistry of water and aqueous solutions. D. Van Nostrand Co., Princeton, 1961.

Ambrose J and Hounsfield G, Computerised transverse axial tomography.*Br.J. Radiol.* **46** 148, 1972.

Andrews H, Murphy R and Lebrun E, Gel dosimeter for depth-dose measurements. *The Review of Scientific Instruments*. **28** 329, 1957.

Appleby A and Leghrouz A, Imaging of radiation dose by visible colour development in ferrous-agarose-xylenol orange gels. *Med. Phys.* **18** 309, 1991.

Audet C and Schreiner LJ. Radiation dosimetry by NMR relaxation time measurement of irradiated polymer solutions. *Proc Soc Magn Reson Med.* 10th Annual Scientific Meeting; 705, 1991.

Baldock C, Burford RP, Billingham N, Wagner GS, Patval S, Badawi RD and Keevil SF, Experimental procedure for the manufacture and calibration of polyacrylamide gel (PAG) for magnetic resonance imaging (MRI) radiation dosimetry. *Phys. Med. Biol.* **43** 695, 1998.

Baldock C, Rintoul L, Keevil SF, Pope JM and George GA, Fourier transform Raman spectroscopy of polyacrylamide gels (PAGs) for radiation dosimetry. *Phys. Med. Biol.* **43**(12) 3617, 1998.

Baldock C, Historical overview of the development of gel dosimetry: a personal perspective, *J. Phys. Conf: Ser* **56** 14**,** 2006.

Boni AL, A polyacrylamide gamma dosimeter, *Radiation Research* **14** 374, 1961.

Brahme A, Dosimetric precision requirements in radiation therapy. *Acta. Radiol. Oncol.* **23** 379, 1984.

Brandrup J, Immergut EH and Grulke EA, Polymer handbook. 4th Edition, Wiley, New York, 1999.

Brindha S, Venning AJ, Hill B and Baldock C, Experimental study of attenuation properties of normoxic polymer gel dosimeters. *Phys. Med. Biol.* **49** N353, 2004.

Cosgrove VP, Murphy PS, McJury PS, The reproducibility of polyacrylamide gel dosimetry applied to stereotactic conformal radiotherapy. *Phys. Med. Biol.* **45** 1195, 2000.

Chu W, Guo W, Wu M, Chung W and Pan H, The radiation induced magnetic resonance image intensity change provides a more efficient three-dimensional dose measurement in MRI-Fricke-agarose gel dosimetry. *Med. Phys.* **25** 2326, 1998.

Chu KC, Jordan KJ, Battista JJ, Van Dyk J and Rutt BK, Polyvinyl alcohol-Fricke hydrogel; and cryogel: two new gel dosimetry systems with low Fe^{3+} diffusion. *Phys. Med. Biol.* **45** 955, 2000.

Chu WC, Guo WY, Wu MC, Chung WY and Pan DHC, The radiation induced magnetic resonance imaging intensity change provides a more efficient three-dimensional dose measurement in MRI-Fricke-agarose gel dosimetry. *Med. Phys.* **25** 2326, 1998.

Clow H and Young IR, Britain's brains produce first NMR images. *New Scientist*. **80** 588, 1978.

Damadian RV, Apparatus and method for detecting cancer in tissue, US Patent 3789832, filed 17th March 1972.

Day MJ and Stein G, Chemical effects of ionising radiation in some gels. *Nature*. **166** 141, 1950.

De Deene Y, De Wagter C, Van Duyse B, Derycke S, De Neve W and Achten E, Three dimensional dosimetry using polymer gel and magnetic resonance imaging applied to the verification of conformal radiation therapy in head-and-neck cancer. *Radiother. Oncol.* **48** 283, 1998.

De Deene Y, Hanselaer P, De Wagter C, Achten E and De Neve W, An investigation of the chemical stability of a monomer/polymer gel dosimeter *Phys. Med. Biol.* **45** 859, 2000.

De Deene Y, Hurley C, Venning A, Vergote K, Mather M, Healy BJ and Baldock C, A basic study of some normoxic polymer gel dosimeters. *Phys. Med. Biol.* **47** 3441, 2002.

De Deene Y, Vergote K, Claeys C and DeWagter C, The fundamental radiation properties of normoxic polymer gel dosimeters: a comparison between a methacrylic acid based gel and acrylamide based gels. *Phys. Med. Biol.* **51** 653, 2006

Doran S and Krstajić N, The history and principles of optical tomography for scanning 3-D radiation dosimeters. *J. Phys. Conf: Ser*. **56** 45, 2006.

Duzenli C, Sloboda R and Robinson D, A spin-spin relaxation rate investigation of the gelatin ferrous sulphate NMR dosimeter. *Phys. Med. Biol.* **39** 1577, 1994.

Fong PW, Keil DC, Dose MD and Gore JC, Development of normoxic polymer gels for MRI dosimetry. Proceedings of DOSGEL 2001, ISBN: 1 86435 549 2, 95, 2001.

Fricke H and Morse S, The chemical action of Roentgen rays on dilute ferrosulphate solutions as a measure of dose. *Am. J. Roentgenol. Radium Therapy. Nucl. Med.* **18** 430, 1927.

Gochberg DF, Kennan RP, Maryanski MJ and Gore JC, The role of specific side groups and pH in magnetization transfer in polymers. *J. Magn. Reson.* **131** 191, 1998.

Gore JC, Kang YS and Schulz RJ, Measurement of radiation distribution by nuclear magnetic resonance (NMR) imaging. *Phys. Med. Biol.* **29** 1189, 1984.

Gore JC, Ranade M, Maryanski MJ and Schultz RJ, Radiation dose distributions in 3 Dimensions from tomographic optical density scanning of polymer gels: 1 Development of an optical scanner. *Phys. Med. Biol.* **41**(12) 2695, 1996.

Gupta BL, In dosimetry in agriculture, industry, biology and medicine. IAEA, Vienna, 421, 1973.

Gupta BL and Gomathy KR, Consistency of ferrous sulphate benzoic orange dosimeter. *Int J Appl. Radiat. Isot.* **25** 509, 1974.

Gupta BL, Bhat RM, Gomathy KR, and Susheela B, Radiation chemistry of ferrous sulphate-benzoic acid-xylenol system. *Radiat. Res* .**75** 269, 1978.

Gupta BL, Bhat RM, Naryan GR and Susheela B, Acid and xylenol orange effects in the FBX dosimeter. *Int J Appl. Radiat. Isot.* **34** 887, 1983.

Haraldsson P, Back SAJ, and Magnusson P, Dose response characteristics and basic dose distribution data for a polymerization-based dosimeter gel evaluated using MR. *Brit. J. Radiol* **73** (865): 58, 2000.

Hawkes RC, Holland GN, Moore WS and Worthington BS, NMR tomography of the brain: a preliminary clinical assessment with demonstration of pathology. *J. Comput. Assist. Tomogr.* **4**(5) 577, 1980.

Hazel J, Hefner L, Nyerick C, Wilson L, and Boyer A, Dose-response characteristics of a ferrous-sulphate-doped gelatin system for determining radiation absorbed dose distributions by magnetic resonance imaging (Fe MRI). *Phys. Med. Biol.* **36** 1117, 1991.

Hurley C, Venning A and Baldock C, A study of normoxic polymer gel dosimeter comprising methacrylic acid, gelatin and tetrakis (hydroxymethyl) phosphonium chloride (MAGAT). *Appl. Radiat. Isot.* **63** 443, 2005.

Hoecker FE and Watkins IW, Radiation polymerisation dosimetry. *Int J Appl Rad Iso*. **3** 31, 1958.

Ibbott GS, Maryanski MJ, Eastman P, Holcomb SD, Zhang YS, Avison RG, Sanders M and Gore JC, 3D visualisations and measurements of conformal dose distributions using MRI of BANG gel dosimeters. *Int J Rad Oncol. Biol Phys.* **38**(5) 1097, 1997.

Jirasek A, Hilts M, Shaw C and Baxter P, Investigation of tetrakis hydroxymethyl phosphonium chloride as an antioxidant for use in x-ray computed tomography polyacrylamide gel dosimetry, *Phys.Med. Biol.* **51** 1891, 2006.

Jordan K, Development issues for optical CT and gel dosimetry. Proc of the 1st Int Workshop on Radiation therapy gel dosimetry. Lexington, July 1999, USA ISBN 0-9684873-1-9, 1999.

Kak AC and Slaney M, Principles of Computerized Tomographic Imaging. IEEE Press, New York, 1988.

Kelly RG, Jordan KJ and Batista JJ, Optical CT reconstruction of 3D dose distributions using ferrous benzoic xylenol (FBX) gel dosimeter. *Med. Phys.* **25** 1741, 1998.

Kron T, Jonas D and Poppe J, Fast T1 imaging of dual gel samples for diffusion measurements in NMR dosimetry gels. *Magn. Reson. Imaging.* **15** 211, 1997.

Kron T, Radiation therapy requirements: What do we expect from gel dosimetry. QUT, Brisbane, 2001.

Lepage M, Whittaker AK, Rintoul L and Baldock C, ^{13}C-NMR, ^{1}H-NMR and FT Raman study of radiation-induced modifications in radiation dosimetry polymer gels. *J. Appl. Polym. Sci.* **79** 1572, 2001.

Liney GP, Knowles AJ, Manton D, Turnbull LW and Blackband SJ, Comparison of conventional single echo and multi echo sequences with a fast spin echo sequence for quantitative T2 mapping: Application to the prostate. *J. Magn. Reson. Imag.* **6** 603, 1996.

MacDougall ND, Pitchford WG and Smith MA, A systematic review of the precision and accuracy of dose measurements in photon radiotherapy using polymer and Fricke MRI gel dosimetry. *Phys. Med. Biol.* **47** R107, 2002.

Magee JL and Chatterjee A, Track reactions of radiation chemistry. In: Freeman GR Kinetics of Non-homogeneous Processes, Chapter 4 (John Wiley & Sons, New York), 1996.

Mansfield P, Pykett IL, Morris PG and Coupand RE, Human whole body line-scan imaging by NMR. *Brit. J. Radiol.* **51** 921, 1978.

Maryanski MJ, Gore JC and Schulz RJ, 3-D radiation dosimetry by MRI: solvent proton relaxation enhancement by radiation-controlled polymerisation and cross-linking in gels. *Proc. Intl. Soc. Mag. Reson. Med,* 1992.

Maryanski MJ, Gore J, Kennan R and Schulz R, NMR relaxation enhancement in gels polymerized and cross-linked by ionizing radiation: A new approach to 3D dosimetry by MRI. *Magn. Reson. Imaging.* **11** 253, 1993.

Maryanski MJ, Schultz RJ, Ibbott GS, Gatenby JC, Xie J, Horton D and Gore JC, Magnetic resonance imaging of radiation dose distributions using a polymer-gel dosimeter. *Phys. Med. Biol.* **39** 1437, 1994.

Maryanski MJ, Zastavker YZ and Gore JC, Radiation dose distributions in 3D from tomographic optical density scanning of polymer gels: 2. Optical properties of the BANG polymer gel. *Phys. Med. Biol.* **41** 2705, 1996.

Maryanski MJ, Audet C and Gore JC, Effects of crosslinking and temperature on the dose response of a BANG polymer gel dosimeter. *Phys. Med. Biol.* **42** 303, 1997.

Mather ML, De Deene Y, Whitakker AK, Simon GP, Rutgers R and Baldock C, Investigation of ultrasonic properties of PAG and MAGIC polymer gel dosimeters. *Phys. Med. Biol.* **47** 4397, 2002.

Mather ML and Baldock C, Ultrasound tomography imaging of radiation dose distributions in polymer gel dosimeters. *Med. Phys.* **30** 2140, 2003.

McJury M, Oldham M, Cosgrove VP, Murphy PS, Doran S, Leach MO and Webb S, Radiation dosimetry using polymer gels: methods and applications, (Review article). *Brit. J. Radiol.* **73** 919, 2000.

Moore CS, Liney GP, Beavis AW. Quality assurance of CT and MR registration for radiotherapy planning of head and neck cancers. *Clin. Oncol.* **15**:S8. 2003.

Oldham M, McJury M, Baustert IB, Webb S and Leach MO, Improving calibration accuracy in gel dosimetry. *Phys. Med. Biol.* **43**(10) 2709, 1998.

Oldham M, Siewerdsen H, Kumar S, Wong J and Jaffray DA, Optical CT gel dosimetry 1: basic investigations. *Med. Phys.* **30**(4) 623, 2003.

Olsson L, Petersson S, Ahlgren L, and Mattson S, Ferrous sulphate gels for determination of absorbed dose distributions using MRI technique: basic studies. *Phys. Med. Biol.* **34** 43, 1989.

Olsson L, Westrin B, Fransson A, and Nordell B, Diffusion of ferrous ions in agarose dosimeter gels. *Phys. Med. Biol.* **37** 2243, 1992.

De Pasquale F, Sebastiani G, Egger E, Guidoni L, Luciani A, Marzola P, Manfredi R, Pacilio M, Piermattei A, Viti V and Barone P, Bayesian estimation of relaxation times T1 in MR images of irradiated Fricke-agarose gels*. J. Magn. Reson. Imaging.* **18** 721, 2000.

Ramm U, Damrau M, Thilmann C, Bottcher HD, Kramer M, Geiss O, Kraft G, Ahlswede J, Bock M and Schad L, 3D heavy ion dosimetry using MRI of polymer gels. Proc of the first Int Workshop on radiation therapy gel dosimetry, Lexington, July 1999, USA ISBN 0-09684873-1-9.

Reddy GG, Nagabhushanam T and Santappa M, Oxygen-ascorbic acid-copper (II) initiating system. A kinetic study of the polymerisation of methyl acrylate in aqueous medium. *Makromol. Chem.* **183** 905, 1982.

Rintoul L, Lepage M and Baldock C, Radiation dose distributions in polymer gels by Raman spectroscopy. *Appl. Spectrosc.* **57** 51, 2003.

Rousseau J, Gibon G, Serrazin T, Doukhan N and Marchandise X, Magnetic resonance imaging of agarose gel phantom for assessment of three-dimensional dose distribution in linac radiosurgery. *Brit. J. Radiology.* **67** 646, 1994.

Senden RJ, De Jean P, McAuley KB and Schreiner LJ, Polymer gel dosimeters with reduced toxicity: a preliminary investigation of the NMR and optical dose–response using different monomers. *Phys. Med. Biol.* **51** 3301, 2006.

Schreiner JL Editor, 1999, Proc of the 1st Int Workshop on radiation therapy gel dosimetry. Lexington, July 1999, USA, ISBN 0-9684873-1-9.

Shortt KR, Fundamentals of fricke dosimetry, *J. Phys. Conf: Ser.* **3** 10**,** 2001.

Schulz R, Maryanski M, Ibbott G, and Bond J: Assessment of the accuracy of stereotactic radiosurgery using Fricke-infused gels and MRI. *Med. Phys*. **20** 1731, 1993.

Spevacek V, Novotny J, Dvorak P, Vymazal J and Cechak T, Temperature dependence of polymer-gel dosimeter nuclear magnetic resonance response. *Med. Phys.* **28** 2370, 2001.

Spinks JWT and Woods RJ, An introduction to radiation chemistry. John Wiley & Sons, New York, 1964.

Swallow AJ, Radiation chemistry: an introduction. Longman Group Limited, London, 1973.

Taqui Khan MM and Martell AE, Metal Ion and chelate catalyzed oxidation of ascorbic acid by molecular oxygen: 1. cupric and ferric Ion catalyzed oxidation. *J. Am. Chem. Soc.* **89** 4176, 1967.

Tarte BJ, Jardine PA and Van Doorn T, Laser scanned agarose gel sections for radiation field mapping, *Int. J. Radiat. Oncol. Biol. Phys.* **36** 175, 1996.

Tarte BJ, Jardine PA, vanDoorn T, Nitschke KN and Poulsen MG, Development of a CCD array imaging system for measurement of dose distributions in doped agarose gels. *Med. Phys.* **24**(9) 1521, 1997.

VanDyk J, Barnett R, Cygler J and Shragge P, Commissioning and quality assurance of treatment planning computers. *Int. J. Radiat. Oncol. Biol. Phys.* **26** 261, 1993.

Venning A, Healy B, Nitschke K and Baldock C, Investigation of the MAGAS normoxic polymer gel dosimeter with Pyrex glass walls for clinical radiotherapy dosimetry. *Nuclear Inst. and Methods in Physics Research A* **555** 396, 2005a.

Venning AJ, Nitschke KN, Keall PJ and Baldock C, Radiological properties of normoxic polymer gel dosimeters. *Med. Phys.* **32** 1047, 2005.

Vergote K, De Deene Y, Vanden Bussche E and De Wagter C, On the relation between the spatial dose integrity and the temporal instability of polymer gel dosimeters. *Phys. Med. Biol.* **49** 4507-4522, 2004.

Watanabe Y, Perera GM and Mooij RB, Image distortion in MRI-based polymer gel dosimetry of gamma knife stereotactic radiosurgery systems. *Med. Phys.* **29** 797-802, 2002.

Webb S, The Physics of Medical Imaging. IOP Publishing Ltd, 1988.

Webb S, From the watching of shadows: the origins of radiological tomography. Bristol. TOP Publishing, 1990.

Whittaker AK, A discussion of the factors influencing the polymerisation processes in polymer gel dosimeters. *J. Phys. Conf: Ser* **3** 23**,** 2001.

WWW references:

http://science.cancerresearchuk.org/
http://www.geocities.jp/nekoone2000v/BBS/physical/comp_methodEnglish.html
http://www.medcyclopaedia.com/library/radiology/chapter04.